Summer 8-15-2018

Developing Multi-Scale Models for Water Quality Management in Drinking Water Distribution Systems

Ahmed A. Abokifa
Washington University in St. Louis

WASHINGTON UNIVERSITY IN ST. LOUIS

School of Engineering & Applied Science

Dissertation Examination Committee:
Pratim Biswas, Chair
John Fortner
Daniel Giammar
Ravindra Gudi
Palghat Ramachandran

Developing Multi-Scale Models for Water Quality Management in Drinking Water Distribution Systems

By

Ahmed A. Abokifa

A dissertation presented to
The Graduate School
of Washington University in
partial fulfillment of the
requirements for the degree
of Doctor of Philosophy

August 2018
St. Louis, Missouri

Table of Contents

List of Figures

List of Tables

Acknowledgments

This dissertation would not have been possible without the support, help, and encouragement I received over the past five years from many individuals, to whom I am sincerely thankful.

First and foremost, I would like to express my deepest and most sincere gratitude to Prof. Pratim Biswas, my Ph.D. advisor and the chair of my dissertation committee. I have been tremendously fortunate and honored to have him as my advisor, and I truly cannot thank him enough for his continuous guidance, support, and encouragement throughout my graduate studies at Washington University. He provided me with the freedom to explore my own research interests and motivated me to pursue my goals on every step of the way. What I learned from him has sure spanned beyond academia, and he will always serve as my inspiration for excellence as I move ahead in my professional career.

I would also like to express my sincere gratitude to my dissertation committee members, Prof. Palghat Ramachandran, Prof. Daniel Giammar, Prof. John Fortner, and Prof. Ravi Gudi for guiding me through my doctoral research and providing valuable inputs to improve this dissertation. I deeply appreciated our fruitful discussions about my future career plans. I am also very thankful to Dr. Cynthia Lo for serving on my dissertation committee for two and half years, and for all the guidance and support she provided throughout the first few years of my Ph.D.

I would like to thank Dr. Jeff Yang from the U.S. EPA and Abhilasha Maheshwari from IIT-Bombay for the extremely productive collaborative research presented in this dissertation. I am also thankful for all the sources that funded my research, especially the U.S. EPA and the Lucy and Stanley Lopata Endowment at Washington University.

I also thank all my colleagues in the Aerosol & Air Quality Research Laboratory for making my graduate school experience so memorable. It is a great honor for me to share this bond with the past, present, and future members of AAQRL. I would like to thank Kelsey Haddad, who apart from being a great collaborator, has also been a very good friend. I am also thankful to Shalinee Kavadyia, Sameer Patel, Ramesh Raliya, Bedia Begüm Karakoçak, Tandeep Chadha, Yao Nie, Sungyoon Jung, Jiayu Li, Girish Sharma, Nathan Reed, Clayton Kacica, Zhichao Li, Sukrant Dhawan, and Robin Wheelus for their friendship and support. I also thank all the past members of the Computational Activated Materials Laboratory (CAML) and all my friends in the EECE Department, especially Alireza Faghaninia, Adewale Adeosun, Kuan-Yu (Mike) Shen, and Tolutola Oyetunde for their friendship and support.

Finally, I want to express my special gratitude to my family; my parents Dr. Amin and Maha Abokifa, my lovely wife Tasbeeh Abdo, and my siblings Mahmoud, Mohamed, and Nada for their continued support and motivation through all these years.

Ahmed Abokifa

Washington University in St. Louis
August 2018

Dedicated to my family

Abstract of the Dissertation

Developing Multi-scale Models for Water Quality Management in

Drinking Water Distribution Systems

by

Ahmed A. Abokifa

Doctor of Philosophy in Energy, Environmental, and Chemical Engineering

Washington University in St. Louis, 2018

Professor Pratim Biswas, Chair

Drinking water supply systems belong to the group of critical infrastructure systems that support the socioeconomic development of our modern societies. In addition, drinking water infrastructure plays a key role in the protection of public health by providing a common access to clean and safe water for all our municipal, industrial, and firefighting purposes. Yet, in the United States, much of our national water infrastructure is now approaching the end of its useful life while investments in its replacement and rehabilitation have been consistently inadequate. Furthermore, the aging water infrastructure has often been operated empirically, and the embracement of modern technologies in infrastructure monitoring and management has been limited. Deterioration of the water infrastructure and poor water quality management practices both have serious impacts on public health due to the increased likelihood of contamination events and waterborne disease outbreaks.

Water quality reaching the consumers' taps is largely dependent on a group of physical, chemical, and biological interactions that take place as the water transports through the pipes of

the distribution system and inside premise plumbing. These interactions include the decay of disinfectant residuals, the formation of disinfection by-products (DBPs), the corrosion of pipe materials, and the growth and accumulation of microbial species. In addition, the highly dynamic nature of the system's hydraulics adds another layer of complexity as they control the fate and transport of the various constituents. On the other hand, the huge scale of water distribution systems contributes dramatically to this deterioration mainly due to the long transport times between treatment and consumption points. Hence, utilities face a considerable challenge to efficiently manage the water quality in their aging distribution systems, and to stay in compliance with all regulatory standards.

By integrating on-line monitoring with real-time simulation and control, smart water networks offer a promising paradigm shift to the way utilities manage water quality in their systems. Yet, multiple scientific gaps and engineering challenges still stand in the way towards the successful implementation of such advanced systems. In general, a fundamental understanding of the different physical, chemical, and biological processes that control the water quality is a crucial first step towards developing useful modeling tools. Furthermore, water quality models need to be accurate; to properly simulate the concentrations of the different constituents at the points of consumption, and fast; to allow their implementation in real-time optimization algorithms that sample different operational scenarios in real-time. On-line water quality monitoring tools need be both reliable and inexpensive to enable the ubiquitous surveillance of the system at all times.

The main objective of this dissertation is to create advanced computational tools for water quality management in water distribution systems through the development and application of a multi-scale modeling framework. Since the above-mentioned interactions take place at different length and time scales, this work aims at developing computational models that are capable of

providing the best description of each of the processes of interest by properly simulating each of its underlying phenomena at its appropriate scale of resolution. Molecular scale modeling using tools of ab-initio quantum chemical calculations and molecular dynamics simulations is employed to provide detailed descriptions of the chemical reactions happening at the atomistic level with the aim of investigating reaction mechanisms and developing novel materials for environmental sensing. Continuum scale reactive-transport models are developed for simulating the spatial and temporal distributions of the different compounds at the pipe level considering the effects of the dynamic hydraulics in the system driven by the spatiotemporal variability in water demands. System scale models are designed to optimize the operation of the different elements of the system by performing large-scale simulations coupled with optimization algorithms to identify the optimal operational strategies as a basis for accurate decision-making and superior water quality management.

In conclusion, the computational models developed in this study can either be implemented as stand-alone tools for simulating the fundamental processes dictating the water quality at different scales of resolution, or be integrated into a unified framework in which information from the small scale models are propagated into the larger scale models to render a high fidelity representation of these processes.

Chapter 1

Introduction

1.1 Background and Motivation

Water supply systems belong to the group of critical infrastructure systems that play a key role in the socioeconomic development of our modern societies and the protection of public health. Their main mission is to provide access to clean and safe water for all our municipal, industrial, and fire-fighting demands. Nevertheless, substantial future challenges face our societies to maintain and upgrade the water infrastructure to cope with the increasing demands under rapid population growth and increased urbanization.

In the United States, much of our national water infrastructure is now approaching the end of its useful life while investments in its replacement and rehabilitation have been consistently inadequate [1]. Treated drinking water is delivered to American households via nearly one million miles of pipes, many of which have been placed in the early to mid-20th century with a lifespan of less than 100 years, and have often been poorly maintained since then. More importantly, the aging water infrastructure has often been operated empirically, and the embracement of the modern technological advances in infrastructure monitoring and management has been limited. The American Society of Civil Engineers (ASCE) estimates that every year nearly 240,000 water main breaks occur. As a result, an estimated 14-18% of the treated drinking water is lost on daily basis due to water leakage. This is around six billion gallons of treated drinking water, equivalent to the consumption of 15 million households [2].

The impacts of the deteriorating drinking water infrastructure, and the lackluster water quality management practices, are not only limited to the environmental and economic aspects, but also extend to pose serious public health concerns. In 2015 alone, almost one-quarter of the U.S. population was served by water systems that had at least one or more reported violations of the Safe Drinking Water Act (SDWA) rules [3]. Approximately 15% of these violations were

reported for breaching health-based standards, such as exceeding the permissible levels or not applying necessary treatment, while the rest included either failing to monitor water for one or more of the regulated contaminants, or failing to report contamination to state authorities or to notify the public. Although health-based violations do not typically constitute the majority of the reported violations [4], they still pose a grave public health hazard, especially when combined with the implications of the weakness in, and the poor enforcement of, the regulatory standards for water contaminants. Indeed, the Centers for Disease Control (CDC) estimates that nearly 19.5 million Americans fall ill every year only from consuming drinking water contaminated by microbiological pathogens, including cryptosporidiosis and Legionnaires' [3,5,6]. This is in addition to the diseases caused by, or directly linked to, other ubiquitous drinking water contaminants. For instance, disinfection byproducts (DBPs), such as trihalomethanes (THMs) and haloacetic acids (HAAs), are known to have carcinogenic, teratogenic, and mutagenic effects [7,8], while exposure to heavy metal contaminants, such as lead and copper, was shown to adversely affect children's cognitive functions [9,10].

1.1.1 Water quality deterioration in the distribution system

Although the quality of the finished drinking water leaving treatment facilities is normally high, water quality deteriorates gradually as it transports through the pipes of the distribution system and inside premise plumbing. The quality of water reaching the consumer's tap is hence largely dependent on a group of physical, chemical, and biological interactions that take place after the water leaves the treatment facility, i.e. where the water utility has the least control over the water quality. For instance, water utilities in the U.S. are required to maintain a sufficient disinfectant residual throughout the distribution system to prevent microbial recontamination. Yet, disinfectants, especially chlorine-based ones, react with the remaining natural organic matter

(NOM) that is left over from water treatment [11], which results in the formation of disinfection byproducts (DBPs). Moreover, the biodegradable fraction of NOM supports the growth of biofilms on the internal walls of the distribution pipes, which can harbor pathogenic species and increase their resistance to disinfectant residuals leading to waterborne disease outbreaks. Furthermore, the consumption of the disinfectant residuals by side reactions with NOM, biofilm, pipe materials, and corrosion products leaves the water with little protection against microbial species that may seep through the cracks of the old pipes and junctions. Corrosion of pipe materials may also result in increasing the frequency of outbreaks, the discoloration of the drinking water [12], or the release of toxic heavy metals [13]. The large scale of water distribution systems contributes dramatically to this deterioration mainly due to the long transport times between treatment and consumption points, which is commonly known as the "water age", since more time is available for the abovementioned interactions to occur [14].

Operating under limited budgets, water utilities face a considerable challenge to preserve water quality in their aging distribution systems and to stay in compliance with all regulatory standards. Operational failures and poor water quality management are the key factors permitting regulatory violations, chemical contamination events, and disease outbreaks, to take place. For instance, in the wake of switching to a more corrosive water source in April 2014, and the discontinuation of mandated corrosion control treatment, a cascade of water quality issues was triggered in the drinking water of the City of Flint, MI. This included widespread lead contamination [15], rapid disappearance of chlorine disinfectant residuals, high levels of THMs, and elevated levels of fecal coliform bacteria and Legionella [16]. Another example of operational failure is the lead contamination crisis that took place in Washington, D.C., 2001-2004, following

the switch of the disinfectant residual from chlorine to chloramine to reduce DBP formation [17,18].

While these events drew substantial public attention, the vast spread of violations across the U.S. necessitates nationwide action. Foremost, voices calling for increasing investments in rehabilitating the drinking water infrastructure have increased. The American Water Works Association (AWWA) estimates the needed investment at more than $1 trillion over the next 25 years [1]. Investments, however, should not be limited to the replacement of old pipes and the upgrading of treatment facilities, but should also extend to include the implementation of modern technologies for water quality monitoring and management to reduce the likelihood of similar operational failures in the future and to promote water quality management.

1.1.2 Smart water systems and real-time water quality management

Many water utilities in the U.S. are starting to show a strong interest in adopting smart technologies in their drinking water distribution systems with the aim of improving their overall performance, efficiency, and reliability. In a recent survey of 340 water utilities across all 50 states, more than 80% of respondents were either already investing, or looking to invest, in some form of smart water technologies to improve their operations [19]. For example, Greater Cincinnati Water Works (GCWW) have been relying on a large-scale real-time water metering system (H_2O Radio) in which readings are automatically transmitted via radio signal. Similarly, the DC water and sewer authority (DCWater) is currently in the process of replacing old water meters with smart, automated meter reading (AMR) systems. Over the next ten years, U.S. water utilities are projected to invest $8.3 billion in smart infrastructure technologies. These investments are expected to grow as cities look to integrate water infrastructure with the broader initiatives of smart cities and Internet of Things (IoT).

Smart water distribution networks belong to the group of modern cyber-physical infrastructure systems, in which on-line monitoring, data collection and transmission, real-time computation, and remote control of the functional processes are tightly integrated [20]. Smart water grids commonly rely on a coordinated network of distributed sensors and remote actuators linked to a supervisory control and data acquisition (SCADA) system, which is a centralized computer that analyzes the data, performs simulations and/or optimization computations, and coordinates the operation of the infrastructure in real-time (Figure 1-1) [21]. The increased interest in embracing smart network technologies over the past decade has been complemented with a consistent growth in the development of related industrial tools and solutions, such as advanced metering technologies [22], sensor networks, data analytics tools, and automation systems.

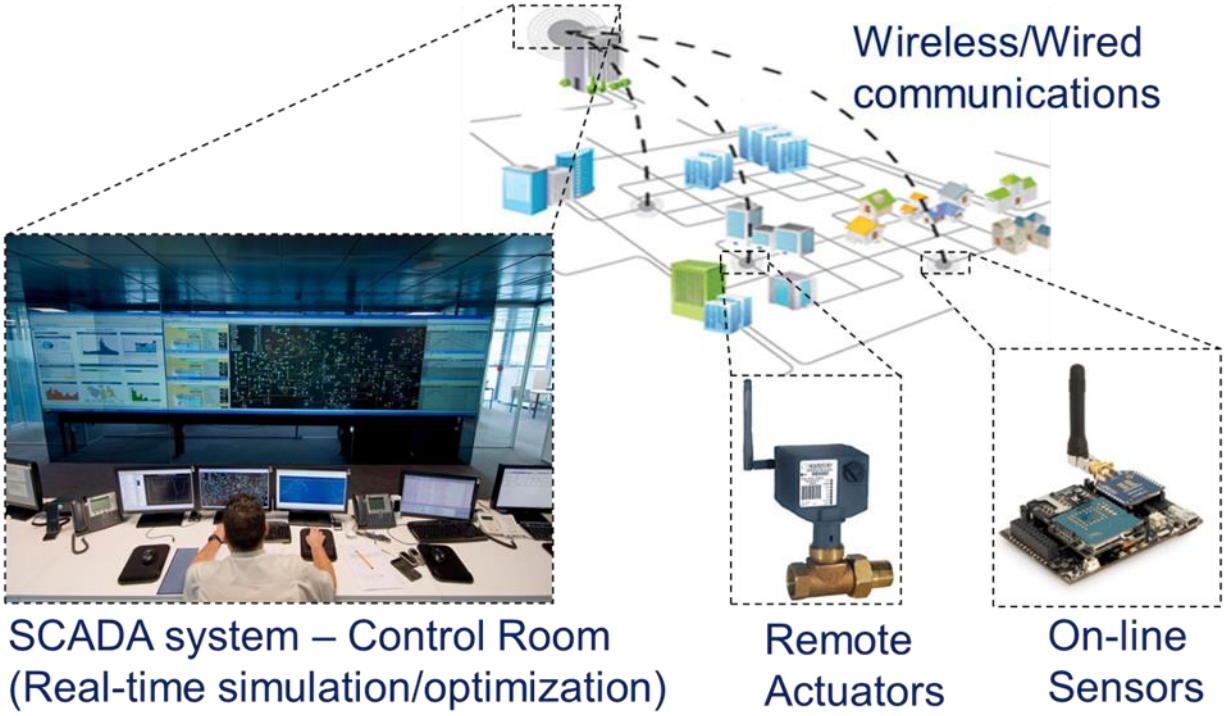

Figure 1-1. Schematic of a smart water infrastructure system integrating on-line monitoring, real-time modeling, and remote-control of the functional processes.

By integrating on-line monitoring with real-time simulation and control, smart water networks offer a paradigm shift to the way utilities manage water quality in their systems. Such framework can enhance the system's *performance* by ensuring the delivery of drinking water to all users at all times with adequate quantity (pressure) and at optimal quality, and enhances the system's *efficiency* by doing so in an economical manner.

Under normal operating conditions**,** the **s**ystem's hydraulics are highly dynamic because they are dependent on water use patterns. Smart meters collect water demand data in real-time, which are then propagated into network hydraulic and water quality simulation models, and optimization algorithms. The latter can sample multiple operational scenarios, and identify the optimal scenario that would achieve the best water quality at the lowest expense. This can be done by controlling pumping patterns in real-time to simultaneously minimize both the pumping energy costs as well as the average water age in the system. A similar framework can also be employed for the optimization of disinfectant dosing schedules to minimize the overall mass doses fed to the system, which reduces disinfection costs as well as DBP levels, while maintaining a sufficient residual throughout the system.

Furthermore, the benefits of implementing smart water systems are not limited to enhancing water quality during regular operations, but also extend to improving the system's *resilience* to extreme events such as deliberate or accidental contamination. By imposing continuous and ubiquitous surveillance over the system via the on-line sensor network, contamination episodes can be ideally detected as soon as they take place. Simulation models running in real-time can then be used to examine different response strategies, and hence can allow the system to absorb, and rapidly recover from, disturbing events with minimal service interruptions and public health consequences. This can be done by the remote control of certain

valves to curb the spread of contaminants by rapidly isolating the infected zones, or by remotely activating booster chlorination stations in case a microbiological contamination takes place.

Despite the substantial potential offered by smart water infrastructure frameworks, their widespread implementation is relatively limited by several fundamental and practical challenges, which is discussed in the following section.

1.2 Scientific Gaps and Engineering Challenges

The successful implementation of a smart water network framework for efficient water quality management relies on three main pillars, computational models for real-time water quality simulation, on-line water quality monitors, and data acquisition and analytics tools. Real-time water quality models should be accurate, to properly simulate the concentrations of the different constituents at the points of consumption, and fast, to allow the implementation in optimization algorithms that sample different scenarios in real-time. On-line water quality monitoring tools should be both reliable and inexpensive. Data analytics tools should be able to handle large quantities of data, while communication routes should be secure to any external breaches or cyber-attacks.

In this section, some of the research gaps and engineering challenges that currently stand in the way of successfully implementing such framework for efficient water quality management are highlighted. The focus of this dissertation is on the key water constituents discussed in the previous sections, namely, disinfectants, disinfection byproducts (DBPs), and lead. Indeed, the highest fractions of the reported SDWA violations in 2015 (by population served) were attributed to the combined disinfectants/disinfection byproducts rule (32%), lead and copper rule (24%), and

total coliform rule (23%) [3]. Hence, improving the control of these key constituents is crucial for making a positive impact on enhancing water quality in the distribution system.

1- The levels of disinfectant residuals in the distribution network are routinely employed by water utilities as a quick and synoptic indicator of the water quality in their distribution systems. Although extensive research efforts have been devoted for modeling the transport and decay of disinfectants in the pipes of DWDSs, the accuracy of most of these models still require significant improvements [23]. This is especially true for the low-flow dead-end zones at the perimeters of the distribution system, where the flow is intermittent and the interplay between the complex hydraulics and the transport of the disinfectant is most pronounced [24–29]

2- While significant modeling efforts have been dedicated over the past three decades to simulate the formation of DBPs during water treatment [30–33], their formation and transport in the distribution system are still not very well understood. Specifically, the role of biofilms in the formation and fate of DBPs has been generally overlooked in previous modeling studies despite their ubiquitous existence in drinking water distribution systems with considerable surface biomass concentrations [34].

3- Since lead release from lead service lines (LSLs) is dictated by multiple parameters, such as pipe age and dimensions, water-use patterns, water chemistry, and previous disturbances to the LSL, computational modeling can offer useful tools for predicting lead release under a diverse range of scenarios. Several studies have pursued modeling the leaching of dissolved lead from LSLs [35–38]. Nevertheless, no previous work has so far addressed the issue of particulate lead mobilization and release into drinking water from a modeling perspective, especially from disturbed or partially replaced LSLs. Moreover, the realistic variation in flow demands under different household consumption patterns was generally overlooked in previous models, yet it is

crucial for accurately simulating both the leaching of soluble lead and the mobilization of lead particulates from LSLs [39].

4- Many water utilities implement booster chlorination as a means to maintaining a uniform residual concentration by injecting the disinfectant at multiple locations in the network with smaller, more distributed, doses [40]. Such practice enables preserving a sufficient residual at all points in the network, while simultaneously reducing the formation of DBPs. Finding the optimal layout and operation of booster chlorination stations has been extensively addressed by several previous studies [41–47], all of which relied on a generic water quality modeling software (EPANET [48]) for the simulation of the decay and transport of the disinfectant. Yet, EPANET's accuracy in simulating chlorine decay and transport in low-flow zones is limited, which can potentially yield flawed results if used to conduct the water quality simulations required to solve network optimization problems, such as the placement and scheduling of booster chlorine stations and real-time boost-response schemes.

5- Due to the complexity and uncertainty of the reactions between chlorine-based disinfectants and the organic matrix, the majority of the kinetic models developed to describe DBPs formation are based on empirical or semi-empirical equations derived by regression analysis [30]. These relationships often include empirical parameters that require fitting to experimental data. Hence, none of these models can be classified as a purely "predictive" model that can be applied to new systems without requiring extensive calibration. In general, a fundamental, molecular-level, understanding of the complex interactions between the disinfectants and organic precursors is missing.

6- Traditional methods used for the analysis of THMs in the aqueous phase include direct aqueous injection, liquid-liquid extraction, and solid-phase extraction. In addition, headspace (HS)

sampling techniques, including static HS, dynamic HS (purge and trap) [49], and solid phase microextraction (SPME) [50] methods, have gained notable popularity because they capitalize on the inherent volatility of THMs enabling direct sampling in the vapor phase to reduce interference [51]. However, most of these techniques still rely on traditional methods, such as gas chromatography (GC) coupled with either mass spectrometry (MS) or electron capture detection (ECD) [52], which makes them costly, bulky, and mostly off-line. Alternative methods for online monitoring are generally expensive, which prohibits ubiquitous and real-time monitoring of DBPs in the system, especially for small systems with limited resources. Recent advances in applied nanoscience offer promising alternatives for developing cheap and highly sensitive sensors that are based on nanostructured materials. Yet, the design and fabrication of such materials have generally been done empirically with a limited understanding of the fundamental interactions between the analytes and the nano-based sensors, which may limit the selectivity and sensitivity of such novel sensors.

Furthermore, despite the numerous merits of implementing modern networking technologies in the sector of critical infrastructure systems, linking the physical components of the infrastructure with cyber-space can expose these systems to the vast realm of cyber-based threats. These attacks can target the SCADA module, the sensors that monitor the system's processes, the PLCs that locally operate the physical components of the infrastructure or the wireless communication routes between the different elements of the CPS. Such cyber-based attacks are capable of remotely perturbing the performance of the system, providing unauthorized parties with access to critical and confidential information, and -if sophisticated enough- can result in physical damage to the assets of the infrastructure. Additionally, such attacks can compromise the water

quality by altering automated treatment schemes or by targeting water quality sensors to suppress contamination warnings, which can pose a significant threat to public safety.

This dissertation addresses some of the abovementioned challenges by developing computational models at different length and time scales as explained in the following section.

1.3 Multi-Scale Modeling Approach

As can be inferred from the research gaps outlined in the previous section, the water supply system is a gigantic reactor in which water quality is controlled by numerous processes that take place at a vast range of length and time scales. Chemical interactions dictate the formation and degradation of the various compounds at the molecular scale, while transport phenomena control the fate and transport of these compounds at the continuum scale. This highlights the need for conducting fundamental studies that consider all the underlying phenomena controlling each of the targeted processes. For instance, accurate description of the fundamental mass-transfer phenomena, such as convection and diffusion, under the dynamic hydraulic conditions of the system is crucial for accurately describing constituent transport in the pipes of the distribution system.

In this dissertation, a multi-scale modeling framework that is capable of providing a fine description of each of the processes of interest at its appropriate scale of resolution is employed to render a high fidelity representation of all the underlying phenomena. Although multi-scale modeling techniques have been frequently applied to chemical reaction engineering problems [53,54], they have seen limited application in environmental systems, particularly engineered aquatic systems. They have been recently introduced to the field of groundwater hydrogeology by integrating models describing phenomena at the microscopic pore scale up to the aquifer scale [55]. In this study, computational models are created and integrated at three interdependent scales

of resolution, namely continuum scale, system scale, and molecular scale as outlined in the coming sub-sections (Figure 1-2).

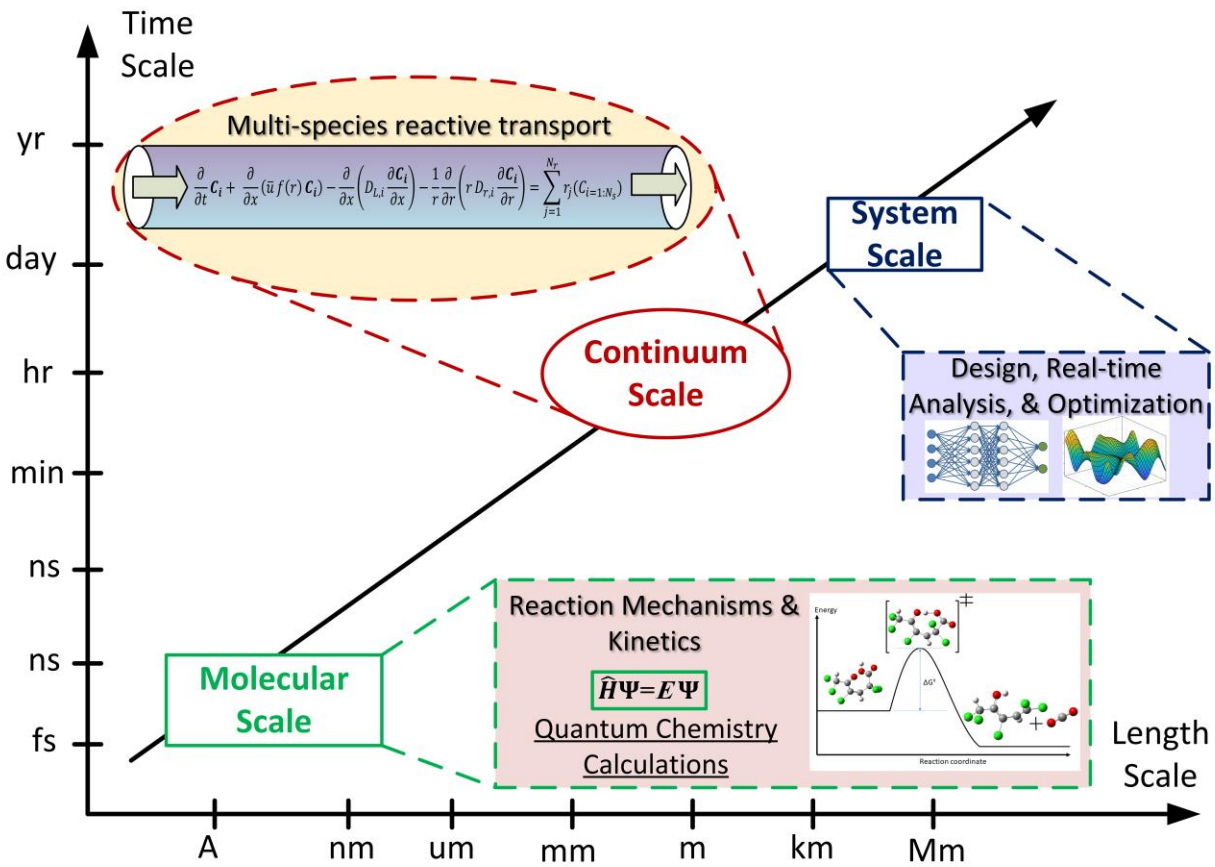

Figure 1-2. Multi-scale modeling and simulation of water quality in environmental systems

Continuum Scale Modeling

The reactive transport of the different water constituents can be modeled by constructing and solving continuum-scale mass-balance equations, which typically take the form of partial differential equations (PDEs) formulated from the fundamental physical principles of mass transfer phenomena, such as convection, diffusion, and dispersion, as well as mass transformation by chemical and biochemical reactions. Numerical schemes are typically employed to solve the resulting system of PDEs since analytical solutions seldom exist for such complex systems of differential equations. Continuum-scale reactive-transport models can simulate the transport and interactions of multiple species, and hence are capable of tracking the chemical and microbiological deterioration of drinking water quality as it travels through the distribution network and inside premise plumbing.

In the context of water distribution systems, continuum-scale models are the most advantageous since they enable the prediction of the spatiotemporal concentration profiles of the different water constituents at the tap. Furthermore, continuum-scale models incorporate the influence of the dynamic hydraulics in the system, which govern the fate and transport of the different constituents. Inputs to such models are usually water quality conditions at the treatment point, and a detailed hydraulic model of the system, while the outputs are the profiles of water quality at the tap. Given their significant utility, most of the work presented in this dissertation is focused on developing and applying continuum scale reactive transport models to simulate the transport and interactions of disinfectants, disinfection byproducts, biomass, and heavy metals (Figure 1-3).

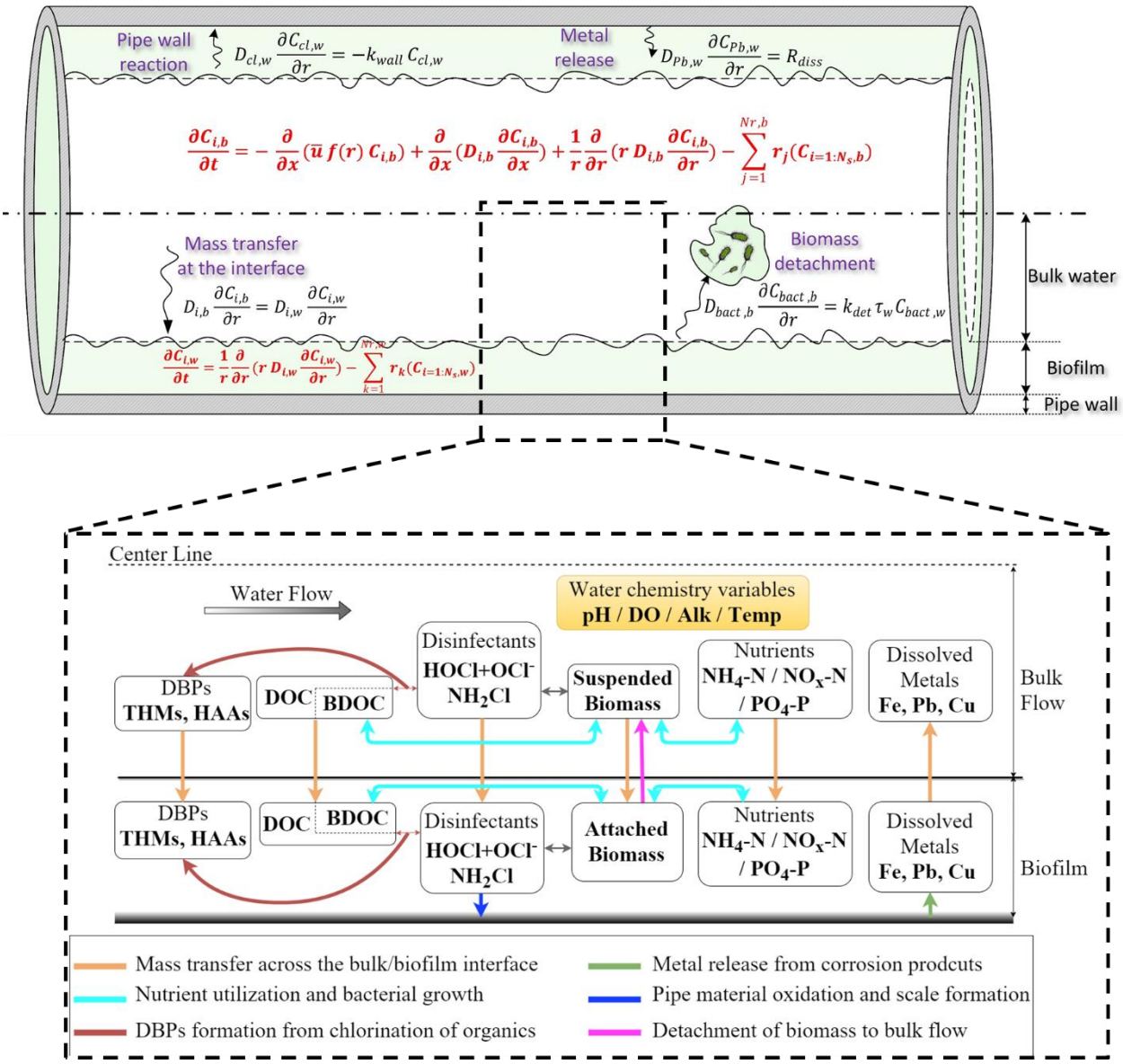

Figure 1-3. Continuum scale reactive transport modeling of multiple interacting chemical and biological species.

Molecular Scale Modeling

Chemical interactions and material properties result from quantum mechanical interactions between atoms or molecules, which can be described by Schrödinger equation. Of the various ab-initio simulation techniques, Kohn-Sham Density Functional Theory (KS-DFT) has become one of the most implemented methods for calculating properties such as electronic structures, adsorption energies, and activation barriers, among many others [56–60]. In this study, a framework for employing first-principles calculations to investigate the mechanisms of chemical reactions is demonstrated by detailing the pathways and kinetics of the reactions leading to the formation of disinfection byproducts. In addition, ab-initio calculations are used to understand the sensing mechanism of novel nano-based sensors for potential applications in the on-line detection of disinfection byproducts.

System Scale Modeling

Systems modeling techniques can be used to sample various possible operational scenarios under both normal operating conditions and extreme events, such as deliberate or accidental contamination. They are capable of identifying the best strategies for running the system, while satisfying multiple economic and environmental objectives and constraints. Thus, systems models can create robust decision-making platforms to promote water quality management and enhance the resilience of the system. In this work, large-scale simulations of the system are coupled with mathematical optimization routines to optimize the water quality reaching all the network users. Over the last decade, genetic algorithms have become one of the most applied optimization techniques in water resources and environmental engineering management [61]. Hence, it has been selected as the optimization routine of choice for the different parts of this dissertation.

Demonstration of a hierarchical multi-scale modeling framework

It is imperative that developing computational models for each of the studied processes at its suitable scale of resolution is expected to give the best results for each process individually and hence enhance the performance of the system as a whole. Yet, multi-scale modeling frameworks work best when models developed at the different scales are connected and the information from one model is propagated into upper-level models in a bottom-up hierarchy. This information can be propagated either directly as the inputs of the upper-level model, or indirectly by providing insights into the formulation and parameterization of the upper-level models.

To give a simple example on how an integrated multi-scale modeling framework can be implemented in the context of water systems modeling, assume that a utility has a certain operational objective, which is to minimize the concentrations of disinfection byproducts at the tap, while maintaining a sufficient residual throughout the system. This can be achieved by optimizing disinfectant dosing patterns at the treatment or booster locations. To find such optimal solution, a system-scale mathematical optimization model is required, which for example, can be a metaheuristic evolutionary optimization routine (e.g. a genetic algorithm). Such system scale model would examine different alternatives for scheduling the disinfectant dosing patterns, and identify the optimal solution that satisfies the DBPs objective and the residual constraint. Yet, this model requires to be connected to a different underlying model that is capable of describing the relationship between the disinfectant doses at the source point(s), and the concentrations at the tap.

Empirical formulae can be used to describe this relationship based on historic water samples collected from the same system. Nevertheless, the accuracy of such empirical formulae in describing the system under operational scenarios outside the range of scenarios that were involved in their derivation will be markedly low, which will affect the accuracy of the overlying

optimization routine. More importantly, such empirical formulae cannot be used to describe any system other than the one they were calibrated to, which limits the usability of such models. A more fundamental approach can be developed instead by employing a continuum-scale reactive-transport model to simulate the formation and transport of DBPs and the decay of the disinfectants in the system. While such a model may still require calibration with field samples when introduced to new systems, it is guaranteed to provide descriptions that are more precise compared to empirical formulae since they are not bound to the specific conditions they were calibrated to.

Similarly, a hierarchical multi-scale modeling approach can be implemented in the description of the formation of disinfection byproducts. The formation of disinfection byproducts (DBPs) is influenced by a wide variety of factors, including the disinfectant type and dose, organic matrix, pH, temperature, bromide concentration, and contact time. Moreover, NOM consists of a heterogeneous and complex array of precursor compounds; each has different reaction kinetics, mechanisms, and pathways for DBPs formation. Hence, due to the complexity and uncertainty of the reactions between chlorine-based disinfectants and the organic matrix, the majority of the kinetic models developed to describe DBPs formation are based on empirical or semi-empirical equations and none of them can be classified as a purely "predictive" model that can be applied to new systems without requiring extensive calibration. As an alternative, fundamental quantum chemistry models, such as Density Functional Theory, can be employed to provide insights on the pathways and kinetics of the chemical reactions leading to DBPs formation. Such insights can be very helpful in developing accurate continuum-scale models describing the reactions between chlorine-based disinfectants and the different fractions of NOM, which would ultimately result in a more accurate model with true prediction abilities.

1.4 Outline of the dissertation

Each chapter of the dissertation aims at addressing one of the gaps or challenges highlighted in section 1.2 by developing and applying computational models at the appropriate scale (Figure 1-4).

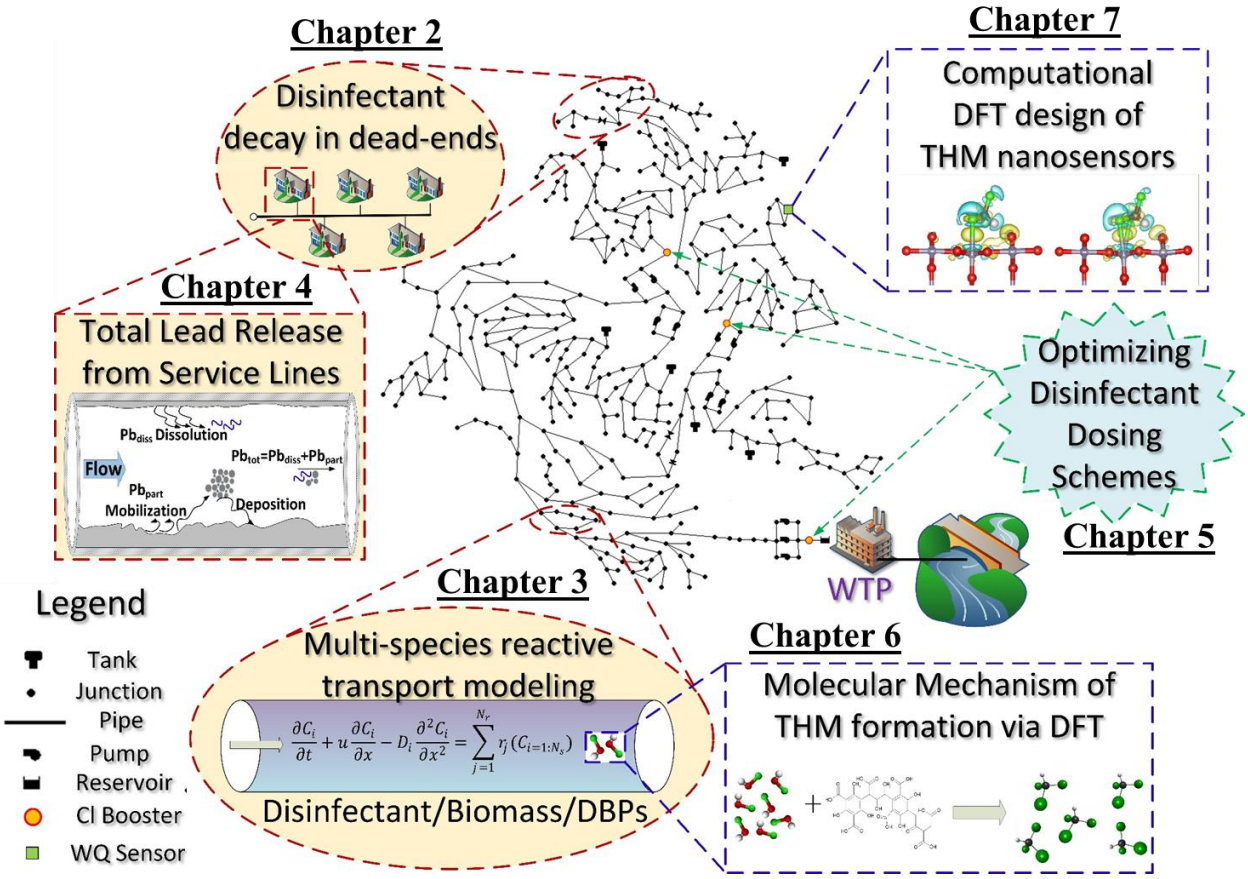

Figure 1-4. A graphical abstract of the work presented in the dissertation highlighting computational models developed at different scales

The remaining of the dissertation is outlined as follows:

Chapter 2 aims at developing an advanced modeling technique for accurately simulating disinfectant transport and decay in dead-end pipes by considering both dispersive solute transport mechanisms and the spatiotemporal distribution of flow demands. Periphery zones of the distribution network, commonly known as the system's *dead-ends*, are where most of the water quality deterioration takes place, mainly due to long stagnation periods and excessive water age. As a result, these zones are particularly more susceptible to water quality monitoring failures [62].

Chapter 3 targets developing a multi-species reactive transport model capable of simulating the disappearance of chlorine residuals, the accumulation of opportunistic pathogens in biofilms, and the formation of regulated DBPs, such as trihalomethanes. The model is used to examine the dynamic interplay between various water constituents to understand the role of biofilms in the formation of DBPs inside the distribution system. This includes the transformation of the biodegradable fraction of natural organic matter into biomass through biofilm growth, biomass release through biofilm detachment, and DBP formation from the parallel reactions of chlorine with precursors of both microbial and non-microbial origin.

Chapter 4 aims to create a computational modeling tool for the simulation of the release and transport of particulate and dissolved lead from full and partially replaced LSLs. A mass transfer model is coupled with a stochastic residential water demand generator to investigate the influence of normal household usage (NHU) flow patterns on lead exposure. This computational tool can enable the estimation of total lead concentrations at the tap as a function of water use patterns.

Chapter 5 aims at demonstrating the impact of implementing an advanced water quality model for simulating the dead-end sections of the distribution network on the outcomes of the

optimization of booster chlorination systems. To this end, an advection-dispersion-reaction (ADR) transport model that considers the spatial distribution of flow demands along the dead-end pipe is coupled with a genetic algorithm based optimization routine.

Chapter 6 proposes a framework for employing first-principles calculations to investigate the mechanisms of the chemical reactions leading to the formation of disinfection byproducts. The proposed framework is demonstrated by investigating the pathways of chloroform formation from the halogenation of dihydroxy aromatic (resorcinol-like) precursor compounds, which have been previously identified as efficient model precursors for trihalomethane formation. Rate coefficients of rate-limiting elementary reactions are calculated from transition state theory (TST) and the minimum-energy path (MEP) is obtained using the intrinsic reaction coordinate (IRC) calculations.

Chapter 7 proposes a framework for implementing ab-initio quantum chemical calculations to investigate and tune the surface chemistry of metal-oxide sensors to enable their on-line operation at ambient temperatures with high sensitivity and selectivity towards regulated DBPs. This framework is demonstrated by focusing on understanding the adsorption and surface interaction mechanisms of chloroform, a model trihalomethane compound, on tin dioxide (SnO_2) nanostructured sensors using theoretical calculations supplemented by sensing experiments.

Chapter 8 lists the conclusions of the present work and provides a number of future directions.

Appendix I proposes an approach for the identification of cyber-physical attacks on WDSs in real-time by detecting suspicious anomalies in the SCADA observations using machine-learning techniques, namely principal component analysis (PCA) and artificial neural networks (ANNs).

Appendix II lists the set of computer codes/programs developed throughout this study.

1.5 References

[1] American Water Works Association, Buried No Longer: Confronting America's water infrastructure challenge, (2012).

[2] American Society of Civil Engineers (ASCE), Infrastructure Report Card: Drinking Water, (2017).

[3] K.P. Fedinick, M. Wu, M. Pandithartne, E. Olson, Threats on Tap: Widespread Violations Highlight Need for Investment in Water Infrastructure and Protections, NRDC-Report. (2017).

[4] S.J. Rubin, Expanded Summary: Evaluating violations of drinking water regulations, J. Am. Water Work. Assoc. 105 (2013) 51–52.

[5] Centers for Disease Control and Prevention, Current Waterborne Disease Burden Data & Gaps, https://www.cdc.gov/healthywater/burden/current-Data.html (Accessed 4/26/2018). (2017).

[6] K. Reynolds, C. Gerba, K.A. Reynolds, K.D. Mena, C.P. Gerba, Risk of Waterborne Illness Via Drinking Water in the United States, Rev. Environ. Contam. Toxicol. 192 (2008) 117–158.

[7] M.J. Nieuwenhuijsen, M.B. Toledano, N.E. Eaton, J. Fawell, P. Elliott, Chlorination Disinfection Byproducts in Water and Their Association with Adverse Reproductive Outcomes : A Review, Occup. Environ. Med. 57 (2000) 73–85.

[8] S.D. Richardson, M.J. Plewa, E.D. Wagner, R. Schoeny, D.M. DeMarini, Occurrence, genotoxicity, and carcinogenicity of regulated and emerging disinfection by-products in

drinking water: A review and roadmap for research, Mutat. Res. 636 (2007) 178–242.

[9] T.A. Jusko, C.R. Henderson Jr, B.P. Lanphear, D.A. Cory-Slechta, P.J. Parsons, R.L. Canfield, Blood lead concentrations< 10 µg/dL and child intelligence at 6 years of age, Environ. Health Perspect. 116 (2008) 243.

[10] B.P. Lanphear, R. Hornung, M. Ho, C.R. Howard, S. Eberly, K. Knauf, Environmental lead exposure during early childhood, J. Pediatr. 140 (2002) 40–47.

[11] M. Sillanpää, M.C. Ncibi, A. Matilainen, M. Vepsäläinen, Removal of natural organic matter in drinking water treatment by coagulation: A comprehensive review, Chemosphere. 190 (2018) 54–71.

[12] J. Nawrocki, U. Raczyk-Stanislawiak, J. Swietlik, A. Olejnik, M. Sroka, Corrosion in a distribution system: Steady water and its composition, Water Res. 44 (2010) 1863–1872.

[13] S. Masters, M. Edwards, Increased Lead in Water Associated with Iron Corrosion, Environ. Eng. Sci. 32 (2015) 361–369.

[14] S. Masters, J. Parks, A. Atassi, M.A. Edwards, Distribution system water age can create premise plumbing corrosion hotspots, Environ. Monit. Assess. 187 (2015) 559.

[15] M. Hanna-Attisha, J. LaChance, R.C. Sadler, A. Champney Schnepp, Elevated Blood Lead Levels in Children Associated With the Flint Drinking Water Crisis: A Spatial Analysis of Risk and Public Health Response., Am. J. Public Health. 106 (2016) 283–290.

[16] D.O. Schwake, E. Garner, O.R. Strom, A. Pruden, M.A. Edwards, Legionella DNA Markers in Tap Water Coincident with a Spike in Legionnaires' Disease in Flint, MI, Environ. Sci. Technol. Lett. 3 (2016) 311–315.

[17] M. Edwards, S. Triantafyllidou, D. Best, Elevated blood lead in young children due to lead-contaminated drinking water: Washington, DC, 2001-2004, Environ. Sci. Technol. 43 (2009) 1618–1623.

[18] M. Edwards, A. Dudi, Role of chlorine and chloramine in corrosion of lead-bearing plumbing materials, J. Am. Water Work. Assoc. 96 (2004) 69–81.

[19] Northeast Group LLC, US Smart Water Infrastructure: Market Forecast (2017 – 2027), http://www.northeast-Group.com (Accessed 4/29/2018). (2017).

[20] E.A. Lee, Cyber Physical Systems: Design Challenges, 11th IEEE Int. Symp. Object Oriented Real-Time Distrib. Comput. (2008) 363–369.

[21] U. Shamir, E. Salomons, Optimal Real-Time Operation of Urban Water Distribution Systems Using Reduced Models, J. Water Resour. Plan. Manag. 134 (2008) 181–185.

[22] A. Cominola, M. Giuliani, D. Piga, A. Castelletti, A.E. Rizzoli, Benefits and challenges of using smart meters for advancing residential water demand modeling and management: A review, Environ. Model. Softw. 72 (2015) 198–214.

[23] W.M. Grayman, A Quarter of a Century of Water Quality Modeling in Distribution Systems, Water Distrib. Syst. Anal. Symp. 2006. (2008) 1–12.

[24] M.R. Islam, M.H. Chaudhry, Modeling of Constituent Transport in Unsteady Flows in Pipe Networks, J. Hydraul. Eng. ASCE. 124 (1998) 1115–1124.

[25] O.N. Ozdemir, A.M. Ger, Realistic numerical simulation of chlorine decay in pipes, Water Res. 32 (1998) 3307–3312.

[26] O.N. Ozdemir, A. Metin Ger, Unsteady 2-D chlorine transport in water supply pipes, Water

Res. 33 (1999) 3637–3645.

[27] V.G. Tzatchkov, A.A. Aldama, F.I. Arreguin, Advection-Dispersion-Reaction Modeling in Water Distribution Networks, J. Water Resour. Plan. Manag. 128 (2002) 334–342.

[28] Z. Li, S.G. Buchberger, V. Tzatchkov, Integrating Distribution Network Models with Stochastic Water Demands and Mass Dispersion, Water Distrib. Syst. Anal. Symp. 2006. (2006) 1–15.

[29] H.A. Basha, L.N. Malaeb, Eulerian-Lagrangian Method for Constituent Transport in Water Distribution Networks, J. Hydraul. Eng. 133 (2007) 1155–1166.

[30] D. Brown, J. Bridgeman, J.R. West, Predicting chlorine decay and THM formation in water supply systems, Rev. Environ. Sci. Biotechnol. 10 (2011) 79–99.

[31] R. Sadiq, M.J. Rodriguez, Disinfection by-products (DBPs) in drinking water and predictive models for their occurrence: A review, Sci. Total Environ. 321 (2004) 21–46.

[32] E.C. Ged, P.A. Chadik, T.H. Boyer, Predictive capability of chlorination disinfection byproducts models, J. Environ. Manage. 149 (2015) 253–262.

[33] S. Chowdhury, P. Champagne, P.J. McLellan, Models for predicting disinfection byproduct (DBP) formation in drinking waters: A chronological review, Sci. Total Environ. 407 (2009) 4189–4206.

[34] J. Woolschlager, B. Rittmann, P. Piriou, Water quality decay in distribution systems – problems, causes, and new modeling tools, Urban Water J. 2 (2005) 69–79.

[35] A. Kuch, I. Wagner, A mass transfer model to describe lead concentrations in drinking water, Water Res. 17 (1983) 1303–1307.

[36] D. Van Der Leer, N.P. Weatherill, R.J. Sharp, C.R. Hayes, Modelling the diffusion of lead into drinking water, Appl. Math. Model. 26 (2002) 681–699.

[37] C.R. Hayes, Computational modelling to investigate the sampling of lead in drinking water, Water Res. 43 (2009) 2647–2656.

[38] P.T. Cardew, Development of a convective diffusion model for lead pipe rigs operating in laminar flow, Water Res. 40 (2006) 2190–2200.

[39] B. Clark, S. Masters, M. Edwards, Profile sampling to characterize particulate lead risks in potable water, Environ. Sci. Technol. 48 (2014) 6836–6843.

[40] M.E. Tryby, D.L. Boccelli, M.T. Koechling, J.G. Uber, R.S. Summers, L. a Rossman, Booster chlorination for managing disinfectant residuals, J. Am. Water Works Assoc. 91 (1999) 95–108.

[41] D.. Boccelli, M.E. Tryby, J.G. Uber, L.A. Rossman, M.L. Zierolf, M. Polycarpou, Optimal Scheduling of Booster Disinfection in Water Distribution Systems, J. Water Resour. Plan. Manag. 124 (1998) 99–111.

[42] M. Tryby, D. Boccelli, J. Uber, L. Rossman, Facility Location Model for Booster Disinfection of Water Supply Networks, J. Water Resour. Plan. Manag. 128 (2002) 322–333.

[43] G.R. Munavalli, M.S.M. Kumar, Optimal Scheduling of Multiple Chlorine Sources in Water Distribution Systems, J. Water Resour. Plan. Manag. 129 (2003) 493–505.

[44] M. Propato, J.G. Uber, Linear Least-Squares Formulation for Operation of Booster Disinfection Systems, J. Water Resour. Plan. Manag. 130 (2004) 53–62.

[45] T.D. Prasad, G.A. Walters, D.A. Savic, Booster disinfection of water supply networks: Multiobjective approach, J. Water Resour. Plan. Manag. 130 (2004) 367–376.

[46] A. Ostfeld, E. Salomons, Conjunctive optimal scheduling of pumping and booster chlorine injections in water distribution systems, Eng. Optim. 38 (2006) 337–352.

[47] Z. Ohar, A. Ostfeld, Optimal design and operation of booster chlorination stations layout in water distribution systems, Water Res. 58 (2014) 209–220.

[48] L.A. Rossman, R.M. Clark, W.M. Grayman, Modeling Chlorine Residuals In Drinking Water Distribution Systems, J. Environ. Eng. 120 (1994) 803–820.

[49] L. Zoccolillo, L. Amendola, C. Cafaro, S. Insogna, Improved analysis of volatile halogenated hydrocarbons in water by purge-and-trap with gas chromatography and mass spectrometric detection, J. Chromatogr. A. 1077 (2005) 181–187.

[50] D.H. Cho, S.H. Kong, S.G. Oh, Analysis of trihalomethanes in drinking water using headspace-SPME technique with gas chromatography, Water Res. 37 (2003) 402–408.

[51] L. Alexandrou, B. Meehan, P. Morrison, O. Jones, A New Method for the Fast Analysis of Trihalomethanes in Tap and Recycled Waters Using Headspace Gas Chromatography with Micro-Electron Capture Detection, Int. J. Environ. Res. Public Health. 14 (2017) 527.

[52] J.L. Pérez Pavón, S. Herrero Martín, C. García Pinto, B. Moreno Cordero, Determination of trihalomethanes in water samples: A review, Anal. Chim. Acta. 629 (2008) 6–23.

[53] S. Raimondeau, D.G. Vlachos, Recent developments on multiscale, hierarchical modeling of chemical reactors, Chem. Eng. J. 90 (2002) 3–23.

[54] P.A. Ramachandran, Advanced Transport Phenomena: Analysis, Modeling, and

Computations, Cambridge University Press, 2014.

[55] T.D. Scheibe, E.M. Murphy, X. Chen, A.K. Rice, K.C. Carroll, B.J. Palmer, A.M. Tartakovsky, I. Battiato, B.D. Wood, An Analysis Platform for Multiscale Hydrogeologic Modeling with Emphasis on Hybrid Multiscale Methods, Groundwater. 53 (2015) 38–56.

[56] A.D. Becke, Perspective: Fifty years of density-functional theory in chemical physics, J. Chem. Phys. 140 (2014).

[57] K. Burke, Perspective on density functional theory, J. Chem. Phys. 136 (2012).

[58] H.S. Yu, S.L. Li, D.G. Truhlar, Perspective: Kohn-Sham density functional theory descending a staircase, J. Chem. Phys. 145 (2016).

[59] J. Klimeš, A. Michaelides, Perspective: Advances and challenges in treating van der Waals dispersion forces in density functional theory, J. Chem. Phys. 137 (2012) 120901.

[60] A.J. Cohen, P. Mori-Sánchez, W. Yang, Challenges for density functional theory, Chem. Rev. 112 (2012) 289–320.

[61] J. Nicklow, P. Reed, D. Savic, T. Dessalegne, L. Harrell, A. Chan-Hilton, M. Karamouz, B. Minsker, A. Ostfeld, A. Singh, State of the art for genetic algorithms and beyond in water resources planning and management, J. Water Resour. Plan. Manag. 136 (2009) 412–432.

[62] V.C.F. Dias, M.C. Besner, M. Prévost, Predicting water quality impact after district metered area implementation in a full-scale drinking water distribution system, J. Am. Water Works Assoc. 109 (2017) E363–E380.

Chapter 2

Water Quality Modeling in the Dead End Sections of Drinking Water Distribution Networks

Results presented in this chapter were published in:

A. A. Abokifa, Y. J. Yang, C. S. Lo, P. Biswas. "Water Quality Modeling in the Dead End Sections of Drinking Water Distribution Networks". Water Research 2016, 89, 107-117.

2.1 Abstract

Dead-end sections of drinking water distribution networks are known hot spots for water quality deterioration. Extended residence time due to water stagnation leads to the decay of disinfectant residuals allowing excessive microbial growth. Water quality models developed so far have employed the approximations of spatial aggregation and temporal averaging of the hydraulic parameters by assigning hourly averaged water demands to skeletonized nodes of the network. Although this practice has generally resulted in minimal loss of accuracy for the predicted disinfectant concentrations in main transmission lines, this has not been the case for the peripheries of the distribution network. This study proposes a new approach for simulating disinfectant residuals in the dead-end pipes by accounting for both spatial and temporal variability in the hydraulic and transport parameters. A stochastic water demand generator was developed to represent residential water use pulses based on a non-homogenous Poisson process. Dispersive solute transport was considered by using highly dynamic dispersion rates. A parametric sensitivity analysis was conducted to assess the model's performance under variability in the transport and reaction parameters. The proposed model showed better agreement with field-measured concentrations of conservative fluoride tracer and free chlorine disinfectant compared to recent advection-dispersion-reaction models in the literature. Accuracy of the simulated concentration profiles showed significant dependence on the spatial distribution of water demands compared to temporal variation. Three correction factors were analytically derived to adjust the residence time, dispersion rate, and wall decay rate in order to overcome simulation errors caused by the spatial aggregation approximation.

2.2 Introduction

Disinfection is routinely applied as the final treatment step in typical drinking water treatment plants. A sufficient residual concentration is typically maintained throughout the distribution system to prevent microbiological contamination of the treated water as it transports through the pipes of the distribution network. For instance, the U.S. Environmental Protection Agency (USEPA) requires water utilities to maintain a detectable chlorine residual throughout the distribution system under the Surface Water Treatment Rule (SWTR) [1,2]. Chlorine, which is the most commonly used disinfectant worldwide, is a highly reactive oxidant that reacts with a variety of materials in both the bulk flow and at the pipe wall.

Over the last three decades, extensive research has been devoted to the development of water quality models that simulate chlorine transport and decay in water distribution systems [3]. In the early work done by Biswas et al. [4], a generalized model for steady state chlorine consumption that accounts for axial convection and radial diffusion was developed. It was the first model to account for chlorine decay at the pipe wall in addition to the bulk liquid phase. Rossman et al. [5] developed a film mass transfer approach to account for radial chlorine transport and its further reaction at the pipe wall. This 1-D advection-reaction model was later incorporated in the water-quality simulation module of the well-known software package EPANET, which is widely used by water utilities worldwide. Although EPANET was able to accurately predict the field observed disinfectant concentrations for the transmission mains, simulations of the secondary branch pipes, a.k.a. the “dead-ends” at the perimeters of the distribution system, were substantially less accurate.

Dead-end zones are generally characterized by intermittent low-flow events and frequent stagnations. They are known to be responsible for most of the water quality deterioration in the

distribution system, and are particularly more susceptible to water quality monitoring failures [6]. The long residence time typically encountered in these zones results in the disappearance of chlorine residuals, excessive growth of biofilms, and high DBPs formation [7–9]. Few researchers gave special attention to water quality modeling in dead-ends, although they typically comprise a non-trivial fraction (≥25%) of the total water infrastructure and tend to service an even larger percentage of the residential consumer base [10].

Axworthy and Karney [11] were the first to shed light on the importance of considering dispersive transport in low flow velocity pipes where they showed that advective transport models would either under- or over-predict the actual concentrations. Following this earlier work, several studies developed numerical advection-dispersion-reaction (ADR) models to accurately simulate water quality under low flow conditions [10,12–16]. Nevertheless, spatial aggregation of water demands was typically employed in the hydraulic, and subsequently water quality, simulations of all the above-mentioned studies. Under this approximation, multiple water uses are lumped into a single demand point assigned to a specific junction on the network grid, a practice commonly known as network "skeletonization".

For main water arteries, spatial aggregation of flow demands is a reasonable approximation because the ratio of the "on-pipe" demands compared to the flows transmitted to the downstream sections of the network is relatively small. For dead-ends, however, all water demands are being directly withdrawn from the pipe at different spatial locations as shown in Figure 2-1a. Hence, applying spatial aggregation to the dead-end links would consistently overestimate the average flow velocity at the different axial locations along the pipe, and more importantly, under-simulate the actual residence time as depicted in Figure 2-1c. The later would cause the simulated disinfectant concentrations to be systematically over-predicted, which was observed in previous

studies [10,17]. Alternatively, unrealistically high wall demand coefficients had been used to fit the field measured concentrations [4,18,19]. The first study to address water distribution network dead-ends was done by Buchberger and Wu [20]. They generated the realistic spatial and temporal distributions of the flow rate and the corresponding Reynolds number at different sections along the dead-end pipe. Yet, their work was only limited to modeling the hydraulics, and was never extended to water quality simulations.

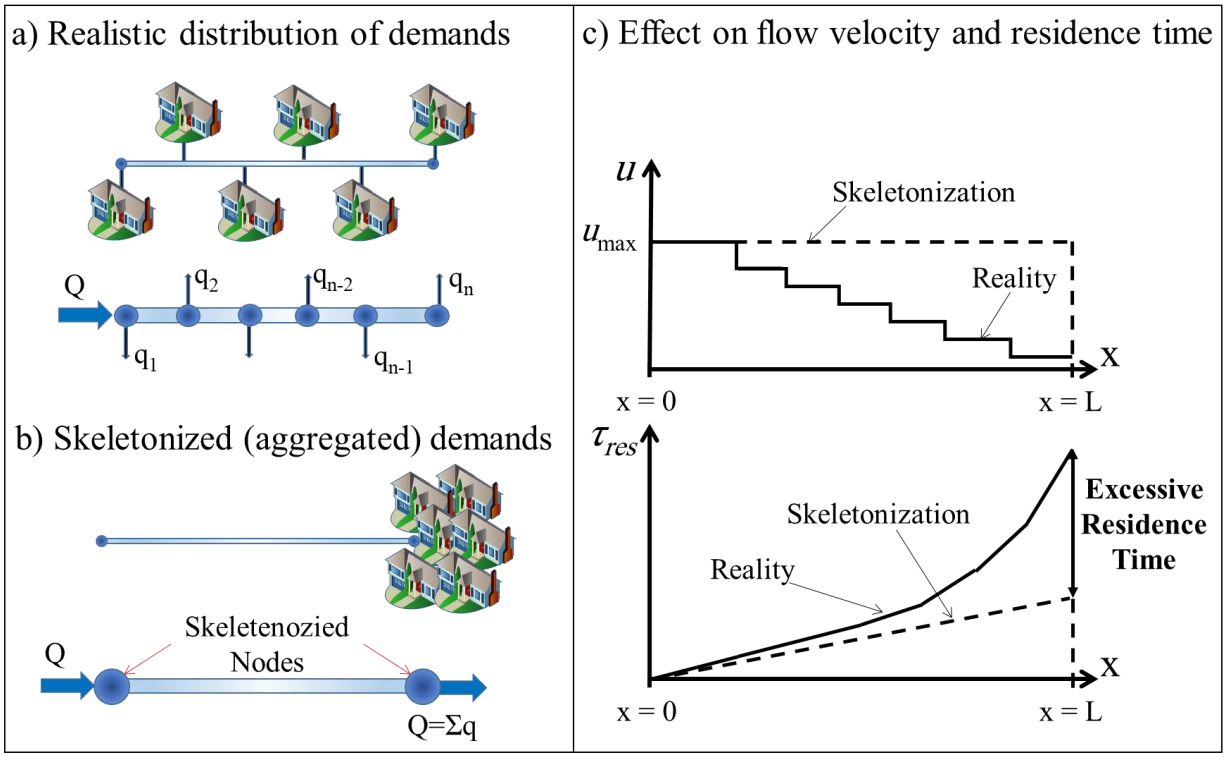

Figure 2-1. (a, b) Realistic vs skeletonized representation of flow demands, and (c) Over and under-estimation of average flow velocity and residence time due to skeletonization.

The primary objective of this study is to develop a realistic modelling approach to simulate water quality in dead-ends while considering both the temporal variation and spatial distribution of flow demands, and the subsequent variability in the transport parameters. The new model (Washington University Dead End Simulator – WUDESIM), is coupled with a stochastic flow demand generator based on a nonhomogeneous Poisson process to simulate residential water use pulses on fine time scales. In addition, the model employs a genetic algorithm optimization routine for the calibration of the hydraulic profile of the dead-end.

2.3 Methodology

2.3.1 Mathematical Background

Disinfectant transport and decay in a dead-end pipe can be appropriately modeled by a dynamic 2-D convection-diffusion-reaction equation in cylindrical coordinates to represent the mass balance on the disinfectant concentration $C(x, r, t)$, which can be written as [4]:

$$\frac{\partial C}{\partial t} = -\frac{\partial}{\partial x}(u\, f(r)\, C) + \frac{\partial}{\partial x}\left(D\frac{\partial C}{\partial x}\right) + \frac{1}{r}\frac{\partial}{\partial r}\left(r\, D\frac{\partial C}{\partial r}\right) - k_b C \qquad (2-1)$$

where, x & r are the axial and radial space coordinates, respectively (m); t is the time (sec); u is the average flow velocity in the pipe (m/sec); $f(r)$ is the radial flow distribution parameter; D is the molecular diffusivity of the disinfectant in water (m^2/sec); and k_b is the first order decay rate constant in the bulk flow (sec^{-1}).

Disinfectant consumption at the pipe wall can be simulated by imposing a Robin type boundary condition to describe the instantaneous exhaustion at the wall ($r = a,\ \ D\partial C/\partial r + W_d C = 0$) where, a is the pipe radius (m), W_d is the wall demand parameter (m/sec). This boundary condition only applies to pipes with fast chlorine reaction at the wall, i.e. is not limited

by the rate of radial diffusion. For thicker pipe scales with significant biofilm buildup, a two layer mass transfer approach would more appropriate [14].

The numerical solutions for the dynamic 2-D convection-diffusion-reaction equation are typically computationally intensive. Previous researchers treated this by either removing the time dependence represented by the accumulation term and then solving a steady state 2-D equation, or reducing the model to an unsteady 1-D advection-dispersion-reaction (ADR) model to preserve the dynamic behavior of solute transport in water distribution systems. The latter approach was implemented in this study. Hence, Equation 2-1 is simplified to:

$$\frac{\partial C}{\partial t} = -u\frac{\partial C}{\partial x} + E\frac{\partial^2 C}{\partial x^2} - KC \qquad (2-2)$$

where, E is the effictive longitudinal dispersion coefficient (m^2/sec), K is the overall lumped first order decay constant (sec^{-1}) that accounts for disinfectant consumption both in the bulk phase and at the pipe wall. Rossman et al. [5] used a lumped mass-transfer coefficient to account for the radial transport of solute and the further first order reaction at the pipe wall analogous to film models for heat transfer: $K = k_b + R_w$, where, $k_b$is the bulk demand coefficient (sec^{-1}); R_w is the overall wall demand: $R_w = k_w k_f/[r_h(k_w + k_f)]$; k_w is the wall decay constant (m/sec); k_f is the mass transfer coefficient (m/sec); and r_h is the pipe hydraulic mean radius (m). Removing the dispersion term in Equation 2-2 gives the 1-D advection-reaction equation incorprated in EPANET.

The 1-D ADR model in the dimensionless form can be written as:

$$\frac{\partial C^*}{\partial t^*} = -\frac{\partial C^*}{\partial x^*} + \frac{1}{Pe}\frac{\partial^2 C^*}{\partial {x^*}^2} - Da\ C^* \qquad (2-3)$$

where, C^* is the dimensionless concentration ($C^* = C/C_0$); t^* is the dimensionless time ($t^* = t/\tau_0$); x^* is the dimensionless axial distance ($x^* = x/L$); Pe is the axial Peclet number ($Pe =$

$u\,L/E$); and Da is the Damkohler number ($Da = K\tau_0$). C_0 is a reference concentration usually taken as the inlet concentration (mg/L); while τ_0 is the characteristic residence time ($\tau_0 = L/u$) (sec); and L is the pipe length (m).

The dimensionless Peclet number (Pe) dictates whether the solute transport is dominated by advection or dispersion/diffusion. For axial mass transfer in a pipe geometry, the Peclet number can also be seen as the ratio between the characteristic time scales of both phenomena. The characteristic advection time can be written as: $\tau_a = \frac{L}{u}$, while the characteristic time for axial dispersion, assuming that molecular diffusion is negligible compared to dispersion under laminar flow conditions, can be expressed as: $\tau_d = \frac{L^2}{E}$. Hence, Peclet number can be written as: $Pe = \frac{\tau_d}{\tau_a} = \frac{uL}{E}$. Thus for conditions where the characteristic time for dispersion is much longer than advection, the transport is advection-dominated (i.e. Peclet number is very large, and the dispersive transport term in equation 2-3 vanishes, which gives the 1-D advection-reaction equation). On the other hand, when both time scales are comparable (Pe is approximately equal to unity), both phenomena must be considered. Under low flow conditions, Pe approaches zero, and the transport is mainly dominated by dispersion (or diffusion in case of stagnation). It is important to note here that, while dead-ends mostly operate under laminar flow conditions, a few events of transitional and turbulent flow regimes do occasionally take place when high flow events are incurred. Hence, it is important to have both advection and dispersion/diffusion terms in the equation to accurately simulate the dead-end pipe under all scenarios. Similarly, the Damkohler number can be seen as the ratio between the characteristic time scales for advection and reaction, which for a first order reaction rate it can be written as: $Da = \frac{\tau_r}{\tau_a} = \frac{(L/u)}{(1/K)} = KL/u$. Here, K is the lumped first order rate constant that includes both bulk and wall reactions and mass transfer to the pipe wall.

The main concern that arises from reducing the 2-D model in Equation (2-1) into the 1-D model in equation (2-2) is the error caused by neglecting the combined effects of radial molecular diffusion and the flow velocity profile in the radial direction (e.g. $f(r) = 2[1 - (r/a)^2]$ for fully developed laminar flow). The incorporation of an appropriate dispersion coefficient is hence crucial for the success of such approximation. For this purpose, the classical work by Taylor [21] has been widely used in the literature, where the dispersion coefficient in the steady laminar flow can be expressed as:

$$E_T = \frac{a^2 u^2}{48D} \qquad (2-4)$$

However, Taylor's formula only reflects the ultimate value that the dispersion coefficient approaches after a certain initialization period has elapsed ($t > 0.5\frac{a^2}{D}$). For a typical dead-end pipe with a 6-inch diameter, this initialization period is approximately twenty weeks for a solute with a molecular diffusivity in the order of 10^{-9} m^2/sec (e.g. chlorine). Furthermore, the extended stagnation periods typically encountered in dead-ends lead to partial loss of the dispersion memory between demand pulses. Therefore, the longitudinal dispersion in pulsating laminar flow is expected to always be within the initialization period, and the use of a highly dynamic time-evolving dispersion coefficient is essential to simulate the complex nature of flow demands in dead-ends. In this study, the dynamic rates of dispersion developed by Lee [22] for pulsating laminar flows are implemented. The instantaneous rate of dispersion is expressed as the dynamic weighted average of two factors: (i) the dispersion memory from previous pulses; and (ii) the nonlinear excitation from current pulse. The instantaneous rate of dispersion during pulse (*k*) is expressed as:

$$E_k(t) = E_{k-1}(t_{k-1})\left(\frac{u_k}{u_{k-1}}\right)\exp\left(-\frac{t - t_{k-1}}{t_0}\right) + E_{T_k}\left[1 - \exp\left(-\frac{t - t_{k-1}}{t_0}\right)\right] \qquad (2-5)$$

where, E_{k-1} is the instantaneous dispersion coefficient for pulse $(k-1)$; t_{k-1} is the ending time of pulse $(k-1)$; E_{T_k} is the Taylor's dispersion coefficient for pulse (k); $t_0 = a^2/16D$ is the Lagrangian time scale. If the flow is intermittent so that pulse $(k-1)$ is stagnant (i.e., $u_{k-1}=0$); then the first term on the RHS telescopes to pulse $(k-2)$. The time-averaged rate of dispersion during any pulse (k) can hence be calculated as:

$$\bar{E}_k = \frac{1}{(t_k - t_{k-1})} \int_{t_{k-1}}^{t_k} E_k(t)dt \qquad (2-6)$$

The present study is the first to use these highly dynamic dispersion rates, which was made possible by coupling the water quality simulator with a stochastic water demands generator that simulates the demand pulses on a second by second basis.

In dead-end pipes, the average flow velocities are generally low and laminar conditions typically prevail. Furthermore, solute transport is mostly dominated by axial dispersion, as the values of Pe are generally small. However, large flow rates can also take place during peak demand hours where occasional transitional or turbulent conditions may occur leading to advection dominated transport. Hence, longitudinal dispersion in the transitional and turbulent regimes (Re>2,300) was also considered in this work by using the empirical formula derived by Sattar [23] using gene expression programming (GEP):

$$D_x^* = \frac{c_1 f^{*^{c_2}} d^{c_3}}{u} \qquad (2-7)$$

where, D_x^* is the inverse of the radial Peclet number; f^* is the pipe friction factor [24]; d is the pipe diameter; $\{c_i\}_{i=1}^{3}$are three empirical parameters: $c_1 = 219$; $c_2 = 2.82$; and $c_3 = -0.82$. The formula (GEP3) was chosen as it showed reasonable description of the experimental data for Reynolds numbers in the range (2,300 < Re <10,000). It's worth mentioning here that, although

widely employed in water distribution system models, the classical formula developed by Taylor [24] for the dispersion rate under turbulent conditions wasn't implemented in this study. The reason is that this formula is only valid under highly turbulent regimes (Re > 20,000) [25], a situation that is highly unlikely to take place in dead-ends where flow regimes are mainly laminar with only occasional transitional to early turbulent flows.

Because of the spatial variation in flow velocity at different axial locations, transport and reaction parameters are not only considered as functions in time, but axial coordinate as well, i.e.: $u = u(x,t)$; $E = E(x,t)$; and, $K = K(x,t)$. This is simulated by splitting the dead-end into a specified number of sections of variable lengths based on the locations of the draw off points (Figure 2-1a). The flow velocity decreases in the axial direction as a result of the withdrawals and the hydraulic profile is simply generated by mass continuity.

The initial condition is expressed by a given concentration profile in the pipe. The boundary conditions are expressed as follows:

(1) at $x = 0$; $C = C_0(t)$. The inlet node concentration is specified as a prescribed time series. This is the solute source.

(2) at $x = L$; $\partial C/\partial x = 0$. The terminal node is described by a no-flux (free discharge) condition.

2.3.2 Numerical Approach

Analytical solutions for the ADR equation have only been developed for limited cases. For example, solutions developed by van Genuchten and Alves [26] can only be applied to cases of steady flow where the dispersion coefficients and reaction rates are time independent. Although a wide range of numerical methods has been developed for solving the dynamic ADR model, mixed Eulerian-Lagrangian numerical methods are particularly known to be efficient in solving both dispersion-dominated and advection-dominated transport problems [27]. They were successfully applied to simulate solute transport in drinking water distribution systems [10,16,17]. In the present study, a two-stage Eulerian-Lagrangian numerical scheme combined with the numerical Green's function technique proposed by Tzatchkov [10] is implemented. First, the Lagrangian step is executed using the explicit method of characteristics (MOCs) to solve the advection and reaction terms, then the Eulerian step is executed to solve the dispersion term using an implicit finite difference scheme. The details of the employed Eulerian-Lagrangian scheme are shown in the supplementary information section 2.10.1. A special form of the original ADR equation is used to describe mass conservation at the withdrawal nodes due to the local discontinuity in the transport and reaction parameters u, E and K; further details are given in supplementary information section 2.10.1.

2.3.3 Stochastic Demand Generator

A stochastic model is developed in this study to simulate the behavior of flow demands in residential dead-ends that exhibit random temporal and spatial fluctuations. The model is connected to the dead-end water quality simulator to provide the time variable flow demands at different withdrawal nodes. The model is developed based on the non-homogenous Poisson process that was first introduced by Buchberger and Wu [20] to stochastically simulate the

intensity, duration and frequency of residential demands. Demand pulses are generated on instantaneous basis (i.e. second-by-second) as Poisson rectangular pulses arriving at consumption nodes at a non-homogenous arrival rate. Demand volumes are calculated as the summation of individual pulse volumes; that is the product of pulse intensity times duration. Flow rates are then averaged over a specified period known as pulse aggregation interval, which was chosen to be 5 minutes in this study to sufficiently represent the potential effects of stochastic demands on model hydraulics and transport based on the results of Yang and Boccelli [28]. Log-normal probability distributions were used to describe the intensity and duration of water pulses as Buchberger and Wells [29] found that they provide favorable description of actual residential demands. The underlying equations used to develop the model are described in [30], and are hence not reproduced here. Indoor and outdoor water demands are generated as separate Poisson pulses and then aggregated to give the total instantaneous nodal demand. The statistical parameters used for both indoor and outdoor demand intensities and durations are taken similar to Nilsson et al. [31].

2.3.4 Case Study for Model Application

The present model is first applied to simulate the concentrations of free chlorine and fluoride tracer in the dead-end links of the Cherry Hills/Brushy Plains (CHBP) service area of the South Central Connecticut Regional Water Authority (SCCRWA). This residential network was previously used by Rossman et al. [5] to compare the results of EPANET with sampling data collected during the field campaign conducted by SCCRWA on August 13-15,1991. The results of this specific campaign were later used by many researchers to verify water quality models in distribution systems [10,16,18]. The original study used a skeletonized grid of the actual all-pipe CHBP network that has 32 dead ends. Sampling was conducted at the pump station and eight other locations through the network, two of which were on the terminal junctions of dead-end links -

Pipes 10 and 34 [5]. A list of the simulations performed using WUDESIM is given in Table 2-1. Eight different simulations were conducted to verify the model against field measurements, four Monte-Carlo ensembles were executed for the uncertainty analysis study, and 15 simulation scenarios were performed to examine the sensitivity of the model results to different input parameters.

Table 2-1. List of simulations performed in Chapter 2

I – Model Verification Simulations			
Simulation No.	Solute	Pipe No.	Axial Hydraulic Profile
1-A, B	Fluoride	10, 34	GA Calibrated
2-A, B	Chlorine	10, 34	GA Calibrated
3-A, B	Fluoride	10, 34	Equal Shares
4-A, B	Chlorine	10, 34	Equal Shares
II – Monte-Carlo Simulations			
MC-Ensemble	Solute	Pipe No.	Demand Variation
5-A	Fluoride	10	Spatial
5-B	Fluoride	10	Temporal
6-A	Chlorine	10	Spatial
6-B	Chlorine	10	Temporal
III – Sensitivity Analysis Simulations			
Simulation No.	Variation Parameter		
7	Base Case		
8-A, B	Flow rate		
9-A, B	Pipe diameter		
10-A, B	Pipe length		
11-A, B	Average inlet concentration		
12-A, B	Amplitude of inlet sine wave		
13-A, B	Period of inlet sine wave		
14-A, B	Bulk decay rate constant		

2.4 Results and Discussion

2.4.1 Model Verification

Since limited data was available on the actual water use locations in the CHBP network, Google Earth® software was used to locate the two dead ends and identify the number of consumption points on each dead end using aerial photos captured on March 15, 1992 – approx. 7 months after the sampling study (Supplementary material section 2.10.2). The axial locations of the withdrawal nodes were scaled from the aerial photos to be used in the simulation. Aerial photos (Figure S 2-2) showed that pipes 10 and 34 could be simulated with seven and five consumption nodes, respectively, with an axial spacing of at least 60 ft between every two consecutive nodes. This number was determined by counting the number of consumption points on each dead end assuming each building to represent a single consumption point. Consecutive buildings with a spacing less than 10% of the total dead end length were lumped into one consumption point.

The accuracy of any water quality simulator is largely controlled by the proper calibration of the underlying hydraulic model. Individual water consumption of each withdrawal node on the dead-end links was unknown, unlike the lumped hourly demands that were available through Example 2 in EPANET as generalized hourly demands. Hence, there was a need for a special technique to calibrate the time-averaged axial hydraulic profile in each of the two dead-ends. Several techniques were previously developed for the calibration of hydraulic models in water distribution systems [32]. Of these techniques, evolutionary optimization algorithms are usually preferred mainly because they do not involve complex mathematical procedures, yet they are robust and accurate in locating optimal solutions. For instance, genetic algorithms (GAs) were previously used for hydraulic calibration in water distribution systems by few researchers [33,34]. In the present study, genetic algorithms were used to calibrate the hydraulic model of each

simulated dead end by optimizing the share of each of the withdrawal nodes from the total pipe demand to minimize the error between simulated and filed measured concentrations. The implemented fitness function represented the Coefficient of Variation of the root mean square deviation (RMSD) between field measured and simulated concentrations CV_{rms}:

$$Fitness = CV_{rms} = \frac{1}{\bar{C}_{meas}} \sqrt{\frac{\sum_{i=1}^{N_{meas}} (C_i - C_{sim})^2}{N_{meas}}} \qquad (2-8)$$

Where, CV_{rms} is the deviation function targeted for minimization; C_i is the field measured concentration at some time *t* (mg/L); $C_{sim}$is the simulated concentration at time *t* (mg/L); N_{meas} is the number of field measurements; $\bar{C}_{meas}$ is the average over all field measured concentrations (mg/L). Fluoride tracer measurements were used for hydraulic calibration because the transport of non-reactive solutes is only controlled by advection and dispersion.

Figure 2-2 shows the simulation results of the present model (WUDESIM) for fluoride tracer in comparison with EPANET and ADRNET [17] models plotted against field measurements. Consistent with the literature, the accuracy of advection-based models, such as EPANET, in simulating solute transport in dead-ends is substantially lower than advection-dispersion models, mainly because solute transport in dead-ends is dispersion-dominated. ADRNET is an advection-dispersion-reaction model that incorporates (Eq. 2-2) as the governing equation. Both the present model and ADRNET use Eulerian-Lagrangian numerical schemes and use stochastic flow demands generated based on Poisson processes. The reason for choosing ADRNET to be compared against WUDESIM is to test the effect of considering the spatial distribution of flow demands and transport parameters as well as the highly dynamic dispersion coefficients implemented in WUDESIM on the simulation accuracy under laminar conditions. It is clear from the fluoride tracer results that the present model predicts field measurements slightly

better than ADRNET, mainly due to the realistic consideration of flow velocity and dispersion coefficient. The optimized average hydraulic flow profile generated from GAs calibration of the shares of the withdrawal nodes indicated that the share of the last withdrawal node on both dead ends was noticeably larger than all other nodes in the optimized flow profile as it alone accounted for 35-40% of the total water volume consumed during the simulation period. Going back to the original sampling study presented by Clark et al. [35], we found that a special fitting was installed on the hydrants where samples were collected to allow continuous flow of water at a rate ranging from 3.79 to 15.14 lpm (1 to 4 gpm). This could explain the reason why the terminal nodes had the largest demand share, and at the same time proved the efficiency of the implemented GA in optimizing the hydraulic profile.

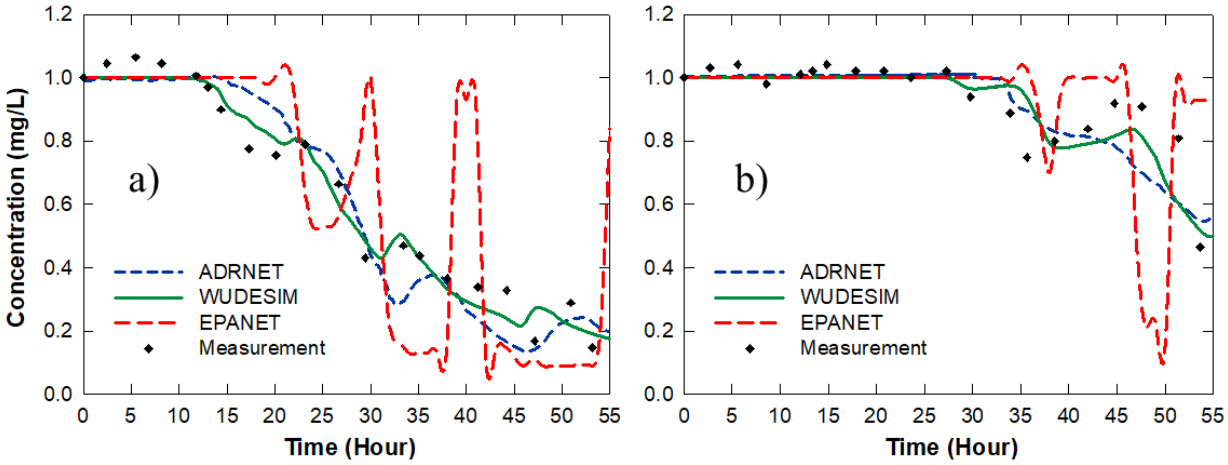

Figure 2-2. Fluoride tracer concentrations simulated by ADRNET model [17], EPANET [5] and WUDESIM (present model) against field measurements for the terminal junctions of: (a) Pipe 10; (b) Pipe 34.

Figure 2-3 shows the results of the simulated concentrations of free chlorine by the three models plotted against field measurements. The values of the bulk and wall decay coefficients were taken as k_b=0.55 day^{-1} and k_w=0.15 m/day, matching the values previously used by EPANET and ADRNET. For both dead ends, the simulated concentrations by WUDESIM were in a remarkably better agreement with field measurements as illustrated by the CV_{rms} values shown in Table 2-2. The present model better simulates the excessive residence times in dead ends compared to ADRNET that tends to systematically overestimate the chlorine concentrations as spatial aggregation approximation under-simulates the residence time in dead ends. Chlorine disappearance in dead ends is mainly caused by long periods of stagnation usually encountered in the times of low demand. This also leads to excessive concentrations of disinfection by products DBPs in the extremities of the distribution network [36].

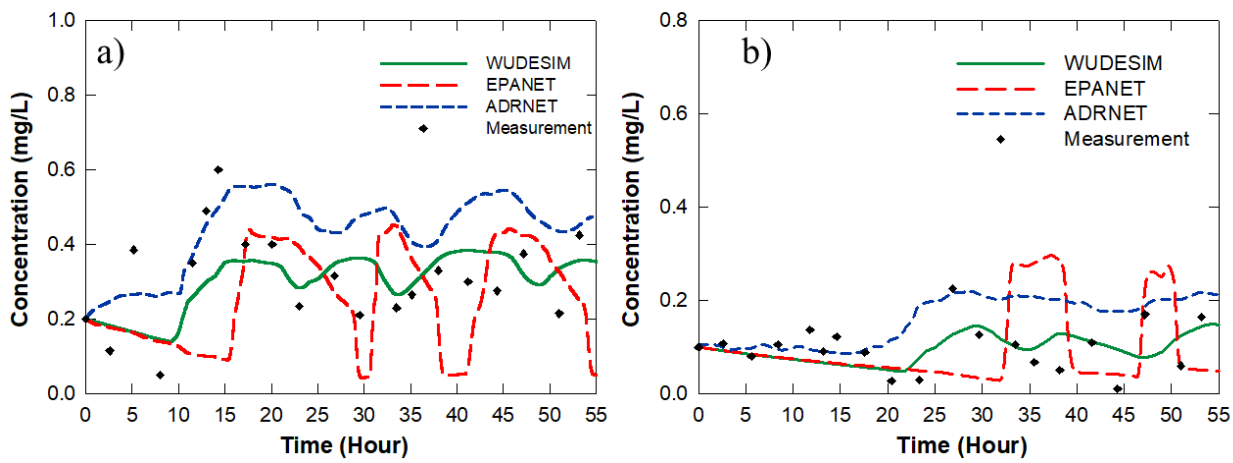

Figure 2-3. Free chlorine concentrations simulated by ADRNET model [17], EPANET [5] and WUDESIM (present model) against field measurements for the terminal junctions of: (a) Pipe 10; (b) Pipe 34.

The high degree of detail used herein to simulate dead end pipes represented by considering the exact axial locations of withdrawal points and the calibrated share of each node of the overall demand may not be available for water utilities in the design stage of the water distribution system. Hence, previous WUDESIM simulations were repeated but with considering equally spaced nodes with equal demand shares instead of the GA calibrated demands, i.e. assuming that the only known dead-end parameter is the number of withdrawal nodes. As shown in Table 2-2, simulation accuracy represented by the deviation function CV_{rms} dropped for all cases as a result of this approximation compared to the calibrated WUDESIM model. However, it still showed higher accuracy compared to both ADRNET and EPANET models especially for the case of chlorine, as the simulated residence time in the dead end is still closer to reality.

Table 2-2. CV_{rms} values between field measurements and simulation results

Solute / Pipe	Simulation Model			
	WUDESIM GA Calibrated Shares	WUDESIM Equal Shares	ADRNET	EPANET
Fluoride Pipe 10	8.45%	13.69%	14.84%	33.49%
Fluoride Pipe 34	8.14%	9.00%	9.26%	21.71%
Chlorine Pipe 10	36.66%	41.59%	54.22%	64.12%
Chlorine Pipe 34	50.10%	51.90%	88.70%	101.10%

The high magnitudes observed for the CV_{rms} in the case of chlorine compared to flouride (Table 2-2) are attributed to the unrealistic first order decay rate with a constant bulk decay coefficient employed by all three models, which is known to be inefficient in simulating bulk decay and compared to higher order models [37], or dynamic reaction rates [38], which was outside the scope of the current study. Using the genetic algorithm to calibrate the wall demand k_w for WUDESIM resulted in a slight enhancement in the simulation accuracy where the CV_{rms} dropped to 34.56% and 48.64% for pipe 10 and 34 respectively, using k_w values of 0.593 m/day and 0.3764 m/day respectively. The results showed minimal sensitivty to the variation of k_w as the bulk demand dominated chlorine decay because of relatively low flow velocities.

2.4.2 Computational Efficiency

As the proposed modeling approach considers the simulation of dead ends with a high level of spatial and temporal detail, this comes with an increased computational cost when compared to simple models with spatially aggregated, temporally averaged flow demands and steady dispersion rates. The increased computational burden takes place due to two main factors:

I. The added computational step required to generate the stochastic flow demands aggregated at minor time steps that subsequently leads to an increased number of hydraulic steps for the total time of simulation. The computational time for this step increases as the required pulse aggregation time decreases where smaller water quality steps are required to capture flow variation at a higher level of temporal detail.

II. As the spatial variation in flow rates is considered, downstream pipe sections experience lower flow velocities, and hence finer discretization grids are generated for a particular water quality step (Equation S-2.3). In addition, the multi-segment model introduces the need to solve an extra set of linear equations every quality step to generate the concentration at the connecting

withdrawal nodes (Eq. S-2.10). The size of the system of equations increases as the number of considered sections increases.

To quantitatively illustrate the added computational burden, the proposed multi-segment modeling approach is used to simulate a typical residential dead end pipe of 244-m (800 ft) length and 20.3 cm (8-inch) nominal diameter. Five model simulations were conducted for a base flow rate of 600 L/hr in a diurnal water demand pattern (Figure 2-4a) for a 7 days period. The inlet chlorine concentration is assumed to have a sinusoidal time distribution (Figure 2-4b) given by: $C_0(t) = \bar{C}_0 + A * \sin\left(\frac{2\pi t}{\lambda}\right)$, where $\bar{C}_0$ = 10mg/L, A = 2.5mg/L and λ=6 hrs. The choice of the sinusoidal time distribution was based on the study of Li et al. [39] where the results showed that axial dispersion plays a key role in solute transport for the cases of instantaneous and sinusoidal profiles of the solute source. A bulk and wall decay rates are 0.5 day^{-1} and 0.5 m/day, respectively.

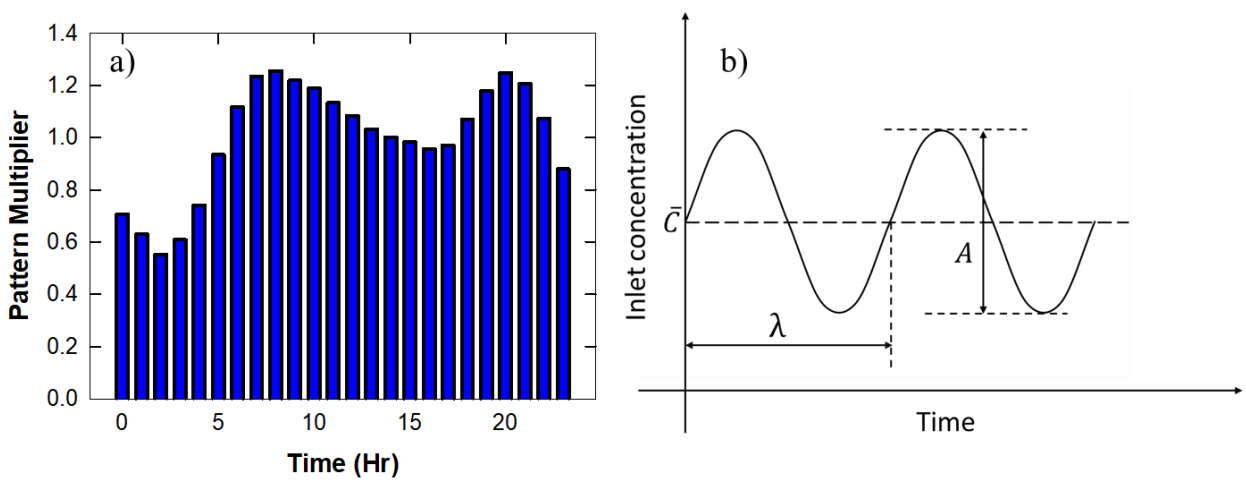

Figure 2-4. (a) Demand pattern for base case scenario; (b) Time distribution of chlorine concentration at pipe inlet.

Under these conditions, the first simulation using the simplified ADR model takes the dead end as a single segment pipe with hourly flow demands lumped at the outlet and a steady Taylor's dispersion coefficient, which overall represents the simplified model. For the other four simulations, the stochastic demand generator was used to produce demand pulses aggregated at a 5 minutes period with each simulation considering a different number of water use points (5, 10, 15 and 20 homes, respectively). These simulations represent the detailed modelling approach using dynamic dispersion coefficients as proposed by the current study. The differences in model setup between the simplified and the detailed models are summarized in Table 2-3. All five simulations were performed on a personal computer equipped with an Intel®Core™i7 3632QM CPU @2.2GHz capable of performing 70.4 GFLOPS – peak theoretical performance. The software environment used to perform the simulations was MATLAB R2013a while the genetic algorithm simulations were performed using the associated Optimization Toolbox 6.3. As shown in (Fig. 2-5), the required CPU time for the 5 segment model is almost 10 times as large as the simplified model. The CPU time then increases linearly with the number of sections considered by the model.

Table 2-3. Summary of the differences between simplistic and high level model.

Parameter	Simplified model	Detailed model
Spatial Demand distribution	Aggregated (single segment)	Multiple Segments
Temporal Demand distribution	Averaged (hourly basis)	Stochastic Demand pulses
Dispersion rate	Steady Taylor's dispersion (Eq. 2-4)	Dynamic (Eq. 2-5)

2.4.3 Sensitivity Analysis

From a practical viewpoint, a typical water distribution system comprises several hundred dead end links. This complexity leads to massive computational requirement, making it very difficult to use such a sophisticated model in real time to account for all network dead ends. Thus we conducted a parametric sensitive analysis to help decide when the simplified single segment model can be used in place of the detailed model (Table 2-3). The objective is to understand how the two models differ under the variation of different simulation parameters in three groups: (i) hydraulic parameters, (ii) pipe specific parameters, and (iii) solute specific parameters. The values for the variable parameters are shown in Table 2-4. The base case scenarios represent the same parameters as in the computation time analysis. One parameter is changed at a time from the base case, resulting in a total of 15 different scenarios. All five simulations described previously are repeated for the simplified model and for the detailed model with 5, 10, 15 and 20 segments/homes.

Table 2-4. Simulation parameter values for the sensitivity analysis study scenarios.

Parameter		Min	Base Case	Max
(i) Hydraulic	Q_b (L/hr)	300	600	900
(ii) Pipe Specific	d (cm)	15.24 [6″]	20.32 [8″]	25.40 [10″]
	L (m)	121.92 [400′]	243.84 [800′]	365.76 [1200′]
(iii) Solute Specific	$\bar{C}_0$ (mg/L)	5	10	15
	A (mg/L)	1	2.5	4
	λ (hr)	3	6	9
	k_b (day^{-1})	0.05	0.5	1.5

The deviation in model outputs was evaluated as the CV_{rms} (Equation 2-8) of the outlet concentrations between the two models. This deviation reflected the error generated by the simplified model compared to the detailed model, assuming detailed the model to be exact. The results show that the deviation scales up as the number of segments increases because the error due to the spatial aggregation approximation increases with the number of withdrawal points in the dead end pipe. The CV_{rms} strongly depends on four out of the seven parameters considered: the increase of the pipe diameter, pipe length, and bulk decay coefficient, and the decrease of the base flow rate resulted in an increase of the CV_{rms}. Parameters controlling the time distribution of inlet concentration profile, showed negligible influence on the deviation between the simplified and the detailed models.

To generalize the findings of the sensitivity analysis, a set of three dimensionless parameters was evaluated for each scenario: the Reynolds number (*Re*), axial Peclet number (*Pe*) and the Damkohler number (*Da*). They were calculated as a time-average value for the single segment case in each simulation scenario. As shown in Figure 2-5 the CV_{rms} dropped as the simulation Reynolds number increased, but increased with the increase in the Peclet number. This shows that the average flow velocity has a critical influence on the error in the simplified model, whereas the error drops rapidly as the flow velocity increases. Although by definition the axial Peclet number is directly proportional to the flow velocity, the dispersion coefficient in the denominator is a function of (u^2) based on Taylor's definition given by Equation (2-4). Thus the overall dependence of Peclet number is inversely proportional to the flow velocity, or more specifically, directly proportional to the characteristic residence time: $\tau_0 = L/u$. It can also be seen from (Fig. 2-5b) that the effect of Reynolds number diminishes as the flow approaches the upper bounds of laminar regime for the 5 segments pipe scenario, a consequence that was expected

as the advective transport becomes mainly dominant and the role of dynamic dispersion diminishes in comparison with the steady Taylor dispersion. From (Fig. 2-5d), it's clear that with an increase in Damkohler number, the CV_{rms} scales up. This further shows that the increase in the flow velocity or the drop in the characteristic residence time will reduce the error associated with the simplified model. The flow velocity plays an interesting role in this case, because the increase in flow velocity enhances mass transfer of disinfectants to the pipe wall or k_f in (Equation 2-2), and thus the calculated overall first-order decay constant. Furthermore, increasing the flow velocity also decreases the residence time, which leades to a smaller Damkohler number.

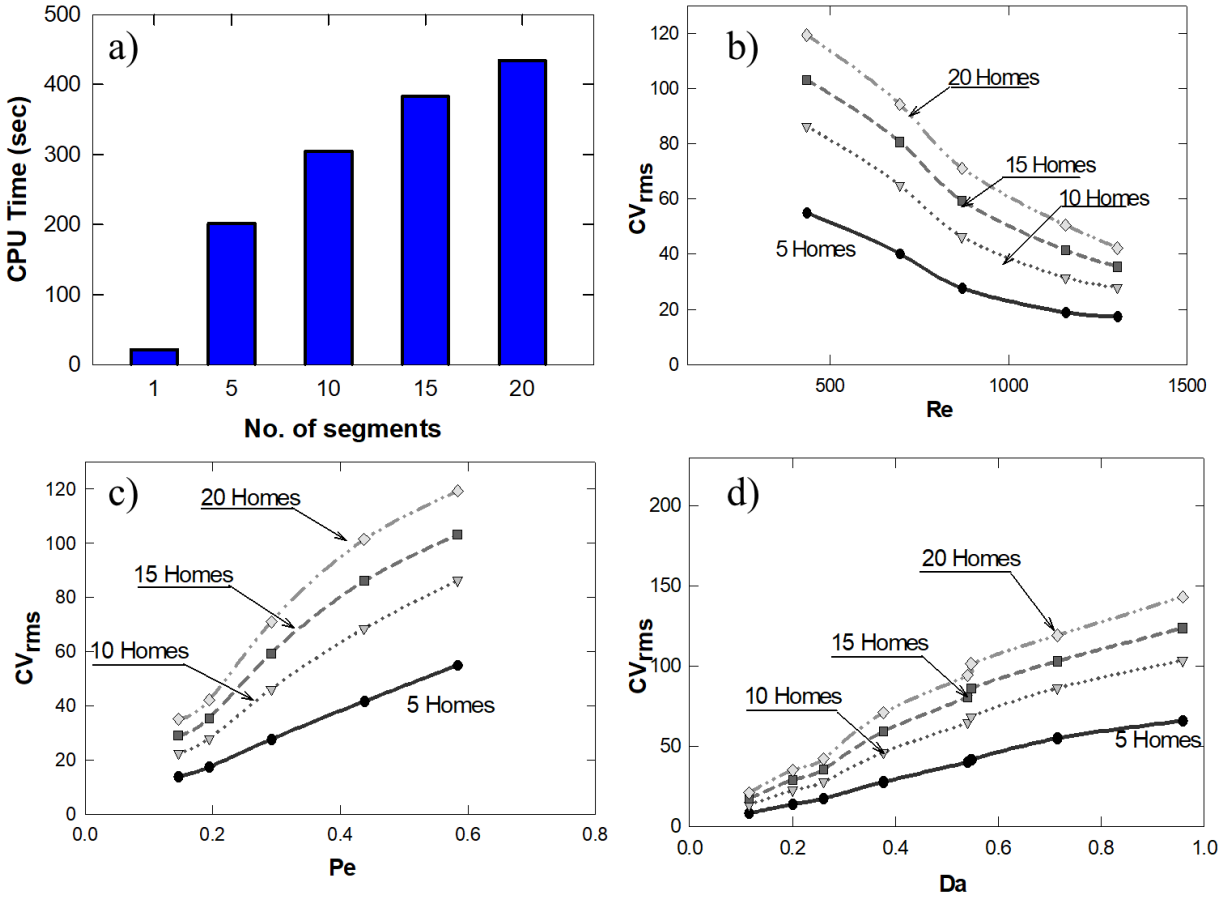

Figure 2-5. (a) Simulation time for base case scenario simulations, (b) – (d) dependence of the CV_{rms} on the time averaged Reynolds number (Re), Peclet number (Pe) and Damkohler number (Da), respectively.

2.4.4 Uncertainty Analysis

Residential water demands exhibit large temporal and spatial fluctuations; both directly affect the disinfectant transport and reaction in the distribution network. A Monte-Carlo simulation approach was implemented to understand the extent to which spatial distribution and temporal variation of water demands affect the efficacy of the simulation model in predicting disinfectant residuals in dead ends. Statistical parameters are typically used to simulate residential demand pulses. This implies that wide disparities exist in the intensity, duration and frequency of outdoor demand pulses compared to indoor demand pulses [40]. Thus the generated time series of aggregated flows heavily depend on the ratio of indoor/outdoor flows to the total demand. In this study, the average and standard deviation for the intensity of indoor demand pulses were taken as 8.52 lpm and 4.73 lpm respectively. For outdoor demand pulses, these values increased to 15.14 lpm and 3.79 lpm, respectively. The uncertainty in temporal distribution of flow demands was considered by taking the percentage of indoor demands out of the total nodal demand to be uncertain. The uncertainty in the spatial distribution of flow demands was studied by considering the share of each withdrawal point from a fixed total pipe demand for the dead end to be the uncertain parameter. Thus four sets of Monte-Carlo ensembles were executed where each set comprised 200 individual simulations (Table 2-1). All simulations were conducted to the dead end pipe 10 in the CHBP study which has seven withdrawal nodes as aforementioned. The first two sets (5-A, B) are intended to compare the uncertainty in the predicted conservative tracer (fluoride) concentration profile due to temporal heterogeneity versus spatial heterogeneity. The other two sets (6-A, B) were investigated for the concentrations of a reactive disinfectant (free chlorine). To isolate the two different sources of uncertainty, the time distribution of the total pipe demand was kept unchanged for all spatial variation simulations.

The share of each withdrawal node was assumed to follow a lognormal distribution with an average of ($1/N_{seg}$), where N_{seg} is the number of considered pipe segments (N_{seg} = 7 for pipe 10), and a standard deviation of the same magnitude. Similarly, for the temporal variation simulations, all withdrawal points were assigned equal shares of the total pipe demand. The indoor demands ratio was given a uniform probability distribution with a minimum of 50% and a maximum of 100%. To ensure the convergence of the simulated 200 realizations, the average and standard deviation of the simulation RMSD were calculated after each realization until reaching a stable value. All four Monte-Carlo simulations converged relatively quickly (<100 simulations). Analysis results showed that the uncertainty in the generated concentration profile due to variability in the spatial distribution of water demands was significantly larger than that caused by temporal variability. This conclusion applies to both conservative tracer and reactive disinfectant cases.

Figure 2-6 shows the time evolution for the coefficient of variation in the outlet concentration-time profiles for the four Monte-Carlo simulation ensembles. The uncertainty in the fluoride concentration profile was consistently larger than that of the reactive free chlorine for both temporal and spatial variability simulations. This effect suggests that the decay term in (Equation 2-2) attenuates the difference between simulation results of hydraulic dispersion under different flow demand distributions. Another factor that showed great dependence on the spatial demand distribution compared to temporal distribution was the simulation accuracy. Figure 2-7 shows the Box-and-Whisker plots of the distribution of the CV_{rms} values of the four Monte-Carlo ensembles. While temporal variation showed minimal effect on the simulation accuracy, spatial distribution showed significant influence for both cases of fluoride tracer and free chlorine. It is also clear that

the variation in the CV_{rms} values for the case of free chlorine is minor compared to fluoride tracer which is consistent with the uncertainty analysis results.

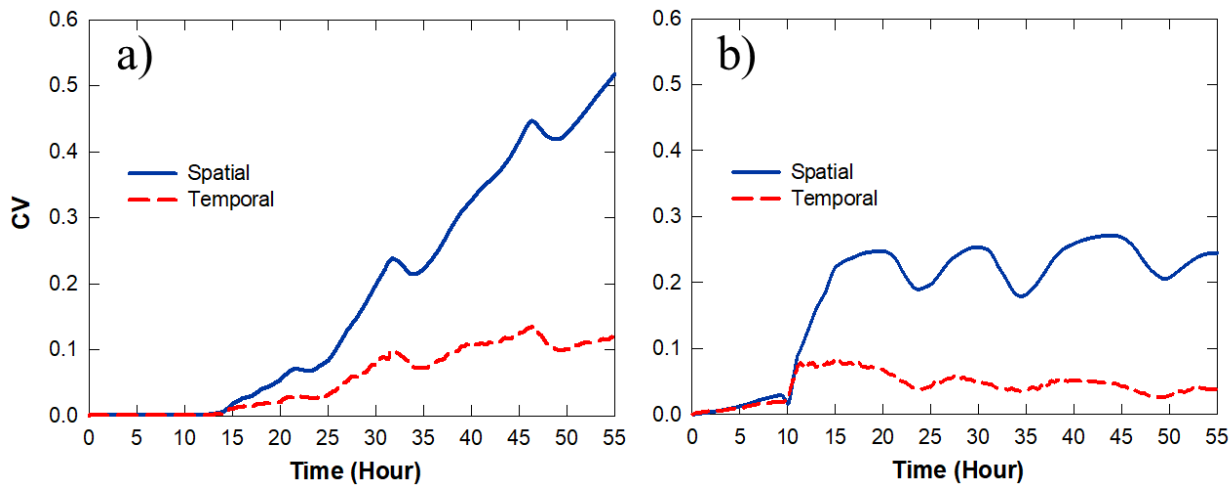

Figure 2-6. Time evolution of the coefficient of variation CV for the concentration profiles of (a) fluoride tracer, and (b) free chlorine.

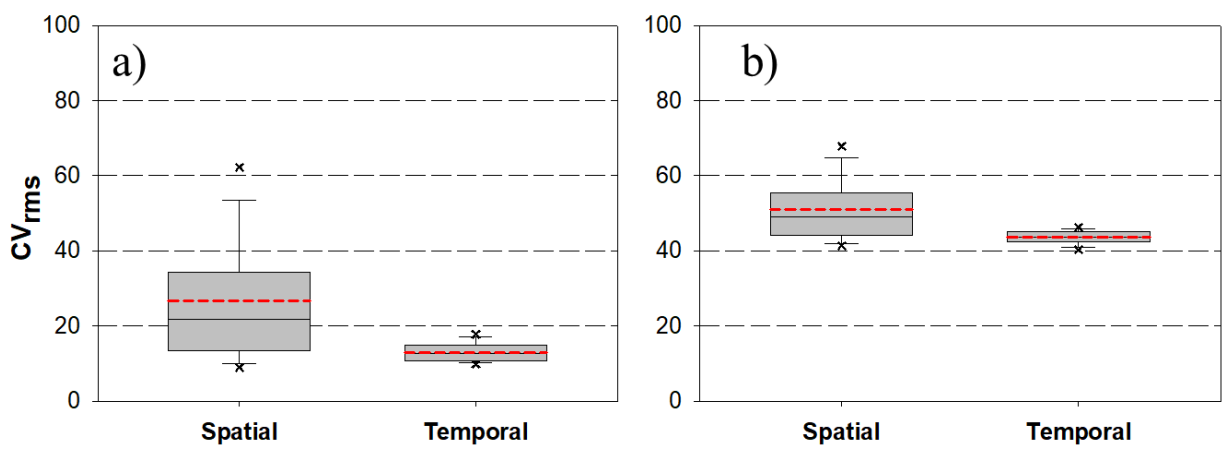

Figure 2-7. Box-and-Whisker plots of the CV_{rms} of (a) fluoride tracer, and (b) free chlorine. Tick marks represent the $5^{th}/95^{th}$ percentile rang.

2.5 Correction Factors for Spatial Aggregation

Temporal distribution of flow demands was shown in the uncertainty analysis to have minimal effect on the solute transport compared to the spatial distribution. In the sensitivity analysis, we further showed that the spatial aggregation in water demand is the primary source of modeling errors using the simplified model as compared to the detailed model. The temporal aggregation at nodes are least important. These modeling and analysis results suggest that the implementation of hourly averaged flow rates and steady dispersion coefficients will not significantly compromise the accuracy, while spatial aggregation would. However, using multi-segment model to simulate the dead end was shown to greatly increase the computational cost compared to the simplified model. Therefore to approximate the behavior of the detailed model and reduce computational demand, we have proposed a set of three correction factors analytically derived for the simplified model when the number of withdrawal points is known for a dead end pipe. The correction factors were developed in a way that translates the three dimensionless groups *Re*, *Pe* and *Da* from a multi-segment to a single-segment model while using hourly averaged demands and steady dispersion rates. The detailed derivation is given in the supplementary material Section 2.10.3. The correction factors for the residence time CF_τ, Taylor's dispersion coefficient CF_E, and the overall wall demand CF_R are:

$$CF_\tau = \frac{\tau_{corr}}{\tau_0} = \sum_{i=1}^{N_{seg}} \frac{1}{N_{seg} - i + 1} \qquad (2-9)$$

$$CF_E = \frac{E_{T,corr}}{E_{T,0}} = \frac{\sum_{i=1}^{N_{seg}} (N_{seg} - i + 1)^2}{N_{seg}^3} \qquad (2-10)$$

$$CF_R = \frac{R_{w,corr}}{R_{w,0}} = \frac{1}{CF_\tau}\sum_{i=1}^{N_{seg}}(N_{seg} - i + 1)^{-2/3} \quad (2-11)$$

The 15 different scenarios considered in the sensitivity analysis study were re-simulated after applying the correction factors to the simplified model. The CV_{rms} was plotted before and after applying the corrections for the cases of 5, 10, 15 and 20 segments. As can be seen from Figure 2-8, the correction factors greatly enhanced the simulation accuracy where the error dropped for all the simulated scenarios. The enhancement of the accuracy increased with increasing pipe diameter, pipe length and bulk decay coefficient, and decreasing the flow rate. This result again affirms the residence time as the main controlling parameter, and the increased effectiveness of the correction factors at higher residence time in the pipe.

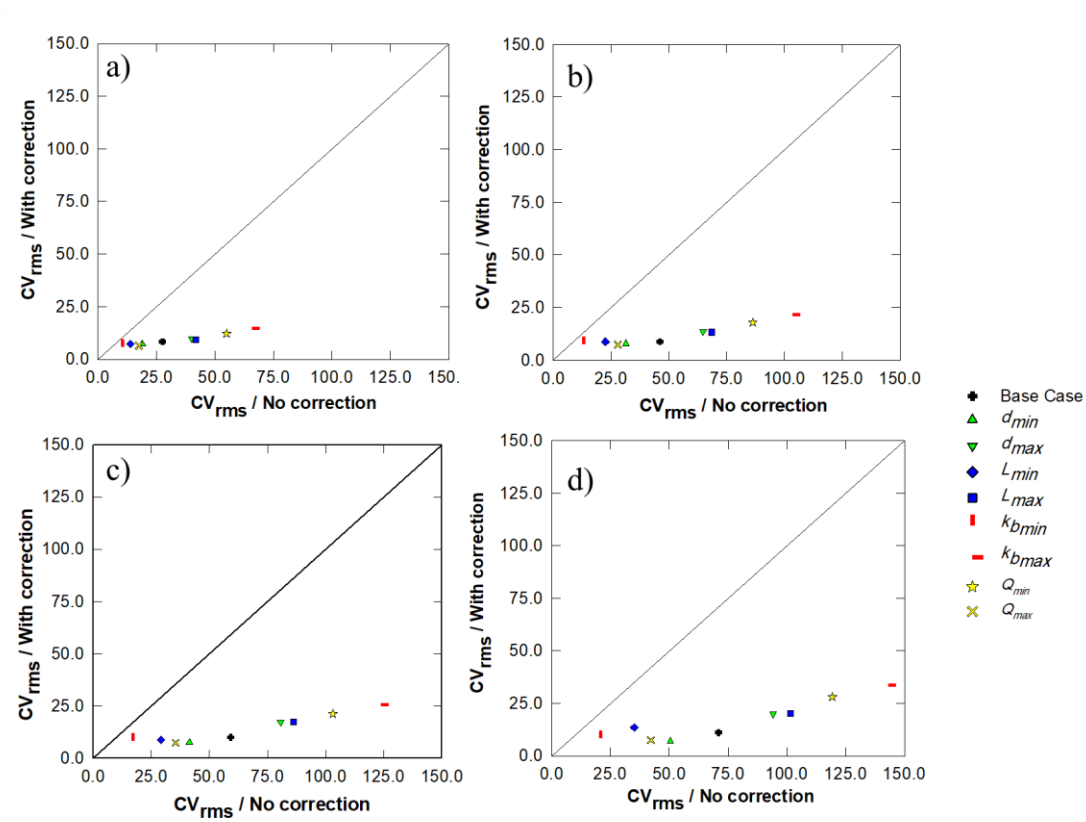

Figure 2-8. Comparison of the CV_{rms} before and after applying the derived correction factors. (a) – (d) represent the 5, 10, 15 and 20 segments scenarios, respectively.

2.6 Conclusions

A numerical model, WUDESIM, was developed to simulate disinfectant residuals in the dead end mains of water distribution systems. This is so far the first study to account for the combined effects of spatial and temporal distribution of flow demands on disinfectant transport in dead ends. The model represents the spatial distribution of flow demands by considering multiple draw-off nodes that withdraw water and disinfectant along the axis of the pipe. Temporal distribution of demand pulses was simulated using a non-homogenous Poisson process. The model implemented highly dynamic dispersion rates for pulsating laminar flows, and employed an Eulerian-Lagrangian numerical scheme to solve the 1-D advection-dispersion-reaction equation. A genetic Algorithm optimization technique was used to calibrate the hydraulic profile of the dead-end. A Monte-Carlo simulation was executed to investigate the influence of spatial and temporal distributions of flow demands on the simulation accuracy.

The simulation results of the new model showed better agreement with field measured concentrations when compared to an advection based model EPANET as well as an advection-dispersion based model ADRNET. Analysis of the results suggests that spatial distribution of flow demands have a significant influence on the generated concentration profile, and subsequently, the simulation accuracy. The approximation of spatial aggregation of flow demands should be avoided in simulating water quality in the dead ends because it might substantially reduce the simulation accuracy. Water quality models treating dead-end pipes as multiple segments with spatially variable hydraulic and transport parameters can yield realistic residence time and disinfectant concentrations.

2.7 List of Symbols

A	Amplitude of inlet concentration sine wave (mg/L)
a	pipe radius (in)
C	instantaneous disinfectant concentration in the dead end (mg/L)
C^*	dimensionless disinfectant concentration = C/C_0
C_0	pipe inlet concentration (mg/L)
CV_{rms}	coefficient of variation of the root mean square deviation
E	longitudinal dispersion coefficient (m^2/sec)
E_T	Taylor's dispersion coefficient (m^2/sec)
D	molecular diffusivity (m^2/sec)
D_x^*	inverse of the radial Peclet number
Da	Damkohler number= $K\,\tau_0$
d	pipe diameter (in)
f^*	pipe friction factor
$f(r)$	radial flow distribution parameter
K	overall first order decay rate constant (sec^{-1})
k_b	decay rate constant for bulk flow (sec^{-1})
k_w	wall decay constant (m/sec)
k_f	mass transfer coefficient (m/sec)
L	pipe length (ft).
λ	period of the inlet concentration sine wave (hr)
N_{seg}	No. of withdrawal points along the axis of the dead end pipe
N_{meas}	No. of field measurements
Pe	axial Peclet number = uL/E
Q_b	base flow demand (L/hr)
R_w	overall wall demand (sec^{-1})
Re	Reynolds number
r	radial space coordinate (m)
r_h	pipe hydraulic mean radius (m).
τ_0	characteristic residence time (sec)
t	time (sec)
t_0	Lagrangian time scale = $a^2/16D$ (sec)
t^*	dimensionless time = t/τ_0;
u	average flow velocity in the pipe (m/sec)
W_d	wall demand parameter (m/sec)
x	axial space coordinate (m)
x^*	dimensionless axial distance = x/L;

2.8 Acknowledgments

This work was partially funded by U.S. EPA through the CB&I Contract EP-C-4-014. The research described herein has been subjected to the Agency's peer and administrative review and has been approved for external publication. Any opinions expressed in this paper are those of the authors and do not necessarily reflect the views of the Agency, therefore, no official endorsement should be inferred. Any mention of trade names or commercial products does not constitute endorsement or recommendation for use. The authors would like to thank Dr. Ravindra Gudi for providing valuable comments on the article.

2.9 References

[1] D.K. Roth, D.A. Cornwell, DBP Impacts From Increased Chlorine Residual Requirements, J. Am. Water Works Assoc. 110 (2018) 13–28.

[2] U.S. Environmental Protection Agency, The Effectiveness of Disinfectant Residuals in the Distribution System, (2007).

[3] W.M. Grayman, A Quarter of a Century of Water Quality Modeling in Distribution Systems, Water Distrib. Syst. Anal. Symp. 2006 (2006) 1–12.

[4] P. Biswas, C. Lu, R.M. Clark, A model for chlorine concentration decay in pipes, Water Res. 27 (1993) 1715–1724.

[5] L.A. Rossman, R.M. Clark, W.M. Grayman, Modeling Chlorine Residuals In Drinking Water Distribution Systems, J. Environ. Eng. 120 (1994) 803–820.

[6] V.C.F. Dias, M.C. Besner, M. Prévost, Predicting water quality impact after district metered area implementation in a full-scale drinking water distribution system, J. Am. Water Works

Assoc. 109 (2017) E363–E380.

[7] B. Barbeau, V. Gauthier, K. Julienne, A. Carriere, Dead-end flushing of a distribution system: Short and long-term effects on water quality, J. Water Supply Res. Technol. 54 (2005) 371–383.

[8] R. Galvin, Eliminate Dead-End Water, OPFLOW - AWWA Mag. 37 (2011) 20–21.

[9] A.A. Abokifa, Y.J. Yang, C.S. Lo, P. Biswas, Water quality modeling in the dead end sections of drinking water distribution networks, Water Res. 89 (2016) 107–117.

[10] V.G. Tzatchkov, A.A. Aldama, F.I. Arreguin, Advection-Dispersion-Reaction Modeling in Water Distribution Networks, J. Water Resour. Plan. Manag. 128 (2002) 334–342.

[11] D.H. Axworthy, B.W. Karney, Modelling low velocity/high dispersion flow in water distribution systems, J. Water Resour. Plan. Manag. 122 (1996) 218–221.

[12] M.R. Islam, M.H. Chaudhry, Modeling of Constituent Transport in Unsteady Flows in Pipe Networks, J. Hydraul. Eng. ASCE. 124 (1998) 1115–1124.

[13] O.N. Ozdemir, A.M. Ger, Realistic numerical simulation of chlorine decay in pipes, Water Res. 32 (1998) 3307–3312.

[14] O.N. Ozdemir, A. Metin Ger, Unsteady 2-D chlorine transport in water supply pipes, Water Res. 33 (1999) 3637–3645.

[15] Z. Li, S.G. Buchberger, V. Tzatchkov, Integrating Distribution Network Models with Stochastic Water Demands and Mass Dispersion, Water Distrib. Syst. Anal. Symp. 2006. (2006) 1–15.

[16] H.A. Basha, L.N. Malaeb, Eulerian-Lagrangian Method for Constituent Transport in Water Distribution Networks, J. Hydraul. Eng. 133 (2007) 1155–1166.

[17] Z. Li, Network Quality Modeling with Stochastic Water Demands and Mass Dispersion,

PhD Dissertation, University of Cincinnati, Cincinnati, Ohio, USA, 2006.

[18] H. Der Yeh, S. Bin Wen, Y.C. Chang, C.S. Lu, A new approximate solution for chlorine concentration decay in pipes, Water Res. 42 (2008) 2787–2795.

[19] O.N. Ozdemir, A. Ucak, Simulation of Chlorine Decay in Drinking Water Distribution Systems, J. Environ. Eng. 128 (2002) 31–39.

[20] S.G. Buchberger, L. Wu, Model for instantaneous residential water demands, J. Hydraul. Eng. 121 (1995) 232–246.

[21] G. Taylor, Dispersion of Soluble Matter in Solvent Flowing Slowly through a Tube, Proc. R. Soc. A Math. Phys. Eng. Sci. 219 (1953) 186–203.

[22] Y. Lee, Mass dispersion in intermittent laminar flow, PhD Diss. Univ. Cincinnati, Cincinnati, Ohio, USA. (2004).

[23] A. Sattar, Gene Expression Models for the Prediction of Longitudinal Dispersion Coefficients in Transitional and Turbulent Pipe Flow, J. Pipeline Syst. Eng. Pract. 5 (2013) 04013011.

[24] G. Taylor, The Dispersion of Matter in Turbulent Flow through a Pipe, Proc. R. Soc. A Math. Phys. Eng. Sci. 223 (1954) 446–468.

[25] K. Ekambara, J.B. Joshi, Axial mixing in pipe flows: Turbulent and transition regions, Chem. Eng. Sci. 58 (2003) 2715–2724.

[26] M.T. van Genuchten, W. J. Alves, Analytical solu- tions of the one-dimensional convective-dispersive solute transport equation, Tech. Bull. No. 1661, U.S. Dept. Agric. Washington, D.C. (1982).

[27] A.E. de M. Baptista, E.E. Adams, K.D. Stolzenbach, Eulerian-Lagrangian analysis of pollutant transport in shallow water, Energy Lab. Rep. No. MIT-EL 84-008, Massachusetts

Inst. Technol. Cambridge, Mass. (1984) 141.

[28] X. Yang, D. Boccelli, Simulation Study to Evaluate Temporal Aggregation and Variability of Stochastic Water Demands on Distribution System Hydraulics and Transport, J. Water Resour. Plan. Manag. 140 (2014) 04014017.

[29] S.G. Buchberger, G.J. Wells, Intensity, Duration, and Frequency of Residential Water Demands, J. Water Resour. Plan. Manag. 122 (1996) 11–19.

[30] S.G. Buchberger, Z. Li, PRPsym : A Modeling System for Simulation of Stochastic Water Demands, World Environ. Water Resour. Congr. (2007).

[31] K. A. Nilsson, S.G. Buchberger, R.M. Clark, Simulating Exposures to Deliberate Intrusions into Water Distribution Systems, J. Water Resour. Plan. Manag. 131 (2005) 228–236.

[32] D. A. Savic, Z.S. Kapelan, P.M.R. Jonkergouw, Quo vadis water distribution model calibration?, Urban Water J. 6 (2009) 3–22.

[33] S. Lingireddy, L.E. Ormsbee, Optimal Network Calibration Model Based on Genetic Algorithms, 29th Annu. Water Resour. Plan. Manag. Conf. (1999).

[34] S. Gözütok, O.N. Özdemir, Refinement of hydraulic calibration for water supply networks with genetic algorithms, World Water Environ. Resour. Congr. (2003) 1–7.

[35] R.M. Clark, W.M. Grayman, R.M. Males, A.F. Hess, Modeling contaminant propagation in drinking-water distribution systems, J. Environ. Eng. 119 (1993) 349–364.

[36] R. Sadiq, M.J. Rodriguez, Disinfection by-products (DBPs) in drinking water and predictive models for their occurrence: A review, Sci. Total Environ. 321 (2004) 21–46.

[37] R.M. Clark, Chlorine Demand and TTHM Formation Kinetics: A Second-Order Model, J. Environ. Eng. 124 (1998) 16–24.

[38] P. Hua, E. Vasyukova, W. Uhl, A variable reaction rate model for chlorine decay in drinking

water due to the reaction with dissolved organic matter, Water Res. 75 (2015) 109–122.

[39] Z. Li, S.G. Buchberger, V. Tzatchkov, Importance of Dispersion in Network Water Quality Modeling, in: Proc. World Water Environ. Resour. Congr. 2005, 2005: pp. 1–12.

[40] Y. Lee, S.G. Buchberger, Modeling Indoor and Outdoor Residential Water Use as the Superposition of Two Poisson Rectangular Pulse Processes, in: Proc. 29th Annual Water Resources Planning and Management Conference. (1999).

2.10 Supplementary Material

2.10.1 Eulerian-Lagrangian Numerical Solution

The governing ADR transport equation (Equation 2-2) is split into two separate steps:

I- Lagrangian Step:

$$\frac{C^a - C^k}{\Delta t} = -u\frac{\partial C^k}{\partial x} - K\,C^k \qquad \text{(S-2.1)}$$

II-Eularian Step:

$$\frac{C^{k+1} - C^a}{\Delta t} = E\frac{\partial^2 C^k}{\partial x^2} \qquad \text{(S-2.2)}$$

The space-time domain for each pipe segment is discretized into a rectangular grid as shown in Figure S 2-1

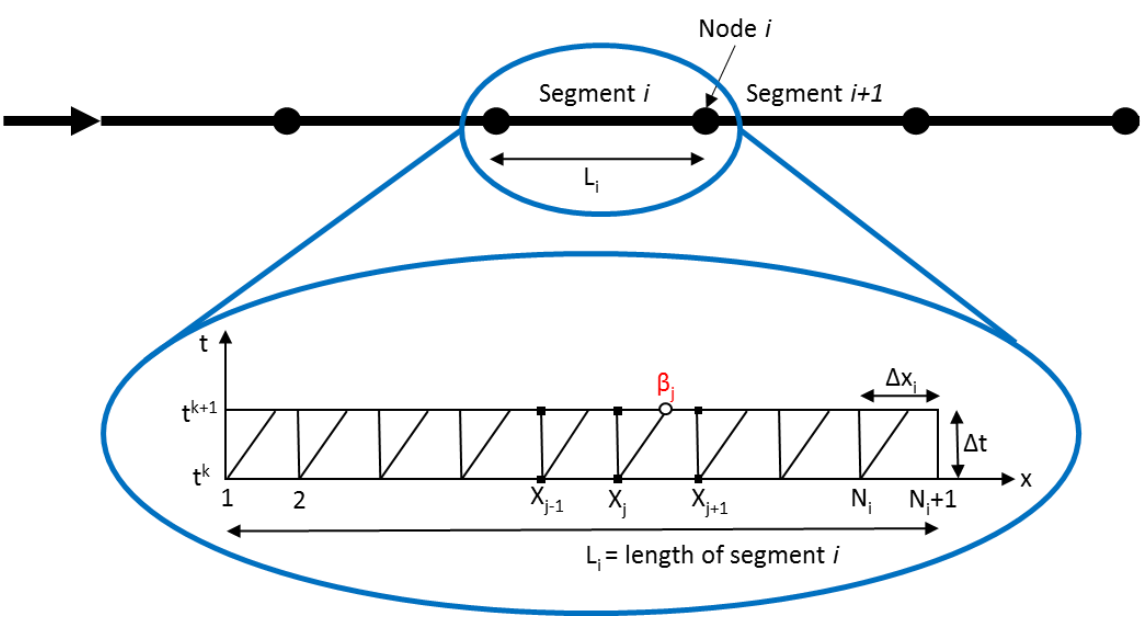

Figure S 2-1 Time space discretization grid for pipe segment i

The total number of axial grid points in any segment is $N_i + 1$ and is calculated as:

$$N_i + 1 = \text{INTEGER}\left(\frac{L_i}{u_i \Delta t}\right) \qquad \text{(S-2.3)}$$

Where: L_i is the length of segment i; u_i is the flow velocity in segment i; and Δt is water quality time step.

The grid size for the pipe segment is then calculated by:

$$\Delta x_i = \left(\frac{L_i}{N_i + 1}\right) \qquad \text{(S-2.4)}$$

In the Lagrangian stage, the current time step (t^k) grid points are projected forwards in time based on the MOCs scheme where their projection locations on the following time step (t^{k+1}) are given the symbol (β_j) (Figure S 2-1). These projections are conducted based on the characteristic advection line described by $dx_i/dt = u_i$. Hence, the forward projection locations can be calculated based on the following equation:

$$\beta_j = x_j + u_i \Delta t \qquad \text{(S-2.5)}$$

Using the known concentration profile for the current time step at all the axial grid points $C^k(X_j)$, the values of the concentration profile can be evaluated at different β_j positions. By applying the reaction term to the advected concentration profile, we can get the advected-reacted concentration profile defined for numerical grid locations $C^a(\beta_j)$ in the next time step for each segment.

$$C^a(\beta_j) = C^k(X_j) * \exp(-K_i \Delta t) \qquad \text{(S-2.6)}$$

The following time-step concentration profile defined at grid locations $C^a(X_j) = C_j^a$ can then be evaluated from $C^a(\beta_j)$ through linear interpolation. The Eulerian step is then introduced using the

fully implicit forward time central space FTCS finite difference discretization of the dispersion equation which gives:

$$\frac{C_j^{k+1}-C_j^a}{\Delta t} = E_i \frac{C_{j-1}^{k+1}-C_j^{k+1} + C_{j+1}^{k+1}}{(\Delta x)^2} \qquad \text{(S-2.7)}$$

The previous equation can be re-arranged to give the following system of linear equations:

$$-r_i C_{j-1}^{k+1} + (1-2r_i)C_j^{k+1} - r_i C_{j-1}^{k+1} = C_j^a \qquad \text{(S-2.8)}$$

Where: $r_i = E_i \Delta t / \Delta x_i^2$. The numerical Green's function technique proposed by Aldama [1] and implemented in the model developed by Tzatchkov [2] is used in this study to efficiently solve the generated system of linear equations numerically. The concentration at each grid point is computed as the superposition of three numerical components:

$$C_j^{k+1} = H_j^{k+1} + Gr_j^{k+1} * C_{j=1}^{k+1} + Gf_j^{k+1} * C_{j=N_i+1}^{k+1} \qquad \text{(S-2.9)}$$

The first term on the LHS represents the homogeneous solution obtained by assigning zero boundary conditions at both front and rear points of each pipe segment (at j=1,and j= N_i+1). The second and third terms represent two particular solutions obtained for both the front and rear end of each segment. To evaluate the values of Greens' functions at different grid locations, the discretized form of the dispersion equation (Equation S-2.8) is used. For the homogenous part, the values of $H_{j=1}$ and $H_{j=Ni-1}$ are set as zeros. For the rear Green's function, the values of $Gr_{j=1}$ and $Gr_{j=Ni-1}$ are set as one and zero respectively, while for the front Green's function $Gf_{j=1}$ and $Gf_{j=Ni-1}$ are taken as zero and one respectively. The values on the RHS of (Equation S-2.8) are set to C^a_j that were evaluated in the previous Lagrangian step when calculating the homogenous part, while taken equal to zeros for the other two particular functions. By applying these conditions in (Eq. S-2.8), three systems of linear equations are generated for each pipe segment, which are solved to

get the values of the three Greens' functions at all grid locations. To generate the concentration profile in each segment, (Eq. S-2.9) is applied for each grid point to calculate the concentration values. However, the values of $C_{j=1}^{k+1}$ and $C_{j=N_i+1}^{k+1}$ (which are the concentration values at the connecting withdrawal nodes) are still unknown at this point. To evaluate the concentration values at the withdrawal nodes, a special numerical discretization for the dispersion equation (Eq. S-2.2) is required to account for the spatial variation in characteristics between the two connected pipe segments. This can be described as:

$$\frac{(\Delta x_i + \Delta x_{i+1})}{2}\frac{Cn_i^{k+1}\text{-}Cn_i^a}{\Delta t} = \left[E_i\frac{(C_{j=N_i}^{k+1})_i\text{-}Cn_i^{k+1}}{\Delta x_i} + E_{i+1}\frac{(C_{j=2}^{k+1})_{i+1}\text{-}Cn_i^{k+1}}{\Delta x_{i+1}}\right] \qquad \text{(S-2.10)}$$

Where: Cn_i is the concentration at withdrawal node i that connects the pipe segments i and i+1 (Figure S 2-1). Using mass balance, the concentration at any node i is always equal to the concentration of the terminal grid point in segment i:

$$Cn_i = (C_{j=N_i+1})_i \qquad \text{(S-2.11)}$$

By substituting the values of $(C_{j=N_i}^{k+1})_i$, $(C_{j=2}^{k+1})_{i+1}$ from (Eq. S-2.9) into (Eq. S-2.10), we get a closed set of linear equations that is solved simultaneously to generate the concentrations at the withdrawal nodes. The latter are plugged in (Eq. S-2.7) to calculate the concentrations at different grid points and the procedure is repeated for all segments. As the model considers extended period simulations (EPS) of hydraulic and transport parameters, pipe flow changes from one hydraulic step to the other while kept steady within the hydraulic step. The duration of the simulation hydraulic step is dictated by the aggregation period of the generated stochastic demands. A new discretization grid is generated for all segments at the beginning of each new hydraulic step and the transport and reaction parameters are recalculated.

2.10.2 Aerial Photos of the Cherry Hill Brushy Plains dead ends

Using the site maps given in the original paper [3], and by comparing the skeletonized grid with the all-pipe layout given in [4], the exact dead end pipes that were included in the sampling study were identified. Google Earth® software was then used to locate the two dead ends and identify the number of consumption points on each dead end through aerial photos captured on March 15, 1992. (Figure S 2-2).

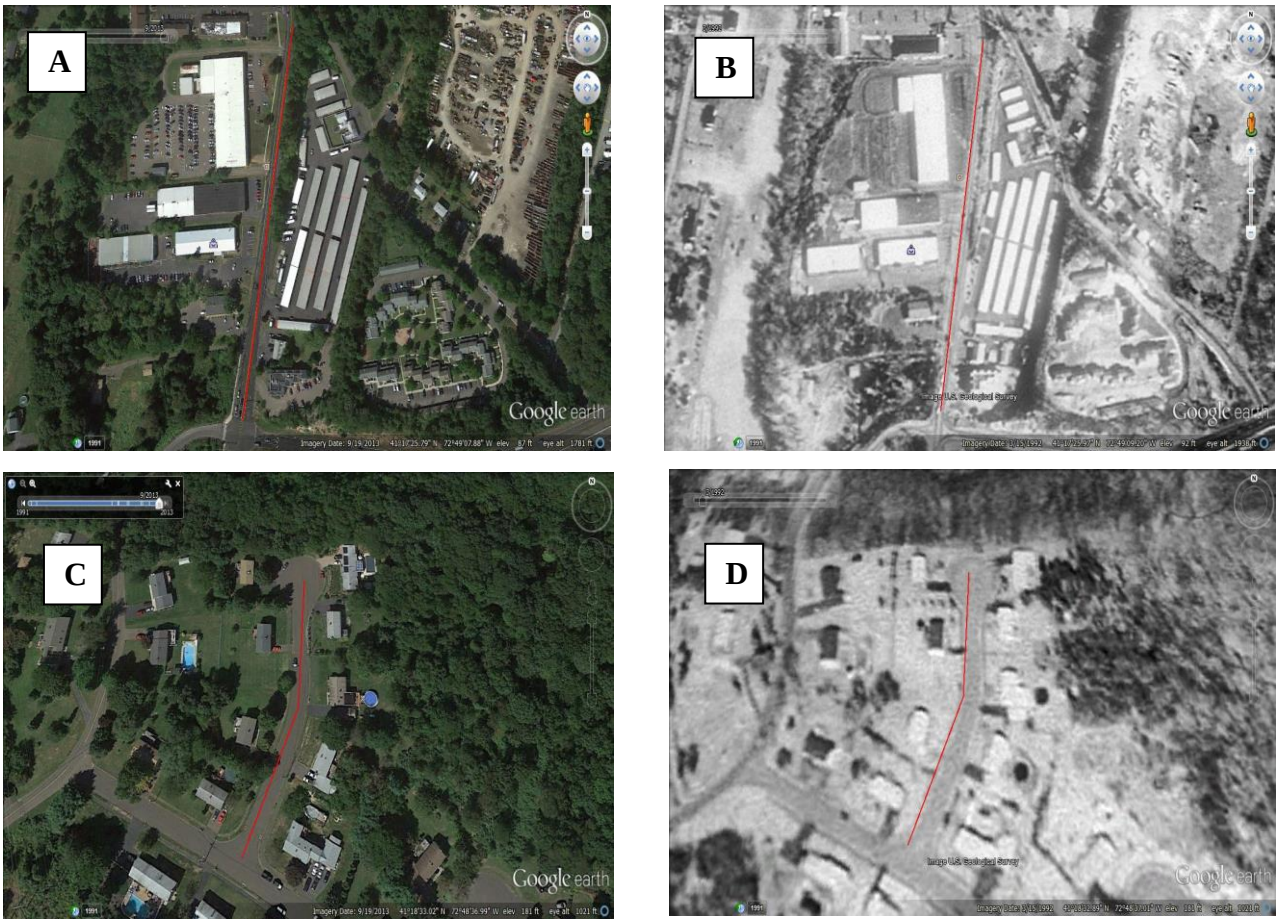

Figure S 2-2. Aerial Photos of Dead End pipes 10 and 34 retrieved by Google® earth® for (a), (c) 9/19/2013; (b), (d) 3/15/1992.

2.10.3 Analytical Derivation of the Correction Factors

I- Residence Time

The corrected residence time τ_{corr} for a multi-segment dead end with N_{seg} withdrawal points is evaluated as the sum of residence times over all segments, which can be written as:

$$\tau_{corr} = \sum_{i=1}^{N_{seg}} \tau_i = A_p \sum_{i=1}^{N_{seg}} \frac{L_i}{Q_i} \qquad \text{(S-2.12)}$$

Where, τ_i is the residence time in segment i; L_i is the length of segment i; Q_i is the flow rate of segment i; and A_p is the pipe cross-sectional area. From mass conservation, Q_i can be written as:

$$Q_i = Q_1 - \sum_{j=1}^{i-1} q_j \qquad \text{(S-2.13)}$$

Where, Q_1 is the total dead end pipe demand; q_j is the flow demand of withdrawal point j. Assuming equally spaced withdrawal nodes with equal demand shares, L_i and Q_i can be written as:

$$L_i = \frac{L}{N_{seg}} \qquad \text{(S-2.14)}$$

$$Q_i = Q_1 - (i-1)\ \frac{Q_1}{N_{seg}} = \frac{Q_1}{N_{seg}}\left[N_{seg} - i + 1\right] \qquad \text{(S-2.15)}$$

Where, L is the total pipe length. Applying in (Eq. S-2.12) yields:

$$\tau_{corr} = \frac{Ap\ L}{Q_1} \sum_{i=1}^{N_{seg}} \frac{1}{N_{seg} - i + 1} = \tau_0 \sum_{i=1}^{N_{seg}} \frac{1}{N_{seg} - i + 1} \qquad \text{(S-2.16)}$$

where, τ_0 is the residence time calculated using the single segment model based on the total demand of the dead end pipe. The correction factor for the residence time in the pipe can then be written as:

$$CF_\tau = \frac{\tau_{corr}}{\tau_0} = \sum_{i=1}^{N_{seg}} \frac{1}{N_{seg}\text{-}i + 1} \qquad \text{(S-2.17)}$$

II- Dispersion Rate

Taylor's dispersion coefficient for each segment i can be written as:

$$E_{T,i} = \frac{u_i^2 a^2}{48D} \qquad \text{(S-2.18)}$$

Where, u_i is the flow velocity in segment i, which based on (Eq. S-2.15) and after applying mass continuity for a steady incompressible flow can be written as:

$$u_i = \frac{u_1}{N_{seg}}\left[N_{seg}\text{-}i + 1\right] \qquad \text{(S-2.19)}$$

The corrected dispersion coefficient can be approximated as the average over different segments of the dead end:

$$E_{T,corr} = \frac{1}{N_{seg}} \sum_{i}^{N_{seg}} E_{T,i} \qquad \text{(S-2.20)}$$

Which after applying (Eq. S-2.18) and (Eq. S-2.19) will be:

$$E_{T,corr} = \frac{u_1^2 a^2}{48D} \frac{\sum_{i=1}^{N_{seg}} (N_{seg}\text{-}i + 1)^2}{N_{seg}^3} = E_{T,0} \frac{\sum_{i=1}^{N_{seg}} (N_{seg}\text{-}i + 1)^2}{N_{seg}^3} \qquad \text{(S-2.21)}$$

where, $E_{T,0}$ is the dispersion coefficient of the single segment model based on the total demand of the dead end pipe. The correction factor for the dispersion rate in the pipe can then be written as:

$$CF_E = \frac{E_{T,corr}}{E_{T,0}} = \frac{\sum_{i=1}^{N_{seg}} (N_{seg}\text{-}i + 1)^2}{N_{seg}^3} \qquad \text{(S-2.22)}$$

III- Wall demand

The overall wall demand for each segment i can be written as:

$$R_{w,i} = \frac{k_w k_{f,i}}{r_h (k_w + k_{f,i})} \qquad \text{(S-2.23)}$$

Where $k_{f,i}$ is the lumped mass transfer coefficient of segment i which is a function of the flow velocity [3]. For laminar flow:

$$k_{f,i} = \alpha + \beta \frac{u_i}{1 + \chi\, u_i^{2/3}} \qquad \text{(S-2.24)}$$

where, $\alpha = 3.65\frac{D}{d}$; $\beta = 0.0668\frac{d}{L_i}$; and $\chi = 0.04(\frac{d^2}{D\,L_i})^{2/3}$. Dead end pipes are typically characterized by low flow velocities, which indirectly results in high wall decay coefficient k_w as a result of significant biofilm growth [5,6]. In addition, it leads to low magnitudes for the mass transfer coefficient, leading the overall wall demand to be consistently mass transfer limited. Under these conditions, (Eq. S-2.23) can then be reduced to:

$$R_{w,i} \cong \frac{k_{f,i}}{r_h} \ldots \forall \frac{k_w}{k_{f,i}} >> 1 \qquad \text{(S-2.25)}$$

The dependence of the overall mass transfer coefficient on the flow velocity is highly nonlinear as shown in (Eq. S-2.24), and therefore some simplifying assumptions were to be made in order to

reduce the wall demand formula. In particular, the magnitude of the term ($\chi\, u_i^{2/3}$) compared to unity is of interest in this case. This term can be written in its original form as:

$$0.04\chi\, u_i^{2/3} = 0.04\left(\frac{\mathrm{Re\ Sc}}{L_i/d}\right)^{2/3} \qquad \text{(S-2.26)}$$

Where, Re is the Reynolds number; and Sc is the Schmidt number. The magnitude of this term for a dead end operating under an average Reynolds number of 500, with Schmidt number in the order of 1000 and with segment length of around 100 diameters will be in the order of 10. Thus, (Eq. S-2.24) can be reduced to:

$$k_{f,i} \cong \alpha + \frac{\beta}{\chi} u_i^{1/3} \ldots \forall\ 0.04\left(\frac{\mathrm{Re\ Sc}}{L_i/d}\right)^{2/3} >> 1 \qquad \text{(S-2.27)}$$

The same analysis can be applied to compare the magnitudes of the two terms in (Eq. S-2.27) as follows:

$$\frac{\beta}{\alpha\chi} u_i^{1/3} = 0.458\left(\frac{\mathrm{Re\ Sc}}{L_i/d}\right)^{1/3}$$

Which will be in the order of 10 considering the same magnitudes for Re, Sc and L_i/d. Therefore, the overall wall demand for segment i in the reduced form can be written as:

$$R_{w,i} \cong \frac{\beta}{\chi\, r_h} u_i^{1/3} = 6.68\left(\frac{D^2}{L_i d^4}\right)^{1/3} u_i^{1/3} \qquad \text{(S-2.28)}$$

The corrected wall demand rate can be approximated as the weighted average over all segments, where weights are evaluated based on the relative residence time in order to conserve the overall dimensionless Damkohler number:

$$R_{w,corr} = \sum_{i}^{N_{seg}} \frac{\tau_i}{\tau_{corr}} R_{w,i} \qquad \text{(S-2.29)}$$

By combining (Eq. S-2.14) and (Eq. S-2.15):

$$\tau_i = \frac{\tau_0}{N_{seg}\text{-}i + 1} \qquad \text{(S-2.30)}$$

And from (Eq. S-2.17) we can get:

$$\frac{\tau_i}{\tau_{corr}} = \frac{1}{CF_\tau} \cdot \frac{1}{N_{seg}\text{-}i + 1} \qquad \text{(S-2.31)}$$

Plugging in (Eq. S-2.29) yields:

$$R_{w,corr} = \frac{1}{CF_\tau} \sum_{i}^{N_{seg}} \frac{6.68(\frac{D^2}{L_i d^4})^{1/3}}{N_{seg}\text{-}i + 1} [\frac{u_1}{N_{seg}} (N_{seg}\text{-}i + 1)]^{1/3} \qquad \text{(S-2.32)}$$

And from (Eq. S-2.28), the wall demand rate based on the total pipe flow demand can be written as:

$$R_{w,0} = 6.68(\frac{D^2}{(L_i N_{seg}) d^4})^{1/3} u_1^{1/3} \qquad \text{(S-2.33)}$$

Therefore, the correction factor for the wall demand rate will be:

$$CF_R = \frac{R_{w,corr}}{R_{w,0}} = \frac{1}{CF_\tau} \sum_{i=1}^{N_{seg}} (N_{seg}\text{-}i + 1)^{-2/3} \qquad \text{(S-2.34)}$$

2.10.4 Supplementary Nomenclature

A_p	pipe cross-sectional area
a	pipe radius (in)
β_j	Advection projections
C	instantaneous disinfectant concentration in the dead end (mg/L)
CF	correction factor
E	longitudinal dispersion coefficient (m^2/sec)
E_T	Taylor's dispersion coefficient (m^2/sec)
D	molecular diffusivity (m^2/sec)
d	pipe diameter (in)
Gf	front solution of numerical green's function
Gr	rear solution of numerical green's function
H	homogenous solution of numerical green's function
K	overall first order decay rate constant (sec^{-1})
k_w	wall decay constant (m/sec)
k_f	mass transfer coefficient (m/sec)
L	pipe length (ft).
N_{seg}	No. of withdrawal points along the axis of the dead end pipe
N_i	No. of grid points in segment i
Q_i	flow rate of segment i
q_j	flow demand of withdrawal point j
R_w	overall wall demand (sec^{-1})
r_h	pipe hydraulic mean radius (m).
τ_0	characteristic residence time (sec)
t	time (sec)
u	average flow velocity in the pipe (m/sec)
x	axial space coordinate (m)

2.10.5 Supplementary References

[1] A.A. Aldama, V.G. Tzatchkov, F.I. Arreguin, The numerical Green's function technique for boundary value problems in networks, Water Stud. Ser. (1998) 121–130.

[2] V.G. Tzatchkov, A.A. Aldama, F.I. Arreguin, Advection-Dispersion-Reaction Modeling in Water Distribution Networks, J. Water Resour. Plan. Manag. 128 (2002) 334–342.

[3] L.A. Rossman, R.M. Clark, W.M. Grayman, Modeling Chlorine Residuals In Drinking Water Distribution Systems, J. Environ. Eng. 120 (1994) 803–820.

[4] K. a. Nilsson, S.G. Buchberger, R.M. Clark, Simulating Exposures to Deliberate Intrusions into Water Distribution Systems, J. Water Resour. Plan. Manag. 131 (2005) 228–236.

[5] H. Der Yeh, S. Bin Wen, Y.C. Chang, C.S. Lu, A new approximate solution for chlorine concentration decay in pipes, Water Res. 42 (2008) 2787–2795.

[6] P. Biswas, C. Lu, R.M. Clark, A model for chlorine concentration decay in pipes, Water Res. 27 (1993) 1715–1724.

Chapter 3

Investigating the Role of Biofilms in Trihalomethane Formation in Water Distribution Systems with a Multi-Species Reactive Transport Model

Results presented in this chapter were published in:

A. A. Abokifa, Y. J. Yang, C. S. Lo, P. Biswas. "Investigating the Role of Biofilms in Trihalomethane Formation in Water Distribution Systems with a Multicomponent Model." Water Research 2016, 104, 208-219.

3.1 Abstract

Biofilms are ubiquitous in the pipes of drinking water distribution systems (DWDSs), and recent experimental studies revealed that the chlorination of the microbial carbon associated with the biofilm contributes to the total disinfection by-products (DBPs) formation with distinct mechanisms from those formed from precursors derived from natural organic matter (NOM). A multiple species reactive-transport model was developed to explain the role of biofilms in DBPs formation by accounting for the simultaneous transport and interactions of disinfectants, organic compounds, and biomass. Using parameter values from experimental studies in the literature, the model equations were solved to predict chlorine decay and microbial regrowth dynamics in an actual DWDS, and trihalomethanes (THMs) formation in a pilot-scale distribution system simulator. The model's capability of reproducing the measured concentrations of free chlorine, suspended biomass, and THMs under different hydrodynamic and temperature conditions was demonstrated. The contribution of bacteria-derived precursors to the total THMs production was found to have a significant dependence on the system's hydraulics, seasonal variables, and the quality of the treated drinking water. Under system conditions that promoted fast bacterial re-growth, the transformation of non-microbial into microbial carbon DBP precursors by the biofilms showed a noticeable effect on the kinetics of THMs formation, especially when a high initial chlorine dose was applied. These conditions included elevated water temperature and high concentrations of nutrients in the influent water. The fraction of THMs formed from microbial sources was found to reach a peak of 12% of the total produced THMs under the investigated scenarios. The results demonstrated the importance of integrating bacterial regrowth dynamics in predictive DBPs formation models.

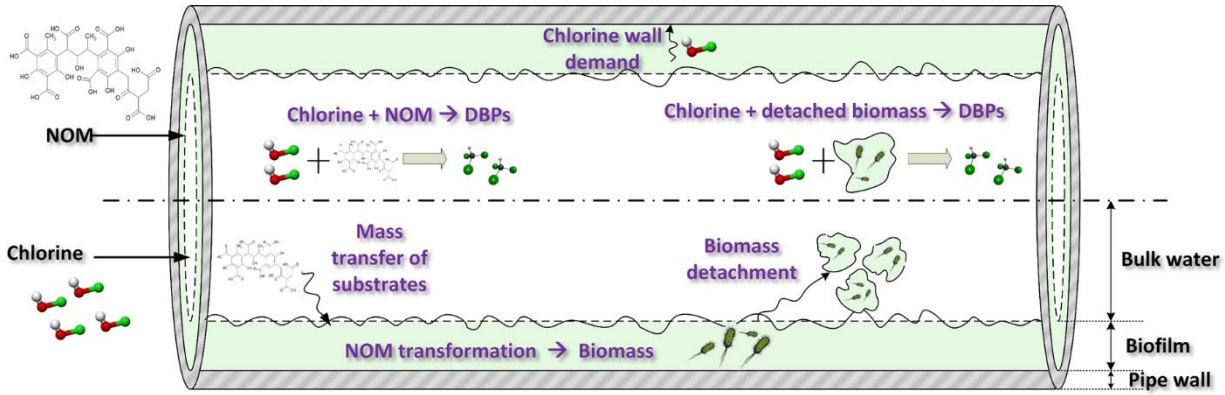

Figure 3-1. Graphical Abstract for the work presented in Chapter 3.

3.2 Introduction

Water quality reaching the consumer's tap is largely dictated by the physical, chemical, and biological processes that take place in the distribution system. While chlorine is routinely used by drinking water utilities to inhibit microbial regrowth in their distribution systems, it reacts with the residual natural organic matter (NOM) leading to the undesired formation of carcinogenic disinfection byproducts (DBPs). Moreover, the biodegradable fraction of NOM fed to the system supports the growth of biofilms [1], which play a major role in the accumulation and release of bacterial and pathogenic species, and thus compromise the microbiological quality of the treated drinking water [2,3]. Significant modeling efforts have been devoted over the past three decades to predict the formation of DBPs during water treatment [4–7]; yet more research is still required to understand their formation and transport in the distribution system. Specifically, the role of biofilms has been generally overlooked in previous modeling studies despite their ubiquitous existence in drinking water distribution systems with considerable surface biomass concentrations (up to 10^4 – 10^7 CFU/cm^2) [8].

Previous field studies found consistently higher levels of trihalomethanes (THMs) in the distribution network and at the points of use compared to finished water [9,10]. Experimental pilot-scale studies showed that the production of THMs in a simulated pipe environment was always higher than that observed for glass bottle tests, which was accompanied by faster chlorine consumption rates in the pipe environment [11]. This observation was attributed to the existence of a reservoir of THMs precursor material attached to the pipe wall, which can be explained by the radial mass transfer of organic compounds to the biofilm, and the bio-sorption of NOM to the extracellular polymeric substance (EPS) [12]. On the other hand, biofilms were found to

biodegrade haloacetic acids (HAAs), which influences their fate since their levels do not typically show a consistent increase with the residence time as in the case of THMs [13].

The microbial carbon content associated with the biofilm has been recently shown to act as a precursor for DBPs formation in the distribution system as a result of the chlorination of both pure bacterial cells [14], or the EPS, which is largely composed of dissolved organic compounds such as polysaccharides, proteins and nucleic acids [15,16]. Hence, the detachment of biomass from the biofilm matrix by either active dispersal of planktonic cells [17] or passive dispersal due to fluid shear or grazing [18] can contribute to the total budget of DBPs precursors. Therefore, the question arises whether this contribution is significant enough to influence the dynamics of DBPs formation in the distribution system? Moreover, what would be the system conditions that might promote or depress this contribution? A multiple-species reactive transport model was developed to help answer these questions.

Numerous mathematical multispecies models have been developed in the literature to describe disinfectant decay and bacterial regrowth in the distribution system [19–24]. A good review of these models and their limitations can be found in [25]. One of the first-generation models was presented by Lu et al. [21], which accounted for the simultaneous transport of substrates, disinfectants and microorganisms in the bulk phase and the biofilm under steady state conditions. However, their model did not account for substrate utilization and bacterial re-growth in the bulk phase, and assumed a simple first order reaction kinetics for chlorine decay. Munavalli and Kumar [19] presented a dynamic multi-component model that considered a more realistic expression for chlorine decay with a parameter that depends on the concentration of the organic carbon, while Zhang et al. [20] applied the alternating split-operator (ASO) algorithm to decouple the transport and reaction processes, which significantly simplified the numerical solution for

complex reaction mechanisms of the multi-component model. Yet, all these models were mainly concerned with simulating the biological processes in the system, and none of them was extended to include the formation and transport of DBPs.

EPANET-MSX [26] is an advection based, public domain, generalized multi-species model that can be used to simulate the reaction and transport of any set of interacting chemical or biological species. However, like most of the other multi-species models, EPANET-MSX does not account for dispersion as a solute transport mechanism. Hence, it is not capable of providing accurate simulations for constituent transport in low flow pipes and dead-end zones. These zones are known to be responsible for most of the water quality degradation that takes place in the system due to extended residence times, and therefore require a special modeling approach such as the one we developed in our previous study (WU-DESIM) [27]. With the increasing public awareness of the need for water conservation, the effect of these zones on water quality deterioration is expected to even magnify because of the generally lower flow rates [28].

In this study, a 1-D multi-component reactive-transport model (WU-MSRT – Washington University Multi-Species Reactive Transport) is developed to simulate the transport and consumption of disinfectants, transformation of the biodegradable fraction of NOM into biomass through bacterial regrowth in the biofilm, the release of biomass to the bulk fluid through detachment from the biofilm, and the formation of DBPs from precursors of both microbial and non-microbial origin. The model considers both advective and dispersive transport mechanisms, and hence is capable of efficiently simulating constituent transport under different flow conditions, ranging from the advection-dominated transport in the main trunk pipes to the dispersion-dominated transport in dead-ends. The model was applied to investigate the system conditions under which microbial carbon can significantly contribute to the overall DBPs budget in the

finished drinking water including the effect of using booster re-chlorination to control bacterial regrowth in the system.

3.3 Methodology

3.3.1 Model development

Mathematical Formulation

For a water parcel moving through a distribution pipe containing disinfectants, organic compounds, nutrients, biomass and disinfection byproducts, the biochemical reactions are considered to take place at two interconnected sites within the bulk flow and in the accumulated biofilm at the pipe wall. Solute transport can be appropriately modeled by a dynamic 2-D convection-diffusion equation in cylindrical coordinates to represent the mass balance on the concentration of each of the bulk phase constituents $C_{i,b}$(x,r,t) as given by:

$$\frac{\partial C_{i,b}}{\partial t} + \frac{\partial}{\partial x}\left(\bar{u}\, f(r)\, C_{i,b}\right) - \frac{\partial}{\partial x}\left(D_{i,L}\frac{\partial C_{i,b}}{\partial x}\right) - \frac{1}{r}\frac{\partial}{\partial r}\left(r\, D_{i,r}\frac{\partial C_{i,b}}{\partial r}\right) = \sum_{j=1}^{N_{r,b}} R_{i,j}\left(C_{i=1\ldots N_{s,b}}\right) \qquad \text{for } 0 < r < r_f \qquad (3\text{-}1)$$

While for wall zone constituents $C_{i,w}$, it can be written as:

$$\frac{\partial C_{i,w}}{\partial t} - \frac{1}{r}\frac{\partial}{\partial r}\left(r\, D_{i,w}\frac{\partial C_{i,w}}{\partial r}\right) = \sum_{k=1}^{N_{r,w}} R_{i,k}\left(C_{i=1\ldots N_{s,w}}\right) \qquad \text{for } r_f < r < r_0 \qquad (3\text{-}2)$$

where, *x & r* are the axial and radial space coordinates, respectively (m); *t* is the time (sec); $\bar{u}$ is the average flow velocity in the pipe (m/sec); *f(r)* is the radial flow distribution parameter; $D_{i,L}$ and $D_{i,r}$ are the longitudinal and radial molecular diffusivities of the solute in bulk water (m^2/sec); $D_{i,w}$

is the molecular diffusivity in the biofilm (m^2/sec); $R_{i,j}$ is the reaction involving species i in the bulk reaction j; and $R_{i,k}$ is the reaction involving species i in the wall reaction k; $N_{s,b}$ and $N_{s,w}$ are the number of species in the bulk and the wall phases; r_f is the radial location of the bulk/biofilm interface (m); and r_0 is the pipe radius (m).

In Chapter 2 [27], the reduction of the 2-D model into a 1-D model for numerical simplicity purposes was discussed, together with the associated incorporation of the dispersive transport mechanism for the case of a single-component (chlorine). The governing 1-D advection-dispersion-reaction (ADR) equation for each of the bulk phase constituents $C_{i,b}$(x,t) can hence be written as:

$$\frac{\partial C_{i,b}}{\partial t} + \bar{u}\frac{\partial C_{i,b}}{\partial x} - D_i\frac{\partial^2 C_{i,b}}{\partial x^2} = \sum_{j=1}^{N_{r,b}} R_{i,j}\left(C_{i=1\ldots N_s,b}\right) - \frac{k_{f,i}}{r_h}\left(C_{i,b} - C_{i,w}\right) \qquad (3\text{-}3)$$

While for wall zone constituents $C_{i,w}$ it can be written as:

$$\frac{\partial C_{i,w}}{\partial t} = \sum_{k=1}^{N_{r,w}} R_{i,k}\left(C_{i=1\ldots N_s,w}\right) + \frac{k_{f,i}}{r_h}\left(C_{i,b} - C_{i,w}\right) \qquad (3\text{-}4)$$

where, D_i is the axial dispersion coefficient of constituent i; $k_{f,i}$ is the lumped mass transfer coefficient of constituent i at the bulk/biofilm interface (m/sec); and r_h is the hydraulic mean radius (m). Although the dynamic 2-D convection-diffusion equation provides a superior description of the solute transport compared to the 1-D model, the computational requirement for the numerical solution of a multi-species 2-D model is immense. Nevertheless, previous studies showed that both models qualitatively generate similar patterns for solute concentration distributions [29]. Therefore, we applied the simplified 1-D ADR formula in this study to create WU-MSRT.

The bulk zone represents the mobile portion with both advection and hydraulic dispersion controlling the transport of bulk phase constituents in the axial direction (Equation 3-3). The wall zone represents a thin biofilm layer uniformly distributed over the inner pipe surface, and it represents the stagnant portion with a behavior resembling a batch reacting system with zero net convective flux (Equation 3-4). Constituents are assumed to have uniform concentration profiles across the pipe cross section in the bulk phase as well as within the biofilm at the wall zone. Mass transfer of constituents at the bulk/biofilm interface is modeled as a thin film concentration boundary layer (CBL) with a lumped mass transfer coefficient (k_f) as appears in the second term on the right side of (Equations 3-3 & 3-4). This coefficient is dependent on the flow conditions and the molecular diffusion coefficient of the component [19].

The disinfectant considered in our model is chlorine, which is the most commonly adopted disinfectant by water utilities worldwide. THMs were selected as the representative DBP species for simulation because they typically constitute the largest fraction of DBPs in drinking water (typically accounts for approximately 50% of identified halogenated DBPs on a weight basis) [30]. However, the developed approach in this study can be applied for simulating any other disinfectant (e.g. chloramines), or DBP species (e.g. HAAs or nitrogenous DBPs) given that the appropriate set of reaction mechanisms is implemented. Total organic carbon (TOC) was adopted as a surrogate of the THMs precursor content derived from NOM, while biodegradable organic carbon (BDOC) was used as a measure of the microbial growth substrate.

Monod kinetics expressions were adopted to simulate bacterial regrowth and substrate utilization in the bulk flow and within the biofilm [19–24]. The rate of biomass detachment from the biofilm is assumed to have a first order dependence on both the shear stress at the pipe wall, and the attached biomass concentration [31,32]. Second order reaction kinetics were used to

describe chlorine-TOC reaction and THMs formation from NOM-based THMs precursors [33–35]. Details of the various processes considered in the model are included in the supplementary material section 3.9.2.

The model consists of 10 mass balance equations (Equations S-3.1 to S-3.10) to represent the spatial and temporal distributions of five constituents: chlorine, TOC, BDOC, biomass, and THMs, in two phases (Figure 3-2): bulk solution (Equations S-3.1 to S-3.5), and within the biofilm at the wall (Equations S-3.6 to S-3.10). To solve the complex system of partial differential equations (PDEs) that constitute the model, we applied the split-operator method (SOM) to decouple the transport and reaction processes of the multi-component system [20,36]. More details on the numerical approach are included in the supplementary material section 3.9.3.

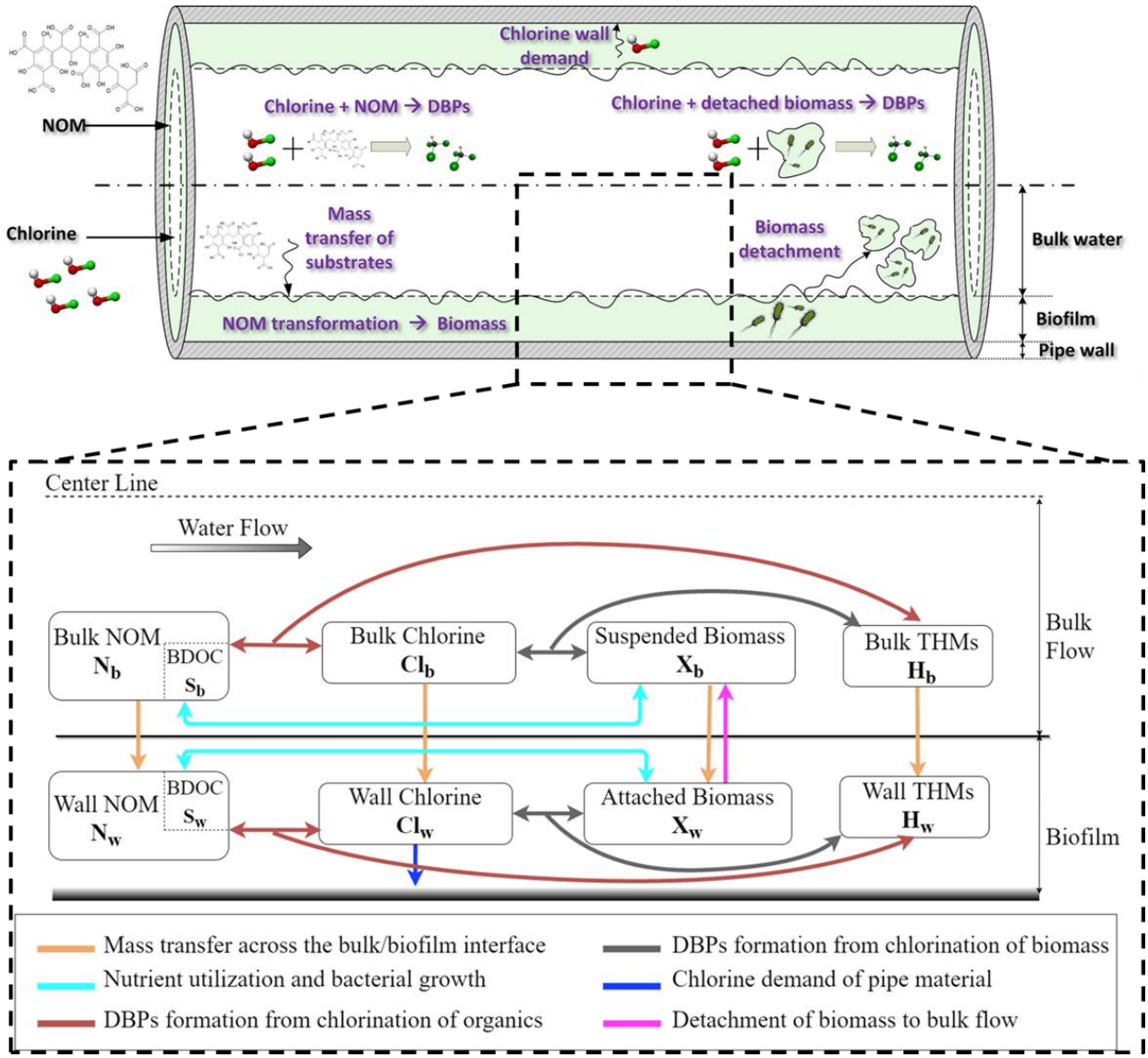

Figure 3-2. Schematic diagram of the fundamental processes considered in the model. NOM: Natural organic matter; BDOC: Biodegradable organic carbon; THMs: Trihalomethanes.

Modeling THMs formation from Biomass

A simple two constituent second order kinetic model was developed to simulate the kinetics of chlorine-biomass reaction, and THMs formation from microbial carbon in the bulk solution:

$$aCl_b + bX_b \rightarrow cH_b \tag{3-5}$$

The reaction rate is assumed to be of second order; first order with respect to both chlorine and biomass. The formation of THMs is then proportional to the chlorine demand of the reaction, which yields the following system of differential equations representing mass balance on each of the constituents:

$$\frac{\partial Cl_b}{\partial t} = -k_{Cl,X} Cl_b X_b \tag{3-6}$$

$$\frac{\partial X_b}{\partial t} = -Y_X k_{Cl,X} Cl_b X_b \,, \quad Y_X = \frac{b}{a} \tag{3-7}$$

$$\frac{\partial H_b}{\partial t} = Y_{H,2} k_{Cl,X} Cl_b X_b \,, \quad Y_{H,2} = \frac{c}{a} \tag{3-8}$$

Where, Cl_b is the free chlorine concentration in the bulk solution (mgCl/L); X_b is the bulk biomass concentration (mgC/L); H_b is the concentration of THMs in the bulk phase (µg/L); $k_{Cl,X}$ is the second order reaction rate (L/mgC.sec); Y_X is the yield coefficient representing the consumption of chlorine reactive sites in the biomass (mgC/mgCl); $Y_{H,2}$ is the THMs formation yield as a fraction of chlorine demand (µgTHM/mgCl). The previous system of equations can be analytically solved to yield the temporal distribution of the three constituents [33]. The model is applied to the experimental data of Wang et al. [15] for chloroform formation at different contact times between a bacterial cell solution and free chlorine in a bench scale reactor, where a non-linear least squares method was used to calibrate the values of $k_{Cl,X}$, Y_X and $Y_{H,2}$. The second order model yielded a

good fit for the experimental measurements (Figure 3-3), and the parameter values that gave the best fit are listed in Table S 3-3. (see supplementary material section 3.9.4 for more discussion). A sensitivity analysis was performed on the given second order model, and the yield parameter for THM formation $Y_{H,2}$ (ugTHM/mgC) was found to have the highest influence on the ultimate concentration of THMs, followed by the rate constant $k_{Cl,X}$ (L/mgC.sec). The yield parameter for the decay of organic carbon Y_X (mgC/mgCl) showed a conditional sensitivity, where increasing this parameter considerably lowered the THM formation, while decreasing it didn't have much effect, which is attributed to the second order reaction being limited by the biomass concentration instead of chlorine concentration.

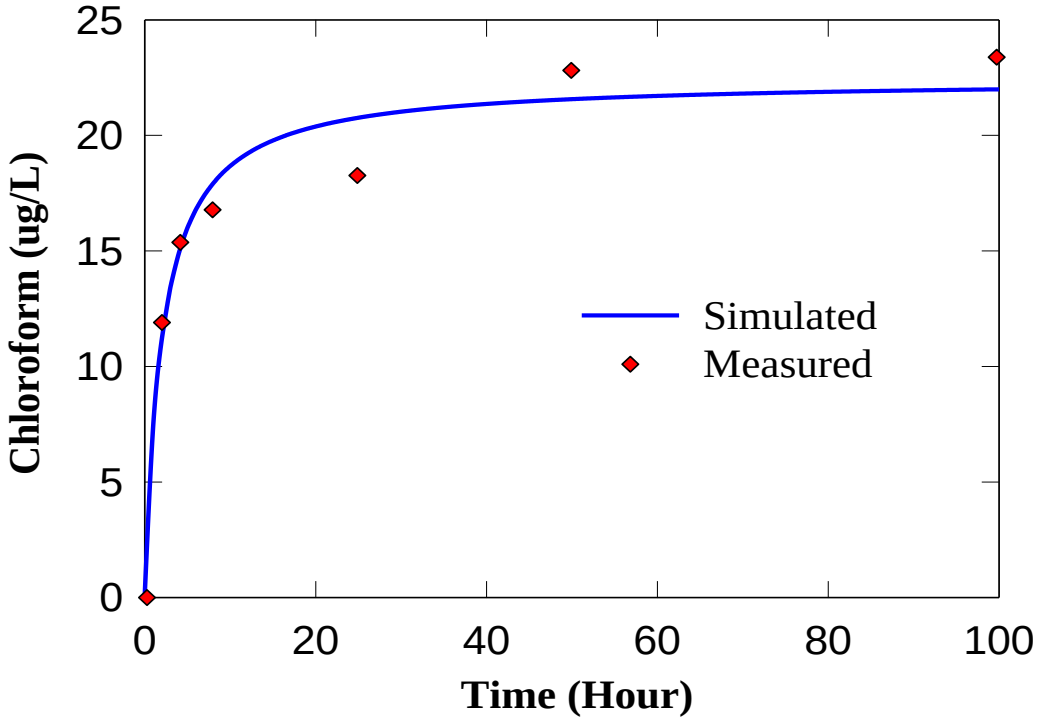

Figure 3-3. Second order model fit of THM formation from the chlorination of bacterial solution. Experimental measurements adopted from Wang et al. [15]

3.3.2 Model Implementation

The model was verified by comparing the simulation results to the field measured concentrations of free chlorine and heterotrophic plate counts (HPCs) in a full-scale DWDS, and THMs in a pilot-scale pipe loop setup. The model was then used to predict THMs levels in the full-scale DWDS and to investigate the effects of hydrodynamics, water temperature, and the concentration of organics on bacterial regrowth and THMs formation from biomass in a hypothetical pipe system. Table 3-1 summarizes the simulations conducted in this study.

Table 3-1. List of simulations conducted in Chapter 3

#	Simulation Type	No. of Simulations	Investigated Property	Comparison Against
1	Model Verification	4	Bacterial regrowth and Chlorine decay	Field measurements - actual DWDS
2		8	THMs formation from NOM	Pilot scale pipe loop system
3	Model Application	4	Total THMs formation	Field measurements – actual DWDS
4	Model Application	6	THMs formation from Biomass	Hypothetical system - Variable Flow
5		5		Hypothetical system - Variable Temperature
6		5		Hypothetical system - Variable TOC_0

Bacterial dynamics module verification

The model was applied to simulate chlorine decay and bacterial regrowth in an actual DWDS. The field measurements conducted by Prevost et al. [37] in the sampling campaign of the distribution system of the city of Laval, Quebec, Canada were used (see Table S 3-5). The published data set included heterotrophic plate counts (HPCs) and free chlorine concentrations measured at estimated progressive residence times downstream the Pont Viau treatment plant. The sampling data revealed the seasonal dependence of organic matter concentrations where BDOC contents were generally higher in warm water samples [38]. Data samples collected from large diameter transmission lines were used for comparison against model simulations with the exception of the final data points at a residence time of 20hr, which were collected from small diameter pipes. The steady state conditions were simulated by running the simulations using the average flow conditions ($\bar{u}$ = 0.1m/s -Re $\cong$ 30,000) until convergence (0.1%) was achieved for the concentrations of the ten constituents.

THMs module verification

The model was implemented to simulate chlorine disappearance and THMs formation in a pilot scale distribution system simulator to understand the effects of flow conditions and pipe materials. Experiments were performed on two pipe loops in the U.S. EPA's Test and Evaluation (T&E) facility in Cincinnati, Ohio, USA [39]. The first loop consisted of a new PVC pipe while the second loop was an aged ductile iron pipe with heavy scale build up. The published data set included the concentrations of THMs and free chlorine in water samples collected at regular time intervals under different flow regimes including turbulent, transitional, laminar, and stagnant flows. To simulate the new PVC pipe, wall zone was omitted from the model, and simulations were performed for only the five bulk-phase species.

Model application

The model, WU-MSRT, was then applied to simulate a hypothetical water distribution pipe that receives the effluent of a water treatment plant with the properties tabulated in Table S 3-4 for a total residence time of 72 hours. Re-chlorination was assumed to take place after 36 hours by introducing a chlorine dose to increase the residual concentration back to the initial level of 1 mg/L. The effects of altering the flow conditions (Re=5,000-30,000), water temperature (T=0°C-30°C), and initial TOC/Cl ratio (TOC_0/Cl_0=1-3) on bacterial regrowth and THMs formation from biomass were investigated.

Parameters acquisition

The model equations comprise 22 parameters that can be categorized into three sets: i- parameters for the bacterial regrowth module; ii- parameters for the THMs formation from chlorine-NOM reaction; and iii-parameters for the THMs formation from the chlorination of biomass. The values or formulae used for the three sets are given in Tables S 3-1, S 3-2, and S 3-3 in the supplementary material, respectively, together with the corresponding literature sources or the actual values used to give the best fit for the verification simulations.

3.4 Results and Discussion

3.4.1 Model Verification

Bacterial regrowth in the full-scale distribution system

Generally, the model showed good capability to simulate microbial regrowth and chlorine disappearance in the Pont Viau system under different temperatures and initial substrate concentrations. Figure 3-4 shows the results of the model simulations plotted against field measurements for HPC and free chlorine concentrations. The model was able to demonstrate the increase in the initial rate of bacterial growth corresponding to an increase in the water temperature. In warm (T=23.1 ^{o}C - Figure 3-4a) and lukewarm (T=13.5 ^{o}C - Figure 3-4b) water samples, rapid bacterial regrowth took place until reaching a maximum value corresponding to near-full substrate utilization. More importantly, the applied high chlorine dose (Cl_0=0.83mg/L) for the high temperature case (T=23.1 ^{o}C) was shown to be unable to inhibit fast microbial regrowth as shown in Figure 3-4a. In the cold-water samples (T=1 ^{o}C - Figure 3-4c, and 1.8 ^{o}C - Figure 3-4d), slower bacterial growth took place, where in one of the cases the chlorine dose has almost completely depleted while microbial growth is still taking place due to the remaining unmetabolized substrate (Figure 3-4c). Simulation results showed a noticeable sensitivity towards four of the model parameters: the maximum substrate utilization rate (u_{max}), the detachment coefficient (k_{det}), the temperature dependence rate constant (T_i), and the rate constant of the second order reaction between chlorine and bacteria ($k_{cl,x}$), which is in good agreement with previous studies [19,40].

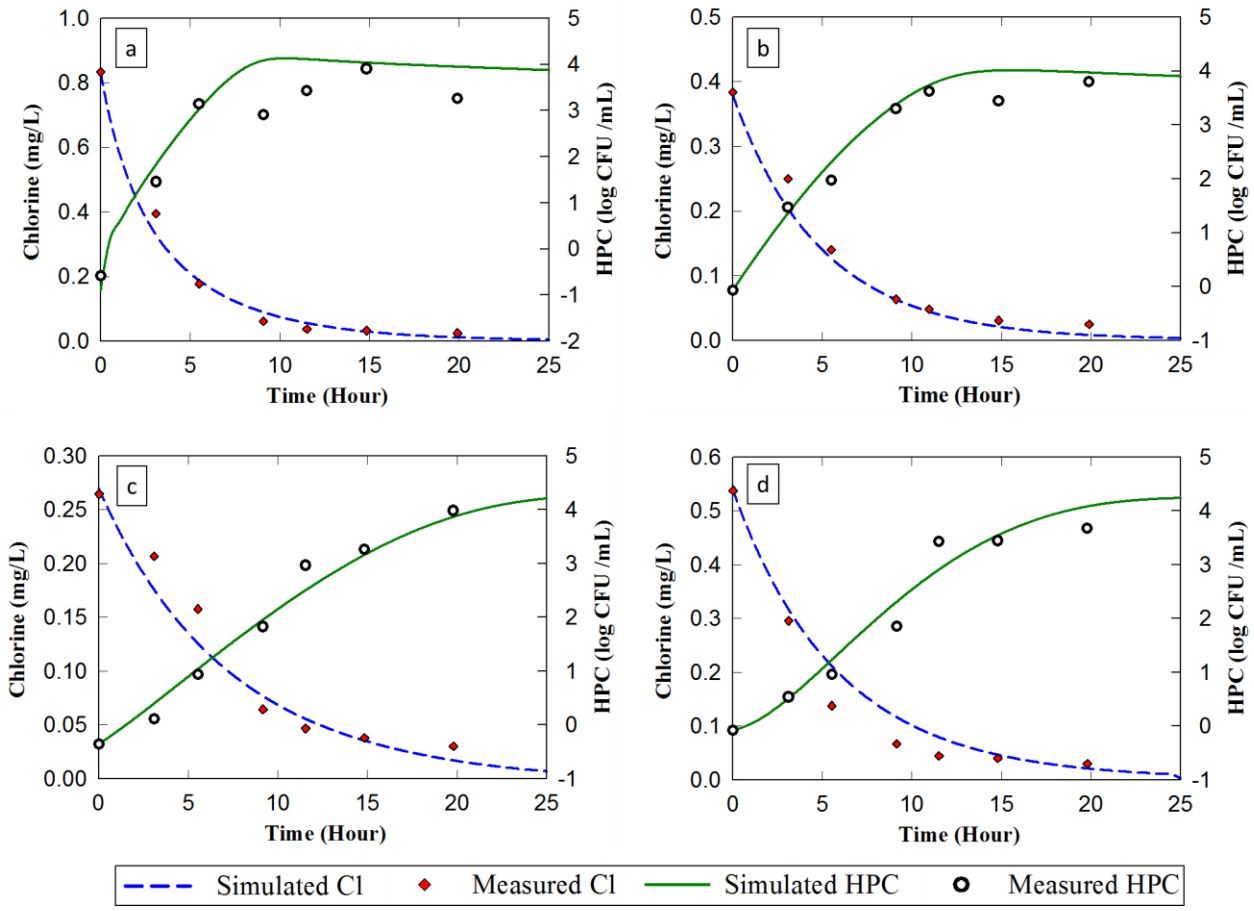

Figure 3-4. Model simulation results against field measured concentrations of free chlorine (mg/l) and HPC (log CFU/ml) for Prevost et al. [37] sampling campaign of the Pont Viau distribution network on: (a) 07-06-93; (b) 05-18-1993; (c) 01-12-1993; and (d) 12-15-1992.

An interesting remark was that the same set of parameters (shown in Table S 3-1) was used to simulate the four scenarios under different temperatures and initial water quality conditions. This implies that the model has a high predictive capability, where after being calibrated for a certain distribution system, it can be used to simulate the given distribution system under different seasonal scenarios without the need for recalibration with every scenario. The only exception was for the rate of biomass detachment, which showed an obvious dependence on the temperature that could not be accounted for using a constant detachment coefficient (k_{det}) as done by previous researchers. Future experimental and modeling studies might be required to elucidate the role of temperature in biomass detachment from the biofilm.

THMs formation in the pilot-scale distribution system simulator

Simulations were performed for all the described experimental cases for both the DI and PVC pipe loops (except for the stagnant flow case). Comparisons with measured concentrations were plotted in Figure 3-5 for the turbulent and transitional flow regimes and Figure 3-6 for the laminar flow regime. Overall, the model results were consistent with the measurements for both pipe loops under different hydrodynamic conditions, although it generated better results for the ductile iron pipe loop, which can be explained by the detailed consideration of the bulk and wall compartments, and properly accounting for mass transfer at the interface under different flow conditions. One important observation was that THMs formation continued in both pipe loops for several hours after complete chlorine disappearance. This illustrated the inadequacy of the second order model that implies that THMs formation should cease once chlorine is totally depleted from the system. A different model that separates the kinetics of THMs formation from chlorine decay through introducing the fast formation of a chlorinated intermediate followed by slower formation of THMs can be more suitable [41]. The model predicted minimal bacterial growth in the PVC pipe

under different flow regimes due to the absence of a biofilm layer that is typically responsible for bacterial production. For the DI loop, bacterial populations showed delayed development because of the high initial chlorine concentrations, which was consistent with the experimental results as no increase in the water turbidity was noticed in the samples collected at different times. The overall THMs production from bacteria was hence negligible under these conditions. Under laminar flow regimes (Figure 3-6), the model showed superior performance when compared to an advection-based technique that was simulated by ignoring the dispersive transport mechanism. Moreover, dispersive transport in real distribution network pipes will have an even higher impact on solute transport due to the dynamic nature of the inlet solute profile compared to the studied pipe loop with a fixed boundary condition [42]. This is the first study to consider dispersive transport in modeling THMs formation in drinking water pipes.

We noted that the dispersion coefficient required to fit the laminar flow regime in the DI pipe was almost one-tenth of the calculated Taylor's dispersion rate, while no adjustment was required to yield a good fit for the smooth PVC pipe. This might be a result of the introduction of local mixing near the pipe wall due to the roughness of the DI pipe, which disturbs the velocity profile. The PVC pipe loop required a slower second order reaction rate constant ($k_{cl,N}$) compared to the DI pipe loop by a factor of 28%, implying faster chlorine decay in the DI pipe, which is in agreement with the literature [43,44]. The yield coefficients for TOC decay (Y_N), and THMs formation ($Y_{H,1}$) were found to consistently increase with the initial TOC/Cl ratio (see Figure S 3-2), which is a characteristic of the second order kinetics, and was observed by previous researchers for bench scale experiments as well [34].

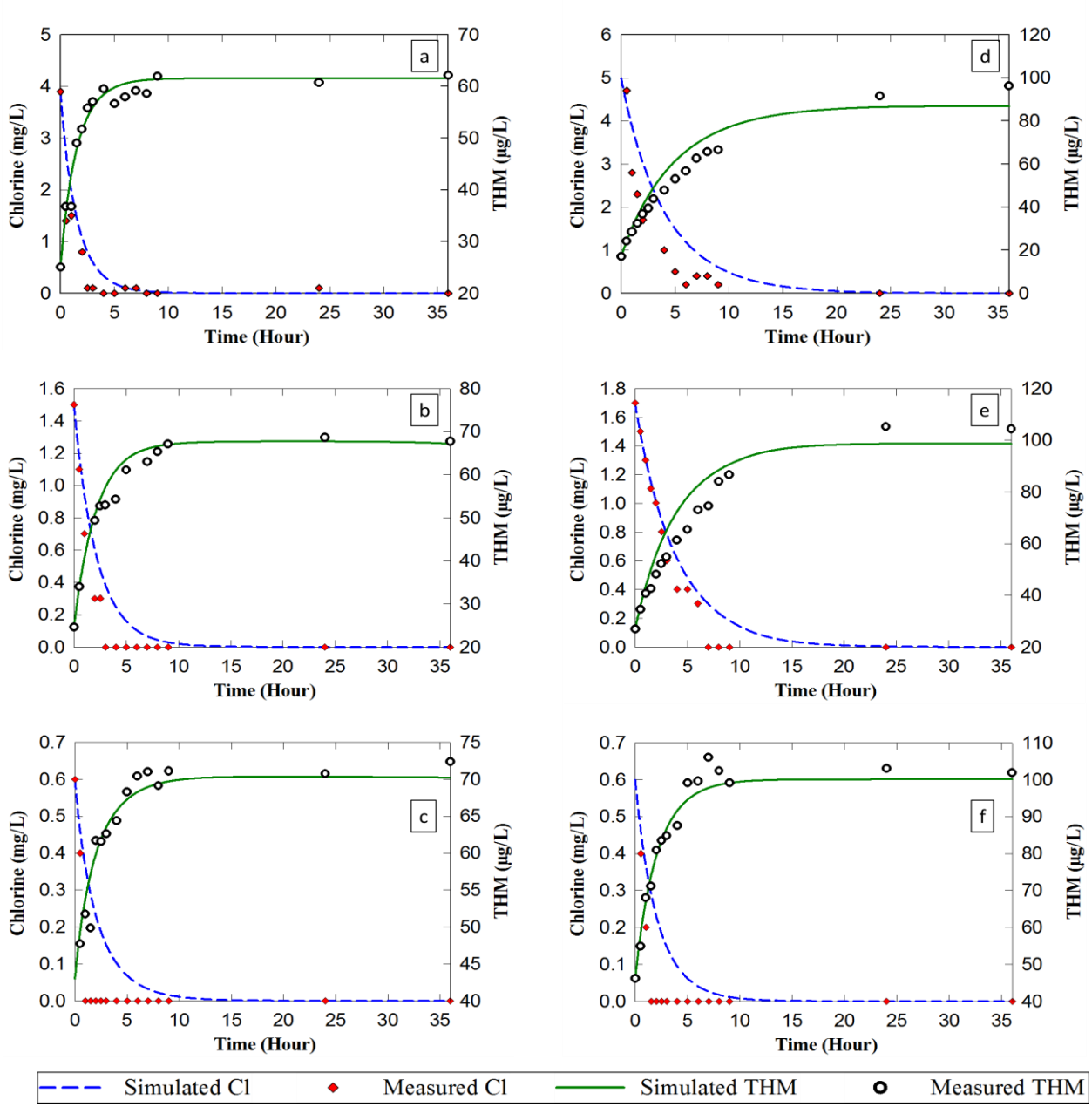

Figure 3-5. Model simulation results against experimentally measured concentrations of free chlorine (mg/l) and TTHM (µg/l) for Yang et al. [39] pilot scale study – DI pipe loop: (a) Re=52,500; (b) Re=5,000 ; and (c) Re=3,500, and PVC pipe loop: (d) Re=52,500; (e) Re=5,000; and (f) Re=3,500.

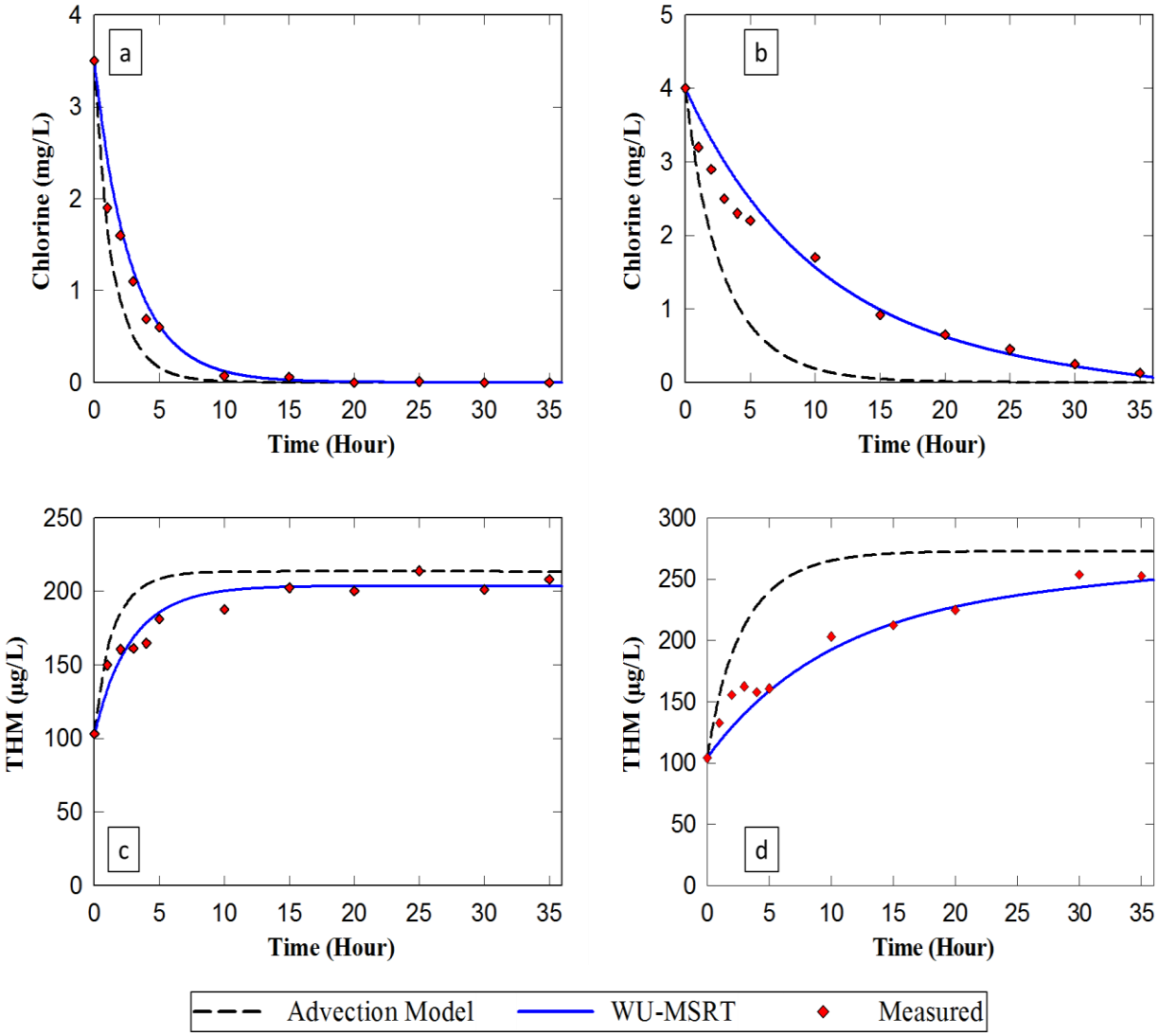

Figure 3-6. Model simulation results against experimentally measured concentrations of Yang et al. [39] pilot scale study for free chlorine (mg/l) in: (a) DI pipe loop; and (b) PVC pipe loop, and TTHM (µg/l) in: (c) DI pipe loop; and (d) PVC pipe loop.

3.4.2 THMs formation in a full-scale distribution system

The model was applied to predict THMs levels in the Pont Viau distribution system that was used to verify the bacterial growth module. The calibrated relationships for the coefficients of THMs formation from NOM-based THM precursors (see Figure S 3-2), and from biomass-derived precursors (see Table S 3-3) were used for simulation. Since THMs formation yields are strongly dependent on the pH level, it is important to remark that the average pH of the water in the distribution system (8.1) [45] was consistent with the pH of the experimental studies used to calibrate the model. Figure 3-7 shows the simulated total THMs concentrations as well as the fraction of THMs formed from biomass-derived precursors. The results indicated that the THMs concentrations in the system are generally lower than the maximum permissible concentration of 80µg/L. During the earlier described sampling study, the concentration of total dissolved halogens (DOX) was sampled with the THMs levels estimated to constitute 3.8~7.9% [45]. The provided regression model (based on field samples in the presence of free chlorine) was used herein to estimate the concentration of THMs for each one of simulated four scenarios. The calculated THMs ranges were: (a) 14.0~29.0µg/L; (b) 9.6~20.0µg/L; (c) 4.3~8.9 µg/L; and (d) 3.9~8.1 µg/L, and they all were in good agreement with what the model predicted (Figure 3-7). This validated the predictive capability of the model to estimate the THMs levels in real DWDSs.

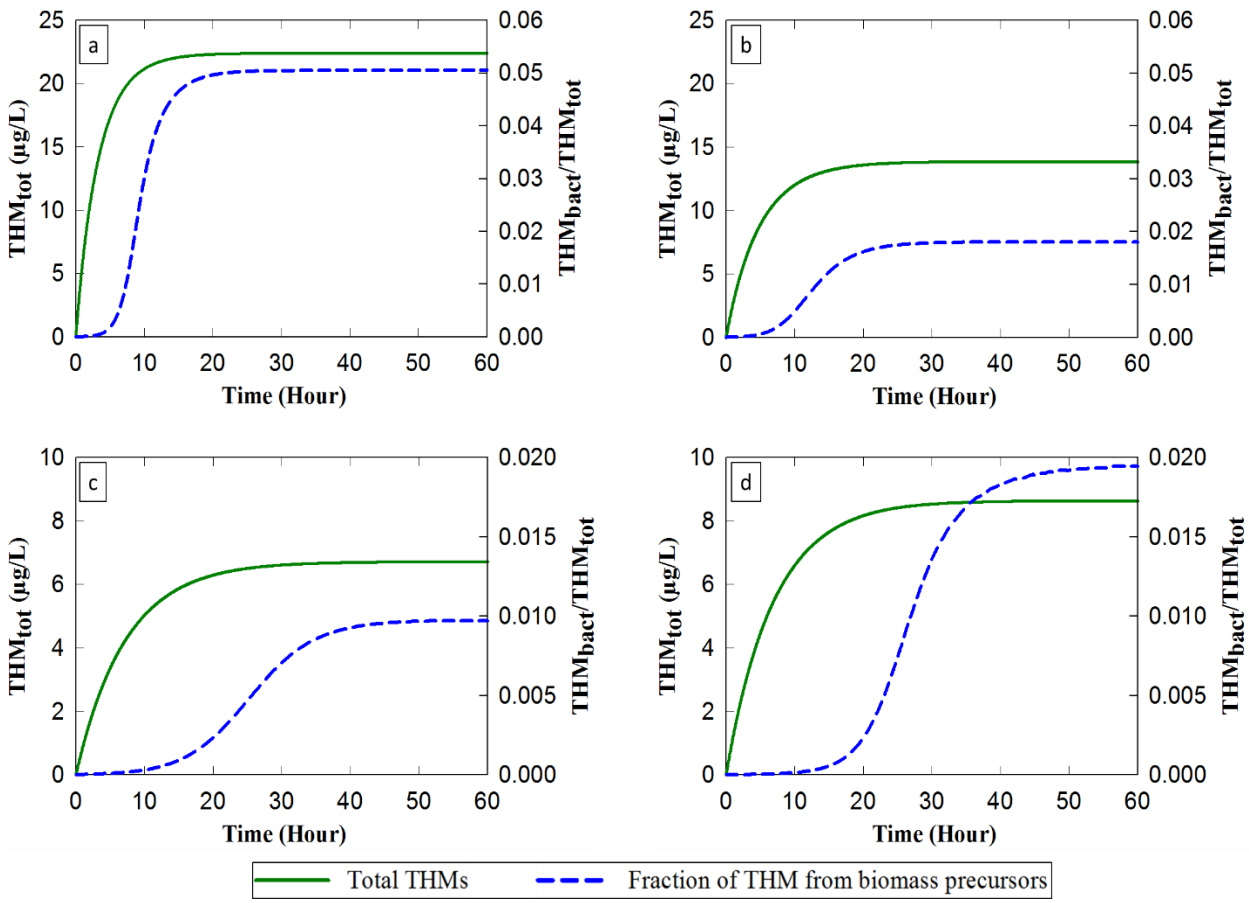

Figure 3-7. Predicted THM concentrations in the Pont Viau distribution network corresponding to Prevost et al. [37] field sampling on: (a) 07-06-93; (b) 05-18-1993; (c) 01-12-1993; and (d) 12-15-1992.

The fraction of THMs generated by biomass-derived precursors was found to depend mainly on the factors controlling the rate of bacterial regrowth, including the concentration of nutrients, water temperature, and the initial chlorination dose. The maximum fraction was observed for sample (a) (Figure 3-7a), which had the highest temperature (T=23.1 ^{o}C) and initial substrate concentration ($BDOC_0$=0.83 mg/L) that lead to a relatively quick bacterial growth (Figure 3-4a). More importantly, the use of a high dose of free chlorine (Cl_0=0.83 mg/L) to control the bacterial regrowth resulted in a high fraction of THMs formed from biomass-derived precursors of about 5% of the total THMs, compared to less than 2% for sample (b) that had the same nutrient concentration ($BDOC_0$=0.82 mg/L) but a much lower chlorine dose (Cl_0=0.38 mg/L). The same remark can be noted by comparing the two cold-water samples (c) and (d), with both having almost similar temperatures (T=1 ^{o}C and 1.8 ^{o}C). More interestingly, the bacterial contribution to THMs formation was slightly higher for the cold-water sample (d) compared to the lukewarm (T=13.5 ^{o}C) sample (b) since it had a higher chlorine dose (Cl_0=0.54 mg/L), despite the higher temperature and BDOC concentration in the latter. To further elucidate the role of initial chlorine dose, we ran two more scenarios of simulation (a), with the first one having the initial chlorine concentration increased to 1.24 mg/L (1.5 times the original dose), while the other having the initial BDOC concentration decreased to 0.55 mg/L (0.66 times the original dose), to represent two alternative measures for controlling bacterial re-growth. Increasing the initial chlorine dose failed to control the fast regrowth observed in the warm sample (results not shown), but more importantly, the contribution of bacteria-derived precursors increased to 7.6%. On the other hand, reducing the influent substrate concentrations was found to be more effective in controlling the fast regrowth, and the contribution dropped to 3.2%. These results highlighted the significant effect of the initial chlorine dose on the contribution of bacteria-derived precursors to THMs formation.

It is important to note that despite the generally low contribution of bacteria-derived precursors observed for the studied system, their formation mechanisms were different from that of NOM based precursors. While THMs formation from NOM proceeds once the chlorine dose is applied, a clear delay is observed in the THMs formation from biomass until bacterial re-growth takes place. This delay period is mainly dictated by the rate of bacterial growth, which depends on the water temperature and the concentration of substrates. Furthermore, this contribution is expected to become more significant if the drinking water was re-chlorinated, where bacterial re-growth would increase rapidly after the complete exhaustion of the initial chlorine dose if enough nutrients still exist in the system.

3.4.3 Model Application – Hypothetical Pipe System

Influence of hydraulic conditions

Applying the model to the hypothetical pipe system at different flow conditions, we found that the flow velocity significantly affects THMs formation from biomass as it controls bacterial regrowth through two simultaneous processes: (1) Increasing the flow velocity enhances the mass transfer of solutes across the bulk/biofilm interface. This includes the transport of disinfectants and substrates, which are the two key species controlling bacterial growth in the biofilm. (2) High shear stresses enhance the detachment of the biomass from the biofilm. The Blasius equation implemented to estimate shear stress under turbulent conditions shows that the shear stress increases with the flow velocity to a power greater than 1.

Figure 3-8a shows the bacterial growth dynamics in the simulated pipe system under different flow conditions. In these simulations, the flow velocity was altered to effectively change the Reynolds number. The growth scheme can be seen to have two distinct patterns based on the

hydraulic conditions. The first pattern takes place at Reynolds numbers in the range (5,000 – 15,000), while the second scheme takes place in the range (25,000-30,000), with a transition stage in between (15,000-25,000). The first pattern is characterized by immediate bacterial growth within the first 6 hours until reaching a maximum peak of HPC=2.5-3*10^4 CFU/mL, followed by a fast mortality within the following 12 hours that kills the major portion of biomass (around 70% of suspended biomass) before introducing re-chlorination after 36 hours. The second growth pattern shows a delayed growth phase, where the peak biomass concentration is reached after 12 hours, followed by a very slow mortality rate during the following 24 hours. In the first pattern, the increase in the flow velocity from Re=5,000 to 15,000 is shown to enhance the initial bacterial growth rate (higher peak concentration at an earlier time), which can be explained by the improved delivery of nutrients to the biofilm where bacterial growth mainly takes place. Although increasing the flow velocity also promotes mass transfer of chlorine to the biofilm, its overall effect on biomass mortality and inactivation is greatly reduced by the resistance factor (k_r) – (See Equation S-3.9). Bacterial growth then reaches a maximum after fully utilizing the substrate (BDOC concentration drops to 10% of initial value in less than 4 hours). However, this happens at a point where high chlorine residuals are still existent in the bulk phase (chlorine concentrations are 20% of initial dose after 6 hours), which can explain the fast mortality of bacteria after reaching this maximum.

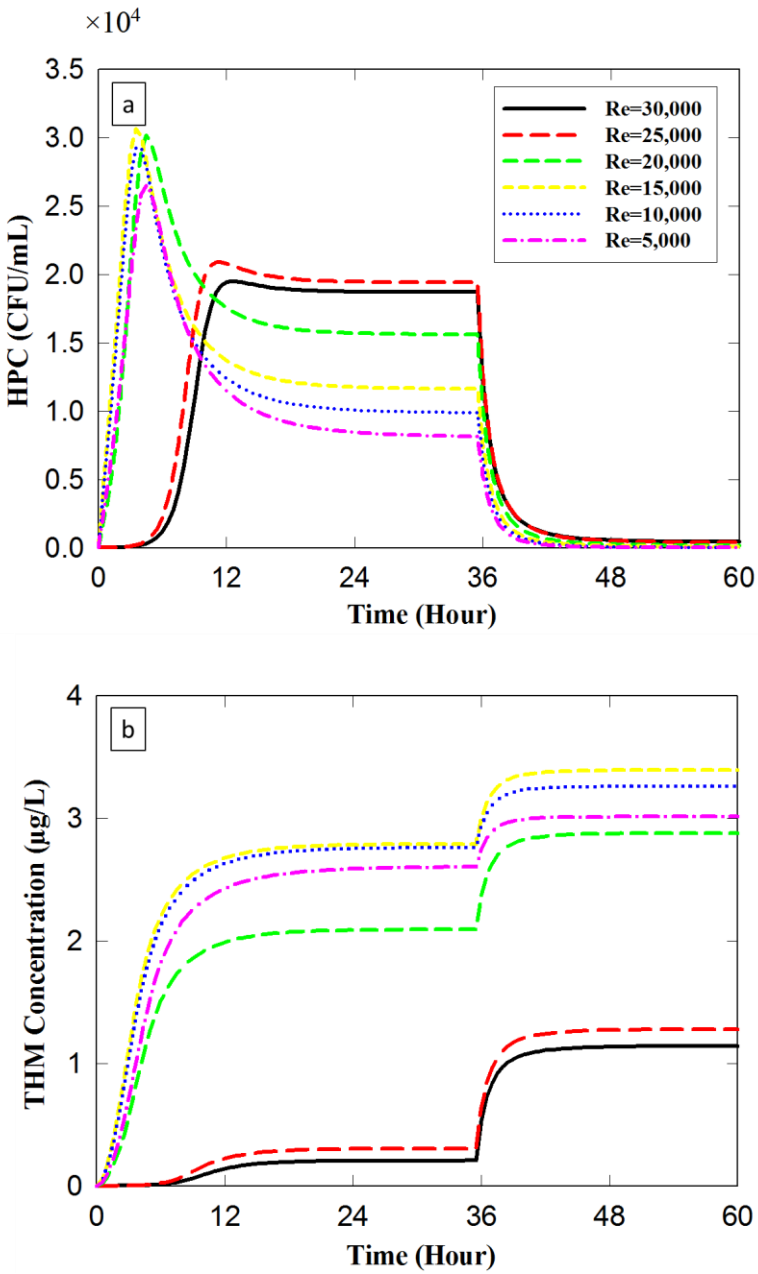

Figure 3-8. Model application results for the concentrations of (a) HPC (log CFU/ml); and (b) THM (µg/l) produced from bacteria-derived precursors, under different flow conditions.

To help better understand the two growth patterns, the total biomass growth rate in the biofilm (Equation S-3.9) can be viewed as a combination of three terms:

$$\frac{\partial X_w}{\partial t} = [\text{substrate utilization-detach. rate-chlorination}]X_w \qquad (3\text{-}9)$$

The rate of mass transfer of bacterial cells from the bulk phase to the biofilm and the rate of natural biomass mortality have small magnitudes compared to the other terms and do not play a significant role in the initial growth phase, and hence were ignored in this analysis. Increasing the flow velocity will generally increase the absolute magnitudes of the three terms but with different rates. In the first pattern, the substrate utilization term dominates over the detachment rate and the chlorination rate terms leading to rapid bacterial growth. A threshold is then reached somewhere at Re=15,000-25,000, where the detachment rate combined with higher chlorine delivery becomes significant enough to initially inhibit the fast bacterial growth in the biofilm. In the second pattern, bacterial growth slowly takes place after some delay period that increases with the flow velocity, or more precisely, with the shear stress as the detachment rate term increases. Since chlorine depletes by parallel reactions with NOM and pipe material demand, bacterial decay then proceeds at a much slower rate compared to the first pattern (chlorine residuals drop to only 4% of the initial dose after 10 hours). When the water is re-chlorinated such that the residual concentration is raised back to the initial chlorine dose of 1 mg/L, a spontaneous death of all the remaining bacteria is observed under all simulated flow regimes. Regrowth is then inhibited after booster chlorination as the substrate has been fully utilized at this point.

The effect of flow conditions on the THMs production from biomass can be realized from Figure 3-8b. THMs formation from biomass can be divided into two phases; the initial-chlorination phase and the re-chlorination event. Both phases can be readily explained by the

bacterial growth dynamics shown in Figure 3-8a. For the initial-chlorination phase, higher THMs formation rates are observed for the first growth pattern corresponding to fast bacterial growth that is concurrent with high chlorine residuals in the system. This leads the THMs yield to increase with the flow velocity until reaching the previously described threshold. For the second growth pattern, the delayed bacterial growth leads to a delay in THMs formation. The re-chlorination event then increases the THMs concentrations with a magnitude that corresponds to the remaining fraction of biomass in the system after the initial-chlorination phase, which reflects the quantity of bacteria-derived precursors available for THMs formation. The maximum THMs yield from biomass took place at the case of Re=15,000 with the ratio of THMs formed from microbial origin of maximum 12% of the total THMs yield of the pipe (see Figure S 3-5a).

Influence of water temperature

Temperature has an interesting effect on the dynamics of bacterial regrowth where an increase in the temperature affects multiple simultaneous processes: (1) A rise in the temperature leads to a faster disappearance of chlorine residuals, due to the increased reaction rate with organic compounds. A simultaneous consumption of the substrate will also take place. (2) Temperature enhances bacterial growth with an exponential dependence term in the Monod's expression to a certain threshold (see Equations S-3.4 & S-3.9). (3) Temperature increases the reaction rate between chlorine and biomass, leading to faster mortality, and faster THMs production. Figure S 3-3a shows the bacterial growth dynamics in the simulated pipe under different temperatures. It can be seen that as the temperature drops from 30°C to 0°C, a clear delay in the bacterial growth takes place, where the peak biomass concentration increases from 5 hrs for 30°C to more than 36 hours for 0°C. This happens since for lower temperatures, substrate utilization proceeds at a slower rate, in addition to the slower chlorine consumption that leads the bulk phase residuals to exist for

a longer residence time at a higher concentration. The peak biomass concentration drops from $3*10^4$ CFU/mL to $2.2*10^4$ CFU/mL (36%) as the temperature rises from 20°C to 30°C, due to the higher chlorine residual concentration at the point where the peak biomass takes place, while it drops from $3*10^4$ CFU/mL to $1*10^4$ CFU/mL (67%) as the temperature drops from 20°C to 0°C due to the consumption of the substrate. Figure S 3-3b illustrates the effect of temperature on THMs formation, where in the initial chlorination phase the production of THMs consistently increases with temperature from 0°C to 25°C. THMs production from the 25°C case was still larger than the 20°C case even though bacterial populations reached a higher magnitude for the latter. THMs production following the re-chlorination event was proportional to the concentration of the suspended biomass in the system at the point of chlorine dosing where the maximum yield was observed for the case of 10°C. However, overall THMs production of the 25°C simulation was the highest with the fraction of THMs from bacteria-derived precursor of (~11%) (see Figure S 3-5b).

Influence of TOC/Cl ratio

Increasing the influent concentration of TOC to the system promotes bacterial growth in the distribution system as this increases the substrate concentration and simultaneously consumes chlorine residuals. Figure S 3-4a shows the HPC concentrations in the simulated pipe under different initial TOC/Cl ratios, where the rate of microbial growth is consistently enhanced as this ratio increases. As the inlet TOC/Cl ratio increases from 1 to 3, the peak biomass concentrations increases from $1*10^4$ CFU/mL to $5*10^4$ CFU/mL, and the time taken to reach this peak drops from 15 to 4 hours. Furthermore, the surviving biomass in the system after chlorine consumption increases consistently with the influent TOC concentration, which leads to even higher THMs formation under re-chlorination condition as shown in Figure S 3-4b. The fraction of THMs

formed from bacteria-derived precursors consistently increases with the inlet TOC concentration where the maximum contribution (~10.5%) was observed for TOC/Cl=3 (see Figure S 3-5c).

3.4.4 Environmental Implications

The results of this study demonstrated the importance of considering a parallel route for DBPs formation represented by the mass transfer of NOM to the biofilm followed by biotransformation and then detachment of biomass-derived precursors back to the bulk phase as an important alternative to the well-known DBP formation route from direct chlorination of NOM based precursors. Previous field studies showed that a BDOC concentration of as low as 0.5 mg/L is sufficient to support bacterial regrowth if low disinfectant residuals existed in the system [46]. If water utilities responded by simply increasing the disinfectant dosage, this might lead to the adverse effect of forming excessive harmful DBPs in the distribution systems, especially if the system conditions, i.e. hydraulics and temperature, assisted fast bacterial regrowth. A safer practice would be to implement a treatment technique that removes microbial substrates, such as bio-filtration [8]. While HPCs are typically used as an indicator of the microbiological quality of drinking water, they are currently not enforced in the US under the safe drinking water act (SDWA), as they do not necessarily reflect a health hazard [25,47]. However, the current practice completely overlooks their important contribution to the formation of disinfection byproducts, which are potential carcinogens, teratogens or mutagens. Future modeling work on other disinfection byproducts, such as HAAs and nitrogenous DBPs can provide the full picture on the role of biofilms in the formation and fate of the overall DBPs.

3.5 Conclusions

A multi-species reactive-transport model for simulating the transport and interactions of disinfectants, organic compounds, biomass, and disinfection byproducts (DBPs) in the pipes of drinking water distribution systems was developed. This study presents the first attempt to model the formation of DBPs from organic precursors of microbial origin, which is implemented to investigate the role of biofilms in the formation and fate of trihalomethanes (THMs) in the distribution system. The capability of the model to simulate chlorine decay, bacterial regrowth dynamics, and THMs formation in an actual distribution system under different hydraulic, seasonal and water quality conditions was demonstrated. Simulation results revealed that fast bacterial regrowth in the system increases the contribution of biomass-derived precursors to the total THMs budget, especially if high initial chlorine doses were applied to preserve the microbiological quality of the finished water. While this contribution was found to increase almost consistently with the water temperature and the concentration of nutrients, system hydraulics had a rather interesting effect, where multiple competing phenomena are significantly controlled by the flow conditions. These phenomena include the rate of mass transfer of nutrients and disinfectants from the bulk flow to the biofilm, and the rate of biomass detachment from the biofilm under shear stresses. Under the studied conditions, the contribution of bacteria-derived precursors was found to reach a maximum of 12% of the total formed THMs, which is significantly less than those formed from NOM-based precursors. However, while the formation of THMs from NOM proceeds instantly after applying the chlorine dose, the mechanisms of THMs formation from bacterial sources were mainly controlled by the rates of bacterial regrowth in the system, which influenced the overall THM formation mechanism. These results highlighted the importance of integrating bacterial dynamics modeling with predictive DBPs formation models. The presented

model can be used by water utilities to balance the risks of microbiological and DBPs contamination, by simulating different scenarios for the quality of the treated drinking water effluent from the treatment plant. The model can also be implemented to identify the locations where excessive microbial regrowth or DBPs formation are expected to take place, and the further optimization of the operational schemes to ensure safe drinking water supply at all points in the network.

3.6 List of Symbols

C_i	concentration of the ith species (mg/L)
D_i	diffusion coefficient of species *i* (m^2/sec)
f(r)	radial flow distribution parameter
$k_{f,i}$	lumped mass transfer coefficient of constituent *i* (m/sec)
Ri	reaction involving species *i* (mg/L.sec)
Re	Reynolds number (-)
r	radial coordinate (m)
r_f	radial location of the bulk/biofilm interface (m)
r_h	hydraulic mean radius (m)
r_0	pipe radius (m)
t	time (sec)
$\bar{u}$	average flow velocity in the pipe (m/sec)
x	axial coordinate (m)

Subscripts

b	bulk phase
i	one of the constituents
j	one of the wall zone reactions
k	one of the bulk phase reaction
L	longitudinal
r	radial
w	wall zone

3.7 Acknowledgements

This work was partially funded by U.S. EPA through the CB&I Contract EP-C-4-014. The research described herein has been subjected to the Agency's peer and administrative review and has been approved for external publication. Any opinions expressed in this paper are those of the authors and do not necessarily reflect the views of the Agency, therefore, no official endorsement should be inferred. Any mention of trade names or commercial products does not constitute endorsement or recommendation for use.

3.8 References

[1] G.A. Gagnon, P.M. Huck, Removal of easily biodegradable organic compounds by drinking water biofilms: Analysis of kinetics and mass transfer, Water Res. 35 (2001) 2554–2564.

[2] Y. Shen, G.L. Monroy, N. Derlon, D. Janjaroen, C. Huang, E. Morgenroth, S.A. Boppart, N.J. Ashbolt, W.T. Liu, T.H. Nguyen, Role of biofilm roughness and hydrodynamic conditions in legionella pneumophila adhesion to and detachment from simulated drinking water biofilms, Environ. Sci. Technol. 49 (2015) 4274–4282.

[3] Y. Shen, C. Huang, G.L. Monroy, D. Janjaroen, N. Derlon, J. Lin, R.M. Espinosa-Marzal, E. Morgenroth, S.A. Boppart, N.J. Ashbolt, W.T. Liu, T.H. Nguyen, Response of simulated drinking water biofilm mechanical and structural properties to long-term disinfectant exposure, Environ. Sci. Technol. 50 (2016) 1779–1787.

[4] D. Brown, J. Bridgeman, J.R. West, Predicting chlorine decay and THM formation in water supply systems, Rev. Environ. Sci. Biotechnol. 10 (2011) 79–99.

[5] R. Sadiq, M.J. Rodriguez, Disinfection by-products (DBPs) in drinking water and predictive models for their occurrence: A review, Sci. Total Environ. 321 (2004) 21–46.

[6] E.C. Ged, P.A. Chadik, T.H. Boyer, Predictive capability of chlorination disinfection byproducts models, J. Environ. Manage. 149 (2015) 253–262.

[7] S. Chowdhury, P. Champagne, P.J. McLellan, Models for predicting disinfection byproduct (DBP) formation in drinking waters: A chronological review, Sci. Total Environ. 407 (2009) 4189–4206.

[8] J. Woolschlager, B. Rittmann, P. Piriou, Water quality decay in distribution systems – problems, causes, and new modeling tools, Urban Water J. 2 (2005) 69–79.

[9] I. Toroz, V. Uyak, Seasonal variations of trihalomethanes (THMs) in water distribution networks of Istanbul City, Desalination. 176 (2005) 127–141.

[10] P. Pieri, S.S. Andra, P. Charisiadis, G. Demetriou, N. Zambakides, K.C. Makris, Variability of Tap Water Residual Chlorine and Microbial Counts at Spatially Resolved Points of Use, Environ. Eng. Sci. 31 (2014) 193-201.

[11] L.A. Rossman, R.A. Brown, P.C. Singer, J.R. Nuckols, DBP formation kinetics in a simulated distribution system, Water Res. 35 (2001) 3483–3489.

[12] Z. Wang, C.M. Hessler, Z. Xue, Y. Seo, The role of extracellular polymeric substances on the sorption of natural organic matter, Water Res. 46 (2012) 1052–1060.

[13] H.-H. Tung, Y.F. Xie, Association between haloacetic acid degradation and heterotrophic bacteria in water distribution systems., Water Res. 43 (2009) 971–8.

[14] J.J. Wang, X. Liu, T.W. Ng, J.W. Xiao, A.T. Chow, P.K. Wong, Disinfection byproduct formation from chlorination of pure bacterial cells and pipeline biofilms, Water Res. 47 (2013) 2701–2709.

[15] Z. Wang, J. Kim, Y. Seo, Influence of bacterial extracellular polymeric substances on the formation of carbonaceous and nitrogenous disinfection byproducts, Environ. Sci. Technol. 46 (2012) 11361–11369.

[16] Z. Wang, O. Choi, Y. Seo, Relative contribution of biomolecules in bacterial extracellular polymeric substances to disinfection byproduct formation, Environ. Sci. Technol. 47 (2013) 9764–9773.

[17] Z. Xue, Y. Seo, Impact of chlorine disinfection on redistribution of cell clusters from biofilms, Environ. Sci. Technol. 47 (2013) 1365–1372.

[18] J.B. Kaplan, Biofilm Dispersal : Mechanisms , Clinical Implications , and Potential Therapeutic Uses, J. Dent. Res. 89 (2010) 205–218.

[19] G.R. Munavalli, M.S.M. Kumar, Dynamic simulation of multicomponent reaction transport in water distribution systems, Water Res. 38 (2004) 1971–1988.

[20] W. Zhang, C.T. Miller, F. a. DiGiano, Bacterial Regrowth Model for Water Distribution Systems Incorporating Alternating Split-Operator Solution Technique, J. Environ. Eng. 130 (2004) 932–941.

[21] C. Lu, P. Biswas, R.M. Clark, Simultaneous transport of substrates, disinfectants and microorganisms in water pipes, Water Res. 29 (1995) 881–894.

[22] S. Dukan, L. Yves, P. Piriou, F. Guyon, P. Villon, Dynamic modelling of bacterial growth in drinking water networks, Water Res. 30 (1996) 1991–2002.

[23] P. Piriou, S. Dukan, L. Kiene, Modelling bacteriological water quality in drinking water distribution systems, Water Sci. Technol. 38 (1998) 299–307.

[24] F.Y. Bois, T. Fahmy, J.C. Block, D. Gatel, Dynamic modeling of bacteria in a pilot drinking-water distribution system, Water Res. 31 (1997) 3146–3156.

[25] S. Chowdhury, Heterotrophic bacteria in drinking water distribution system: A review, Environ. Monit. Assess. 184 (2012) 6087–6137.

[26] F. Shang, J.G. Uber, L. a Rossman, Modeling reaction and transport of multiple species in water distribution systems., Environ. Sci. Technol. 42 (2008) 808–814.

[27] A.A. Abokifa, Y.J. Yang, C.S. Lo, P. Biswas, Water quality modeling in the dead end sections of drinking water distribution networks, Water Res. 89 (2016) 107–117.

[28] C. Nguyen, C. Elfland, M. Edwards, Impact of advanced water conservation features and new copper pipe on rapid chloramine decay and microbial regrowth, Water Res. 46 (2012) 611–621.

[29] G. Naser, B.W. Karney, A 2-D transient multicomponent simulation model: Application to pipe wall corrosion, J. Hydro-Environment Res. 1 (2007) 56–69.

[30] S.W. Krasner, M.J. McGuire, J.G. Jacangelo, N.L. Patania, K.M. Reagan, E.M. Aieta, The Occurrence of Disinfection By-products in US Drinking Water, J. Am. Water Works Assoc. 81 (1989) 41–53.

[31] I. Schrottenbaum, J. Uber, N. Ashbolt, R. Murray, R. Janke, J. Szabo, D. Boccelli, Simple Model of Attachment and Detachment of Pathogens in Water Distribution System Biofilms, in: World Environ. Water Resour. Congr. 2009, 2009: pp. 1–13.

[32] H. Horn, S. Lackner, Modeling of Biofilm Systems: A Review, Adv. Biochem. Eng. Biotechnol. (2014) 53–76.

[33] R.M. Clark, Chlorine Demand and TTHM Formation Kinetics: A Second-Order Model, J. Environ. Eng. 124 (1998) 16–24.

[34] R.M. Clark, M. Sivaganesan, Predicting Chlorine Residuals in Drinking Water: Second Order Model, J. Water Resour. Plan. Manag. 128 (2002) 152–161.

[35] D.L. Boccelli, M.E. Tryby, J.G. Uber, R.S. Summers, A reactive species model for chlorine decay and THM formation under rechlorination conditions, Water Res. 37 (2003) 2654–2666.

[36] D. A. Barry, C.T. Miller, P.J. Culligan, K. Bajracharya, Analysis of split operator methods for nonlinear and multispecies groundwater chemical transport models, Math. Comput. Simul. 43 (1997) 331–341.

[37] M. Prevost, A. Rompre, J. Coallier, P. Servais, P. Laurent, B. Clement, P. LaFrance, M. Prévost, A. Rompré, J. Coallier, P. Servais, Suspended bacterial biomass and activity in full-scale drinking water distribution systems: impact of water treatment, Water Res. 32 (1998) 1393–1406.

[38] M. Prévost, A. Rompré, H. Baribeau, J. Coallier, Service lines:, J. Am. Water Works Assoc. 89 (1997) 78–92.

[39] Y.J. Yang, D. Wre, C.A. Impellitteri, R.M. Clark, R.C. Haught, D.A. Schupp, S. Panguluri, E.R. Krishnan, Chlorine decay and DBP formation under different flow regions in PVC and ductile iron pipes: Preliminary results on the role of flow velocity and radial mass transfer, in: World Environ. Water Resour. Congr., 2008: pp. 1–10.

[40] F.A. Digiano, W. Zhang, Uncertainty analysis in a mechanistic model of bacterial regrowth in distribution systems, Environ. Sci. Technol. 38 (2004) 5925–5931.

[41] A. Adin, J. Katzhendler, D. Alkaslassy, C. Rav-Acha, Trihalomethane formation in chlorinated drinking water: A kinetic model, Water Res. 25 (1991) 797–805.

[42] Z. Li, S.G. Buchberger, V. Tzatchkov, Importance of Dispersion in Network Water Quality Modeling, in: Proc. World Water Environ. Resour. Congr. 2005, 2005: pp. 1–12.

[43] L. Cong, Y.J. Yang, Y. Jieze, Z. Tu-qiao, M. Xinwei, S. Weiyun, Second-Order Chlorine Decay and Trihalomethanes Formation in a Pilot-Scale Water Distribution Systems, Water Environ. Res. 84 (2012) 656–661.

[44] D. Zhong, Y. Yuan, W. Ma, C. Cui, Y. Wu, Influences of pipe materials and hydraulic conditions on the process of trihalomethanes formation in water distribution network, Desalin. Water Treat. 49 (2012) 165–171.

[45] H. Baribeau, M. Prévost, R. Dessardins, P. Lafrance, Changes in Chlorine and DOX Concentrations in Distribution Systems, J. Am. Water Works Assoc. 93 (2001) 102–114.

[46] F.A. DiGiano, W. Zhang, D.E. Francisco, M. Wood, Data Collection to Support a Simplified Bacterial Regrowth Model for Distribution Systems, Water Resour. Res. Inst. Univ. North Carolina. (2001).

[47] W. Robertson, T. Brooks, The role of HPC in managing the treatment and distribution of drinking-water, Heterotrophic Plate Counts Drink. Safety. WHO IWA Publ. (2003) 233–244.

3.9 Supplementary Material

3.9.1 Mathematical expressions for mass balance

1- Bulk Chlorine: Cl_b

$$\frac{\partial Cl_b}{\partial t} + \bar{u}\frac{\partial Cl_b}{\partial x} - D_{cl}\frac{\partial^2 Cl_b}{\partial x^2} = -k_{Cl,N}N_b Cl_b - k_{Cl,X}Cl_b X_b - \frac{k_{f,cl}}{r_h}(Cl_b - Cl_w) \qquad \text{(S-3.1)}$$

2- Bulk NOM: N_b

$$\frac{\partial N_b}{\partial t} + \bar{u}\frac{\partial N_b}{\partial x} - D_N\frac{\partial^2 N_b}{\partial x^2} = -\frac{1}{Y}\mu_{max}\frac{S_b}{k_s + S_b}\left[\exp(-k_{inact}Cl_b)\exp\left(-\left(\frac{T_{opt}-T}{T_{opt}-T_i}\right)^2\right)\right]X_b + a\left[Y_X k_{Cl,X}Cl_b + k_{mort}\right]X_b - Y_N k_{Cl,N}N_b Cl_b - \frac{k_{f,N}}{r_h}(N_b - N_w) \qquad \text{(S-3.2)}$$

3- Bulk BDOC: S_b

$$\frac{\partial S_b}{\partial t} + \bar{u}\frac{\partial S_b}{\partial x} - D_s\frac{\partial^2 S_b}{\partial x^2} = -\frac{1}{Y}\mu_{max}\frac{S_b}{k_s + S_b}\left[\exp(-k_{inact}Cl_b)\exp\left(-\left(\frac{T_{opt}-T}{T_{opt}-T_i}\right)^2\right)\right]X_b + a\left[Y_X k_{Cl,X}Cl_b + k_{mort}\right]X_b - Y_S k_{Cl,N}S_b Cl_b - \frac{k_{f,s}}{r_h}(S_b - S_w) \qquad \text{(S-3.3)}$$

4- Suspended Biomass: X_b

$$\frac{\partial X_b}{\partial t} + \bar{u}\frac{\partial X_b}{\partial x} - D_X\frac{\partial^2 X_b}{\partial x^2} = \mu_{max}\frac{S_b}{k_s + S_b}\left[\exp(-k_{inact}Cl_b)\exp\left(-\left(\frac{T_{opt}-T}{T_{opt}-T_i}\right)^2\right)\right]X_b + k_{det}\tau_w\frac{X_w}{r_h} - \left[Y_X k_{Cl,X}Cl_b + k_{mort}\right]X_b - \frac{k_{f,X}}{r_h}\left(X_b - \frac{X_w}{r_h}\right) \qquad \text{(S-3.4)}$$

5- Bulk Trihalomethanes: H_b

$$\frac{\partial H_b}{\partial t} + \bar{u}\frac{\partial H_b}{\partial x} - D_H\frac{\partial^2 H_b}{\partial x^2} = Y_{H,1}k_{Cl,N}N_bCl_b + Y_{H,2}k_{Cl,X}Cl_bX_b - \frac{k_{f,H}}{r_h}(H_b - H_w) \quad \text{(S-3.5)}$$

6- Wall Chlorine: Cl_w

$$\frac{\partial Cl_w}{\partial t} = -k_{Cl,N}N_wCl_w - k_{Cl,X}Cl_w\frac{X_w}{r_h} - k_wCl_w + \frac{k_{f,cl}}{r_h}(Cl_b - Cl_w) \quad \text{(S-3.6)}$$

7- Wall NOM: N_w

$$\frac{\partial N_w}{\partial t} = -\frac{1}{Y}\mu_{max}\frac{S_w}{k_s + S_w}\left[\exp\left(-\frac{k_{inact}}{k_r}Cl_w\right)\exp\left(-\left(\frac{T_{opt}-T}{T_{opt}-T_i}\right)^2\right)\right]\frac{X_w}{r_h}$$
$$+ a\left[Y_X\frac{k_{Cl,X}}{k_r}Cl_w + k_{mort}\right]\frac{X_w}{r_h} - Y_Nk_{Cl,N}N_wCl_w + \frac{k_{f,N}}{r_h}(N_b - N_w) \quad \text{(S-3.7)}$$

8- Wall BDOC: S_w

$$\frac{\partial S_w}{\partial t} = -\frac{1}{Y}\mu_{max}\frac{S_w}{k_s + S_w}\left[\exp\left(-\frac{k_{inact}}{k_r}Cl_w\right)\exp\left(-\left(\frac{T_{opt}-T}{T_{opt}-T_i}\right)^2\right)\right]\frac{X_w}{r_h}$$
$$+ a\left[Y_X\frac{k_{Cl,X}}{k_r}Cl_w + k_{mort}\right]\frac{X_w}{r_h} - Y_Sk_{Cl,N}S_wCl_w + \frac{k_{f,s}}{r_h}(S_b - S_w) \quad \text{(S-3.8)}$$

9- Fixed Biomass (Biofilm): X_w

$$\frac{\partial X_w}{\partial t} = \mu_{max}\frac{S_w}{k_s + S_w}\left[\exp\left(-\frac{k_{inact}}{k_r}Cl_w\right)\exp\left(-\left(\frac{T_{opt}-T}{T_{opt}-T_i}\right)^2\right)\right]X_w - [Y_X\frac{k_{Cl,X}}{k_r}Cl_w$$
$$+ k_{mort}]X_w - k_{det}\tau_wX_w + k_{f,X}\left(X_b - \frac{X_w}{r_h}\right) \quad \text{(S-3.9)}$$

10- Wall Trihalomethane: H_w

$$\frac{\partial H_w}{\partial t} = Y_{H,1}k_{Cl,N}N_wCl_w + Y_{H,2}k_{Cl,X}Cl_b\frac{X_w}{r_h} - \frac{k_{f,H}}{r_h}(H_b - H_w) \quad \text{(S-3.10)}$$

3.9.2 Fundamental processes considered in the model

Bacterial regrowth and biofilm dynamics.

Monod kinetics expressions were adopted to simulate bacterial regrowth and substrate utilization in the bulk flow and within the biofilm (first term on the right in Equations S-3.2-4 & S-3.7-9). The effect of chlorine concentration on reducing biomass activity is accounted for using an empirical inactivation coefficient of exponential dependence. An empirical relationship is adopted to model the effect of temperature on the maximum rate of substrate utilization. [1],[2,3] A resistance factor is considered to account for the additional impedance supplied by the biofilm for the attached biomass against chlorine action and was integrated in the Monod kinetics expression as well as the adopted formulae for chlorine-induced mortality (first and second terms on the right in Eq. S-3.9).[4] Mass transfer of the biomass from the bulk phase to the biofilm is simulated using the thin film CBL model, followed by spontaneous attachment. The kinetic formula describing the detachment rate of bacteria from the wall zone is assumed to have a first order dependence on the concentration of the attached bacteria per unit surface area, and first order with the shear stress (third term on the right in Eq. S-3.4&9). [5,6] Shear stress is calculated by the Blasius equation. [7] Detached bacteria is added to the bulk phase bacteria and assumed to have similar reaction mechanisms as suspended planktonic cells. Release of biodegradable organic matter from bacterial cell lysis is considered as a fraction of chlorine-induced biomass mortality (second term on the right Eq. S-3.2-3 & S-3.7-8).

Chlorine consumption and THMs formation from NOM.

A simple two constituent reaction model was used to simulate the kinetics of chlorine-TOC reaction (first term on the right Eq. S-3.1&6). The reaction rates were assumed to be of second

order, first order with respect to both chlorine and TOC. Yield coefficients were used to represent the depletion of chlorine-reactive sites upon chlorination (third term on the right Eq. S-3.2-3 & S-3.7-8). [8,9] The adopted second order model has previously shown superior results compared to the first order models to describe bulk chlorine decay because of the variable reactant concentration instead of constant decay. The rate constant ($k_{Cl,N}$) was considered to have an Arrhenius dependence on water temperature (Table S 3-2). [10] THM formation from chlorination of TOC was assumed to take place in proportion to the loss of chlorine (i.e. the chlorine demand) (first term on the right in Eq S-3.5&10). [8] Chlorine demand by the wall material was assumed to have a first order dependence on the chlorine concentration in the biofilm phase (third term on the right in Eq. S-3.6).

3.9.3 Numerical solution of the governing equations

An efficient numerical method is essential to appropriately solve the described dynamic non-linear mathematical model represented by equations (S-3.1 to S-3.10). In this study, the split-operator method (SOM) was used to decouple the transport and reaction processes of the multi-component system. SOM has been commonly applied for the solution of multi-species reactive transport models in groundwater [11,12], as well as drinking water distribution systems [3,13]. Splitting the governing partial differential equations by the separation of the transport operators from the reaction operators significantly reduces the model complexity. The simple sequential SOM is implemented in this study where the solution advances by solving the transport component over the full water quality time step Δt, and then solving the reaction component over Δt. Applying the SOM, the previously described generalized governing equation (Eq. 3-3) for the mass balance of species *i* is split into two separate components. The first component comprises the transport

operators, which constitute advection and dispersion processes for bulk phase species, while for the wall species; no solution is required in this step:

$$\frac{\partial C_{i,b}^{*}}{\partial t} + \bar{u}\frac{\partial C_{i,b}^{*}}{\partial x} - D_i \frac{\partial^2 C_{i,b}^{*}}{\partial x^2} = 0 \qquad \text{(S-3.11)}$$

Where C_i* is the intermediate solution for the concentration of species *i* after applying the transport operators. No interaction takes place between the modeled species during the transport step and hence the solution of the advection-dispersion equation can proceed independently for each component. Although a wide range of numerical methods has been developed for solving the dynamic advection-dispersion equation, the mixed Eularian-Lagrangian numerical methods are particularly known to be efficient in solving both dispersion-dominated and advection-dominated transport problems [14]. They were successfully applied to simulate solute transport in drinking water distribution systems [15–17]. In the present model, a two stage Eularian-Lagrangian numerical scheme combined with the numerical Green's function technique is used [15]. First, the Lagrangian step is executed using the explicit method of characteristics (MOCs) to solve the advection term, then the Eularian step is executed to solve the dispersion term using an implicit finite difference scheme. Detailed numerical solution for the Eularian-Lagrangian technique is described elsewhere [18] . The second step comprises the solution of the reaction and mass transfer processes in the bulk phase and within the biofilm:

$$\frac{\partial C_{i,b}^{n+1}}{\partial t} = \sum_{j=1}^{N_{r,b}} r_{i,j}\left(C_{i=1\ldots N_s,b}^{*}\right) - \frac{k_{f,i}}{r_h}\left(C_{i,b} - C_{i,w}\right) \qquad \text{(S-3.12)}$$

$$\frac{\partial C_{i,w}^{n+1}}{\partial t} = \sum_{k=1}^{N_{r,w}} r_{i,k}\left(C_{i=1\ldots N_s,w}\right) + \frac{k_{f,i}}{r_h}\left(C_{i,b} - C_{i,w}\right) \qquad \text{(S-3.13)}$$

The above local reaction step is always in the form of a set of first order ordinary differential equations (ODEs) that are solved using an explicit Runge-Kutta (4,5) with a variable time step solver (ODE45 in MATLAB R2013a). The software environment used to perform all simulations in the study was MATLAB R2013a.

3.9.4 Second order kinetic model for THM formation from chlorination of bacterial cells.

The model was applied to the experimental data provided by Wang et al., 2012[19] for DBP formation at different contact times between a bacterial cell solution and free chlorine in a bench scale reactor. The initial concentrations for chlorine and biomass where 5 mg/L and 10^8 CFU/mL, respectively, at pH=7.5. In a different study by Wang et al., 2013[20], the total organic carbon content of the cell solution was measured to be 43.8 µgC/10^{10}Cells for the same bacterial culture strain (Pseudomonas aeruginosa – wild type PAO1). This was used to convert the initial cell density into biomass carbon concentration. The model gave good results against experimental measurements as shown in Fig. 3-3. The parameter values that gave the best fit are given in Table S 3-3, and were found to be consistent with the literature. In the same study by Wang et al., 2012[19], the formation of chloroform was found to linearly increase with increasing the chlorine dosage in the DBP formation experiments that were chlorine limited as shown in Fig. S 3-1, with an average slope of 4.89 ugTHM/mgCl, which is consistent with the fitted value of $Y_{H,2}$. This implies that the developed second order model can be extended to describe any chlorine dosage in a real distribution system.

Several previous studies investigated the kinetics of chlorine reaction with biomass [21–24]. The fitted second order reaction rate constant $k_{Cl,X}$ was consistent with the value reported by Chen and

Stewart, 1996 [24] for chlorine-cell reaction of pseudomonas aeruginosa in the long-duration batch experiment which was 4.7E-4±1E-4 (L/mg.sec). J. J. Wang et al., 2013 [25] reported a trihalomethane formation potential of 57.3±3 ugTHM/mgC, which is comparable to the value of $\frac{Y_{H,2}}{Y_X} = 49.86$ in our study, or the 46.9 ugTHM/mgC reported by Wang et al., 2012[19] for P. aeruginosa.

3.9.5 Supplementary Tables

Table S 3-1. Parameters used in the bacterial growth simulation

Parameter	Unit	Value or Formula	Source	Remarks/ Value used if different
D_i	m^2/sec	$D_i = \frac{a^2u^2}{48D_{diff}}$	[26]	Re < 2,300
		$D_x{*} = c_1 f^{*c_2} d^{c_3} / u$	[27]	Re > 2,300
$k_{f,i}$	m/sec	$k_{f,i} = Sh_i(Re, Sc)*(\frac{D_i}{d})$	[28]	
β	CFU/mgC	10^8 For P. aeruginosa	[29]	10^9
		10^9	[3]	
Y	mgC/mgC	0.15	[3,4]	
μ_{max}	sec^{-1}	4.2×10^{-4}	[4]	7.0×10^{-4}
		1.7×10^{-4}	[30]	
k_s	mgC/L	0.4	[3]	0.195
k_{mort}	sec^{-1}	8.3×10^{-6}	[30]	
		9×10^{-7}	[4]	
k_{inact}	L/mgCl_2	0.35	[4]	0.25
a	[-]	0.3	[4]	
Y_S	mgC/mgCl_2	1.4985*($BDOC_0/Cl_0$)-0.4		(best fit)
k_{det}	m.sec/g	6.618×10^{-7}	[6]	13.8×10^{-6} for 23.1°C 10.5×10^{-6} for 13.5°C
	sec^{-1}	4×10^{-4}	[4]	3.2×10^{-6} for 1.8°C 3.1×10^{-6} for 1°C
τ_w	g/m.sec^2	$\tau_w = 0.0395 Re^{-0.25} \rho_{water} u^2$	[7]	Variation of water dynamic viscosity with Temp. was considered
T_i	°C	7	-	(best fit)

T_{opt}	°C	37	-	(best fit)
k_r	[-]	3-3000	[4]	100
$BDOC_0$/ TOC_0	[-]	0.1-0.3	[31]	(best fit)‡
k_w	m/sec	0.2	-	(best fit)

‡ Since the exact initial TOC concentrations were not provided in the study by Prevost et al. [32], a value within this range was separately chosen for each simulation to yield the best fit for chlorine decay. The used concentrations were close to the published range (2.8-3.3 mg/L) for the same field campaign in a different publication.[33] The evaluated second order rate constant for chlorine-TOC decay ($k_{Cl,N}$) in the distribution system was slower than the value in table S 3-2 by a factor of 40%.

Table S 3-2. Parameters used for the THM formation and NOM decay

Parameter	Unit	Value or Formula	Source	Calibrated range
$k_{Cl,N}$	L/mgC.sec	$\frac{1.8*10^6}{60}\exp(-\frac{6050}{T+273})$	[10]	A smaller value by 27% was used for the PVC pipe loop
$Y_{H,1}$	µgTHM/mg Cl	31.6-58.1	[9]	DI pipe loop: 9.5-82 (see Fig S 3-2a)
		36.27-188.60	[8]	
		5.68-39.73	[34]	PVC pipe loop: 15.8-139.1 (see Fig S 3-2b)
Y_N	mgC/mgCl	0.4-4.88	[8]	DI pipe loop: 0.365-2.50 (see Fig S 3-2d)
		0.46-1.76	[9]	PVC pipe loop: 0.154-1.8 (see Fig S 3-2e)

Notes: The yield coefficients for TOC decay and THM formation were assumed to be relative to the overall chlorine consumption based on the initial and final measured concentrations in the pipe loop experiments: $Y_N = (TOC_0\text{-}TOC_f)/(Cl_0\text{-}Cl_f)$; and $Y_H = (THM_f\text{-}THM_0)/(Cl_0\text{-}Cl_f)$.

Table S 3-3. Parameters used to fit the second order model of chlorine-biomass reaction

Parameter	Best fit Value
$k_{Cl,X}$ (L/mgC.sec)*	3.19E-4
Y_X (mgC/mgCl)**	0.09
$Y_{H,2}$ (ugTHM/mgCl)	4.487

*A temperature dependence was added to the second order rate constant for the bacterial regrowth simulation to have the same exponential dependence as chlorine-TOC reaction as reported by Kiéné et al., 1998[10]:

$$k_{Cl,X} = 2.959*10^5 \exp(-\frac{6050}{T + 273})$$

$$= 3.19 \times 10^{-4} @T = 20°C$$

** The value of Y_X was shown in a previous study [24] to vary with the initial chlorine to biomass concentration. Hence, a different value was used for the model verification simulations of bacterial regrowth. A value of 0.8 gave the best fit, which is consistent with an assumption of a linear relationship with the initial chlorine concentration as well as the value given by Chen and Stewart [24] of 0.59±0.15 for the long duration experiments.

Table S 3-4. Parameters used in the hypothetical pipe system for model application

Parameter	Base Value	Variation
Influent Chlorine concentration (Cl_0)	1 mg/L	
Influent HPC (X_0)	10 CFU/mL	
Pipe diameter	0.254m [10”]	
Reynolds number (Re)	20,000	30,000 – 25,000 – 20,000– 15,000 – 10,000 – 5,000
Temperature (T)	20ºC	30ºC – 25ºC – 20ºC – 10ºC – 0ºC
Influent TOC concentration (TOC_0)	2 mg/L	3 - 2.5 – 2 - 1.5 – 1 mg/L
Influent BDOC concentration ($BDOC_0$)	0.6 mg/L	30% of TOC_0

Table S 3-5. Water quality parameters for the Pont Viau treatment plant effluent (adopted from Prevost et al.[32])

Sample	Sampling date	$BDOC_0$ (mg/L)	Cl_0 (mg/L)	Temperature (ºC)
(a)	7/6/1993	0.83	0.83	23.1
(b)	5/18/1993	0.82	0.38	13.5
(c)	1/12/1993	0.47	0.27	1
(d)	12/15/1992	0.35	0.54	1.8

3.9.6 Supplementary Figures

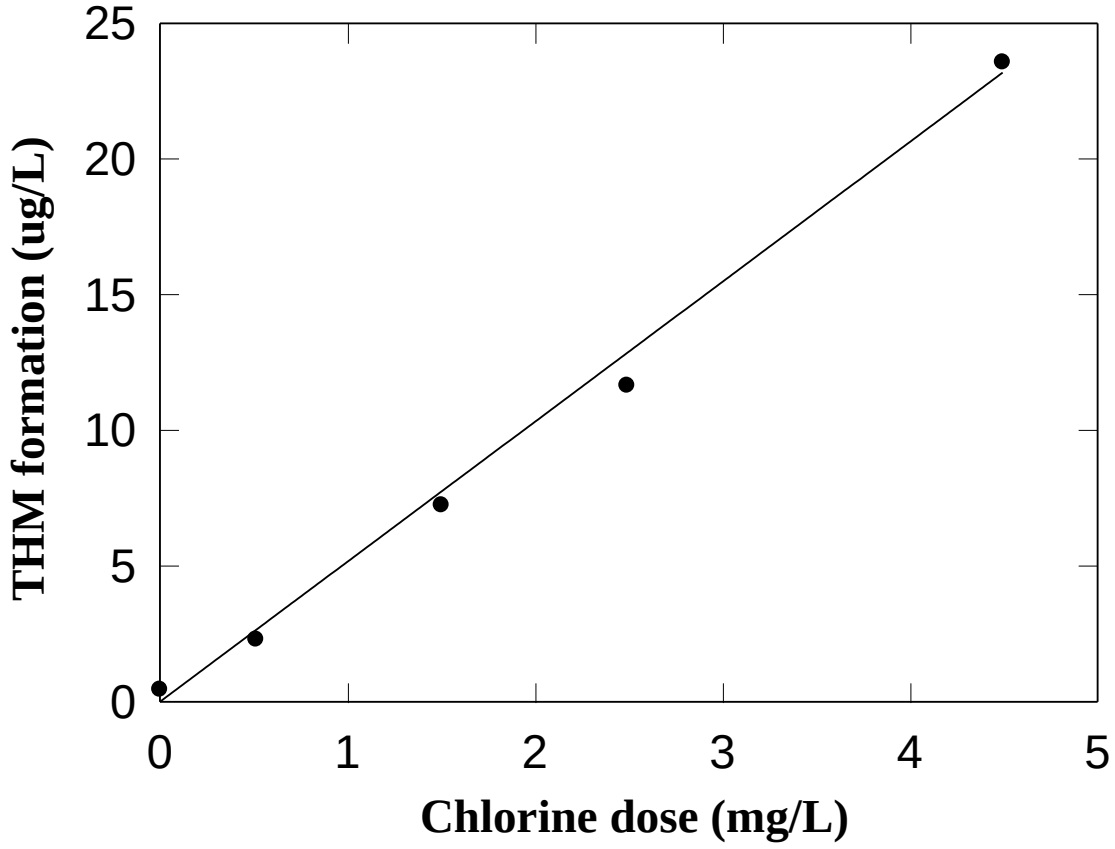

Figure S 3-1. THM formation from bacterial precursors at different chlorine doses.

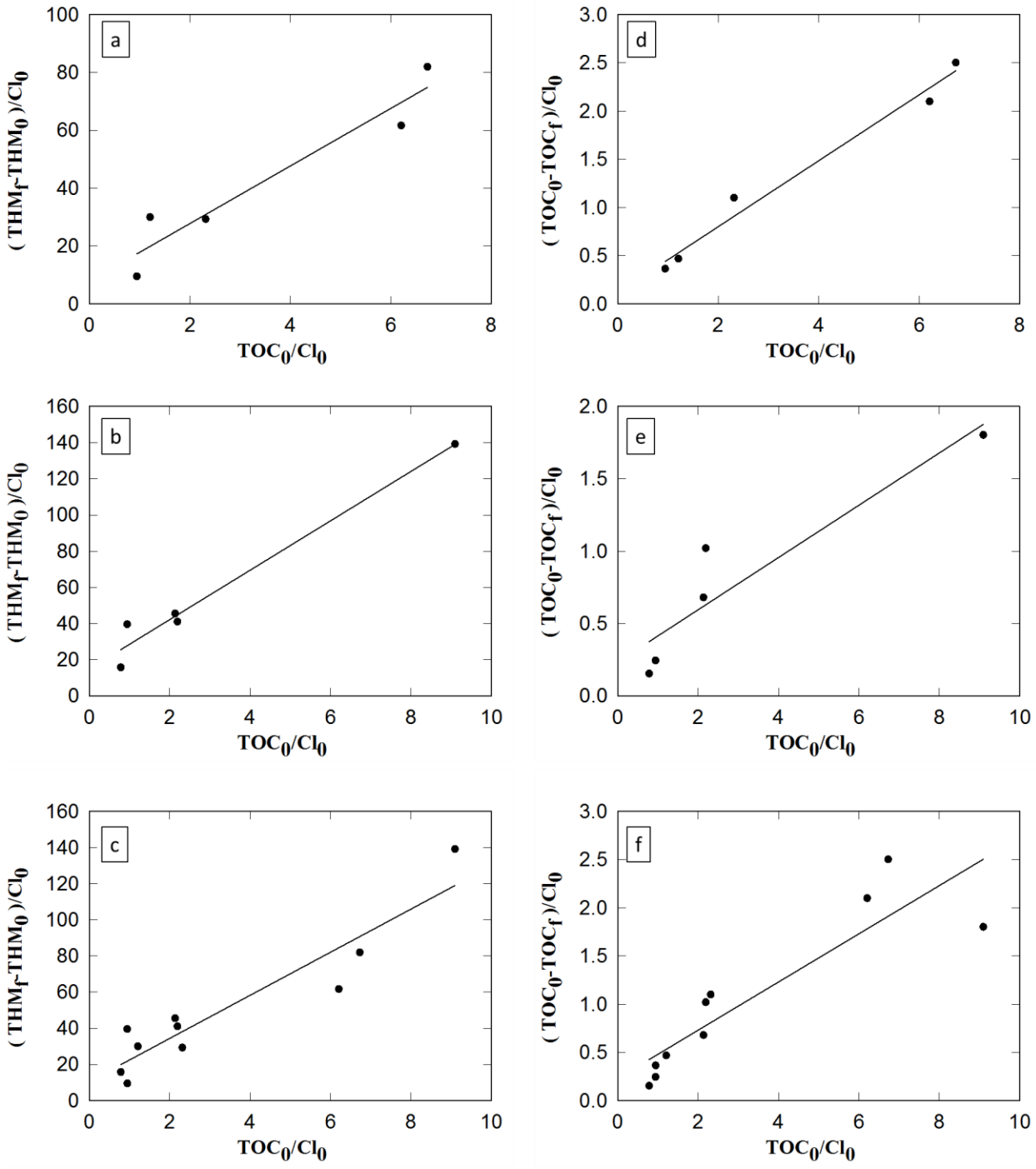

Figure S 3-2. Yield coefficients for TOC decay and THM formation used to simulate the pilot-scale study by Yang et al.[35] : $Y_{H,1}$ (µgTHM/mgCl) values for: (a) DI pipe; (b) PVC pipe; and (c) Combined, Y_N (mgC/mgCl) values for: (d) DI pipe; (e) PVC pipe; and (f) Combined.

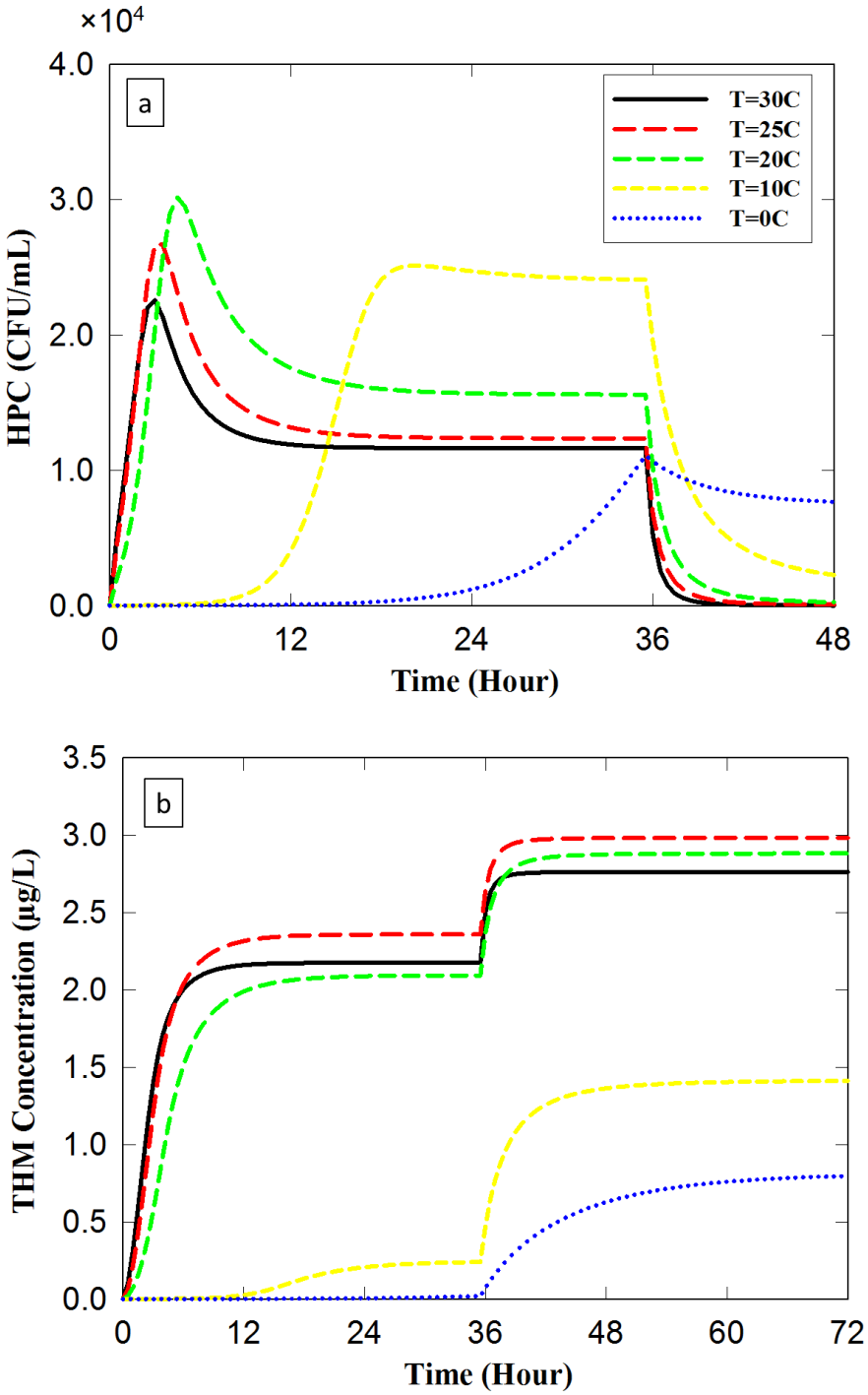

Figure S 3-3. Model application results for the concentrations of (a) HPC (log CFU/ml); and (b) THM (µg/l), produced from bacterial biomass precursors, under different temperature conditions.

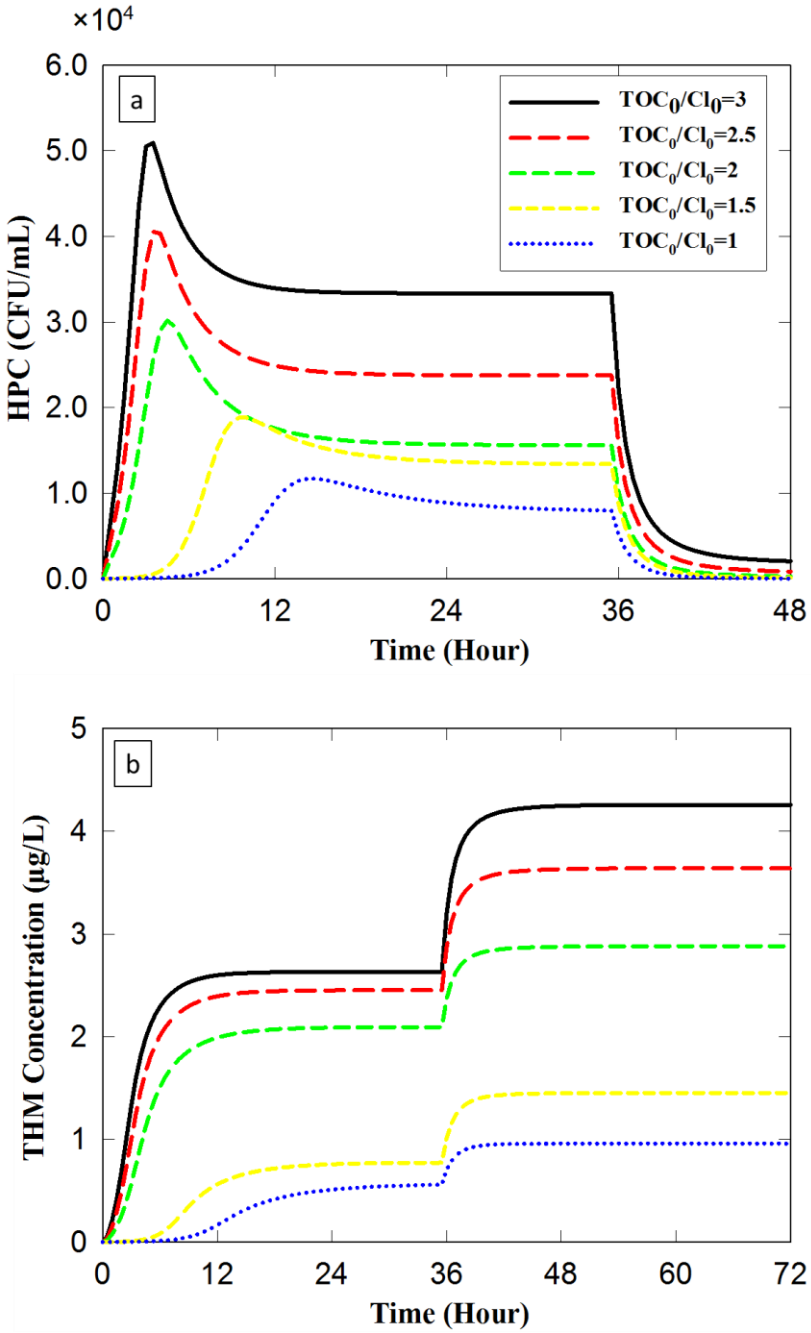

Figure S 3-4. Model application results for the concentrations of (a) HPC (log CFU/ml); and (b) THM (µg/l), produced from bacterial biomass precursors, under different initial TOC/Cl ratios.

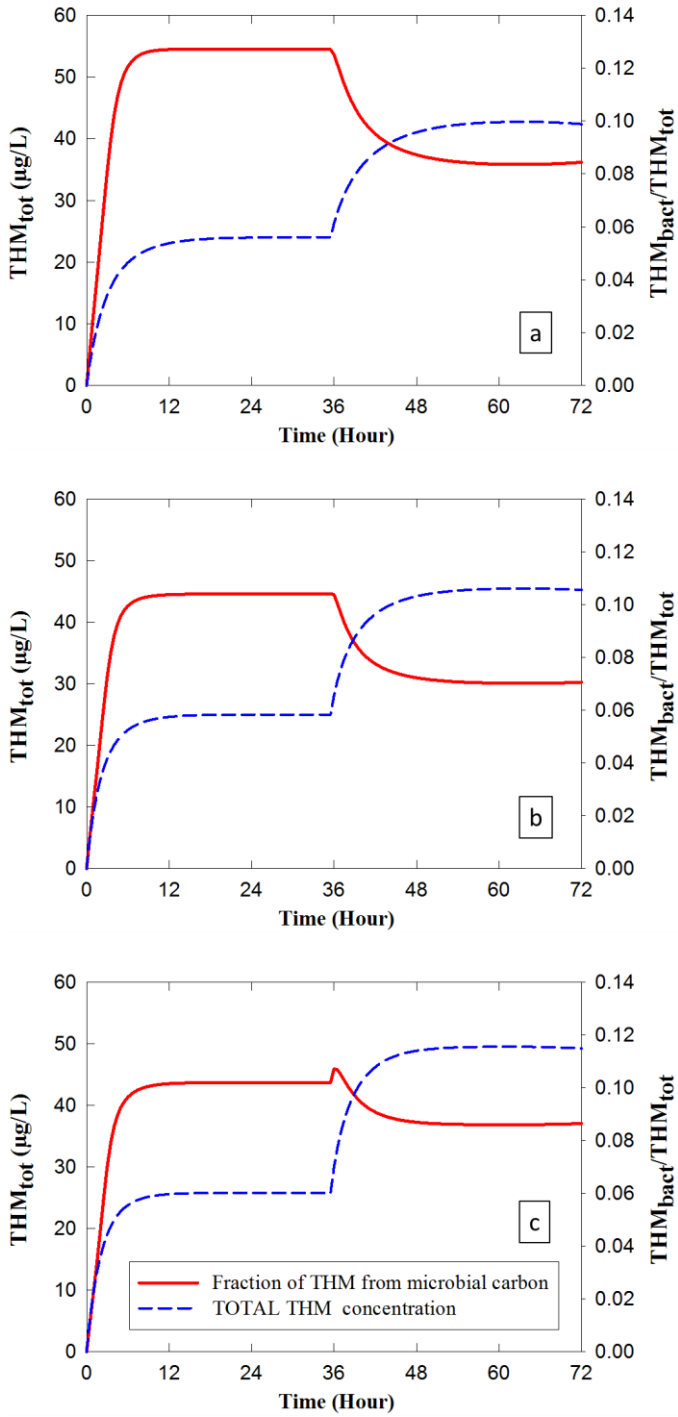

Figure S 3-5. Total THMs concentration and the fraction of THMs formed from bacterial precursor for the peak scenarios of: (a) Re=15,000; (b) T=25ºC; and (c) TOC_0/Cl_0=3. THM formation from NOM was simulated using: $Y_{H,1}$ =27 µgTHM/mgCl, a value that approximately corresponds to TOC_0/Cl_0=2 in Figure S 3-2c.

3.9.7 Supplementary Nomenclature

a	fraction of dead bacteria converted into substrate after lysis (-)
β	equivalent number of bacteria per mg organic carbon in cell biomass (CFU/mgC)
Cl	concentration of free chlorine as a function of time and axial dimension (mg/L)
N	concentration of NOM in the pipe (mg/L)
D_i	longitudinal dispersion coefficient for species i (m^2/sec)
H	concentration of TTHM in the pipe (ug/L)
i	identifier for one of the model species
k_{det}	coefficient of bacterial detachment from biofilm by shear stress (m.sec/g)
$k_{f,i}$	mass transfer coefficient for species i (cm/sec)
$k_{i1,i2}$	second order reaction rate between any two constituents i1 and i2 (L/mg.sec)
k_{inact}	coefficient of chlorine inactivation to bacterial growth (L/mg.sec)
k_s	half saturation constant of bacterial growth (mgC/L)
k_w	first order chlorine consumption rate by pipe material (sec^{-1})
r_h	hydraulic mean radius of the pipe (cm)
Re	Reynolds number (-)
S	concentration of BDOC in the pipe (mg/L)
T	temperature (^oC)
t	time (sec)
τ_w	shear stress at the pipe wall (g/m.sec^2)
u	flow velocity (m/sec)
μ_{max}	maximum substrate utilization by bacterial species (sec^{-1})
X_b	bulk concentration of bacteria HPC (mgC/L)
X_w	surface concentration of bacteria HPC (mgC/cm^2)
x	axial dimension (m)
Y_i	reaction yield coefficient of constituent i (mass/mass)

Subscripts

b	bulk phase
w	wall zone

3.9.8 Supplementary References

[1] M. Bianchi, D. Marty, J.-C. Bertrand, P. Caumette, M. Gauthier, Micro-organismes dans les écosystèmes océaniques, (1989).

[2] S. Dukan, L. Yves, P. Piriou, F. Guyon, P. Villon, Dynamic modelling of bacterial growth in drinking water networks, Water Res. 30 (1996) 1991–2002.

[3] W. Zhang, C.T. Miller, F. a. DiGiano, Bacterial Regrowth Model for Water Distribution Systems Incorporating Alternating Split-Operator Solution Technique, J. Environ. Eng. 130 (2004) 932–941.

[4] G.R. Munavalli, M.S.M. Kumar, Dynamic simulation of multicomponent reaction transport in water distribution systems, Water Res. 38 (2004) 1971–1988.

[5] R. Bakke, M.G. Trulear, J.A. Robinson, W.G. Characklis, Activity of Pseudomonas aeruginosa in Biofilms: Steady State, Biotechnol. Bioeng. XXVI (1984) 1418–1424.

[6] I. Schrottenbaum, J. Uber, N. Ashbolt, R. Murray, R. Janke, J. Szabo, D. Boccelli, Simple Model of Attachment and Detachment of Pathogens in Water Distribution System Biofilms, in: World Environ. Water Resour. Congr. 2009, 2009: pp. 1–13.

[7] H. Horn, H. Reiff, E. Morgenroth, Simulation of growth and detachment in biofilm systems under defined hydrodynamic conditions, Biotechnol. Bioeng. 81 (2003) 607–617.

[8] R.M. Clark, Chlorine Demand and TTHM Formation Kinetics: A Second-Order Model, J. Environ. Eng. 124 (1998) 16–24.

[9] D.L. Boccelli, M.E. Tryby, J.G. Uber, R.S. Summers, A reactive species model for chlorine decay and THM formation under rechlorination conditions, Water Res. 37 (2003) 2654–2666.

[10] L. Kiéné, W. Lu, Y. Lévi, Relative importance of the phenomena responsible for chlorine decay in drinking water distribution systems, Water Sci. Technol. 38 (1998) 219–227.

[11] D. a. Barry, K. Bajracharya, M. Crapper, H. Prommer, C.J. Cunningham, Comparison of split-operator methods for solving coupled chemical non-equilibrium reaction/groundwater transport models, Math. Comput. Simul. 53 (2000) 113–127.

[12] D. A. Barry, C.T. Miller, P.J. Culligan, K. Bajracharya, Analysis of split operator methods for nonlinear and multispecies groundwater chemical transport models, Math. Comput. Simul. 43 (1997) 331–341.

[13] F.A. Digiano, W. Zhang, Uncertainty analysis in a mechanistic model of bacterial regrowth in distribution systems, Environ. Sci. Technol. 38 (2004) 5925–5931.

[14] A.E. de M. Baptista, E.E. Adams, K.D. Stolzenbach, Eulerian-Lagrangian analysis of pollutant transport in shallow water, Energy Lab. Rep. No. MIT-EL 84-008, Massachusetts Inst. Technol. Cambridge, Mass. (1984) 141.

[15] V.G. Tzatchkov, A.A. Aldama, F.I. Arreguin, Advection-Dispersion-Reaction Modeling in Water Distribution Networks, J. Water Resour. Plan. Manag. 128 (2002) 334–342.

[16] H.A. Basha, L.N. Malaeb, Eulerian-Lagrangian Method for Constituent Transport in Water Distribution Networks, J. Hydraul. Eng. 133 (2007) 1155–1166.

[17] Z. Li, Network Quality Modeling with Stochastic Water Demands and Mass Dispersion, PhD Dissertation, University of Cincinnati, Cincinnati, Ohio, USA, 2006.

[18] A.A. Abokifa, Y.J. Yang, C.S. Lo, P. Biswas, Water quality modeling in the dead end sections of drinking water distribution networks, Water Res. 89 (2016) 107–117.

[19] Z. Wang, J. Kim, Y. Seo, Influence of bacterial extracellular polymeric substances on the formation of carbonaceous and nitrogenous disinfection byproducts, Environ. Sci. Technol. 46 (2012) 11361–11369.

[20] Z. Wang, O. Choi, Y. Seo, Relative contribution of biomolecules in bacterial extracellular polymeric substances to disinfection byproduct formation, Environ. Sci. Technol. 47 (2013) 9764–9773.

[21] D.E. Helbling, J.M. VanBriesen, Free chlorine demand and cell survival of microbial suspensions, Water Res. 41 (2007) 4424–4434.

[22] C. Shang, E.R. Blatchle, Chlorination of pure bacterial cultures in aqueous solution, Water Res. 35 (2001) 244–254.

[23] W. Lu, L. Ki??n??, Y. L??vi, Chlorine demand of biofilms in water distribution systems,

Water Res. 33 (1999) 827–835.

[24] X. Chen, P.S. Stewart, Chlorine penetration into artificial biofilm is limited by a reaction-diffusion interaction, Environ. Sci. Technol. 30 (1996) 2078–2083.

[25] J.J. Wang, X. Liu, T.W. Ng, J.W. Xiao, A.T. Chow, P.K. Wong, Disinfection byproduct formation from chlorination of pure bacterial cells and pipeline biofilms, Water Res. 47 (2013) 2701–2709.

[26] G. Taylor, Dispersion of Soluble Matter in Solvent Flowing Slowly through a Tube, Proc. R. Soc. A Math. Phys. Eng. Sci. 219 (1953) 186–203.

[27] A. Sattar, Gene Expression Models for the Prediction of Longitudinal Dispersion Coefficients in Transitional and Turbulent Pipe Flow, J. Pipeline Syst. Eng. Pract. 5 (2013) 4013011.

[28] L.A. Rossman, R.M. Clark, W.M. Grayman, Modeling Chlorine Residuals In Drinking Water Distribution Systems, J. Environ. Eng. 120 (1994) 803–820.

[29] Dong-ju Kim, Relation of microbial biomass to counting units for Pseudomonas aeruginosa, African J. Microbiol. Res. 6 (2012) 4620–4622.

[30] P. Laurent, P. Servais, M. Prévost, D. Gatel, B. Clément, Testing the SANCHO model on distribution systems, J. / Am. Water Work. Assoc. 89 (1997) 92–103.

[31] I.C. Escobar, A.A. Randall, Assimilable organic carbon (AOC) and biodegradable dissolved organic carbon (BDOC): Complementary measurements, Water Res. 35 (2001) 4444–4454.

[32] M. Prevost, A. Rompre, J. Coallier, P. Servais, P. Laurent, B. Clement, P. LaFrance, M. Prévost, A. Rompré, J. Coallier, P. Servais, Suspended bacterial biomass and activity in full-scale drinking water distribution systems: impact of water treatment, Water Res. 32 (1998) 1393–1406.

[33] H. Baribeau, M. Prévost, R. Dessardins, P. Lafrance, Changes in Chlorine and DOX Concentrations in Distribution Systems, J. Am. Water Works Assoc. 93 (2001) 102–114.

[34] R.M. Clark, M. Sivaganesan, Predicting Chlorine Residuals in Drinking Water: Second Order Model, J. Water Resour. Plan. Manag. 128 (2002) 152–161.

[35] Y.J. Yang, D. Wre, C.A. Impellitteri, R.M. Clark, R.C. Haught, D.A. Schupp, S. Panguluri, E.R. Krishnan, Chlorine decay and DBP formation under different flow regions in PVC and ductile iron pipes: Preliminary results on the role of flow velocity and radial mass transfer, in: World Environ. Water Resour. Congr., 2008: pp. 1–10.

Chapter 4

Modeling the Release and Transport of Dissolved and Particulate Lead from Lead Service Lines

Results presented in this chapter were published in:

A. A. Abokifa and P. Biswas. Modeling Soluble and Particulate Lead Release into Drinking Water from Full and Partially Replaced Lead Service Lines. Environmental Science & Technology 2017, 51 (6), 3318-3326.

4.1 Abstract

Partial replacement of lead service lines (LSLs) often results in the excessive long-term release of lead particulates due to the disturbance of pipe scale and galvanic corrosion. In this study, a modeling approach to simulate the release and transport of particulate and dissolved lead from full and partially replaced LSLs is developed. A mass transfer model is coupled with a stochastic residential water demand generator to investigate the effect of normal household usage (NHU) flow patterns on lead exposure. The model is calibrated by comparing simulation results against experimental measurements from pilot-scale setups where lead release under different flow rates and water chemistry scenarios was reported. Applying the model within a Monte-Carlo simulation framework, the partial replacement of the LSL was predicted to result in releasing spikes with significantly high concentrations of particulate lead (1011.9±290.3 μg/L) that were five times higher than those released from the full LSL. Sensitivity analysis revealed that the intensity of flow demands significantly affects particulate lead release, while dissolved lead levels were more dependent on the lengths of stagnation periods. Pre-flushing of the LSL prior to regulatory sampling was found to under-estimate the maximum monthly exposure of dissolved lead by 19%, while sampling at low flow rates (<5.2 LPM) was found to consistently suppress the high spikes induced by particulate lead mobilization.

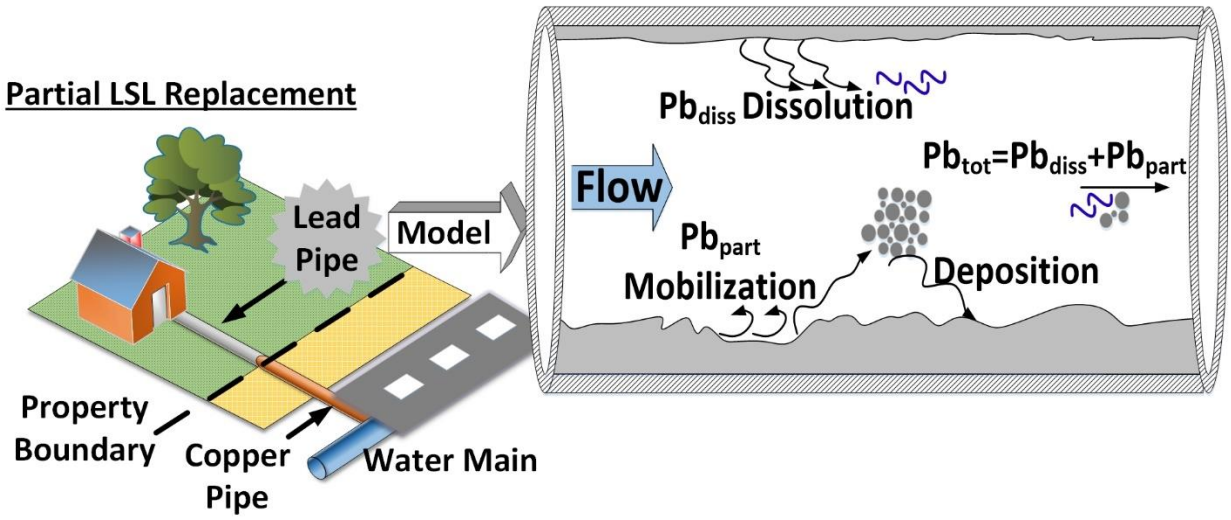

Figure 4-1. Graphical Abstract of the work presented in Chapter 4

4.2 Introduction

Lead is a hazardous neurotoxin that can irreversibly affect the intellectual development in children, even at blood lead levels (BLLs) as low as 5 µg/dL [1–4]. The recent events in Flint, Michigan, have drawn attention to drinking water contamination by lead and its associated public health concerns [5–8]. Lead contamination takes place as a result of the internal corrosion of Pb-containing materials in contact with drinking water, including lead pipes, solder, and premise plumbing components, with the major source being the lead service lines (LSLs) that connect the water main to the building inlet [9,10]. Although the use of lead pipes in drinking water systems was banned in 1986, partial or full LSLs still supply millions of households in the United States with drinking water [11,12]. This legacy infrastructure of aging pipes may pose a future hazard to the quality of drinking water, especially if changes to the water chemistry are introduced without sufficient planning. For example, changing the secondary disinfectant from chlorine to chloramine triggered the lead poisoning crisis in Washington, DC [13,14], while in Flint, MI, the trigger was shifting to a more corrosive water source and the discontinuation of corrosion control treatment [6].

LSL replacement remains the most effective long-term solution to eliminate this potential threat; however, replacing the existing legacy of ~6.1 million lines is expected to come with significant expense [15]. Since the ownership of the LSL is typically shared between the consumer and the utility, both parties are responsible for the replacement costs. A partial replacement situation, in which the water utility replaces the part of the line from the water main to the property boundary – typically with a copper pipe –, arises if the consumer chooses not to replace their part or if the water utility does not inform the consumer about the replacement plans. Partial replacement of the LSL can result in the acceleration of lead release due to galvanic corrosion [16–

18], whose effects were found to persist, and even magnify, for months after the replacement [19]. Furthermore, the replacement of LSLs disturbs the stable thin layer of lead oxide scale that has formed over decades [16], which ultimately leads to the release of lead particulates and lead-containing iron-rusts [20,21] that can either directly flush out of the tap or accumulate in the household premise plumbing components and gradually release soluble lead [22]. The release of particulate lead introduces sporadic spikes of very high lead concentrations that can become bioavailable after ingestion and result in hazardous BLLs [2,13,23,24].

Since lead release from LSLs is dictated by multiple parameters, such as pipe age and dimensions, water-use patterns, water chemistry, and previous disturbances to the LSL, computational modeling can offer helpful tools to predict and control lead release under a diverse range of scenarios. Several studies have pursued modeling the leaching of dissolved lead from LSLs. Kuch and Wagner [25] proposed two mass transfer models to describe lead release into drinking water under both steady state turbulent flow and stagnant conditions. Van Der Leer et al. [26] developed an exponential model to describe the mass transfer of lead under stagnant conditions, and combined it with an advection-based model to describe lead transport under different flow regimes. Their model was later implemented by Hayes [27] in a Monte-Carlo probabilistic framework to assess lead release within a water supply zone. Cardew [28] developed a convective-diffusion model to simulate lead transport under laminar flow conditions. Nevertheless, no previous work has so far addressed the issue of particulate lead release into drinking water from a modeling perspective, especially from disturbed or partially replaced LSLs. Moreover, the realistic variation in flow demands under different household consumption patterns was generally overlooked in previous models, but it is crucial in accurately simulating both the leaching of soluble lead and the mobilization of lead particulates from LSLs [29].

This study presents an approach for modelling particulate lead release from LSLs through coupling the concept of stacked cohesive scale layers with a convective-diffusion mass transfer equation. To generate realistic flow patterns, a stochastic model is developed to represent the instantaneous residential demands based on non-homogenous Poisson pulses. The model is applied to investigate release schemes of particulate and dissolved lead from full and partial LSLs under normal household usage (NHU) conditions.

4.3 Methodology

The model comprises two independent modules for the simulation of the release of both particulate and dissolved lead in LSLs. In the dissolved lead module, lead release from the LSL is described by applying an equilibrium boundary condition at the pipe wall, while a cohesive transport model was developed to simulate the mobilization of particulate lead due to turbulent shear stresses at the pipe wall. Both modules were calibrated and verified through comparisons with experimental measurements from pilot-scale experiments in the literature.

4.3.1 Model development

Mathematical formulation

The mass balance on the concentration of the dissolved lead in the LSL is described by a dynamic 2-D convection-diffusion equation in the axial and radial directions:

$$\frac{\partial C_s}{\partial t} = -\frac{\partial}{\partial x}(\bar{u}\, f(r)\, C_s) + \frac{\partial}{\partial x}\left(D_{L,s}\frac{\partial C_s}{\partial x}\right) + \frac{1}{r}\frac{\partial}{\partial r}\left(r\, D_{r,s}\frac{\partial C_s}{\partial r}\right) \qquad (4\text{-}1)$$

where, C_s is the dissolved lead concentration (μg/L), $\bar{u}$ is the average flow velocity in the pipe (cm/sec), $f(r)$ is the radial flow velocity profile (-), $D_{L,s}$ and $D_{r,s}$ are respectively the apparent diffusivities of dissolved lead in the longitudinal and radial directions (cm^2/sec), t is the time (sec), and x and r are the axial and radial space co-ordinates, respectively (cm). The term on the left

accounts for the dynamic change in solute concentration with time, while the terms on the right account for, from left to right, the convective flux in the axial direction, the diffusive flux in the axial direction, and the diffusive flux in the radial direction. The mass balance equation is solved under the following boundary conditions: $C_s = C_0,\ x = 0$; $\frac{\partial C_s}{\partial x} = 0,\ x = L$; $\frac{\partial C_s}{\partial r} = 0,\ r = 0$; and $C_s = C_{eq},\ r = r_0$. Here C_0 is the influent concentration at the pipe inlet (μg/L), L is the pipe length (cm), and r_0 is the pipe radius (cm).

The fourth boundary condition describes a situation where dissolved lead concentration at the pipe wall is at equilibrium with the lead corrosion products, i.e., lead release is rate limited by diffusion [28,30]. An alternative boundary condition can be applied if lead release from the lead scale is limited by the rate of the dissolution reaction, which can be written as $D_{r,s}\frac{\partial C_s}{\partial r} = R_{diss}$, $r = r_0$ [31,32]. In this case, lead concentrations at the pipe wall are not equivalent to the equilibrium solubility of the lead corrosion products, and therefore a precipitation reaction should be considered to simulate the concurrent removal of dissolved lead from the solution [33].

Particulate transport in a fluid flow is governed by multiple phenomena that include convection, diffusion, coagulation, and deposition. These phenomena are dependent on the particle size; hence, particulate transport is best described by the distribution of the particle sizes. The governing transport equation of particulate lead in a flow stream can be written as [34]:

$$\frac{\partial}{\partial t} n(v,\vec{x},t) = -\nabla \cdot \left(n(v)\vec{U}_p\right)$$

$$+\frac{1}{2}\int_0^v \beta\left(v',v-v'\right) n\left(v'\right) n\left(v-v'\right) dv' - n(v)\int_0^\infty \beta\left(v,v'\right) n\left(v'\right) dv' \qquad (4\text{-}2)$$

where n is the dimensionless particle size distribution function ($=n^*/n_0^*$), n^* is the dimensional size distribution function ($n^* = dN^*/dv$; N^* is the particle number concentration per unit volume

of the fluid (#/cm^3), and v is the particle size (μm^3)), n_0^* is the size distribution function at the pipe inlet, $\vec{U}_p$ is the dimensionless particle velocity vector =($\overrightarrow{U_p^*}/\bar{u}$), $\overrightarrow{U_p^*}$ is the dimensional particle velocity vector (cm/sec), and β is the collision frequency function. The particle velocity vector for subcritical Stokes numbers can be written as

$$\vec{U}_p = \vec{U} - \frac{2}{Pe}(\nabla \ln(n)) - Stk\left(\vec{U} \cdot \nabla\right)\vec{U} \qquad (4\text{-}3)$$

where, $\vec{U}$ is the dimensionless fluid velocity vector = ($\vec{U}^*/\bar{u}$), $\vec{U}^*$ is the dimensional fluid velocity vector (cm/sec), and Pe, and Stk are the Peclet and the Stokes numbers. The terms on the right-hand side of the equation account for transport by, from left to right, advection, diffusion, and inertia. The relative importance of the effect of inertia is described by the Stokes number ($Stk = \tau_p/\tau_f$), where τ_p is the particle relaxation time $\tau_p = (\rho_s - \rho_f)D_p^2/18\rho_f\nu$, and τ_f is the characteristic flow time, which can be described as the viscous (turbulence) time $\tau_f = \nu/u_*{}^2$ [35].

For a LSL with a typical diameter of 1.9 cm (3/4”), a turbulent flow regime can be established by a flow rate as low as 0.06 L/sec, which is less than the intensity of most of the typical flow demands at the household level [36]. Hence, the flow regime in the LSL is expected to be turbulent for most cases where a flow demand exists. It can be shown that under modest turbulent flow regimes, the behavior of a suspended particle as large as 44 μm (about 100 times the 0.45 μm threshold for particulate lead) will be dominated by turbulent diffusivity rather than inertia (Stk < 0.2). At such a low Stokes number, particles are expected to precisely follow the turbulent fluctuations of the flow stream [37], and hence their transport can be modeled as a solute tracer. Therefore, the transport of mobilized particulate lead with the bulk flow is described by a 2-D convective-diffusion equation:

$$\frac{\partial C_p}{\partial t} = -\frac{\partial}{\partial x}\left(\bar{u}\, f(r)\, C_p\right) + \frac{\partial}{\partial x}\left(D_{L,p}\frac{\partial C_p}{\partial x}\right) + \frac{1}{r}\frac{\partial}{\partial r}\left(r\, D_{r,p}\frac{\partial C_p}{\partial r}\right) - R_{set} \qquad (4\text{-}4)$$

where C_p is the particulate lead concentration in the bulk flow (μg/L), $D_{L,p}$ and $D_{r,p}$ are the apparent diffusivities of particulate lead in the longitudinal and radial directions, respectively (cm^2/sec), and R_{set} is the rate of particulate lead settling (μg/L/sec).

The critical particle size that can be suspended by the turbulent flow can be simply calculated by comparing the settling velocity $w_s = (\rho_s\text{-}\rho_f)gD_p^2/18\mu$, to the shear velocity at the pipe wall $u_* = (\tau_w/\rho_f)^{0.5}$. Using this analysis, particles with diameters as large as 57 μm will become fully suspended by the flow, even under the modest turbulent flow conditions. Therefore, particle settling is assumed to only take place under stagnant condition, and is described in this study by a first order reaction in the concentration of mobilized particulate lead: $R_{set} = k_{set}C_p\delta(\bar{u}\text{-}0)$. Here, k_{set} is the first order settling rate constant (sec^{-1}), and δ is a function that takes a value of one when $\bar{u} = 0$ (i.e., stagnation), and zero otherwise. The transport equation is solved under the following boundary conditions: $C_p = 0,\ x = 0$; $\frac{\partial C_p}{\partial x} = 0,\ x = L$; $\frac{\partial C_p}{\partial r} = 0,\ r = 0$; and $D_{r,p}\frac{\partial C_p}{\partial r} = R_{det},\ r = r_0$. The fourth boundary condition describes particulate lead detachment from the accumulated scale by a flux boundary condition at the pipe wall, where R_{det} is the rate of mass detachment of particulate lead per unit surface area of the pipe wall (μg/cm^2/sec). The potentially releasable mass of particulate lead stored in the cohesive scale layers at the pipe wall is described by

$$\frac{dP}{dt} = R_{gen}\text{-}R_{det} + R_{set}r_h \qquad (4\text{-}5)$$

where P is the mass of potentially releasable lead particles accumulated at the pipe surface (μg/cm^2), R_{gen} is the rate of generation of particulate lead due to galvanic corrosion and other

disturbances of the pipe scale (μg/cm^2/sec), and r_h is the hydraulic mean radius (cm). The accumulated particles are assumed to be held in successive cohesive layers of varying strengths. Each layer has a certain shear strength that is inversely proportional to the instantaneous releasable potential of the attached particles. A similar concept was previously applied by Boxall and Saul to simulate discoloration in drinking water distribution systems due to the mobilization of rust particles [38,39]. An empirical equation is formulated to describe the relationship between the shear strength of the current layer and the instantaneous releasable potential:

$$\tau_s = \frac{(P_{max}\text{-}P)^l}{m} \tag{4-6}$$

where τ_s is the shear strength of the current layer of accumulated particles (N/cm^2), P_{max} is the maximum potential for the attached particles (μg/cm^2), m and l are two empirical parameters controlling the slope and the non-linearity of the relationship, respectively.

The rate of particle detachment is a function of the shear stress residual, which is the difference between the applied shear stress under the given hydraulic conditions, and the shear strength of the current layer:

$$R_{det} = k_{det}(\tau_a\text{-}\tau_s)^n \tag{4-7}$$

where τ_a is the instantaneous shear stress at the pipe wall (N/cm^2), k_{det} and n are two empirical parameters controlling the magnitude and the non-linearity of the relationship, respectively. Regular flow events impose a turbulent shear stress that can be calculated by the Blasius equation $\tau_a = 0.0395Re^{-0.25}\rho_{water}\bar{u}^2$.

Particle generation is assumed to take place under stagnant conditions due to galvanic corrosion [17,18], at a rate that linearly diminishes as the releasable potential approaches the maximum threshold:

$$R_{gen} = k_{gen}(P_{max}\text{-}P)\delta(\bar{u}\text{-}0) \tag{4-8}$$

where k_{gen} is an empirical parameter controlling the magnitude of the rate of particle generation (sec^{-1}). The derived dimensionless forms of the governing transport equations, as well as the alternating direction implicit (ADI) numerical scheme used to solve the model, are given in the supporting information.

Stochastic water demands generation.

Synthetic water demand patterns at the scale of an individual household are modeled by a stochastic Poisson pulse process at a fine time resolution (1 sec) [40–43]. Demands are modeled as rectangular pulses with a non-homogenous (time dynamic) arrival rate λ (sec^{-1}), where each pulse is assigned a randomly selected intensity *I* (l/sec) and duration *T* (sec) based on lognormal probability distributions. The mutual dependence between pulse duration and intensity is considered by modeling the natural logarithms of the two characteristic variables (i.e., ln(*I*), and ln(*T*)) using a bivariate normal distribution[44] which is given by

$$f(y_1, y_2) = \frac{1}{\sqrt{(2\pi)^2|\Sigma|}} \exp\left\{\frac{-1}{2(1-\dot{\rho}^2)}\left[\left(\frac{y_1-\mu_1}{\sigma_1}\right)^2 + \left(\frac{y_2-\mu_2}{\sigma_2}\right)^2 - \frac{2\dot{\rho}(y_1-\mu_1)(y_2-\mu_2)}{\sigma_1\sigma_2}\right]\right\} \quad (4\text{-}9)$$

where $y_1 = \ln(T)$, $y_2 = \ln(I)$, μ_i, and σ_i are the mean and the standard deviation of variables y_i $(i = 1, 2)$, $\dot{\rho}$ is the Pearson correlation coefficient between y_1 and y_2, and Σ is the covariance matrix given by

$$\Sigma = \begin{pmatrix} \sigma_1^2 & \dot{\rho}\sigma_1\sigma_2 \\ \dot{\rho}\sigma_1\sigma_2 & \sigma_2^2 \end{pmatrix} \quad (4\text{-}10)$$

4.3.2 Model Calibration and Verification

Dissolved lead module

The model was used to simulate the release of dissolved lead in a pilot-scale pipe experiment under stagnation conditions. The simulation results were compared with the experimental measurements made by Xie et al. [45] for five different water chemistry compositions: high dissolved inorganic carbon (DIC = 50 mgC/L), high free chlorine (Cl_2 = 2 mg/L), high monochloramine (NH_2Cl = 2 mg/L as Cl_2), high pH (pH = 10), and high orthophosphate (PO_4^{3-} = 1 mg/L as P). The experiment setup consisted of a group of 24-inch long lead pipes with a 1.9 cm nominal diameter that were conditioned by being repeatedly emptied and filled with an aqueous solution made from Milli-Q water at pH = 10 with DIC = 10 mgC/L, and 3.5 mg/L free chlorine, for eight months. Lead scales on the conditioned sections included Pb(II) hydrocerussite ($Pb_3(OH)_2(CO_3)_2$), and lead(IV) oxides scrutinyite (α-PbO_2) and plattnerite (β-PbO_2). After conditioning, the effluent water was sampled at different stagnation stages: 0, 1, 2, 3, 8, and 24 hrs, for each of the five water chemistry compositions. The experimental study investigated the release of dissolved lead triggered by water chemistry changes from the conditions under which the scales have originally developed.

Under stagnation, the governing transport equation (Equation 4-1) reduces to a dynamic 1-D diffusion equation in the radial direction because the axial convective flux term vanishes ($\bar{u}$=0), while the axial diffusive flux can be dropped because of symmetry (C_0=0). In the simulations, the equilibrium concentration implemented in the boundary condition (C_{eq}) was always set equal to the experimentally measured concertation after 24 hours of stagnation [26,28]. Therefore, the sole parameter that required calibration in this case was the radial diffusion coefficient $D_{r,s}$, which was adjusted by a genetic algorithm (GA) to minimize the root mean square error (RMSE) between the measured and the simulated concentrations.

Particulate lead module

Model simulations were compared to the results of the long term (7 months) pilot scale study by Cartier et al. [46], which investigated lead leaching from different service line configurations under variable flow conditions. To understand the role of galvanic corrosion in releasing lead particulates, we simulated two of the experimental scenarios considered in their study: a full LSL (100%-Pb), and a partially replaced LSL (50% lead downstream Pb-D). The simulated pipe rigs had a 1.9 cm nominal diameter and a length of 3 m (1.5 m for the case of Pb-D). To study the role of hydraulic conditions in mobilizing lead particulates, three sampling flow rates were examined: low flow (1.3 LPM), normal (medium) flow (8 LPM), and high flow (32 LPM).

For each one of the simulated monitoring sampling scenarios, the simulation started with a three-day period of normal water use, in which a flow event lasting 100 minutes at a flow rate of 1.3 LPM was simulated to match the sampling procedure adopted in the experiments. This event was followed by a 16 hours stagnation period, after which the simulated concentrations were compared to the collected samples at each flow rate. Cartier et al. [46] also performed an intensive sequential sampling at high flow with a series of 11 sampling events after the initial monitoring sampling of the high flow case, which we also simulated in this study.

The five empirical parameters in the relationships describing the shear strength of the cohesive layers and the detachment process (Equations 4-6 and 4-7) (i.e., l, m, n, k_{det} and P_{max}) were calibrated by comparing the model simulations with the measured concentrations from the monitoring sampling events under different flow rates. Simulations of the intensive sampling events were used to calibrate the generation parameter k_{gen} by simulating particle regeneration during the stagnation periods between the successive intensive flow events.

4.3.3 Model Validation and Application

The calibrated model was applied to simulate two hypothetical LSLs: a full pipe (100% Pb, L=20 m), and a partially replaced pipe with 50% lead downstream (50% PbD, L=10 m) pipe. The chosen pipe length was based on literature ranges, where the national average LSL length in the US was found to be 55-68 ft (16.8-20.7 m), of which only 40-45% is under the utilities' jurisdiction [10]. The calibrated transport model for both particulate and dissolved lead was linked to the stochastic demand generator to represent realistic flow demands for daily normal household usage (NHU) scenarios. For both particulate and dissolved lead, the simulations were performed in a Monte-Carlo framework with 200 different NHU scenarios for each one of the two cases (100% Pb and 50% PbD), (i.e., total = 2*2*200 = 800 simulations). Each NHU scenario represented a 4-week period (1 month) of realistic flow simulations. Although the same stochastic demand generation parameters (λ , μ_i, and σ_i) were used to generate the residential demand pulses for all 200 scenarios, each scenario had a different demand pattern based on the pulse arrival rate, pulse intensity, and pulse duration, all randomly drawn from the probability distributions as previously described.

The model was validated by comparing the predicted lead levels from the Monte-Carlo simulation with field-measured concentrations from the sampling study by Clark et al. [29] that included 24 homes in the cities of Washington, D.C., and Providence, RI. The sampling sites consisted of nine partial LSLs, and eight full LSLs, while the seven remaining sites had unknown connections. Sampling was conducted at a range of flow rates between 0.8 to 14.2 LPM to represent the range of normal household water use. Following a stagnation period of minimum 6 hours, three sequential profiles (10 L each) were collected from each tap beginning with low flow (1 L/min), then medium flow with the kitchen tap fully opened but without removing the faucet aerator (3-10 L/min), and finally a high flow profile after removing the aerator (4-14 L/min). The

published study reported a data set of the collected samples that had visible particulates or Pb concentrations above 15 μg/L, mostly from sites with high particulate lead concentrations [29]. These samples were compared to our Monte-Carlo simulation results at the corresponding sampling flow rates to validate the simulated ranges of lead concentrations.

4.4 Results and Discussion

4.4.1 Model Calibration and Verification

Dissolved lead module

Simulations were conducted using the soluble lead module for the five different water chemistry compositions sampled in the experimental study of Xie et al. [45] The measured and simulated stagnation curves are shown in Figure 4-2a, where the diffusion model performed well in describing the buildup of dissolved lead in the pipe for different water chemistries. The error between the simulated and the measured concentrations was calculated as:

$$\mathrm{RMSE\%} = \left[\sqrt{\sum_{i=1}^{N_{meas}} \left(C_{meas,i}\text{-}C_{sim}\right)^2 \Big/ N_{meas}}\right] \Big/ \bar{C}_{meas} \qquad (4\text{-}11)$$

The RMSE% ranged from 11% for the high DIC case to 44% for the high orthophosphate case. The poorest fit was observed for the high pH and the high orthophosphate cases due to the drop in the concentrations measured at 8 hours compared to 4 hours, which is not consistent with the increasing trends typically observed in stagnation curves. The calibrated radial diffusion coefficients ($D_{r,s}$) and equilibrium concentrations after 24 hours (C_{eq}) are given in Table S 4-3. An interesting outcome was observed for the calibrated model, where a positive linear correlation between the two parameters was noticed ($r^2 = 0.965$) (see Figure S 4-1). This finding suggests that the need for explicitly calibrating the radial diffusion coefficient under different water chemistry

scenarios might be eliminated if the ultimate equilibrium solubility was known for the given scenario.

The alternative boundary condition representing the dissolution-limited release scenario was also applied, where precipitation was taken as a first order reaction in the concentration of dissolved lead as proposed by Xie [33]. Figure 4-2b compares the simulation results for both the diffusion-limited and the dissolution-limited formulations of the model against measured concentrations for the high DIC case. Both models reproduced the experimental results well, however, the diffusion-limited model gave a slightly better description of the initial stagnation stage (0-10 hrs), while the dissolution limited model better predicted the ultimate concentration after 24 hours. It should however be noted that, as suggested by Van Der Leer et al. [26], the radial diffusion coefficient requires calibration for the diffusion model to give accurate descriptions. Otherwise, using the molecular diffusivity of lead (1E-5 cm^2/sec) will lead to excessively fast release rates in the initial stagnation stage compared to the measured stagnation curves [33]. During normal water use, stagnation periods rarely exceed 10 hours, hence the diffusion model was found to be more suitable for simulating dissolved lead release under NHU conditions in this study. Moreover, since the stagnation periods required before sample collection are typically either 30 minutes (30MS) or 6 hours (6HS), implementing the diffusion model for designing or assessing zonal sampling surveys [27] might be more suitable.

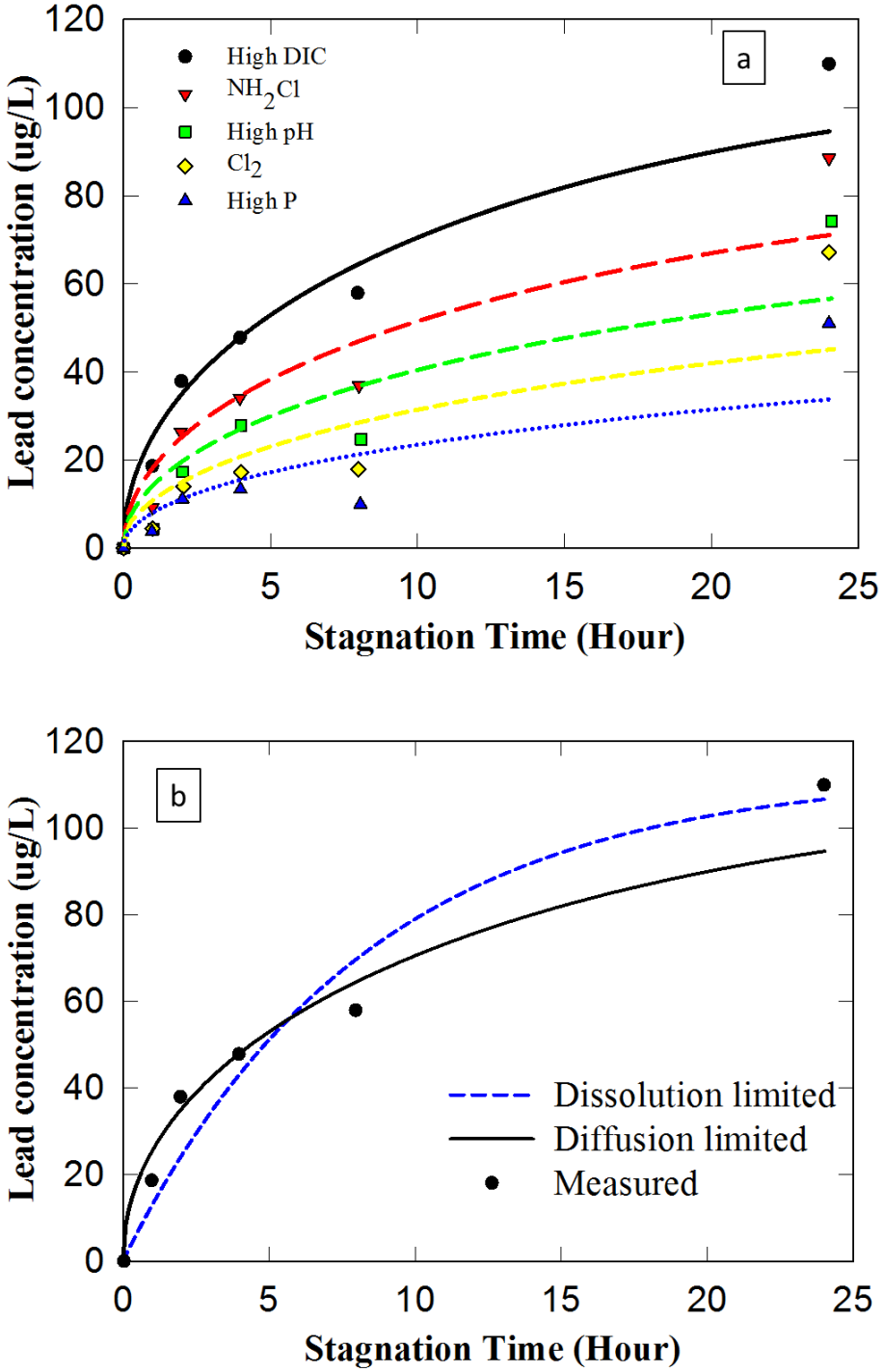

Figure 4-2. (a) Dissolved lead simulation results at different stagnation stages for different water compositions plotted against experimental measurements; and (b) Simulation results of the dissolution-limited vs. diffusion-limited models.

Particulate lead module

The particulate lead model was applied to simulate the monitoring sampling at different flow rates for the two simulated pipe configurations (100%-Pb and 50%Pb-D) in the study of Cartier et al. [46]. The calibrated model performed well in describing the measured release of particulate lead from both the full and the partially replaced LSLs under different flow conditions (Table 4-1). The RMSE% between the simulated and mean measured concentrations for the full pipe case was 13%, while for the partial pipe case it was 25.6%. Generally, the deviation between the simulation and the mean measurement was between 2% to 29% of the standard deviation of the measurements collected at the same flow rate (Figure S 4-2). The calibration parameters for the particulate lead module are given in Table S 4-4. The simulated particulate lead release from the partially replaced pipe under medium flow (simulation: 196 μg/L; experiment: 254±390 μg/L) and high flow (simulation 858 μg/L; experiment: 724±683 μg/L) was significantly higher compared to the full service line under medium flow (simulation: 51 μg/L; experiment 35±55 μg/L) and high flow (simulation: 180 μg/L; experiment: 187±343 μg/L). In contrast, almost no difference was observed between the two LSLs under low flow. Accordingly, this was reflected in the calibrated model parameters, where the detachment coefficients k_{det} for the 50%Pb-D case was almost 10 times higher than the 100%Pb case (Table S 4-4).

The simulation of the intensive sampling events was used to calibrate the model compartment describing particle generation under successive consecutive stagnation and unidirectional flushing events. The concentration was higher for the 50%Pb-D configuration (simulation: 160 μg/L; experiment: mean=151 μg/L), than for the 100%-Pb configuration (simulation: 44 μg/L; experiment: mean=66 μg/L). This was also reflected in the calibrated generation coefficient k_{gen}, which was 20% higher for the partial LSL than for the full LSL.

Generally, the model showed high sensitivity towards small changes in the detachment coefficient k_{det} and the empirical exponent l in the shear stress relationship.

The dissolved lead release was predicted for the 100%-Pb monitoring sampling at different flow rates, where the best fit was achieved by the combination of ($D_{r,s}$=1.935 x 10^{-6} cm^2/sec and C_{eq}=74.16 µg/L), which is consistent with the linear relationship derived from the dissolved lead module verification (Figure S 4-1). These parameters were used for simulating dissolved lead under NHU in the model application simulations described in the following section.

Table 4-1. Simulated vs Experimentally measured particulate lead concentrations

	Low Flow (1.3 lpm)		Medium Flow (8 lpm)		High Flow (32 lpm)	
	Simulation	Experiment	Simulation	Experiment	Simulation	Experiment
Full	11 µg/L	12±7 µg/L	51 µg/L	35±55 µg/L	180 µg/L	187±343 µg/L
Partial	14 µg/L	12±9 µg/L	196 µg/L	254±390 µg/L	858 µg/L	724±683 µg/L

4.4.2 Model Validation and Application

Comparison with field samples

To validate the simulated release of particulate and dissolved lead under typical NHU demand patterns, the results from the Monte-Carlo simulation were compared to the field samples with Pb concentrations above 15 μg/L from the field study of Clark et al. [29]. The reported field concentrations were re-categorized into three groups based on the sampling flow rate (site independent): low flow (0.8-6.5 L/min; N= 32 samples), medium flow (6.5 - 10.3 L/min; N= 45 samples), and high flow (10.3 – 14.2 L/min; 31 samples). Figure 4-3 shows the box and whisker plots of the simulated and field measured levels at the three different flow ranges. Model results were generally higher than the field measurements especially for the medium and high flow categories, where the Pb levels for the low flow were (field: 46.7±37.1 μg/L; simulation: 54.9±48.9 μg/L), medium flow: (field: 60.2±53.8 μg/L; simulation: 84.64±81.81 μg/L), and high flow: (field: 64.86±68.29 μg/L; simulation: 88.4±101.5 μg/L). This might be attributed to the profile sampling technique that was used in the field, where the three profiles were collected in series; consequently, by the time the first samples of the medium and the high flow profiles were collected, the lead service line has been flushed for around 13 and 18 minutes, respectively. Despite the potential variability in the nature of the pipe scales between the LSLs in the field study and the pipe sections in the pilot studies used for model calibration, the simulation results were in qualitative agreement with the field-measured trends at similar flow ranges. This can be seen from the consistent increase in the lead levels with increasing the sampling flow rate, which reflects the increase in particulate lead release. These results are also in agreement with a recently published field study in which elevated lead release after LSL replacement was found to be dominated by lead particulates, with samples containing Pb levels above 100 μg/L comprising almost 100% particulate lead [47].

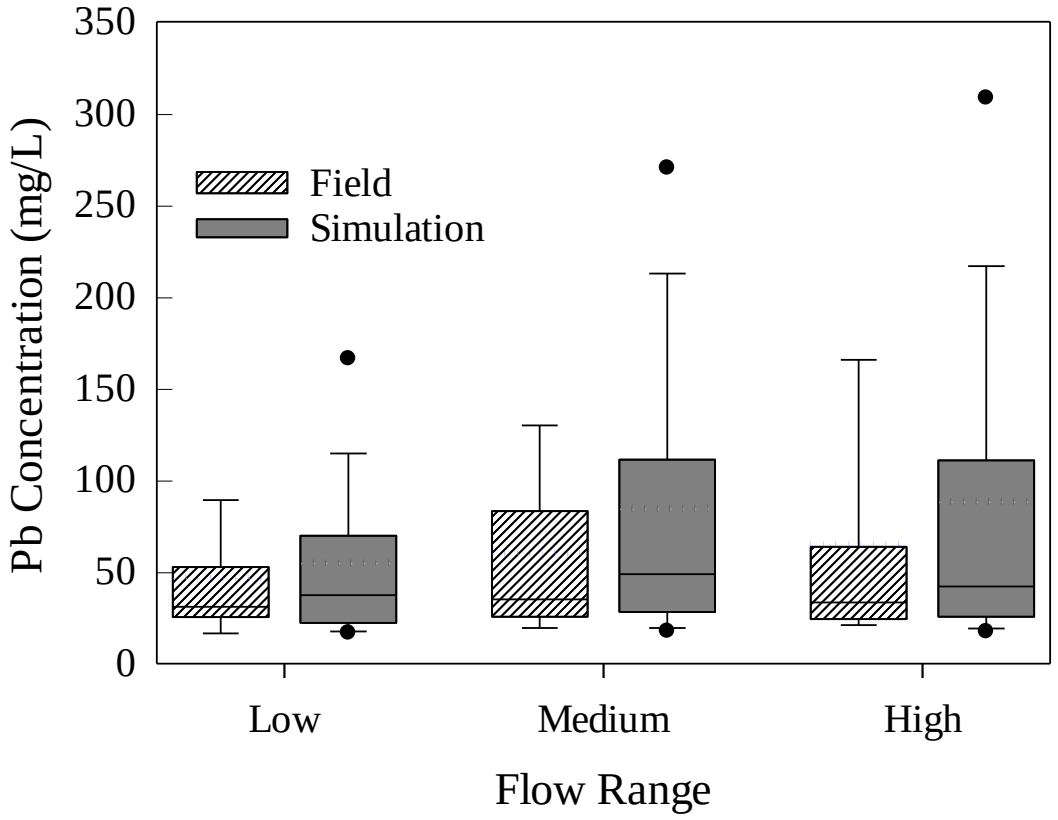

Figure 4-3. Box and whisker plots of Pb levels from Monte-Carlo simulations and field samples grouped by sampling flow rate (Low Flow = 0.8-6.5 LPM; Medium Flow = 6.5-10.3 LPM; High Flow = 10.3-14.2 LPM). Whiskers and dots represent the 10th/90th and 5th /95th of the plotted data ranges, respectively.

Particulate and dissolved lead release under daily NHU

To demonstrate the daily trends of water consumption, Figure 4-4a shows a typical daily demand pattern randomly selected from one of the simulated 200 NHU scenarios. The trend shows two peak demand periods, one in the morning and one in the afternoon, which reflects the typical diurnal nature of water consumption in US homes. During the night, a long stagnation period (~6 hours) that was only interrupted by a single demand pulse took place. Between the two peak demand periods, a second stagnation period with a shorter duration existed, which can correspond to the time when the house is partially or un-occupied. As illustrated in Figure 4-4b, the dissolved lead concentration in the full LSL builds up during the periods of no consumption as lead continuously leaches from the pipe wall and diffuses into the water. This buildup is repeatedly interrupted by the demand pulses that flush part of the dissolved lead out of the pipe. The drop in the dissolved lead concentration is dependent on the flow rate (pulse intensity), as well as the pulse duration (Figure 4-4a). If the duration of the flow pulse is long enough, dissolved lead will continue to flush out until a certain minimum concentration threshold is reached, where the radial mass flux from the pipe wall is equivalent to the convective mass flux transporting the lead out of the pipe. In general, dissolved lead concentrations were lowest during the two daily peak demand periods, while they were highest during the two stagnation periods. Unlike dissolved lead, particulate lead showed “spikes” of relatively higher concentrations that were induced by high flow demands. In the given example, the two particulate lead peaks corresponded to the highest demand pulses encountered during the selected day (20 LPM and 22 LPM). The concentrations drop shortly after these spikes, since the releasable particulate potential has become exhausted by the applied shear stress residual. It can also be noticed that, although the second peak demand pulse has a higher intensity (higher shear stress) than the first peak pulse, the released particulate concentration from

the second peak is lower, since particle generation has not completely replenished the releasable particulate potential.

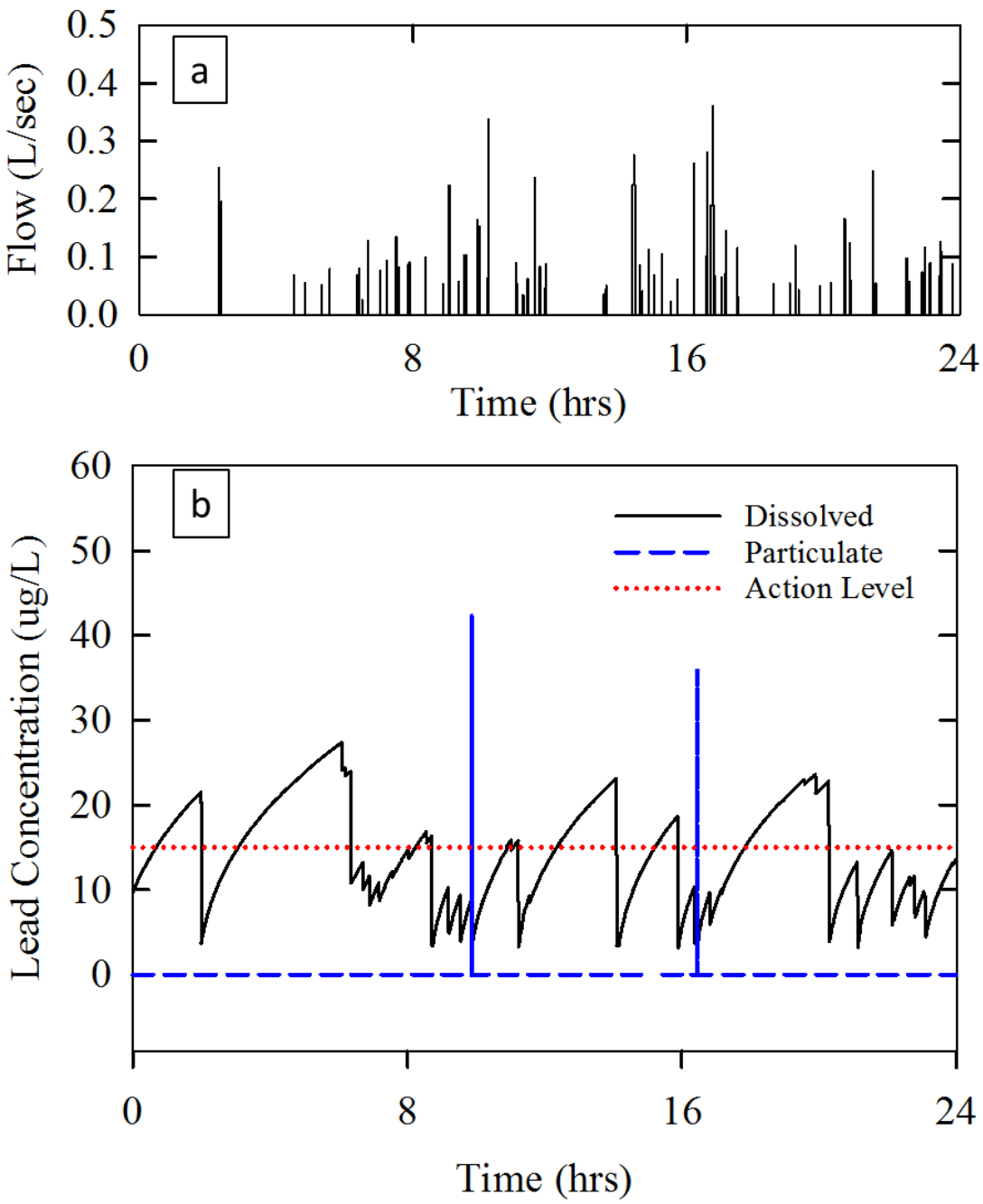

Figure 4-4. (a) 1 day flow demand pattern from one realization randomly selected from the Monte-Carlo pool; and (b) Particulate vs. dissolved lead release under NHU for the full LSL.

While the highest peak introduced by particulate lead for the example day had a concentration of 42.3 µg/L for the full LSL, this concentration significantly increased when the partial replacement situation was simulated to a maximum level of 147.5 µg/L, about 10 times the action level of lead (Figure S 4-3). During those two spikes, the mass of lead released was 434 µg for the full pipe case, and 809.37 µg for the partially replaced LSL, which confirms the hazardous nature of the particulate lead release, especially for partial LSLs. To put these numbers into perspective, a lead paint chip of approximately the size of a penny has around 310 µg of lead [23]. On the other hand, the maximum concentration of dissolved lead for the selected day was 27.4 µg/L for the full pipe (Figure 4-4b), and dropped to 23.6 µg/L for the partially replaced pipe (Figure S 4-3).

Maximum monthly levels of particulate and dissolved lead

Figure 4-5 shows box and whisker plots of the maximum monthly concentrations of particulate vs. dissolved lead from the full and the partial LSLs for the conducted 200 NHU simulations. The maximum concentrations from particulate lead for both the full pipe (195.7±45.6 µg/L), and the partially replaced pipe (1011.9±290.3 µg/L) were significantly higher than dissolved lead for the full pipe (35.5±1.5 µg/L), and the partial pipe (32.9±1.3 µg/L), which was consistent with the trends seen at the daily level. It is important to note that while the partial replacement of the LSL reduced the levels of dissolved lead for all scenarios, the drop in the maximum monthly concentration compared to the full pipe was never more than 14%, and the benefit of replacing half the pipe never translated to an equivalent 50% reduction in the dissolved lead concentrations, which is consistent with previous pilot scale studies.[46] Moreover, partial LSL replacement only decreased the total monthly mass released in the form of dissolved lead by 30% from (91.1±0.83 mg/month) for the full LSL to (63.0±0.58 mg/month) for the partially replaced line, while

particulate mass release almost doubled from 13.1±0.58 mg/month to 23.7±1.58 mg/month). These results are also consistent with recent field sampling studies which concluded that partial LSL replacement may be worse than leaving the LSL intact due to the potential for elevated particulate lead release [47].

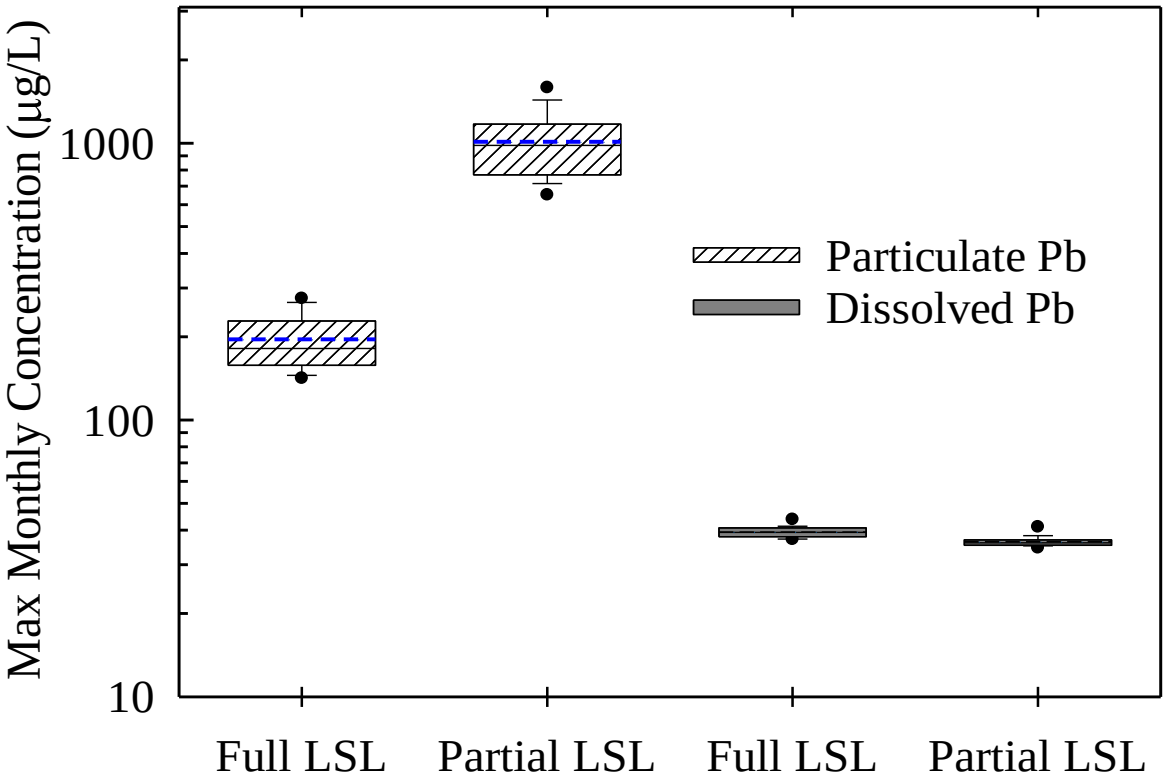

Figure 4-5. Box and whisker plots of Pb levels for the maximum monthly Pb levels. Whiskers and dots represent the $10^{th}/90^{th}$ and $5^{th}/95^{th}$ of the plotted data ranges, respectively.

It is important to note that the lead mass released from the LSL in the particulate form is not necessarily equivalent to the direct exposure experienced by the household occupants. Depending on their size distribution, lead particulates might accumulate within the interior of the premise plumbing system, where they can slowly dissolve as they come in contact with the drinking water. Moreover, larger particles can be retained by the faucet aerator installed on the kitchen tap [2,24]. The configuration, age, size, and materials of the internal premise plumbing fixtures will, therefore, play a significant role in determining the breakthrough of lead particles and the subsequent customer exposure, which needs future investigation from both modeling and experimental perspectives.

Effect of water use patterns on lead release

To test the sensitivity of lead release to the variability in the patterns of water use, two other Monte-Carlo ensembles were performed (800 simulations each) representing the cases of a higher flow frequency, and higher mean flow intensity. In the first ensemble, the overall demand volume was increased from 421.8±0.7 L/day to 1261.7±1.5 L/day by tripling the rates of pulse arrival λ (Table S2), while the mean flow intensity and duration were unchanged. This resulted in lowering the overall concentrations of both dissolved and particulate lead, where the maximum monthly concentration of particulate lead dropped to 179.9±50.2 μg/L (-8%) for the full LSL and to 946.2±322.3 μg/L (-6.5%) for the partial LSL. The reduction in dissolved lead levels was more profound, where the maximum monthly concentration dropped to 28.7±1.1 μg/L (-19.2%) for the full LSL, and to 26.6±1.3 μg/L (-19%) for the partial LSL. This drop is mainly caused by the increase in the rate of pulse arrival, which means that the LSL is being flushed more often as the average period of uninterrupted stagnation events decreased from 17.6 minutes to 5.9 minutes.

The second ensemble tested the effect of increasing the mean flow intensity from 4.3 LPM to 8.7 LPM, which increased the overall demand volume from 421.8±0.7 L/day to 842.5±0.7 L/day, while the pulse arrival rates and the mean pulse duration were kept constant. The increase in the mean pulse intensity had a significant effect on particulate lead release, where the maximum monthly concentrations increased to 314.2±83.8 μg/L (+61%) for the full LSL and to 2,296.6±766.5 μg/L (+127%) for the partial LSL. On the other hand, it had an opposite effect on the dissolved lead concentrations, which dropped by 6% and 5% for the full and partial LSL, respectively.

Effect of pre-flushing and sampling flow rate on regulatory sampling

The lead concentration profile in Figure 4-4b shows that the dissolved lead concentrations exceeded the action level more than once during the example day. Our results also showed that if the LSL was pre-flushed for 5 minutes at an average flow rate of 8 LPM prior to the typical sampling procedure (6 hr stagnation, then 1 L first draw sample), the observed sampling concentration would be 30.1 μg/L. Although this concentration is well above the action level, it is still 19% below the maximum monthly concentration recorded for this simulation (36.8 μg/L). Thus pre-flushing of the LSL prior to regulatory sampling can mask the actual exposure of lead encountered during NHU. More importantly, excessive concentrations of particulate lead were mainly induced by high flow rates, where more than 90% of the flow events that induced particulate release higher than 15 μg/L were above 5.2 LPM. Hence, these spikes would be consistently missed if the sampling were performed at the low flow rates (< 3 LPM) typically used for regulatory sampling.

4.5 Limitations and recommendations for future development

Although the particulate lead module presents a simple way to simulate the complex processes that control particulate release and transport, it is still dependent on a group of semi-empirical parameters that are problem-specific. Therefore, accurate calibration of the presented model using data from pilot studies might be required before applying it to simulate other systems. In these pilot studies, it is preferred to utilize pipe sections cut from aged LSLs harvested from the same water system to match the prevalent scales in the existing LSLs [18,22]. Calibration of the particulate lead model can be accomplished by collecting a systematic series of samples under variable flow conditions that represent the expected flow ranges in the system. The dissolved lead model can be calibrated through comparisons with experimentally determined stagnation curves using water composition that is consistent with the water reaching the consumer taps.

It is also important to note that the detachment of particulate lead from pipe scales is a semi-random process that comprises a huge degree of variability between different systems and different LSLs [12,48,49]. This is attributed to a group of factors that include the inherent variability in the pipe scales, history of disturbances to the LSLs, water chemistry conditions, the presence of iron mains, connection type between lead and copper pipes [50], flow patterns, and temperature. Even for the same LSL sampled under the same flow conditions, the release of particulate lead might still significantly vary from one sample to another as indicated by the typical large standard deviations in the results of pilot studies at high sampling flows [22,46]. Hence, the presented modeling approach is not intended to be applied in a deterministic style to predict particulate lead release in a single LSL for a particular scenario, but rather in a more probabilistic manner to delineate the trends of lead release in a given system based on an ensemble of simulations.

Since this is the first effort to model particulate lead, the probabilistic components of the model were limited to the description of the flow conditions as we used a stochastic demands generator to represent the NHU flow patterns. Other important components of the transport model, such as the description of particle generation and detachment, were assumed deterministic. However, given the semi-random nature of particulate lead release, future studies should consider a more probabilistic formulation for these model components, and further build on the presented model to provide a stochastic description of these phenomena.

4.6 Acknowledgments

The authors would like to thank Dr. Cynthia Lo for providing valuable comments on the article. The work was partially supported by the Lucy and Stanley Lopata Endowment at Washington University in St. Louis.

4.7 References

[1] E. Deshommes, M. Prévost, P. Levallois, F. Lemieux, S. Nour, Application of lead monitoring results to predict 0-7 year old children's exposure at the tap, Water Res. 47 (2013) 2409–2420.

[2] E. Deshommes, M. Prévost, Pb particles from tap water: Bioaccessibility and contribution to child exposure, Environ. Sci. Technol. 46 (2012) 6269–6277.

[3] T.A. Jusko, C.R. Henderson Jr, B.P. Lanphear, D.A. Cory-Slechta, P.J. Parsons, R.L. Canfield, Blood lead concentrations< 10 μg/dL and child intelligence at 6 years of age, Environ. Health Perspect. 116 (2008) 243.

[4] B.P. Lanphear, R. Hornung, M. Ho, C.R. Howard, S. Eberly, K. Knauf, Environmental lead exposure during early childhood, J. Pediatr. 140 (2002) 40–47.

[5] D.C. Bellinger, Lead Contamination in Flint — An Abject Failure to Protect Public Health, N. Engl. J. Med. 374 (2016) 1101–1103.

[6] M. Hanna-Attisha, J. LaChance, R.C. Sadler, A. Champney Schnepp, Elevated Blood Lead Levels in Children Associated With the Flint Drinking Water Crisis: A Spatial Analysis of Risk and Public Health Response., Am. J. Public Health. 106 (2016) 283–290.

[7] D.S. Wheeler, Flint, Curr. Treat. Options Pediatr. 2 (2016) 4–6.

[8] J.L. Schnoor, Recognizing Drinking Water Pipes as Community Health Hazards, J. Chem. Educ. 93 (2016) 581–582.

[9] M.A. Del Toral, A. Porter, M.R. Schock, Detection and evaluation of elevated lead release from service lines: A field study, Environ. Sci. Technol. 47 (2013) 9300–9307.

[10] A. Sandvig, P. Kwan, G. Kirmeyer, B. Maynard, D. Mast, R.R. Trussell, S. Trussell, A. Cantor, A. Prescott, Contribution of service line and plumbing fixtures to lead and copper rule compliance issues, AWWA Res. Found. (2008).

[11] D.A. Cornwell, R.A. Brown, S.H. Via., National Survey of Lead Service Line Occurrence, J. Am. Water Work. Assoc. 108 (2016) E181–E191.

[12] S. Triantafyllidou, M. Edwards, Lead (Pb) in tap water and in blood: implications for lead exposure in the United States, Crit. Rev. Environ. Sci. Technol. 42 (2012) 1297–1352.

[13] M. Edwards, S. Triantafyllidou, D. Best, Elevated blood lead in young children due to lead-contaminated drinking water: Washington, DC, 2001-2004, Environ. Sci. Technol. 43 (2009) 1618–1623.

[14] M. Edwards, A. Dudi, Role of chlorine and chloramine in corrosion of lead-bearing plumbing materials, J. Am. Water Work. Assoc. 96 (2004) 69–81.

[15] D.B. LaFrance, Open Channel -- Restoring Faith, J. Am. Water Work. Assoc. 108 (2016)

10.

[16] S. Triantafyllidou, M. Edwards, Galvanic corrosion after simulated small-scale partial lead service line replacements, J. Am. Water Works Assoc. 103 (2011) 85–99.

[17] Y. Wang, H. Jing, V. Mehta, G.J. Welter, D.E. Giammar, Impact of galvanic corrosion on lead release from aged lead service lines, Water Res. 46 (2012) 5049–5060.

[18] Y. Wang, V. Mehta, G.J. Welter, D.E. Giammar, Effect of connection methods on lead release from galvanic corrosion, J. Am. Water Work. Assoc. 105 (2013) 39–40.

[19] J. St. Clair, C. Cartier, S. Triantafyllidou, B. Clark, M. Edwards, Long-Term Behavior of Simulated Partial Lead Service Line Replacements, Environ. Eng. Sci. 33 (2016) 53–64.

[20] S. Masters, M. Edwards, Increased Lead in Water Associated with Iron Corrosion, Environ. Eng. Sci. 32 (2015) 361–369.

[21] E. Camara, K.R. Montreuil, A.K. Knowles, G.A. Gagnon, Role of the water main in lead service line replacement: A utility case study, J. Am. Water Works Assoc. 105 (2013) 423–431.

[22] C. Cartier, E. Dore, L. Laroche, S. Nour, M. Edwards, M. Prevost, Impact of treatment on Pb release from full and partially replaced harvested Lead Service Lines (LSLs), Water Res. 47 (2013) 661–671.

[23] S. Triantafyllidou, J. Parks, M. Edwards, Lead particles in potable water, J. Am. Water Work. Assoc. 99 (2007) 107–117.

[24] E. Deshommes, L. Laroche, S. Nour, C. Cartier, M. Prévost, Source and occurrence of particulate lead in tap water, Water Res. 44 (2010) 3734–3744.

[25] A. Kuch, I. Wagner, A mass transfer model to describe lead concentrations in drinking water, Water Res. 17 (1983) 1303–1307.

[26] D. Van Der Leer, N.P. Weatherill, R.J. Sharp, C.R. Hayes, Modelling the diffusion of lead into drinking water, Appl. Math. Model. 26 (2002) 681–699.

[27] C.R. Hayes, Computational modelling to investigate the sampling of lead in drinking water, Water Res. 43 (2009) 2647–2656.

[28] P.T. Cardew, Development of a convective diffusion model for lead pipe rigs operating in laminar flow, Water Res. 40 (2006) 2190–2200.

[29] B. Clark, S. Masters, M. Edwards, Profile sampling to characterize particulate lead risks in potable water, Environ. Sci. Technol. 48 (2014) 6836–6843.

[30] C. Lu, Theoretical Study of Particle, Chemical and Microbial Transport in Drinking Water Distribution Systems, University of Cincinnati, 1991.

[31] Y. Wang, J. Wu, Z. Wang, A. Terenyi, D.E. Giammar, Kinetics of lead(IV) oxide (PbO2) reductive dissolution: Role of lead(II) adsorption and surface speciation, J. Colloid Interface Sci. 389 (2013) 236–243.

[32] Y. Wang, J. Wu, D.E. Giammar, Kinetics of the reductive dissolution of lead(IV) oxide by iodide, Environ. Sci. Technol. 46 (2012) 5859–5866.

[33] Y. Xie, Dissolution , Formation , and Transformation of the Lead Corrosion Product PbO 2 : Rates and Mechanisms of Reactions that Control Lead Release in Drinking Water Distribution Systems, Washington University in St. Louis, 2010.

[34] H. Bai, P. Biswas, Deposition of lognormally disributed aerosols accounting for simultaneous diffusion, thermophoresis and coagulation., J. Aerosol Sci. 21 (1990) 629–640.

[35] P. van Thienen, J.H.G. Vreeburg, E.J.M. Blokker, Radial transport processes as a precursor to particle deposition in drinking water distribution systems, Water Res. 45 (2011) 1807–

1817.

[36] E.J.M. Blokker, J.H.G. Vreeburg, J.C. Van Dijk, Simulating Residential Water Demand with a Stochastic End-Use Model, J. Water Resour. Plan. Manag. 136 (2010) 19–26.

[37] A. Hossain, J. Naser, M. Imteaz, Extended Analytical Turbulent Diffusion Model for Particle Dispersion and Deposition in a Horizontal Pipe: Comparison with CFD Simulation, Environ. Model. Assess. 16 (2011) 295–311.

[38] I.J.H.G. Vreeburg, D.J.B. Boxall, Discolouration in potable water distribution systems: A review, Water Res. 41 (2007) 519–529.

[39] J.B. Boxall, A.J. Saul, Modeling Discoloration in Potable Water Distribution Systems, J. Environ. Eng. 131 (2005) 716–725.

[40] S.G. Buchberger, L. Wu, Model for instantaneous residential water demands, J. Hydraul. Eng. 121 (1995) 232–246.

[41] S. Buchberger, Y. Lee, Evidence supporting the Poisson pulse hypothesis for residential water demands, Water Ind. Syst. Model. Optim. Appl. (1999) 216–227.

[42] S.G. Buchberger, Z. Li, PRPsym : A Modeling System for Simulation of Stochastic Water Demands, World Environ. Water Resour. Congr. (2007).

[43] S.G. Buchberger, G.J. Wells, Intensity, Duration, and Frequency of Residential Water Demands, J. Water Resour. Plan. Manag. 122 (1996) 11–19.

[44] E. Creaco, R. Farmani, Z. Kapelan, L. Vamvakeridou-Lyroudia, D. Savic, Considering the Mutual Dependence of Pulse Duration and Intensity in Models for Generating Residential Water Demand, J. Water Resour. Plan. Manag. 141 (2015) 4015031.

[45] Y. Xie, D.E. Giammar, Effects of flow and water chemistry on lead release rates from pipe scales, Water Res. 45 (2011) 6525–6534.

[46] C. Cartier, R.B. Arnold, S. Triantafyllidou, M. Prevost, M. Edwards, Effect of Flow Rate and Lead/Copper Pipe Sequence on Lead Release from Service Lines, Water Res. 46 (2012) 4142–4152.

[47] B.F. Trueman, E. Camara, G.A. Gagnon, Evaluating the Effects of Full and Partial Lead Service Line Replacement on Lead Levels in Drinking Water, Environ. Sci. Technol. 50 (2016) 7389–7396.

[48] S. Masters, G.J. Welter, M. Edwards, Seasonal Variations in Lead Release to Potable Water, Environ. Sci. Technol. 50 (2016) 5269–5277.

[49] S. Masters, J. Parks, A. Atassi, M.A. Edwards, Inherent variability in lead and copper collected during standardized sampling, Environ. Monit. Assess. 188 (2016) 1–15.

[50] B. Clark, C. Cartier, J.S. Clair, S. Triantafyllidou, M. Prevost, M. Edwards, Effect of connection type on galvanic corrosion between lead and copper pipes, J. Am. Water Works Assoc. 105 (2013) 69–70.

4.8 Supplementary Material

4.8.1 Non-dimensional forms of the governing equations.

The governing transport equation for dissolved lead (Eq. 4-1) can be put in the following non-dimensional form:

$$\frac{\partial C_s^*}{\partial t^*} = -f(r^*)\frac{\partial C_s^*}{\partial x^*} + \frac{1}{Pe_{L,s}}\frac{\partial^2 C_s^*}{\partial x^{*2}} + \frac{A_{r,s}}{r^*}\frac{\partial}{\partial r^*}\left(r^*\frac{\partial C_s^*}{\partial r^*}\right) \quad \text{(S-4.1)}$$

where $C_s^* = C_s/C_{eq}$; $x^* = x/L$; $r^* = r/r_0$; $t^* = t/T_{res}$; $T_{res} = L/\bar{u}$; $Pe_{L,s} = \frac{\bar{u}L}{D_{L,s}}$; and $A_{r,s} = \frac{D_{r,s}}{{r_0}^2}T_{res}$. The boundary conditions can hence be written as: $C_s^* = C_0/C_{eq}$, $x^* = 0$; $\frac{\partial C_s^*}{\partial x^*} = 0$, $x^* = 1$; $\frac{\partial C_s^*}{\partial r^*} = 0$, $r^* = 0$; and $C_s^* = 1$, $r^* = 1$.

Similarly, the governing equation for the particulate phase (Eq. 4-4) can be written as:

$$\frac{\partial C_p^*}{\partial t^*} = -f(r^*)\frac{\partial C_p^*}{\partial x^*} + \frac{1}{Pe_{L,p}}\frac{\partial^2 C_s^*}{\partial x^{*2}} + \frac{A_{r,p}}{r^*}\frac{\partial}{\partial r^*}\left(r^*\frac{\partial C_p^*}{\partial r^*}\right) - A_{set}C_p^*\delta(\bar{u}-0) \quad \text{(S-4.2)}$$

where, $C_p^* = C_p/(\frac{P_{max}}{r_h})$; $Pe_{L,p} = \frac{\bar{u}L}{D_{L,p}}$; $A_{r,p} = \frac{D_{r,p}}{{r_0}^2}T_{res}$; and $A_{set} = k_{set}T_{res}$. The boundary conditions can therefore be written as: $C_p^* = 1$, $x^* = 0$; $\frac{\partial C_p^*}{\partial x^*} = 0$, $x^* = 1$; $\frac{\partial C_p^*}{\partial r^*} = 0$, $r^* = 0$; and $\frac{\partial C_p^*}{\partial r^*} = A_{det}$, $r^* = 1$. where, $A_{det} = \frac{R_{det}\ r_0\ r_h}{D_{r,p}\ P_{max}} = \frac{R_{det}\ {r_0}^2}{2P_{max}D_{r,p}}$.

The attached particulate concentration can be put in dimensionless form as follows:

$$\frac{dP^*}{dt^*} = [A_{gen}(1-P^*) + A_{set}C_p^*]\delta(\bar{u}-0) - 2A_{det}A_{r,p} \quad \text{(S-4.3)}$$

where, $A_{gen} = k_{gen}T_{res}$. Reformulating the governing equations (Eq. 4-1, 4-4, and 4-5) in dimensionless forms gave rise to a set of non-dimensional groups that govern the emission and transport of dissolved and particulate lead. For example, the Peclet numbers $Pe_{L,s}$ and $Pe_{L,p}$ govern the rate of solute transport by advective compared to dispersive transport mechanisms in the axial direction, while their peers $A_{r,s}$ and $A_{r,p}$ govern the same in the radial direction. Particulate lead generation, detachment, and settling are controlled by the three dimensionless groups A_{gen}, A_{det} and A_{set}. Hence, these three groups dictate the relative contribution of each one of the three phenomena to the overall release of particulate lead.

4.8.2 Numerical Solution of the governing equations

The Alternating Direction Implicit (ADI) scheme is used to solve the two governing convection-diffusion equations (Eq. 4-1, & 4-4), where each time step is divided into two half steps such that the numerical integration is first performed in the r-direction to evaluate the solution at $t+\Delta t/2$, followed by the integration in the x-direction to obtain the solution at $t+\Delta t$ [1]. In the first half step, the finite difference scheme is implicit in the radial direction but explicit in the axial direction, while in the second half step the scheme is implicit in the axial direction and explicit in the radial direction. The advection term was treated using the explicit first order upwind scheme in the first half step, and an implicit central difference scheme in the second half step. A central difference scheme was used to discretize the diffusion terms in both the axial and the radial directions. The resulting system of linear equations was solved using the Thomas algorithm for tridiagonal coefficient matrices. Detailed description of the ADI numerical scheme can be found elsewhere [2,3].

4.8.3 Stochastic water demands generation

The detailed procedure of generating demand pulses by drawing random values for y_1 and y_2 is described elsewhere [4]. Based on equations 4-9 and 4-10, the stochastic demand generation model comprises five parameters: μ_1, μ_2, σ_1, σ_2, and $\dot{\rho}$. These parameters were adopted from the data fitting made previously done by Creaco et al. [4], where the method of moments was used to fit the simulated flow rates to the residential demands monitored with a 1 sec time step resolution during a field campaign of 21 households in Milford, Ohio [5]. In terms of the pulse arrival time, the arrival rate λ is assumed to take different values during the day, where each day is divided into 12 time slots to account for the sub-daily trends of water consumption. The mean values from the fitting study for the five parameters, as well as the demand arrival rates for the 12 slots, were used in this model (see Tables S 4-1 and S 4-2).

4.8.4 Supplementary Tables

Table S 4-1. Stochastic demands generation model parameters.

Parameter	**unit**	**value**
μ_1	$\ln(\text{sec})$	3.01
μ_2	$\ln(\text{L/sec})$	1.23
σ_1	$\ln(\text{sec})$	-2.63
σ_2	$\ln(\text{L/sec})$	0.66
$\dot{\rho}$	(-)	0.63

Table S 4-2. Pulse arrival rate for the 12 slots during one day.

Time Slot	**λ (sec^{-1})**
0:00-2:00	0.0002326
2:00-4:00	0.0001936
4:00-6:00	0.0006166
6:00-8:00	0.0015811
8:00-10:00	0.0013878
10:00-12:00	0.0012466
12:00-14:00	0.0009728
14:00-16:00	0.0009890
16:00-18:00	0.0014566
18:00-20:00	0.0012724
20:00-22:00	0.0010900
22:00-24:00	0.0008136

Table S 4-3. Calibration parameters for the dissolved lead simulation module

Simulation	$D_{r,s}$* (1 x 10^{-6} cm^2/sec)	C_{eq}** (μg/L)
High DIC	2.890	109.88
NH_2Cl	2.265	88.51
High pH	1.935	74.16
Cl_2	1.350	67.21
High P	1.105	51.04

* Calibration of the radial diffusion coefficient $D_{r,s}$ was done by a genetic algorithm (GA) to minimize the root mean square error (RMSE) between the measured and the simulated concentrations. The optimization was performed using the genetic algorithm (GA) toolbox in MATLAB 2013, with the following main parameters: Population size = 50; Crossover fraction = 0.7; Adaptive feasible Mutation function; and Constraint dependent crossover function.

** The equilibrium concentration implemented in the boundary condition (C_{eq}) was always set equal to the experimentally measured concertation after 24 hours of stagnation.

Table S 4-4. Calibration parameters for the particulate lead simulation module

Parameter	100%Pb	50%PbD
k_{set}*	2.3 x 10^{-3}	2.3 x 10^{-3}
k_{gen}	3.0 x 10^{-6}	3.5 x 10^{-6}
k_{det}	5.5 x 10^{-2}	6.0 x 10^{-1}
l	2.8	1.6
m	0.8	2.5
n	1.05	1.15
P_{max}**	50	50

***** For all simulations, particle settling was assumed to take place only under stagnant conditions, and was described by a first order reaction in the concentration of mobilized particulate lead C_p with a half-life time ($t_{1/2}$) of 5 minutes. This time represents the gravitational settling time required by a particle of a size equal to 4 μm across a LSL of a diameter = ¾". The settled mass, i.e., the mass removed from the suspended phase, was added to the releasable particulate potential after each time step.

****** The maximum potential P_{max} tended to have no effect on the concentration profiles since the change in the particulate potential was typically small, hence an arbitrary value (P_{max}=50 μg/cm^2) was used for all simulations. The initial condition for the stored releasable potential *P(t=0)* is calculated by assuming that the initial layer strength is equivalent to the shear stress induced by the 50th percentile of the monthly flow rates.

4.8.5 Supplementary Figures

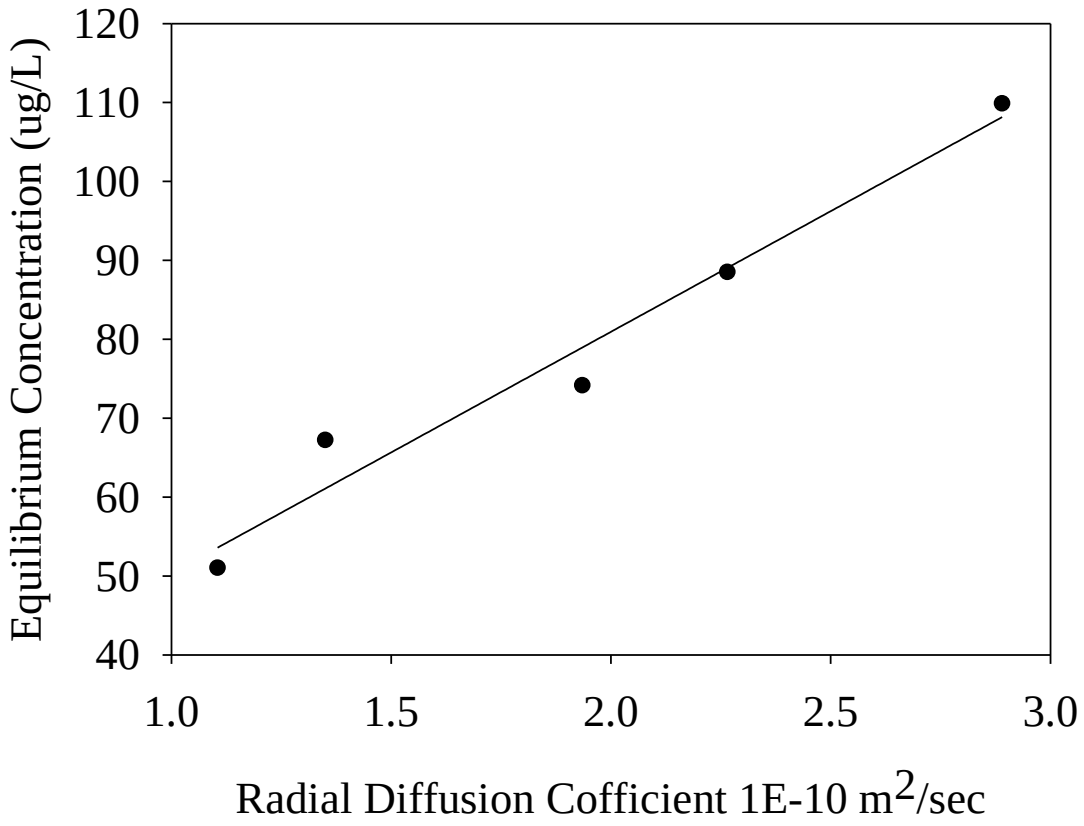

Figure S 4-1. Correlation between the calibrated radial diffusion coefficient and the equilibrium concentration.

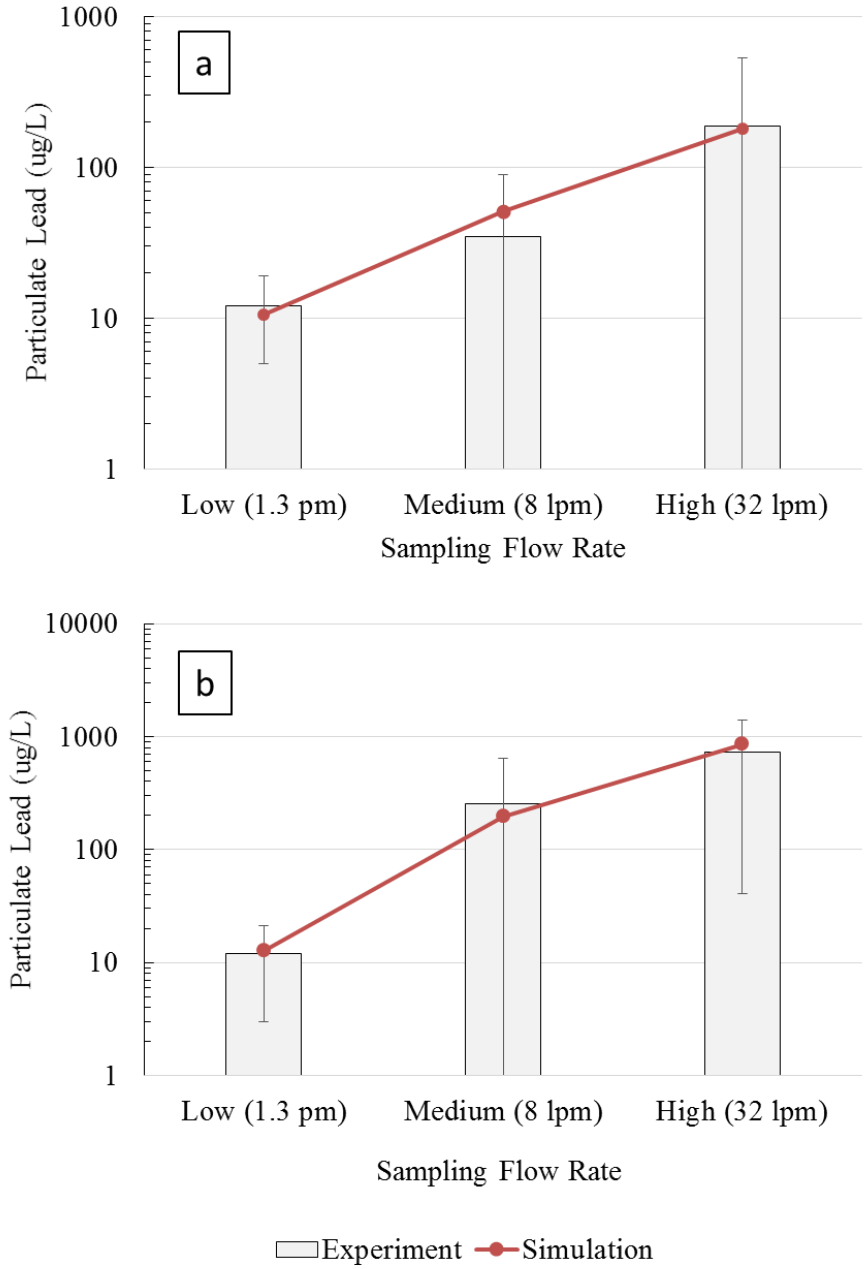

Figure S 4-2. Particulate lead release from (a) Full lead pipe (100% Pb), and (b) Partially replaced pipe (50% PbD) from simulations against experimental measurements under different sampling flow rates.

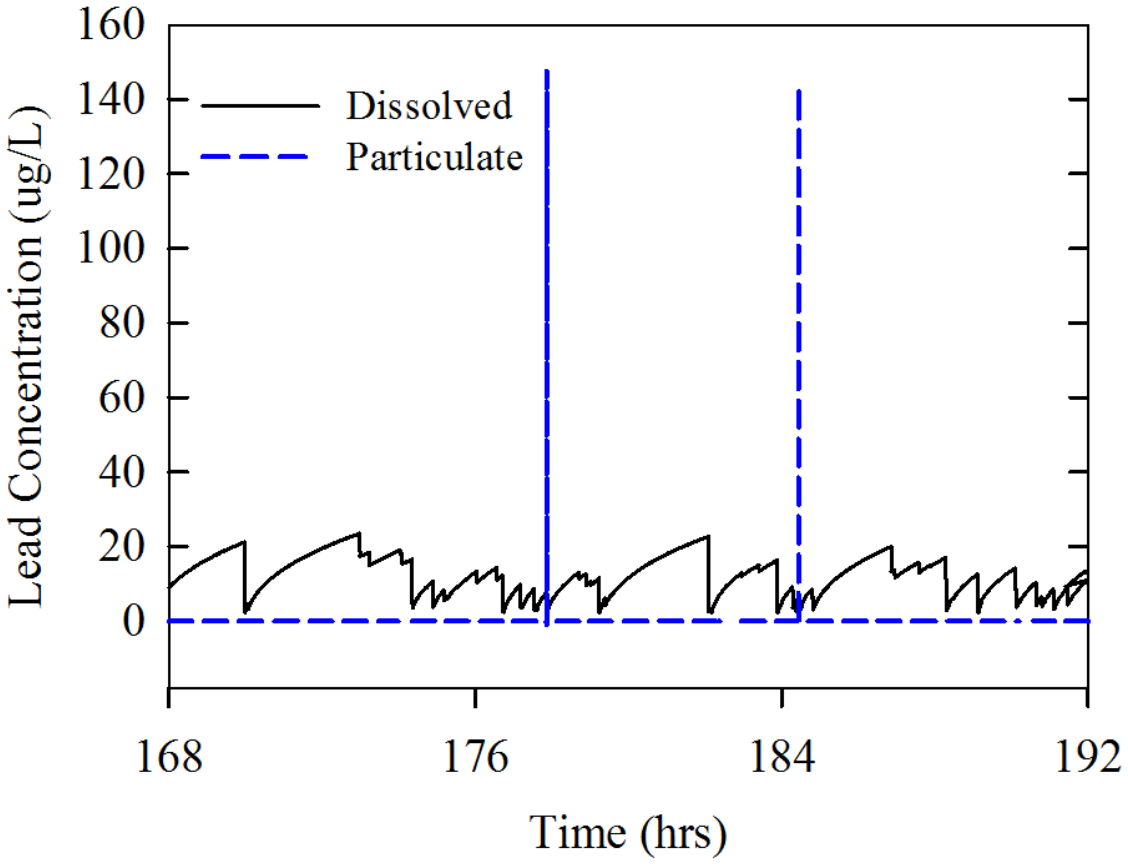

Figure S 4-3. Particulate vs dissolved lead release under NHU for the partial LSL.

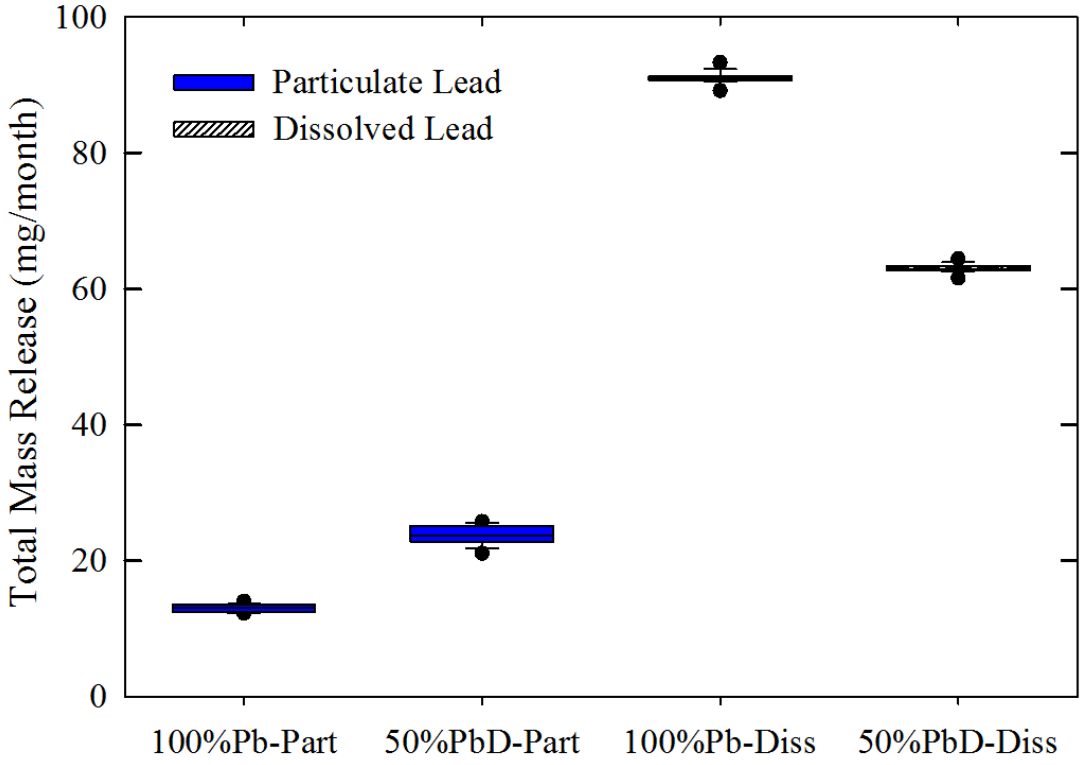

Figure S 4-4. Box and whisker plots of the 200 Monte-Carlo simulations total lead mass released during one month for the four scenarios.

4.8.6 Supplementary References

[1] J.H. Ferziger, Numerical methods for engineering application, John Wiley & Sons, 1981.

[2] O.N. Ozdemir, A.M. Ger, Realistic numerical simulation of chlorine decay in pipes, Water Res. 32 (1998) 3307–3312.

[3] G. Naser, B.W. Karney, A 2-D transient multicomponent simulation model: Application to pipe wall corrosion, J. Hydro-Environment Res. 1 (2007) 56–69.

[4] E. Creaco, R. Farmani, Z. Kapelan, L. Vamvakeridou-Lyroudia, D. Savic, Considering the Mutual Dependence of Pulse Duration and Intensity in Models for Generating Residential Water Demand, J. Water Resour. Plan. Manag. 141 (2015) 4015031.

[5] S.G. Buchberger, Random demands, travel times, and water quality in deadends, Awwa Research Foundation and National Science Fondation, 2003.

Chapter 5

Influence of the Dead-End Sections of Drinking Water Distribution Networks on the Optimization of Booster Chlorination Systems

Results presented in this chapter were submitted to:

A. A. Abokifa, A. Maheshwari, R. D. Gudi, and P. Biswas. Optimizing Booster Chlorination in Water Distribution Systems: Impact of the Dead-End Sections. Water Research (Submitted – May 2018)

5.1 Abstract

The design challenge of finding the optimal layout and scheduling of booster chlorination stations has stimulated considerable research over the last two decades. The majority of previous studies that addressed this topic relied on EPANET, an advection-based water quality model, for the simulation of the transport and decay of disinfectant residuals in the pipes of the distribution network. Nevertheless, EPANET is known to produce erroneous predictions for the dead-end branches of the distribution network where low-flow conditions and frequent stagnations are abundant, especially when a skeletonized representation of the flow demands is employed. This study aims at investigating the impact of implementing an advanced water quality model for simulating the dead-end sections of the distribution network on the outcomes of the optimization of booster chlorination systems. To this end, an advection-dispersion-reaction (ADR) transport model that considers the spatial distribution of flow demands along the dead-end pipe is linked to a genetic algorithm based optimization routine. The objective function is formulated and solved to find the optimal locations and chlorine-dosing schedules of the booster stations that minimize the total cost of booster construction and operation, while maintaining a sufficient residual throughout the distribution network. Taken together, the results of this study suggest that optimization outcomes generated by EPANET simulations may produce a booster chlorination system that fails to maintain an adequate residual concentration in the periphery pipes of a real-life water distribution system.

5.2 Introduction

Chlorine is broadly adopted by water supply utilities worldwide as the disinfecting agent of choice for drinking water treatment. A sufficient residual concentration is typically maintained throughout the distribution system to prevent microbiological contamination of the treated water as it transports through the pipes of the distribution network. However, applying large doses of the disinfectant at the treatment point has traditionally been associated with several issues, including consumer complaints about water taste and odor problems near the treatment locations, and high disinfection byproduct (DBP) levels especially at the far ends of the network [1,2]. As an alternative, booster chlorination can be implemented to maintain a uniform residual concentration by injecting the disinfectant at multiple locations in the network with smaller, more distributed, doses [3]. Such practice enables preserving a sufficient residual at all points in the network, while simultaneously reducing the formation of DBPs. Booster stations can also be activated in case a contamination event is detected, which can potentially curb the spread of contaminants by rapidly injecting large doses of the disinfectant in the proximity of the infected zones [4].

Finding the optimal layout and operation of booster chlorination stations has been extensively addressed by several previous studies. Boccelli et al. [5] formulated an optimization model for booster injection scheduling with the objective of minimizing the total disinfectant mass dose. Tryby et al. [6] extended their work by considering the locations of booster stations as decision variables in the optimization problem, which was formulated as a mixed integer linear programming (MILP) problem. Munavalli and Kumar [7] formulated the objective function to determine chlorine injection rates for boosters with known locations that minimize the residual concentration deviations at the demand nodes from the minimum specified concentration, which

was solved by means of a genetic algorithm (GA). Propato and Uber [8] proposed a linear least squares (LSL) method to minimize the deviations of residual concentrations from desired levels. Prasad et al. [9] formulated a multi-objective optimization model to minimize the total disinfectant dose and maximize the volumetric demand within specified residual limits, which was solved using a multi-objective genetic algorithm (NSGA-II). Ostfeld and Salomons [10] used a GA to simultaneously optimize pump scheduling and the layout and operation of booster chlorination stations. Ohar and Ostfeld [11] built upon their work by linking a GA to a multi-species water quality simulation model in order to incorporate DBP levels in the constraints. DBP formation was also included in more recent studies [12–14]. A comprehensive literature review on the optimization of booster chlorination systems can be found in the recent works of Islam et al. [13], and Mala-Jetmarova et al. [15].

The majority of the above-mentioned studies adopted a simulation-optimization approach, in which an optimization algorithm is coupled with a water quality simulator to compute the objective function and to determine constraint violations corresponding to each of the candidate solutions. EPANET is a generic, open-source, software package for simulating both the hydraulics and water quality in water distribution networks. It has been implemented in most of these studies, in either its original single-species release or its multi-species extension EPANET-MSX, to simulate the decay and transport of chlorine in the studied distribution systems. Nevertheless, the water quality module incorporated in EPANET is based on an advection-reaction transport model [16] that does not account for dispersion as a solute transport mechanism [17–21]. While this simplification does not generally compromise the accuracy of water quality simulations for main transmission lines where the flow is highly turbulent, previous studies showed that EPANET fails

to accurately predict field observed disinfectant concentrations in the dead-end branches at the perimeters of the distribution system where laminar flow conditions prevail [16,22].

Dead-end zones are generally characterized by intermittent low-flow events and frequent stagnations. They are known to be responsible for most of the water quality deterioration in the distribution system, and are particularly more susceptible to water quality monitoring failures [23]. The long residence time typically encountered in these zones results in the disappearance of chlorine residuals, excessive growth of biofilms, and high DBPs formation [24–28]. Furthermore, dead-end sections typically comprise a non-trivial fraction (≥25%) of the total water infrastructure and tend to service an even larger percentage of the residential consumer base [22]. Therefore, relying on EPANET for simulating chlorine decay and transport in these low-flow zones can potentially yield flawed results if used to conduct the water quality simulations required to solve network optimization problems. This includes the optimization of booster chlorination systems, real-time boost-response systems [4], pump scheduling with water quality constraints [29], sensor placement for reactive contaminant detection [30], and contaminant source identification [31].

In addition to the fundamental shortcoming of neglecting dispersive transport, spatial aggregation of water demands is typically employed in hydraulic, and subsequently water quality, simulations conducted with EPANET [32,33]. Under this approximation, multiple water uses are lumped into a single demand point assigned to a specific junction on the network grid, a practice known as network skeletonization. For main water arteries, spatial aggregation of flow demands is a reasonable approximation because the ratio of “on-pipe” demands compared to the flows transmitted to downstream sections of the network is relatively small. For dead-ends, however, all water demands are being directly withdrawn along the pipe at different spatial locations. Hence, applying spatial aggregation to dead-end links would consistently overestimate the average flow

velocity at different axial locations of the pipe, and more importantly, under-predict the residence time [34]. The later will cause the simulated disinfectant concentrations to be systematically over-predicted as observed in previous studies [16,22,35]. Hence, chlorine doses determined by such simulations will most likely be insufficient to sustain the minimum residual in the extremities of the distribution system.

In Chapter 2, a special model for simulating water quality in the dead-end branches of water distribution networks (WUDESIM) was developed. The model considers both advective and dispersive solute transport mechanisms as well as the realistic spatial distribution of water demands along the pipe. The model displayed better agreement with field-measured concentrations of fluoride tracer and free chlorine compared to those simulated by EPANET. In addition, a set of three correction factors were analytically derived to adjust the residence time, dispersion rate, and chlorine wall demand in order to overcome simulation errors caused by the spatial aggregation of demands associated with network skeletonization. In this Chapter, WUDESIM is used to explore the influence of considering a more accurate model to conduct water quality simulations of the dead-end sections on the optimization of booster-chlorination systems. The effects of employing network skeletonization and neglecting solute dispersion in low-flow pipes on the optimal placement and operation of the boosters are investigated. The sensitivity of the optimization results to seasonal variations in chlorine decay rates and water demands is examined.

5.3 Methodology

5.3.1 Mathematical formulation of the transport model

Chlorine transport and decay in a dead end pipe can be modeled by a dynamic 2-D convection-diffusion equation in cylindrical coordinates representing the mass balance on the disinfectant concentration:

$$\frac{\partial}{\partial t}C(x,r,t) = -\frac{\partial}{\partial x}(u\,f(r)\,C) + \frac{\partial}{\partial x}\left(D\frac{\partial C}{\partial x}\right) + \frac{1}{r}\frac{\partial}{\partial r}\left(r\,D\frac{\partial C}{\partial r}\right) - \sum_{k=1}^{N_r} r_k \qquad (5\text{-}1)$$

where, C is the chlorine concentration in the pipe (mg/L), x & r are the axial and radial space coordinates, respectively (m); t is the time (sec); u is the average flow velocity across the pipe cross section (m/sec); $f(r)$ is the radial velocity distribution parameter; D is the molecular diffusivity of chlorine in water (m^2/sec); and r_k is the kth reaction of chlorine in the bulk flow (sec^{-1}). This 2-D model can be simplified into a 1-D model by incorporating dispersive solute transport, which gives the following 1-D advection-dispersion-reaction (ADR) equation [34]:

$$\frac{\partial C}{\partial t} = -u\frac{\partial C}{\partial x} + E\frac{\partial^2 C}{\partial x^2} - K\,C \qquad (5\text{-}2)$$

where, E is the effective longitudinal dispersion coefficient (m^2/sec), K is the overall lumped first-order decay constant (sec^{-1}) that accounts for disinfectant decay in the bulk flow, and radial mass transfer and reaction at the pipe wall [16]. Removing the dispersion term in the previous equation gives the 1-D advection-reaction (AR) equation incorporated in EPANET. The longitudinal dispersion coefficient under laminar flow conditions is calculated by the classical formula of Taylor, (1953): $E_T = \frac{a^2u^2}{48D}$. The model uses a two-stage Eulerian-Lagrangian numerical scheme

combined with the numerical Green's function technique for solving the dynamic ADR equation [34].

5.3.2 Correction factors for network skeletonization

In addition to dispersion, the spatial aggregation of water demands due to network skeletonization is a significant source of modeling errors encountered when using EPANET as revealed by the sensitivity analysis conducted in Chapter 2. Nevertheless, breaking down each dead-end link into multiple segments, with a decreasing flow in the axial direction, was also shown to substantially increase the computational cost of solving the ADR equation compared to the skeletonized (single-segment) model. Therefore to approximate the behavior of the detailed, multi-segment, model while simultaneously reducing the computational demand, a set of three correction factors were analytically derived to enhance the accuracy of the skeletonized model [34]. The correction factors were developed in a way that translates the three dimensionless groups: Reynolds number (Re), Peclet number (Pe) and Damkohler number (Da) of the single-segment model, to match its multi-segment equivalent. In Chapter 2, these correction factors were tested for a wide range of scenarios, and were shown to significantly enhance the simulation accuracy of the skeletonized (single-segment) representation. The correction factors for the residence time CF_τ, Taylor's dispersion coefficient CF_E, and the chlorine wall demand CF_R are given as:

$$\mathrm{CF}_\tau = \frac{\tau_{\mathrm{corr}}}{\tau_0} = \sum_{i=1}^{N_{\mathrm{seg}}} \frac{1}{N_{\mathrm{seg}}\text{-}i + 1} \tag{5-3}$$

$$\mathrm{CF}_\mathrm{E} = \frac{E_{\mathrm{T,corr}}}{E_{\mathrm{T},0}} = \frac{\sum_{i=1}^{N_{\mathrm{seg}}} (N_{\mathrm{seg}}\text{-}i + 1)^2}{N_{\mathrm{seg}}^3} \tag{5-4}$$

$$CF_{Rw} = \frac{R_{w,corr}}{R_{w,0}} = \frac{1}{CF_{\tau}} \sum_{i=1}^{N_{seg}} (N_{seg}\text{-}i + 1)^{-2/3} \tag{5-5}$$

As can be seen from the previous equations, all three-correction factors are functions of a single parameter: the number of segments (N_{seg}) of the multi-segment equivalent of the single-segment model. This resembles the spacing between each two consecutive water uses, assuming that all water uses are equally spaced and have equal demands. Model users can simply define a global segment length for the entire network, which is then used by the model to calculate the equivalent number of segments for each dead-end pipe by rounding up the ratio of the pipe length to the segment length. It is noteworthy that these correction factors are particularly useful for use in network optimization problems, where numerous water quality simulations are typically executed. Moreover, for large network models, the computational cost of evaluating the objective function can be very expensive. Hence, relying on these correction factors to approximate the high-level of detail required to simulate dead-end branches, while eliminating the additional complexity of such a spatially resolved representation is essential.

5.3.3 Objective function, constraints, and decision variables

The objective function is formulated with the aim of minimizing the total cost of placing, constructing, and operating the booster chlorination system, while ensuring that the residual concentrations at all network junctions are within the acceptable bounds. The objective function is formulated as the summation of the capital cost of booster system design (BCD), chlorine injection cost (BCI), and constraint violation penalty function (PEN) [11].

The operational cost of booster chlorine injection BCI ($/day) can be defined as [10]:

$$BCI = \lambda \sum_{b=1}^{n_b} \{ \sum_{i=1}^{n_i} Cl_{b,i} * \Delta t_i \} \tag{5-6}$$

where, $Cl_{b,i}$ is the chlorine mass injection dose of booster b during injection pattern interval i in (kgCl/min); n_b is the number of chlorine boosters in the design; n_i is the number of injection pattern intervals in one day (intervals/day); Δt_i is the length of the injection pattern interval i in minutes (min/interval); λ is the chlorine injection cost per unit mass of chlorine (= 2 \$/kgCl).

The capital cost of the booster chlorination system design BCD (\$/day) is written as [10]:

$$BCD = DRV(AI, BLD) \left[\sum_{b=1}^{n_b} \alpha (Cl_b^{max})^{\beta} + \gamma V_b \right] \tag{5-7}$$

where, DRV is the daily return value coefficient (day^{-1}), which is a function of AI, the annual interest rate (%), and BLD booster station life duration (years); Cl_b^{max} is the maximum injection rate (mgCl/min) of booster station b; V_b is the total injected mass (mgCl) of booster station b; and α, β and γ are empirical booster chlorination capital cost coefficients [$\alpha = 2.21\ \$(mg/min)^{-\beta}, \beta = 0.13(-), \text{and } \gamma = 0(\$/mg)$].

The penalty function for constraint violations PEN is calculated as [11]:

$$PEN = \emptyset \times \sum_{j=1}^{n_j} \{ \sum_{t=1}^{n_t} \max(C_{t,j} - C^{max}, 0) + \sum_{t=1}^{n_t} \max(C^{min} - C_{t,j}, 0) \} \tag{5-8}$$

where, $C_{t,j}$ is the residual concentration at junction j during time step t in (mg/L); n_j is the number of junctions in the system; n_t is the number of time steps during the water quality monitoring window; C^{max} is the maximum permissible concentration (= 4 mg/L); C^{min} is the minimum

required residual concentration (= 0.2 mg/L); and Ø is a constraint violation penalty coefficient of 500.

The decision variables are: (i) the locations of the chlorine boosters, and (ii) the patterns of chlorine mass injection rates for each booster. A system of five chlorine boosters is considered herein with an injection pattern interval of four hours (240 min/interval). Therefore, for each booster station, six different injection doses are determined, and hence the total number of variables is 35 (five locations + 5×6 doses). Although the mass injection rates are kept constant during the four-hour pattern interval, the outgoing concentration may change on an hourly basis since the outgoing flow rate has a pattern time step of 1 hour.

The solution scheme is depicted in Figure 5-1. The genetic algorithm (GA) function in MATLAB R2016b Optimization Toolbox™ is used to solve the optimization problem because it can handle the integer variables representing booster locations [30]. For each generation, GA creates a population of strings (population size = 100 individuals), each comprises a different combination of the decision variables, i.e. a different configuration for booster locations (integer), and injection rates (real). For each candidate solution, EPANET simulation of the hydraulics and water quality is first executed. This is followed by the execution of WUDESIM, a C++ application linked to EPANET programmer's toolkit, for the simulation of all dead-end branches of the network. The objective function is then evaluated for each solution by determining constraint violations and adding the penalty function to the capital and injection costs. The GA then performs the operations of selection, crossover, and mutation based on the fitness of each solution in the previous generation, and generates the individuals for the new generation. This process is repeated until either one of the two stopping criteria is met, namely reaching the selected maximum number

of generations (=1500 generations), or observing no improvement in the objective function for a specified number of consecutive generations (max stall generations = 150, tolerance = 10^{-6}).

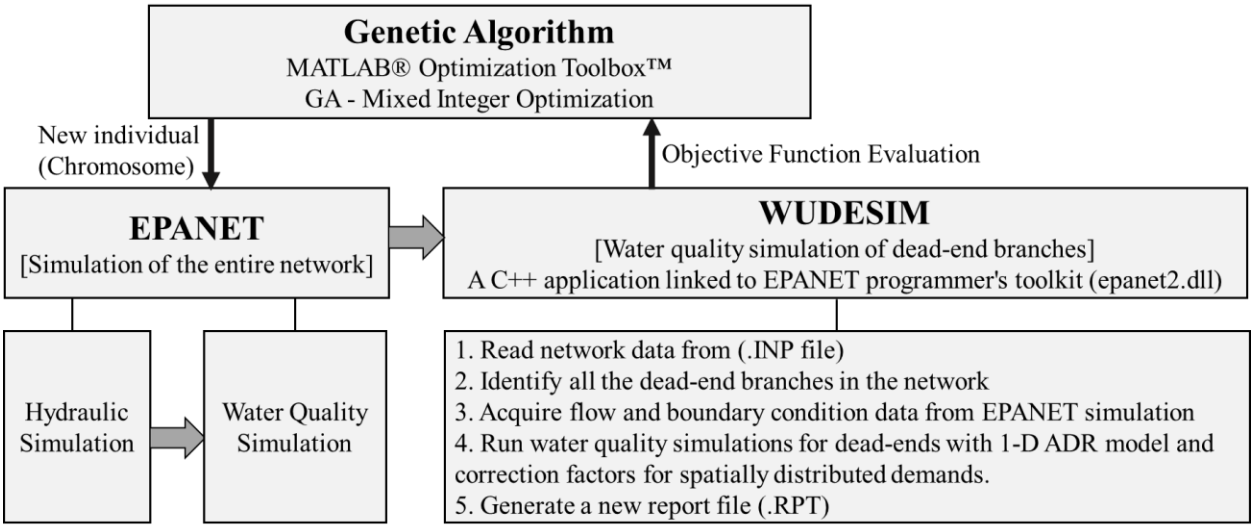

Figure 5-1. Schematic of the solution scheme.

5.3.4 Case Study Description: C-Town network

A medium-sized water distribution network, C-Town network, is used as a benchmark for examining the booster-chlorination optimization problem with both EPANET and WUDESIM. C-Town network, displayed in Figure 5-2, comprises 388 nodes connected by 429 links. The network is supplied by a single water source (Reservoir R1). Water storage and distribution across the network are supplied by seven elevated tanks (T1-T7) whose water levels control the operation of eleven pumps (PU1-PU11) grouped into five pumping stations and one control valve (V2). This network was previously used as a model water distribution system for the Battle of the Water Calibration Networks (BWCN) [37], and more recently for the Battle of the Attacks Detection Algorithms [38]. The considered network has 72 dead-end branches comprising a total of 102

links. The network consists of five district-metered areas (DMA); the nodes of each have a different water demand pattern. Chlorine decay is assumed to take place in the bulk phase with a first-order decay constant of $K_b = -0.5\ day^{-1}$, and at the pipe wall with a first-order decay constant of $K_w = -0.5\ m/day$.

The repetitive cyclical simulation (RCS) approach is adopted herein to establish periodicity in the hydraulic and water quality parameters similar to previous studies [11]. The total simulation time is chosen to be 2 weeks (336 hours) to ensure that the water quality in the system has converged into a consistent periodic cycle that is independent of the initial conditions before the start of the water quality monitoring window. The monitoring window is represented by the final 3 days (72 hours) of the simulation, during which residual chlorine concentrations are evaluated to calculate the objective function and determine constraint violations. In the calibrated network model that was given as the solution of the BWCN [37], each DMA had a 168 hours pattern, with a 1-hour time step. In this study, we reduced the length of the demand pattern to 24 hours by taking the average of the 168 hour-long pattern to achieve periodic cyclical conditions within a feasible simulation duration (14 cycles). The hydraulic and water-quality time steps are set to 1:00 hour and five minutes, respectively. Junctions with zero flow and zero concentrations throughout the simulation duration were excluded during the evaluation of the objective function.

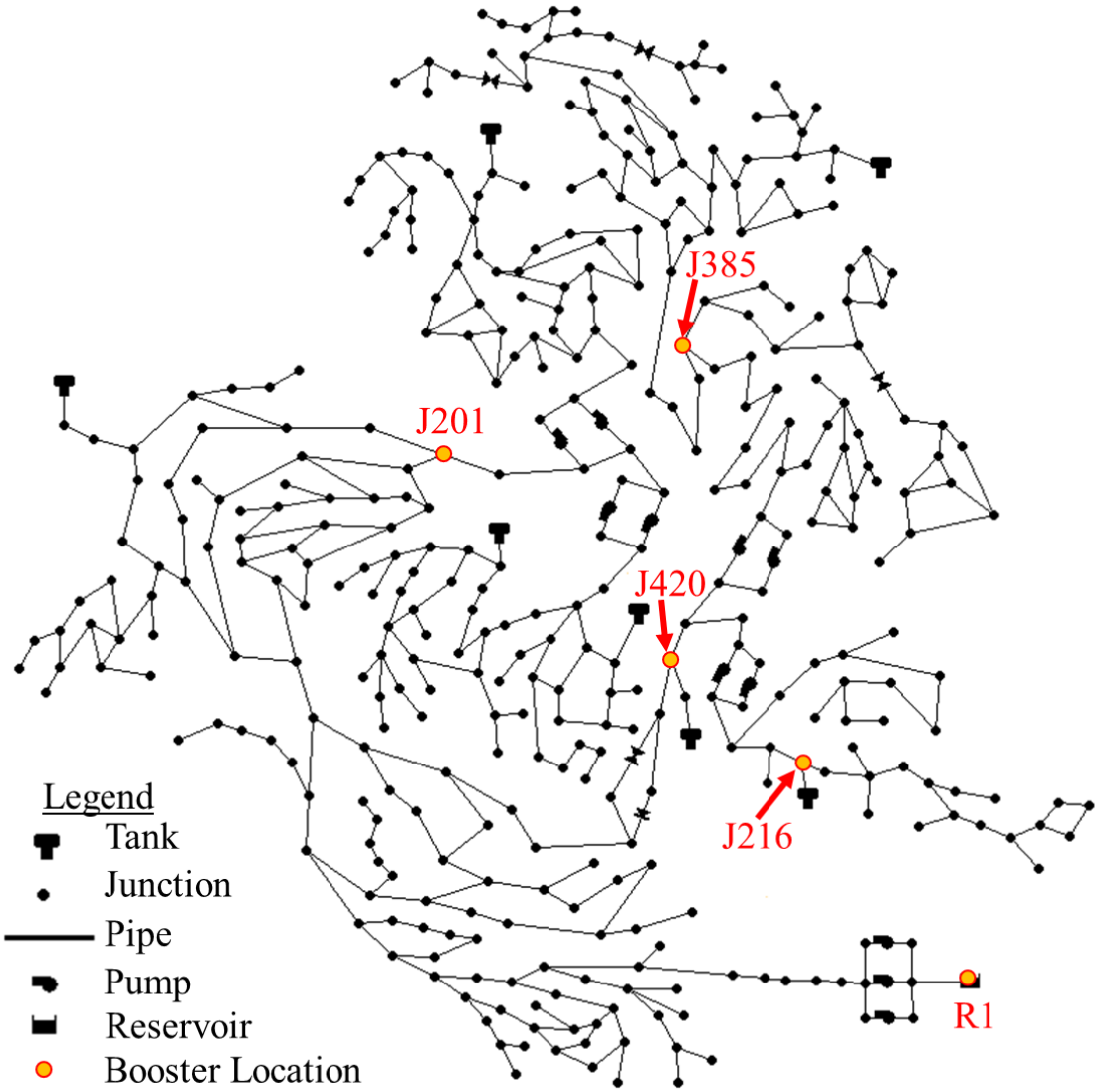

Figure 5-2. Optimal layout of booster stations using EPANET for water quality simulations.

5.4 Results and Discussion

5.4.1 Error in EPANET optimization

First, we start by optimizing the booster chlorination system by linking the Genetic Algorithm to EPANET, which is used for executing the water quality simulations of the entire network, including dead-end branches. We then conduct a water quality simulation for the optimized booster system design, this time using WUDESIM for simulating the dead-end branches, to demonstrate the deviation between the two models. We investigate the effects of considering dispersive solute transport and spatially distributed demands on optimization outcomes. This is followed by a discussion of the influence of the flow regime, and the spacing between user demands on the deviation between the two models.

EPANET optimization results

Figure 5-2 depicts the optimal layout of a booster chlorination system consisting of five booster stations in the C-TOWN network. Here, only EPANET is used to simulate the water quality in all the network pipes. The GA finds a near-feasible optimal solution, in which almost all (99.88%) of the simulated residual concentrations for the entire network, during the monitoring window, are within 0.2 and 4.0 mg/L. The total injection and capital costs as calculated by equations 6, and 7 are 111.40 $/day and 33.94 $/day, respectively. The optimal layout features a booster station located at the water source (reservoir R1), while the other four are distributed across the network. Two of the boosters are located near storage tanks, namely the boosters at junctions J420 (located near T3), and J216 (located near T2). The other two boosters (J385 and J201) are located at downstream sections of the network, mainly to boost the residual concentration at the far-end zones. Chlorine residuals simulated by EPANET for the entire network have an average

concentration of 1.45 mg/L, while junctions located on dead-end branches have a lower average concentration of 1.11 mg/L. This reflects the adverse effects of the higher water ages at these locations on the decay of the disinfectant residual, and highlights the importance of implementing an accurate water quality model for dead-end branches.

Deviation from WUDESIM simulation results

To demonstrate the effects of using EPANET compared to a more accurate water quality model for simulating dead-end branches on the resulting booster design, water quality in the dead-end links is simulated using WUDESIM for the optimal solution that was generated by EPANET in the previous step. For WUDESIM simulations, a global segment length, i.e. spacing between each two consecutive water uses, of 20 m is first selected to demonstrate the deviation between the two models. In the following section, the sensitivity of the results towards the selected segment length is examined. Figure 5-3 displays two histograms showing the distribution of the residual concentrations for all the junctions located on dead-end branches as simulated by EPANET and WUDESIM-20m. For EPANET simulation, only 0.46% of all the simulated concentrations for junctions on dead-end branches were less than 0.2 mg/L, which is slightly higher than the corresponding fraction for the entire network (0.12%). For WUDESIM-20m simulation, the fraction of violating concentrations within dead-end junctions is 6.64%, which is significantly higher than that simulated by EPANET. In addition, the average concentrations for the violating instances for EPANET and WUDESIM-20m are 0.179 mg/L and 0.123 mg/L, respectively. This implies that optimization results generated by EPANET may produce a booster chlorination system that fails to preserve the minimum residual concentration in the dead-end pipes of the water distribution system.

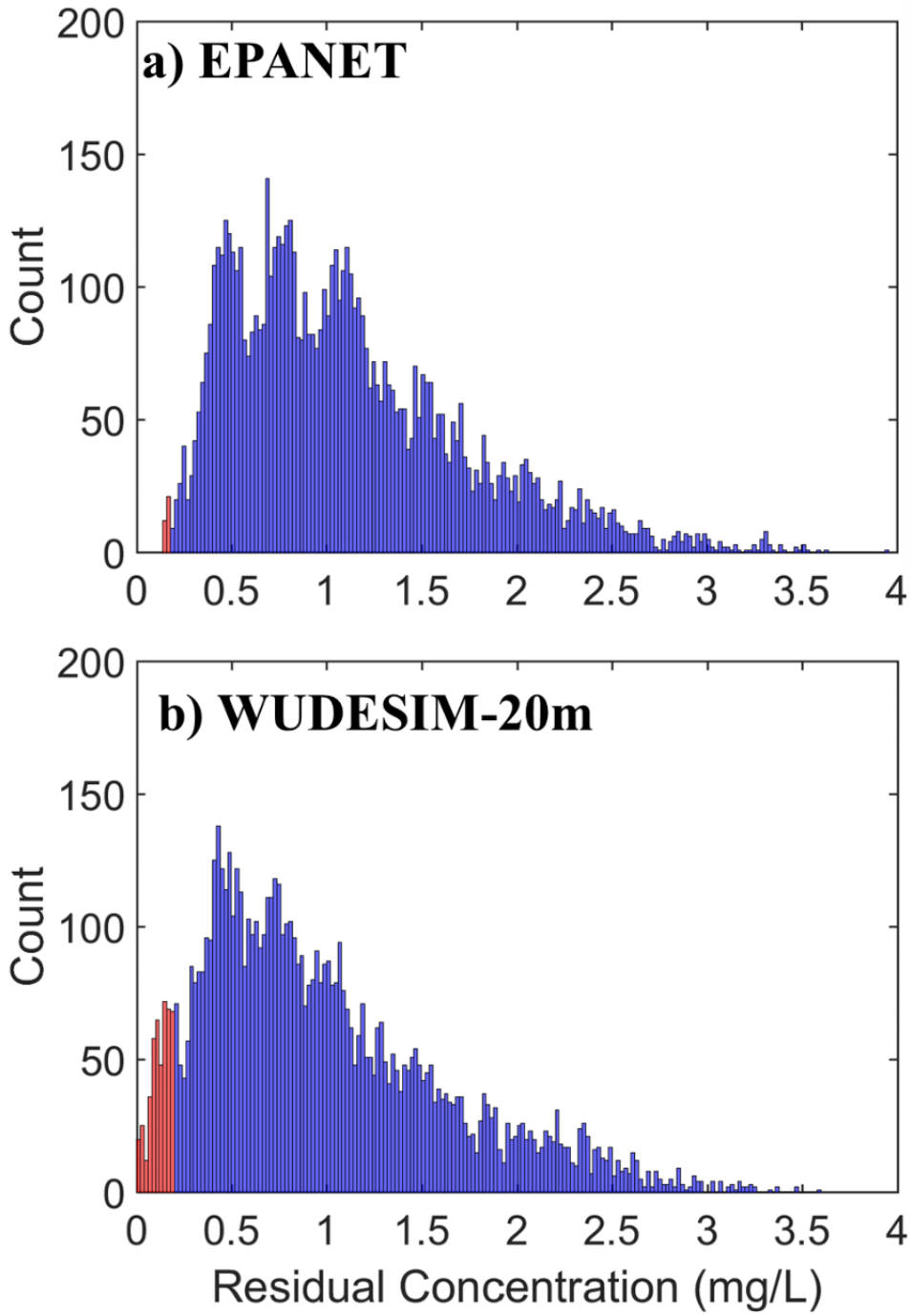

Figure 5-3. Distribution of residual concentrations for all the junctions located on dead-end branches as simulated by: a) EPNAET, and b) WUDESIM with a 20 m segment length.

The average concentration simulated by WUDESIM-20m for all dead-end junctions is 0.97 mg/L, which is 12.6% less than that simulated by EPANET. The generally lower concentrations simulated by WUDESIM compared to EPANET reveal that the main reason behind the deviation between the two models is the extended, yet more realistic, residence times simulated by WUDESIM. As previously mentioned, the aggregation of flow demands due to network skeletonization associated with EPANET results in residence times that are considerably shorter than those encountered by real-life dead-end links with spatially distributed demand uses. This is further demonstrated by plotting the residual concentration profiles as simulated by both models for two of the network junctions (J184, and J52) that featured the highest deviations between the two models (Figure 5-4).

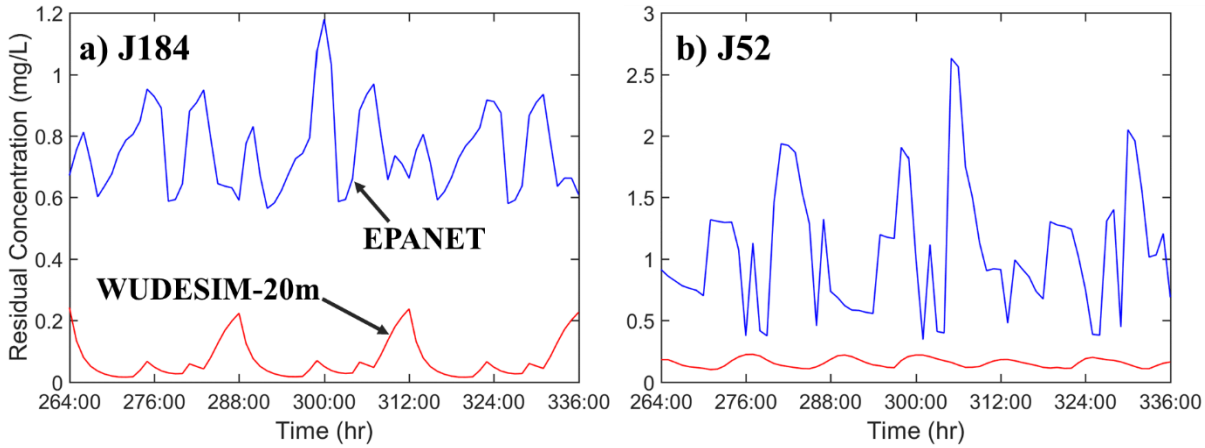

Figure 5-4. Residual concentration profiles during the window period for the two of the dead-end junctions: a) Junction J184, and b) Junction J52, as simulated by EPANET vs WUDESIM with a 20 m segment length.

The deviation is calculated herein as the normalized root mean squared deviation (nRMSD) between the hourly concentrations reported by the two models for any given junction (j):

$$\mathrm{nRMSD_j} = \frac{\sqrt{\frac{1}{n_t}\sum_{t=1}^{n_t}(C_{t,j}^{EPANET}\text{-}C_{t,j}^{WUDESIM})^2}}{\frac{1}{n_t}\sum_{t=1}^{n_t}(C_{t,j}^{WUDESIM})} \tag{5-9}$$

The first junction (J184), is the terminal junction of pipe (P776), which operates under laminar flow conditions during almost the entire simulation period, and with an average Reynolds number of ($\overline{\mathrm{Re}} = 2135.67$). Hence, longitudinal dispersion is expected to play a significant role in the transport of the disinfectant since the value of Taylor's dispersion rate under laminar conditions increases with the square of the flow velocity. It can also be seen that the concentration profile simulated by WUDESIM is somehow "smoothed" compared to EPANET, which is another evidence of the significant role of dispersive transport. Dispersion is known to cause spreading of advective wave fronts, which dampens the temporal variations in the concentrations at the terminal junction [20]. Furthermore, the length of the upstream pipe (421.07 m) is significantly longer than most of the other dead-end links (longer than 97% of all the links on dead-end branches), and is hence characterized by a long residence time ($\overline{\mathrm{R.T.}} = 5.87$ hrs), which is longer than 89% of all dead-end links in the network. This long residence time gets even longer when simulated by WUDESIM since the pipe is split into 22 segments, corresponding to the selected 20 m segment length, which results in a corrected residence time that is almost 3.7X that simulated by EPANET. The combination of the extended residence time and laminar flow conditions resulted in the strongest deviation between the two models among all the simulated dead-end junctions ($\mathrm{nRMSD_{J184}} = 10.38$).

The second highest deviation corresponds to junction J52 ($\mathrm{nRMSD}_{\mathrm{J52}} = 7.06$), which is the terminal junction of pipe P37 that has a length of 180.61 m (>82% of the dead-end links). Similarly, the flow in the upstream pipe is fairly within the laminar regime ($\overline{\mathrm{Re}} = 1167.3$), and the mean residence time is significantly longer than other dead-ends ($\overline{\mathrm{RT}} = 9.16\ \mathrm{hrs}$, longer than 97% of all dead-end links). Furthermore, when simulated by WUDESIM, this pipe is split into 10 segments, which increases the residence time by a factor of 2.93X after applying the correction factor. Similar behavior is also observed for all the junctions that displayed high deviation between the two models. On the other hand, dead-end junctions that are located downstream of links operating under high turbulent conditions, or characterized by short residence times, exhibited negligible deviations between the two models.

Error dependence on Reynolds number and segment length

In the previous section, we demonstrated that the deviation between EPANET and WUDESIM appears to be mainly dependent on two factors: flow regime, and pipe length (equivalent number of segments for the correction factors). To further investigate the effects of these two parameters on the deviation between the two models, the nRMSD of all the dead-end junctions in the network is plotted against the average Reynolds number of their upstream pipes for both the original and the corrected cases. Here, the corrected Reynolds number is equivalent to the original value multiplied by the inverse of the correction factor for residence time ($1/\ \mathrm{CF}_{\tau}$). As can be seen from Figure 5-5, the deviation between the two models appears to decrease exponentially with the Reynolds number, and the correlation is notably more pronounced when the correction factors for the residence time are factored in. Looking at Figure 5-5b, it can be clearly seen that for pipes with a corrected Reynolds number above 4,000 (i.e. turbulent regime), the deviation between the two models is negligible (nRMSD < 0.2).

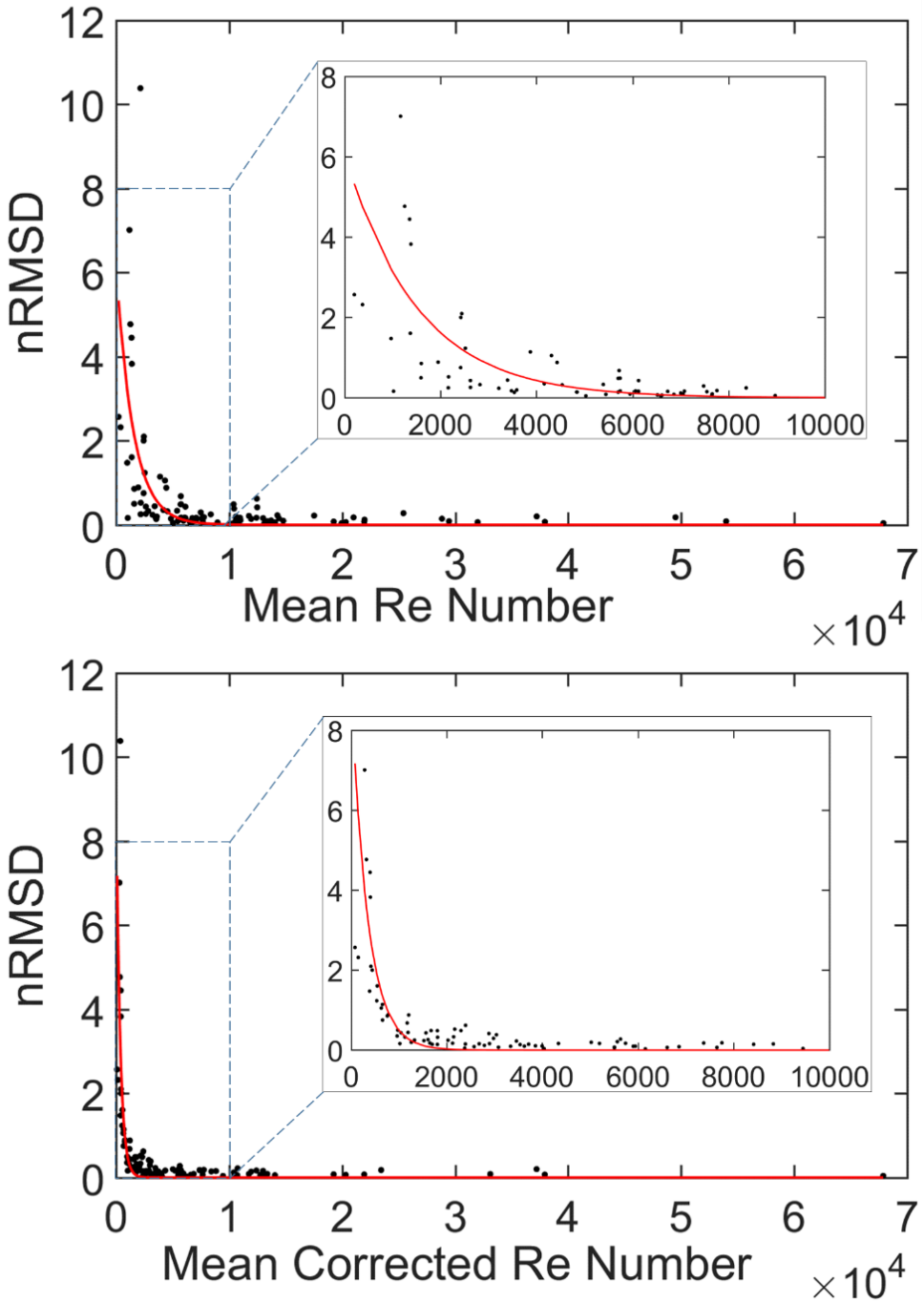

Figure 5-5. Normalized root mean squared deviation (nRMSD) between EPANET and WUDESIM with a 20 m segment length for all the simulated dead-end junctions plotted against the average Reynolds number of the upstream link before and after factoring by the correction factor for residence time.

It is also worth noting that the strong correlation observed between the nRMSD and the corrected Reynolds number is unique, and that similar correlations between the deviation and other dimensionless quantities, such as Peclet and Damkohler numbers, or other parameters, such as the residence time, corrected residence time, dispersion coefficient, or pipe length, could not be established. This indicates that the corrected Reynolds number can be used as a quick guide to determining whether WUDESIM must be executed to correct EPANET simulations of specific dead-end links. This observation is of significant value for network optimization problems that comprise numerous water quality simulations since solving the ADR transport equation is computationally more expensive compared to the simpler AR equation.

To further elucidate the role of the equivalent number of segments (or segment length) in the deviation between the two models, the cumulative distribution of the residual concentrations at dead-end junctions simulated by EPANET and WUDESIM for four different segment lengths is plotted in Figure 5-6. As can be seen from the figure, the overall concentration distribution reflects the higher concentrations simulated by EPANET compared to WUDESIM for all segment lengths. The deviation between the two models decreases consistently as the segment length increases from 15 m to 60 m. As previously mentioned, only 0.46% of all the dead-end concentrations simulated by EPANET are less than 0.2 mg/L, and the average residual concentration for dead-end junctions is 1.11 mg/L. On the other hand, the fraction of violating dead-end concentrations simulated by WUDESIM decreases from 8.6% for a segment length of 15 m, to 2.1% for a segment length of 60 m, while the mean residual concentrations of all dead-end junctions increases from 0.96 mg/L for the 15 m spacing to 1.04 mg/L for the 60 m spacing.

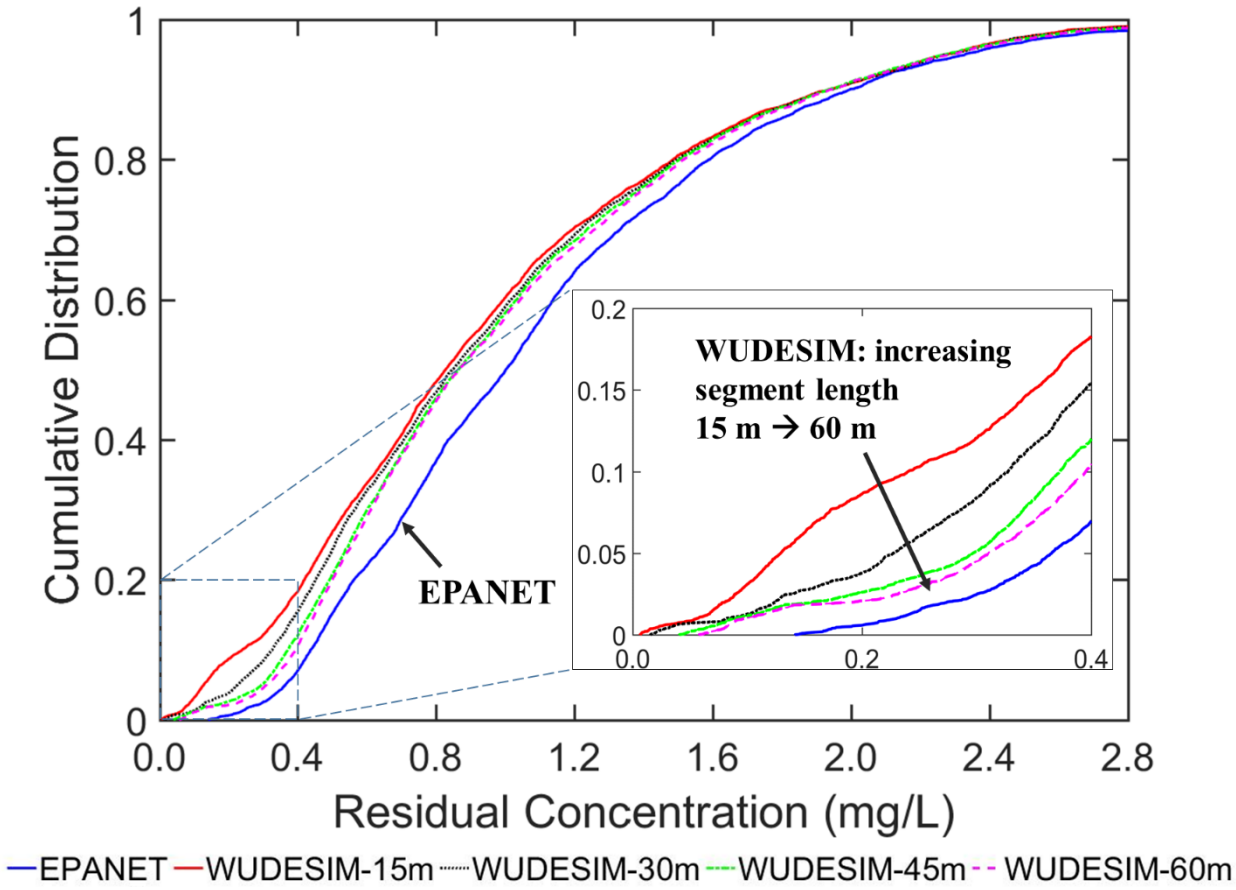

Figure 5-6. Cumulative distribution of residual concentrations at the dead-end junctions as simulated by EPANET vs WUDESIM with varying segment lengths of 15, 30, 45, and 60 meters.

5.4.2 Optimization using WUDESIM simulations

In the previous section, we demonstrated how using the more realistic water quality model (WUDESIM) to simulate the dead-end branches reveals the potential inadequacy of EPANET in designing booster systems that are capable of maintaining the minimum residual concentration at the extremities of the distribution network. To reduce the magnitude and frequency of violations, we examine two alternative approaches. First, booster locations are kept similar to those optimized using EPANET simulations, while injection doses (booster scheduling) are re-optimized using WUDESIM-20m simulations of the dead-end branches. Second, we employ WUDESIM-20m simulations to re-optimize both the layout (locations) and doses (scheduling) of the booster chlorination system. We then compare the enhancement in the booster system performance for both scenarios against the original case in which the full optimization was done using EPANET simulations.

Optimizing doses for the same booster locations

Assuming that the utility operators find that several of the dead-end branches consistently suffer from violations of the minimum residual constraint. As a first response, they examine re-optimizing the doses using WUDESIM-20m simulations for the same booster layout previously designed by EPANET. The resulting optimal schedule effectively reduces the fraction of violating concentrations for the dead-end junctions from 6.64% to 5.56%. In addition, the average concentration of the violating junctions slightly increases from 0.123 mg/L to 0.131 mg/L, while the overall concentration of dead-end junctions increases from 0.97 mg/L to 1.07 mg/L. Nevertheless, the total chlorine injection cost would increase by about 8.1% from 111.40 $/day to 120.42 $/day. This indicates that simply increasing the doses, while effective in reducing both the

frequency and magnitude of violating residual concentrations, may not be an efficient solution to alleviate all the violations, which highlights the need for re-designing the booster chlorination system with a new layout using WUDESIM.

Optimizing both doses and locations

As an alternative to optimizing only the injection doses (booster scheduling), both the layout and scheduling of the booster chlorination system are optimized using WUDESIM-20m simulation. Figure 5-7 displays the new optimal layout of the five booster stations. The new design features a booster station located at the water source (reservoir R1) similar to the previous design that employed EPANET simulations. In addition, two of the other four boosters only slightly moved from their previous locations (J420 → J287) and (J201 → J301), reflecting the importance of these two locations in controlling the residual concentration in the entire network, not just the dead-end zones. The remaining two boosters are completely moved from their original locations and are stationed at the proximity of two dead-end branches in the new layout. The first booster is located at junction J178, which is the inlet of pipe P776 that was previously found to have to the highest deviation between EPANET and WUDESIM-20m, i.e. the worst decay of the chlorine residual due to the extended residence time (Figure 5-4a). Similarly, the second booster is located at junction J142, which is the second junction upstream a relatively long dead-end branch consisting of five links with a total length of about 2 km. The total residence time of this branch is (23.5 hrs), and the nRMSD at the terminal junction of this branch (junction J144) is 1.054 (more than 87% of all dead-end junctions).

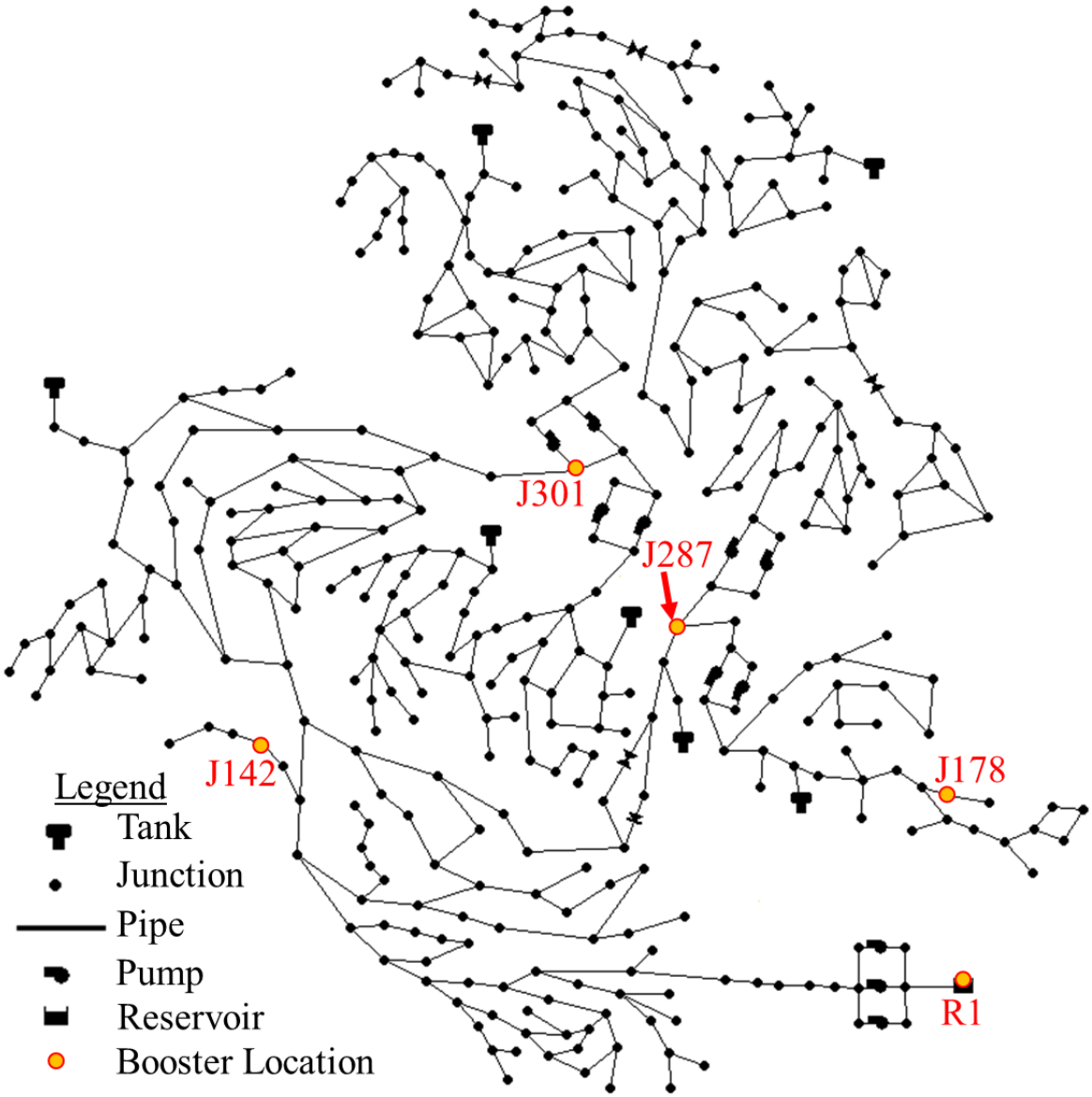

Figure 5-7. Optimal layout of booster stations using WUDESIM with a 20 m spacing length for water quality simulations.

More importantly, by re-optimizing both the layout and scheduling, the fraction of dead-end concentration violations is reduced to 4.56% compared to 5.56% for the case where only the doses are re-optimized. Furthermore, the average concentration of violating concentrations increases from 0.131 mg/L to 0.145 mg/L, and the mean residual concentration for all dead-end junctions increases from 1.07 mg/L to 1.12 mg/L. It is also noteworthy that the injection cost only increases by 1.7% from 120.42 $/day to 122.45 $/day reflecting a better distribution of the chlorination dose by re-optimizing the layout. It is important to note that, while the performance of the dead-end branches was generally enhanced by moving two of the booster stations from their original locations to the inlets of two dead-end branches, this does not affect the concentration in other non-dead-end junctions in the network and does not induce any additional violations. Moreover, the average concentration in the entire network is 1.57 mg/L, which is slightly higher than the case where only the doses are re-optimized 1.54 mg/L. This shows that considering a more accurate model for simulating the realistic residence time in dead-end branches can significantly influence the optimization results.

5.4.3 Sensitivity Analysis

To generalize the findings of this study, we consider two sensitivity analysis scenarios in which system conditions are varied from the base case considered in the previous sections. The first scenario is simulated by increasing the global chlorine decay rates, in both the bulk phase and pipe wall, by 20%. This may happen due to seasonal variations in network conditions, such as an increase in the water temperature or in the organic content of the treated water [2]. The second scenario features lowering the global flow demands in the entire network by 20%, which may happen as a result of the wide implementation of water conservation practices and the recent spread of green buildings [39,40]. For each scenario, the optimal layout of the booster chlorination system

that was previously designed using EPANET simulation (Figure 5-2) is used, while the scheduling is re-optimized by employing EPANET for water quality simulations. Afterward, WUDESIM-20m is used to simulate the re-optimized configuration to determine the constraint violations.

Effect of chlorine decay rate

In the first sensitivity analysis scenario, the global chlorine decay rates are increased by 20% to K_b = -0.6 day^{-1} and K_w = -0.6 m/day. By running an EPANET simulation of the same layout and doses from the base case, the lower concentration constraint (0.2 mg/L) is violated in 1% of the concentrations of all the network junctions, and 2.1% of those for dead-end junctions. To overcome this, booster chlorination dosing is increased by re-optimizing the scheduling of the boosters. This slightly reduces the fraction of violating concentrations within all junctions to 0.5%, and within dead-end junctions to 1.7%, while the chlorine injection cost increases by 7% form 111.3 $/day to 119.08 $/day. When the simulations are redone using WUDESIM-20m, the fraction of violating concentrations across the entire network significantly increases to 2.4%, and for dead-end junctions, it increases to 8.26%. Furthermore, the average concentration of violating dead-end concentrations drops from 0.123 mg/L for the base case to 0.114 mg/L for the high decay rate scenario. It is also noteworthy that under such scenario, the utility is restricted from increase the dosing rates above the optimized schedule to avoid violating the upper residual concentration limit (4.0 mg/L). For example, increasing the chlorination doses by only 10%, while reduces the fraction of violating concentrations to 0.3%, it results in concentrations as high as 4.5 mg/L in several of the network junctions, especially ones immediately downstream of booster locations. This demonstrates the difficulty to maintain a sufficient residual in the far-ends of the network under high chlorine decay conditions, while simultaneously respecting the upper residual constraint near the injection locations. A potential solution to this problem is to increase the number of booster

stations, which will provide better control of the water quality but at the expense of increasing the capital cost.

Effect of flow demands

In the second sensitivity analysis scenario, the global demand for all the network junctions is reduced by 20%. As a result, the average demand of the water source (reservoir R1) decreases from 170.03 LPS to 136.08 LPS. By running an EPANET water quality simulation using the same layout and doses of the base case, the upper concentration constraint (4.0 mg/L) is violated in 2.3% of the residual concentrations of all junctions. As a response, the utility operators decide to reduce the chlorine dosing rates at the pre-optimized booster locations by re-optimizing the booster chlorination schedule. This results in reducing the injection cost by 15% from 111.40 $/day to 94.84 $/day. While this effectively eliminates all high concentration violations in the network, it also results in a few violations of the lower residual constraint compared to the base case (0.39% of all network concentrations, and 1.27% of all dead-end concentrations) as predicted by EPANET simulations. This happens due to the higher water age in the network resulting from lowering the global demand, which highlights the potential implications of widespread deployment of water conservation fixtures on the overall water quality in the distribution system. Furthermore, when water quality simulations are run using WUDESIM-20m, the dead-end violations increased significantly to 10.087%, with the average concentration for violating observations of 0.10 mg/L. This indicates an even more severe deviation from EPANET predictions compared to the base scenario, and confirms the critical role played by the extended residence time in dictating the water quality in the peripheries of the network.

5.5 Conclusions

This study investigated the effects of employing an advanced water quality model on finding the optimal design of booster chlorination systems. Previous studies have generally relied on EPANET to simulate the transport and decay of disinfectant residuals in the pipes of the distribution network. Yet, EPANET was previously found to give inaccurate simulations of the residual concentrations in the dead-end branches, especially when a skeletonized (aggregated) representation of the flow demands is used. In this study, an advection-dispersion-reaction (ADR) transport model that considers the realistic spatial distribution of flow demands along the dead-end pipe is linked to a genetic algorithm to find the optimal layout and operation of booster stations. The results highlight the importance of considering dispersive solute transport, as well as the excessive residence times encountered in the dead-end sections, in the water quality simulations conducted for network optimization problems. While this study addressed the optimization of booster chlorination systems, its implications extend to a wide array of network optimization applications, including pump scheduling for water quality optimization, optimal sensor placement for reactive contaminant detection, and design of real-time boost-response systems.

5.6 Acknowledgments

Partial support from the Lucy and Stanley Lopata Endowment at Washington University in St. Louis is gratefully acknowledged.

5.7 References

[1] P. Hua, E. Vasyukova, W. Uhl, A variable reaction rate model for chlorine decay in drinking water due to the reaction with dissolved organic matter, Water Res. 75 (2015) 109–122.

[2] I. Fisher, G. Kastl, A. Sathasivan, Evaluation of suitable chlorine bulk-decay models for water distribution systems, Water Res. 45 (2011) 4896–4908.

[3] M.E. Tryby, D.L. Boccelli, M.T. Koechling, J.G. Uber, R.S. Summers, L. a Rossman, Booster chlorination for managing disinfectant residuals, J. Am. Water Works Assoc. 91 (1999) 95–108.

[4] S.L.I. Parks, J.M. VanBriesen, Booster Disinfection for Response to Contamination in a Drinking Water Distribution System, J. Water Resour. Plan. Manag. 135 (2009) 502–511.

[5] D.. Boccelli, M.E. Tryby, J.G. Uber, L.A. Rossman, M.L. Zierolf, M. Polycarpou, Optimal Scheduling of Booster Disinfection in Water Distribution Systems, J. Water Resour. Plan. Manag. 124 (1998) 99–111.

[6] M. Tryby, D. Boccelli, J. Uber, L. Rossman, Facility Location Model for Booster Disinfection of Water Supply Networks, J. Water Resour. Plan. Manag. 128 (2002) 322–333.

[7] G.R. Munavalli, M.S.M. Kumar, Optimal Scheduling of Multiple Chlorine Sources in Water Distribution Systems, J. Water Resour. Plan. Manag. 129 (2003) 493–505.

[8] M. Propato, J.G. Uber, Linear Least-Squares Formulation for Operation of Booster Disinfection Systems, J. Water Resour. Plan. Manag. 130 (2004) 53–62.

[9] T.D. Prasad, G.A. Walters, D.A. Savic, Booster disinfection of water supply networks: Multiobjective approach, J. Water Resour. Plan. Manag. 130 (2004) 367–376.

[10] A. Ostfeld, E. Salomons, Conjunctive optimal scheduling of pumping and booster chlorine injections in water distribution systems, Eng. Optim. 38 (2006) 337–352.

[11] Z. Ohar, A. Ostfeld, Optimal design and operation of booster chlorination stations layout in water distribution systems, Water Res. 58 (2014) 209–220.

[12] A. Maheshwari, A.A. Abokifa, R.D. Gudi, P. Biswas, Two-Point Constraint Control of Water Quality in Distribution Networks, in: CCWI 2017 – Comput. Control Water Ind., 2017.

[13] N. Islam, R. Sadiq, M.J. Rodriguez, Optimizing Locations for Chlorine Booster Stations in Small Water Distribution Networks, J. Water Resour. Plan. Manag. 143 (2017) 4017021.

[14] A. Maheshwari, A.A. Abokifa, R.D. Gudi, P. Biswas, Co-ordinated, Decentralization based Optimization of Disinfectant Dosing in Large Scale Water Distribution Networks, J. Water Resour. Plan. Manag. (2018) Accepted.

[15] H. Mala-Jetmarova, N. Sultanova, D. Savic, Lost in optimisation of water distribution systems? A literature review of system operation, Environ. Model. Softw. 93 (2017) 209–254.

[16] L.A. Rossman, R.M. Clark, W.M. Grayman, Modeling Chlorine Residuals In Drinking Water Distribution Systems, J. Environ. Eng. 120 (1994) 803–820.

[17] P. Romero-Gomez, C.Y. Choi, Axial Dispersion Coefficients in Laminar Flows of Water-

Distribution Systems, J. Hydraul. Eng. 137 (2011) 1500–1508.

[18] O.N. Ozdemir, A.M. Ger, Realistic numerical simulation of chlorine decay in pipes, Water Res. 32 (1998) 3307–3312.

[19] H.A. Basha, L.N. Malaeb, Eulerian-Lagrangian Method for Constituent Transport in Water Distribution Networks, J. Hydraul. Eng. 133 (2007) 1155–1166.

[20] Z. Li, S.G. Buchberger, V. Tzatchkov, Importance of Dispersion in Network Water Quality Modeling, in: Proc. World Water Environ. Resour. Congr. 2005, 2005: pp. 1–12.

[21] D.H. Axworthy, B.W. Karney, Modelling low velocity/high dispersion flow in water distribution systems, J. Water Resour. Plan. Manag. 122 (1996) 218–221.

[22] V.G. Tzatchkov, A.A. Aldama, F.I. Arreguin, Advection-Dispersion-Reaction Modeling in Water Distribution Networks, J. Water Resour. Plan. Manag. 128 (2002) 334–342.

[23] V.C.F. Dias, M.C. Besner, M. Prévost, Predicting water quality impact after district metered area implementation in a full-scale drinking water distribution system, J. Am. Water Works Assoc. 109 (2017) E363–E380.

[24] B. Barbeau, V. Gauthier, K. Julienne, A. Carriere, Dead-end flushing of a distribution system: Short and long-term effects on water quality, J. Water Supply Res. Technol. 54 (2005) 371–383.

[25] R. Galvin, Eliminate Dead-End Water, OPFLOW - AWWA Mag. 37 (2011) 20–21.

[26] P. Biswas, C. Lu, R.M. Clark, A model for chlorine concentration decay in pipes, Water Res. 27 (1993) 1715–1724.

[27] H. Der Yeh, S. Bin Wen, Y.C. Chang, C.S. Lu, A new approximate solution for chlorine concentration decay in pipes, Water Res. 42 (2008) 2787–2795.

[28] A.A. Abokifa, Y.J. Yang, C.S. Lo, P. Biswas, Investigating the role of biofilms in trihalomethane formation in water distribution systems with a multicomponent model, Water Res. 104 (2016) 208–219.

[29] E. Price, A. Ostfeld, Optimal Pump Scheduling in Water Distribution Systems Using Graph Theory under Hydraulic and Chlorine Constraints, J. Water Resour. Plan. Manag. 142 (2016) 4016037.

[30] Z. Ohar, O. Lahav, A. Ostfeld, Optimal sensor placement for detecting organophosphate intrusions into water distribution systems, Water Res. 73 (2015) 193–203.

[31] A. Seth, K.A. Klise, J.D. Siirola, T. Haxton, C.D. Laird, Testing Contamination Source Identification Methods for Water Distribution Networks, J. Water Resour. Plan. Manag. 142 (2016) 4016001.

[32] G. Farina, E. Creaco, M. Franchini, Using EPANET for modelling water distribution systems with users along the pipes, Civ. Eng. Environ. Syst. 31 (2014) 36–50.

[33] A. Menapace, D. Avesani, M. Righetti, A. Bellin, G. Pisaturo, Uniformly Distributed Demand EPANET Extension, Water Resour. Manag. 32 (2018) 2165–2180.

[34] A.A. Abokifa, Y.J. Yang, C.S. Lo, P. Biswas, Water quality modeling in the dead end sections of drinking water distribution networks, Water Res. 89 (2016) 107–117.

[35] Z. Li, Network Quality Modeling with Stochastic Water Demands and Mass Dispersion,

PhD Dissertation, University of Cincinnati, Cincinnati, Ohio, USA, 2006.

[36] G. Taylor, Dispersion of Soluble Matter in Solvent Flowing Slowly through a Tube, Proc. R. Soc. A Math. Phys. Eng. Sci. 219 (1953) 186–203.

[37] A. Ostfeld, E. Salomons, L. Ormsbee, J.G. Uber, C.M. Bros, P. Kalungi, R. Burd, B. Zazula-Coetzee, T. Belrain, D. Kang, K. Lansey, H. Shen, E. McBean, Z.Y. Wu, T. Walski, S. Alvisi, M. Franchini, J.P. Johnson, S.R. Ghimire, B.D. Barkdoll, T. Koppel, A. Vassiljev, J.H. Kim, G. Chung, D.G. Yoo, K. Diao, Y. Zhou, J. Li, Z. Liu, K. Chang, J. Gao, S. Qu, Y. Yuan, T.D. Prasad, D. Laucelli, L.S. Lyroudia Vamvakeridou, Z. Kapelan, D. Savic, L. Berardi, G. Barbaro, O. Giustolisi, M. Asadzadeh, B.A. Tolson, R. McKillop, Battle of the water calibration networks, J. Water Resour. Plan. Manag. 138 (2012) 523–532.

[38] R. Taormina, S. Galelli, N.O. Tippenhauer, E. Salomons, A. Ostfeld, D.G. Eliades, M. Aghashahi, R. Sundararajan, M. Pourahmadi, M.K. Banks, B.M. Brentan, E. Campbell, G. Lima, D. Manzi, D. Ayala-Cabrera, M. Herrera, I. Montalvo, J. Izquierdo, E. Luvizotto, S.E. Chandy, A. Rasekh, Z.A. Barker, B. Campbell, M.E. Shafiee, M. Giacomoni, N. Gatsis, A. Taha, A.A. Abokifa, K. Haddad, C.S. Lo, P. Biswas, M.F.K. Pasha, B. Kc, S.L. Somasundaram, M. Housh, Z. Ohar, The Battle of the Attack Detection Algorithms: Disclosing Cyber Attacks on Water Distribution Networks, J. Water Resour. Plan. Manag. Accepted (2018).

[39] W.J. Rhoads, A. Pearce, A. Pruden, M.A. Edwards, Anticipating the Effects of Green Buildings on Water Quality and Infrastructure, Journal-American Water Work. Assoc. 107 (2015) 50–61.

[40] W.J. Rhoads, A. Pruden, M.A. Edwards, Survey of green building water systems reveals elevated water age and water quality concerns, Environ. Sci. Water Res. Technol. 2 (2016) 164–173.

Chapter 6

Chloroform Formation Mechanism from the Chlorination of Resorcinol as a Model Humic Precursor: Insights from Quantum Chemical Calculations

To be submitted.

6.1 Abstract

Reactions between chlorine-based disinfectants and the different fractions of natural organic matter leading to the formation of disinfection byproducts (DBPs) are not very well understood due to the complexity of the aquatic humic material. The majority of the kinetic models developed to describe the formation of DBPs are based on empirical or semi-empirical equations derived by regression analysis from experimental measurements. Recent studies focused on identifying the propensity of different individual components of the organic matrix to form certain DBPs. This study proposes employing first-principles calculations to investigate the molecular mechanisms of trihalomethane formation from the chlorination of model humic precursors. Quantum chemical computations are used to explore the reaction mechanism, and to study the kinetics and thermodynamics of the reaction pathways. The proposed framework is demonstrated by elucidating the chlorination mechanism of resorcinol (1,3-dihydroxybenzene), which has been identified in the literature as an efficient surrogate precursor for the formation of chloroform. Computational results bring new insights into the structures of intermediates and transition states, kinetics of the elementary reactions along the mechanism, and identifying the dominant formation pathways.

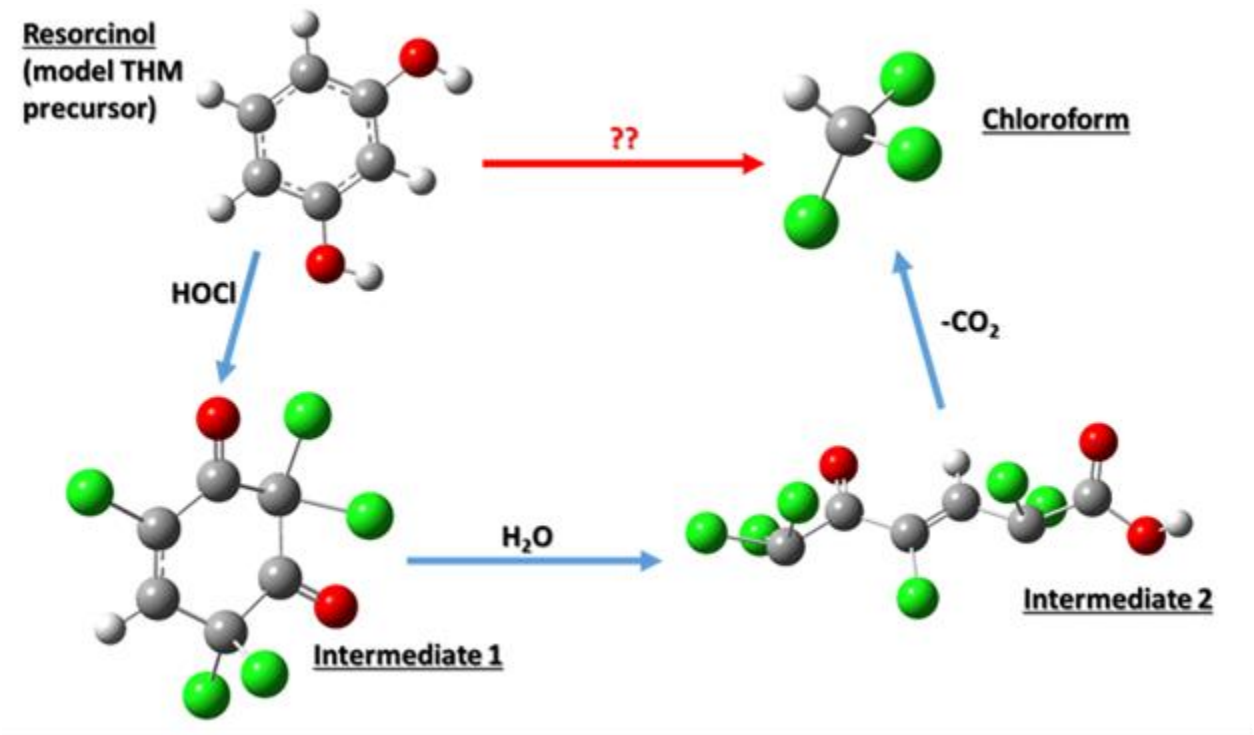

Figure 6-1. Graphical abstract of the work presented in Chapter 6. Investigating the pathways of chloroform formation from the chlorination of resorcinol as a model humic precursor.

6.2 Introduction

The formation of disinfection byproducts (DBPs) is influenced by a wide variety of factors, including the disinfectant type and dose, organic matrix, pH, temperature, bromide concentration, and contact time. The quantity of natural organic matter (NOM) generally reflects the amount of precursor material in the water matrix, which is typically measured through various representative parameters, such as the total or dissolved organic carbon (TOC/DOC) or the ultraviolet absorbance at 254 nm (UV254), to assess DBPs formation potential. However, NOM consists of a heterogeneous and complex array of precursor compounds; each has different reaction kinetics, mechanisms, and pathways for DBPs formation.

For instance, humic fractions of NOM were found to have a higher yield of trihalomethane (THM) compounds compared to the fulvic fraction. Similarly, the hydrophobic fractions were consistently found to produce higher THM concentrations. Hence, due to the complexity and uncertainty of the reactions between chlorine-based disinfectants and the organic matrix, the majority of the kinetic models developed to describe DBPs formation are based on empirical or semi-empirical equations derived by regression analysis (Brown et al., 2011). These relationships often include empirical parameters that require fitting to experimental data. Hence, none of these models can be classified as a purely “predictive” model that can be applied to new systems.

Since the reactivity of organic substrates strongly depends on the presence of certain moieties in their molecules, recent studies focused on identifying the propensity of different individual components of the organic matrix to form certain DBPs (Yang, 2017). For instance, an increase in the electron-rich aromatic content of NOM was found to correlate with higher THMs formation. Such studies demonstrate the strong potential for the development of analytically

derived mechanistic models to predict DBPs formation via developing a molecular understanding of the reaction mechanisms and kinetics (Lebedev et al., 2004).

Ab-initio quantum chemical calculations can provide a valuable tool for exploring the chemical reaction pathways by identifying transient species, kinetic, and thermodynamic information. The objective of this chapter is to propose a framework for implementing first-principles calculations to derive theoretical models for the formation of disinfection byproducts. This framework is demonstrated by investigating the mechanisms of THM formation from the halogenation of dihydroxy aromatic precursor compounds. Particularly, this study is focused on outlining the detailed reaction pathway for m-dihydroxybenzene structures (resorcinol-like structures), which have been identified as efficient precursors for THM formation. Rate coefficients of rate-limiting elementary reactions are calculated from transition state theory (TST) and the minimum-energy path (MEP) is obtained using the intrinsic reaction coordinate (IRC) calculations for each of the elementary reactions along the pathway. The proposed approach can be expanded to investigate the reaction mechanisms of other model precursors, which can pave the road towards creating mechanistic DBP formation of a true predictive nature. A complete understanding of the processes leading to DBP formation has the potential to optimize the predictions of DBP formation and to lead to improved DBP control strategies (Arnold et al., 2008).

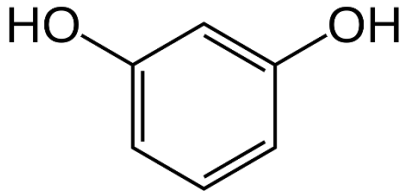

Figure 6-2. Resorcinol (1,3-dihydroxybenzene) as a model humic precursor

6.3 Methodology

6.3.1 Resorcinol like structures as model precursors

Structures related to 1,3-dihydroxybenzenes (1,3-benzenediols), such as, resorcinol and orcinol, were found to be the most efficient precursors of $CHC1_3$ formation by multiple previous studies (Arnold et al., 2008; Bond et al., 2009; Bond and Graham, 2017; Deborde and von Gunten, 2008; Heasley et al., 2004; Rebenne et al., 1996). They could possibly be responsible for the fast reacting fraction of THM precursors, which represents 15–30% of the THM precursors of natural waters (Bond et al., 2012; Gallard and Von Gunten, 2002). Hence, several previous studies focused on understanding the reaction mechanism of resorcinol, as a model precursor compound, with chlorine to understand the formation of trihalomethane compounds.

The concentration of free chlorine residual is the summation of both hypochlorous acid (HOCl) and hypochlorite ion (OCl^-). The pKa of HOCl is approximately 7.53, hence at neutral pH, ca. 80% of the free chlorine exists in the protonated form, which is a strong electrophile that is known to participate in addition and substitution reactions with a variety of organic molecules. Analysis by GC/MS showed that l,3-aromatic diols were converted to several metastable trichloro-substituted intermediates during reaction with chlorine in acidic and neutral solution, which were subsequently decomposed to $CHC1_3$. While these studies have identified several important mechanisms for the formation of trihalomethane, many details of the conversion of these substrates to trihalomethanes require clarification. Chlorination of functional groups in NOM leads to a variety of coexisting chlorinated compounds via multistep, parallel reactions. Furthermore, a reaction-specific characterization of NOM, which includes key intermediates resulting in THM formation, is still lacking.

6.3.2 Proposed Mechanism of Resorcinol Chlorination

The only in-depth investigation of the reaction pathway was conducted by (Boyce and Hornig, 1983), in which the conversion of 1,3-dihydroxyaromatic precursors to THMs was systematically investigated by GC/MS. They proposed that the reaction mechanism occurs in two stages: (1) extensive incorporation of halogen by electrophilic substitution and addition processes, followed by (2) a complex series of hydrolysis and decarboxylation steps leading to $CHC1_3$ formation via carbon-carbon bond cleavage about the C_2-site of the aromatic ring (Figure 6-3).

It is well established that phenolic compounds react with bromine or chlorine by either oxidation (electron transfer, ET) or electrophilic aromatic substitution (EAS) processes. The dominant process mainly depends on the relative position of the hydroxyl substituents and the possibility of quinone formation (Criquet et al., 2015). Hence, the presence of an unsubstituted carbon atom at the ortho-position with respect to both phenolic hydroxyl substituents seems to be required for the efficient reaction of 1,3-aromatic diols such as resorcinol. The observations by (Boyce and Hornig, 1983) are indicative of an electrophilic substitution in the aromatic ring, which is highly favored when both OH groups are located at an appropriate orientation to stabilize the transition state of the reaction through the donation of electron density.

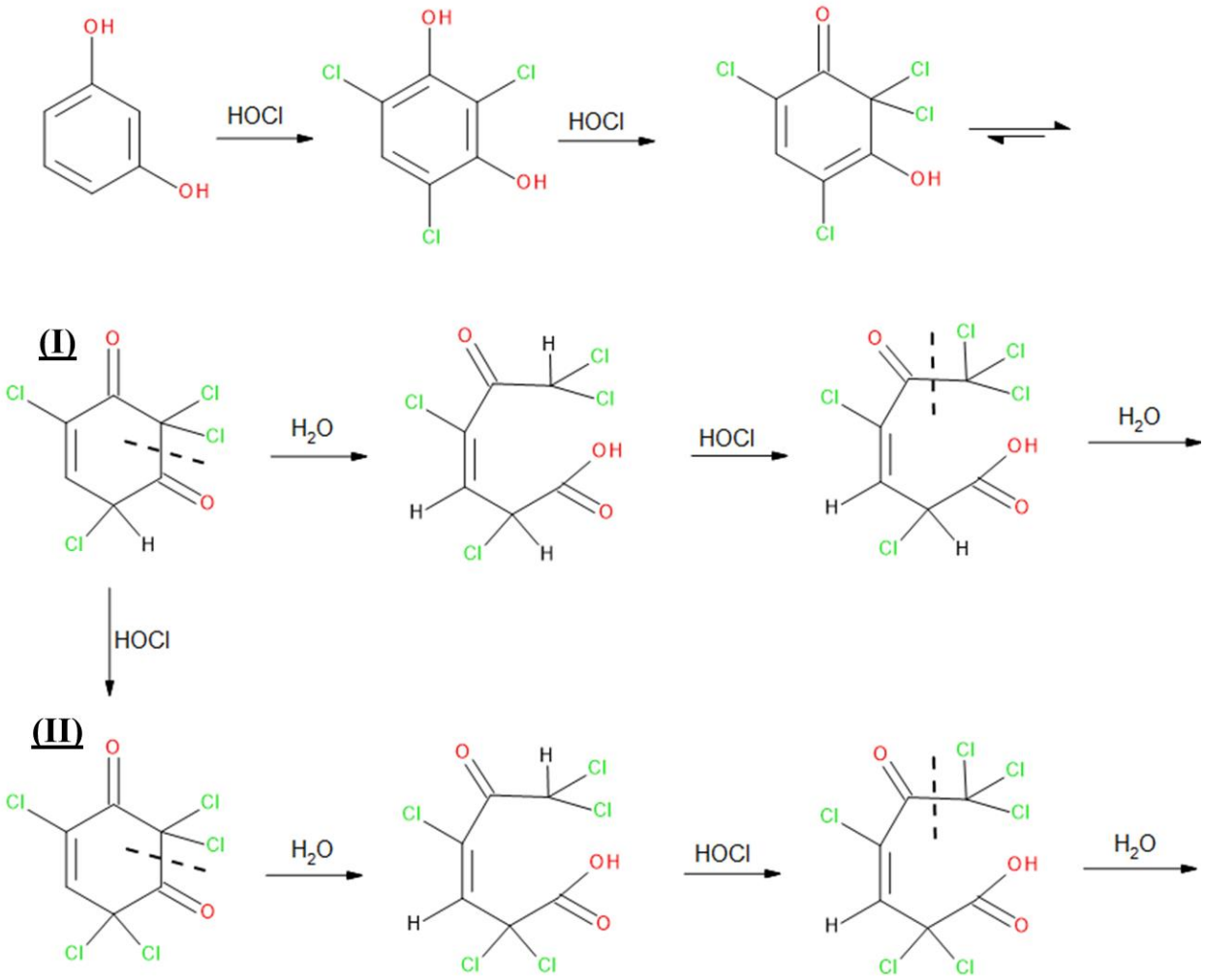

Figure 6-3. Simplified reaction pathway for the conversion of 1,3-dihydroxyaromatic substrates to $CHCl_3$ as proposed by (Boyce and Hornig, 1983).

The proposed reaction scheme involves the following four basic stages:

1- Initially, multiple steps of electrophilic substitution in resorcinol take place yielding trichloro-l,3-dihydroxybenzene:

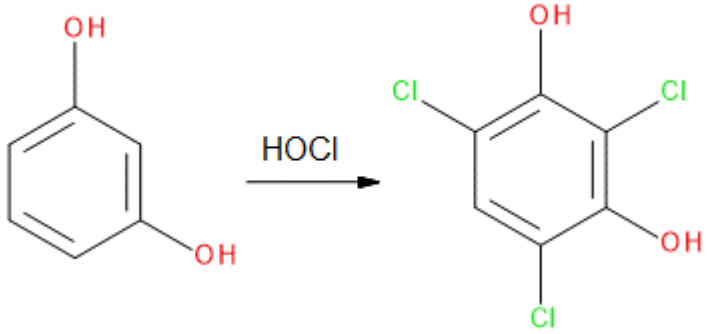

2- Further addition of chlorine forms the cyclohexenedione intermediates, which can be either tetrachloro (I in Figure 6-3) or pentachloro (II in Figure 6-3). This is followed by hydrolysis and oxidative ring cleavage on either side of the 3- position of the ring structure.

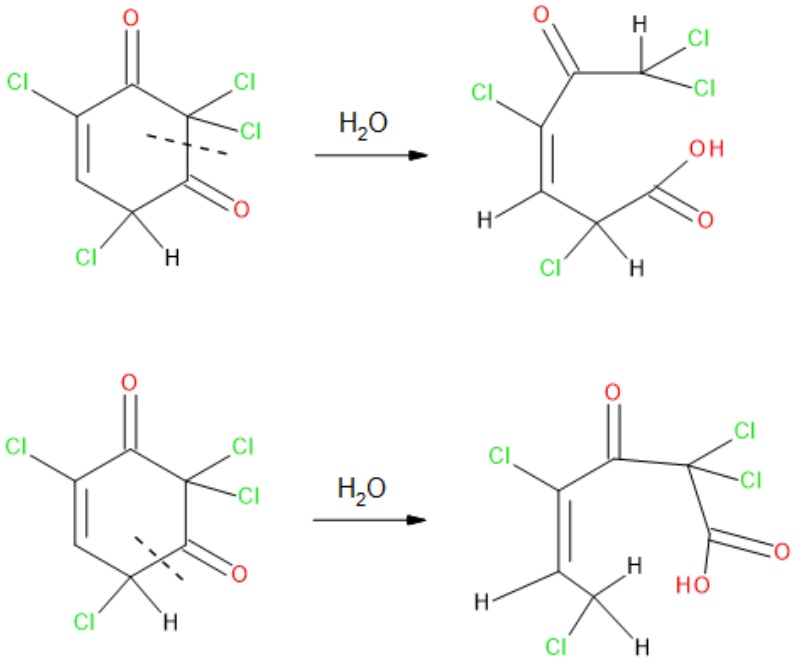

3- The reaction then proceeds by a complex series of decarboxylation of the resulting keto-carboxylic acids, which is accompanied by the incorporation of chlorine.

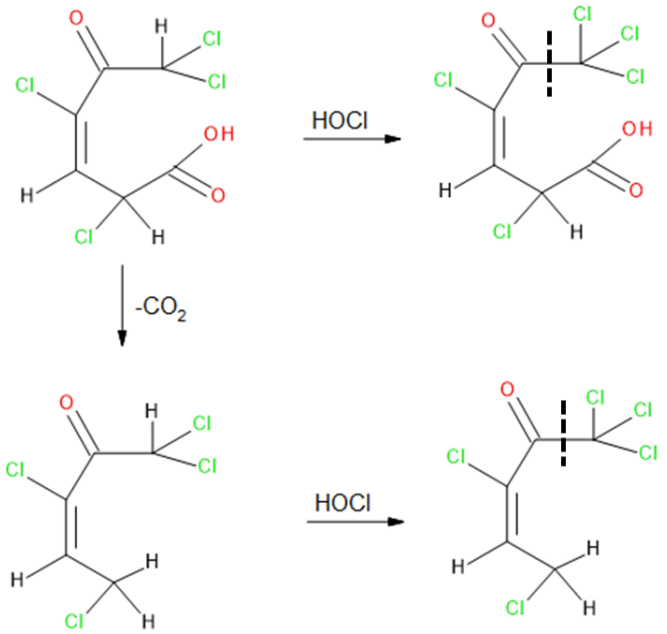

4- The final step is usually base-catalyzed hydrolysis of the resulting chlorinated ketones (or keto carboxylic acids) to form chloroform.

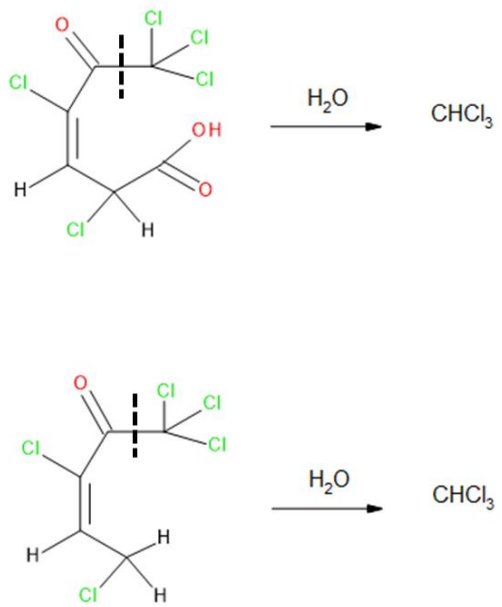

A similar process of electrophilic substitution, followed by multiple steps of hydrolysis and decarboxylation was also proposed by (Heasley et al., 1989). In their study, it was concluded that the 4- (or 6-) position is about 1.5 times more reactive for electrophilic substitution than the sterically hindered 2-position (the position between the hydroxyl groups). They tetrachloro intermediate (I in Figure 6-3) that follows the initial electrophilic substitution on the reaction pathway was not detected. Hence, they concluded that it is rapidly converted to the pentachloro intermediate (II in Figure 6-3), which in turn undergoes immediate ring-cleavage to produce $CHC1_3$ and other products after a series of decarboxylation, Cl incorporation, and hydrolysis.

Gaps in the Proposed Mechanism

Although a concerted effort has been made in the previous studies to outline the possible reaction mechanisms leading to chloroform formation, a clear understanding of the thermodynamics and kinetics is still missing. A few clear gaps in the proposed mechanism are outlined below:

1- The mechanism proposes multiple probable pathways to chloroform formation, without discussing which pathway is expected to dominate the reaction. For example:

- Is ring cleavage by hydrolysis more favorable for the tetrachloro or the pentachloro cyclohexenedione intermediates?
- On which side of C_3 site in the aromatic ring is the cleavage more favorable?
- In what order do the decarboxylation and Cl incorporation reactions happen after ring cleavage?

2- The mechanism proposes the presence of several short-lived intermediates along the reaction pathway that were not directly measured by GC/MS. Hence, a complete understanding of the mechanism is missing.

3- In each pathway, how does the kinetics of each of the three main stages (electrophilic substitution, hydrolysis, and decarboxylation) compare?

4- In each pathway, which of the proposed elementary reaction steps is rate limiting?

Investigating the pathway with first principles calculations

In this study, we propose a framework for employing first-principles calculations to investigate the mechanisms of the chemical reactions leading to the formation of disinfection byproducts. The previously proposed pathway of chloroform formation from the chlorination of resorcinol is investigated by means of quantum chemical calculations. Using density functional theory (DFT), both the thermodynamics and kinetics of the elementary reaction steps along the pathway are modeled, allowing the evaluation of the detailed mechanism.

Particularly, we aim to verify the presence of the proposed intermediate structures involved in the mechanism, and to determine which one of the three steps (electrophilic substitution, hydrolysis, and decarboxylation) is rate limiting. In addition, computational results bring new insights into the electronic nature, chemical equilibria, and kinetics of the elementary reactions of this pathway, enabled by computed energies of structures that are not possible to access experimentally (Bond and Graham, 2017; Liu et al., 2014; Liu and Zhong, 2017; Trogolo et al., 2015; Yu et al., 2017; Zhang et al., 2014).

6.3.3 Computational Methods

Density functional theory (DFT) calculations are performed by using the B3LYP method (Becke's three-parameter functional with the correlation functional of Lee, Yang, and Parr), in conjunction with the 6-31+G(d) basis set. The findings of (Boyce and Hornig, 1983) are used to postulate the potential reactants and products, and their associated intermediates along the reaction pathway. Each proposed reaction is examined using DFT models to evaluate its kinetics and thermodynamics. In the proposed pathway, all structures of the reactants, transition states, and products involved in the formation reactions of chloroform during chlorination of resorcinol are fully optimized. Vibrational frequencies are calculated at the same level of theory to characterize the nature of the stationary points as minima (no imaginary frequency) or transition states (only one imaginary frequency). All computations are carried out with the GAUSSIAN-09 suite of programs (g09)

The minimum-energy path (MEP) for each reaction is obtained using intrinsic reaction coordinate (IRC) calculations to confirm the connection of each transition state with the designated reactants/products. Since aqueous solvent effects are expected to play an important role in the reaction thermodynamics and kinetics, the solvent effect of water on the reactions of chloroform formation from resorcinol are considered by conducting the optimization and frequency calculations with the polarizable continuum model (PCM) using the integral equation formalism variant (IEF-PCM) in conjunction with the B3LYP/6-31+G(d) level of theory.

For a given reaction step, minimum energy pathway (MEP) calculations are used to estimate the free energy of activation, defined as the difference between the estimated highest free energy value along the profile of the reaction coordinate and the free energy of the preceding stable reactant or stable intermediate structure. Gibbs free energies of reactions (ΔG_r) are hence

calculated as ($\Delta G_{products} - \Delta G_{reactants}$), while activation free energy barriers ($\Delta G^{\ddagger}$) are calculated as ($\Delta G_{TS} - \Delta G_{reactants}$). Approximate reaction rate constants are estimated from computed activation free energies based on transition state theory and the Eyring−Polanyi equation to estimate a transition-state theory (TST) rate constant:

$$k_{TST} = \frac{k_B T}{h} \exp\left(\frac{-\Delta G^{\ddagger}}{RT}\right) \qquad (6\text{-}1)$$

6.4 Results and Discussion

Assuming that the electrophilic substation in the aromatic ring proceeds fairly quickly, the focus here is on the reaction pathway following ring cleavage. The first, and perhaps the most import, question here is: at what site does ring opening take place? In their proposed mechanism, Boyce and Hornig, 1983 suggested two different locations for the hydrolysis and oxidative ring cleavage as depicted in Figure 6-4 for both the tetra- and penta- chloro cyclohexedione intermediates. In both cases, ring opening is proposed to take place around the 3- position to yield carboxy enolate intermediates that proceed to form their corresponding keto carboxylic acids.

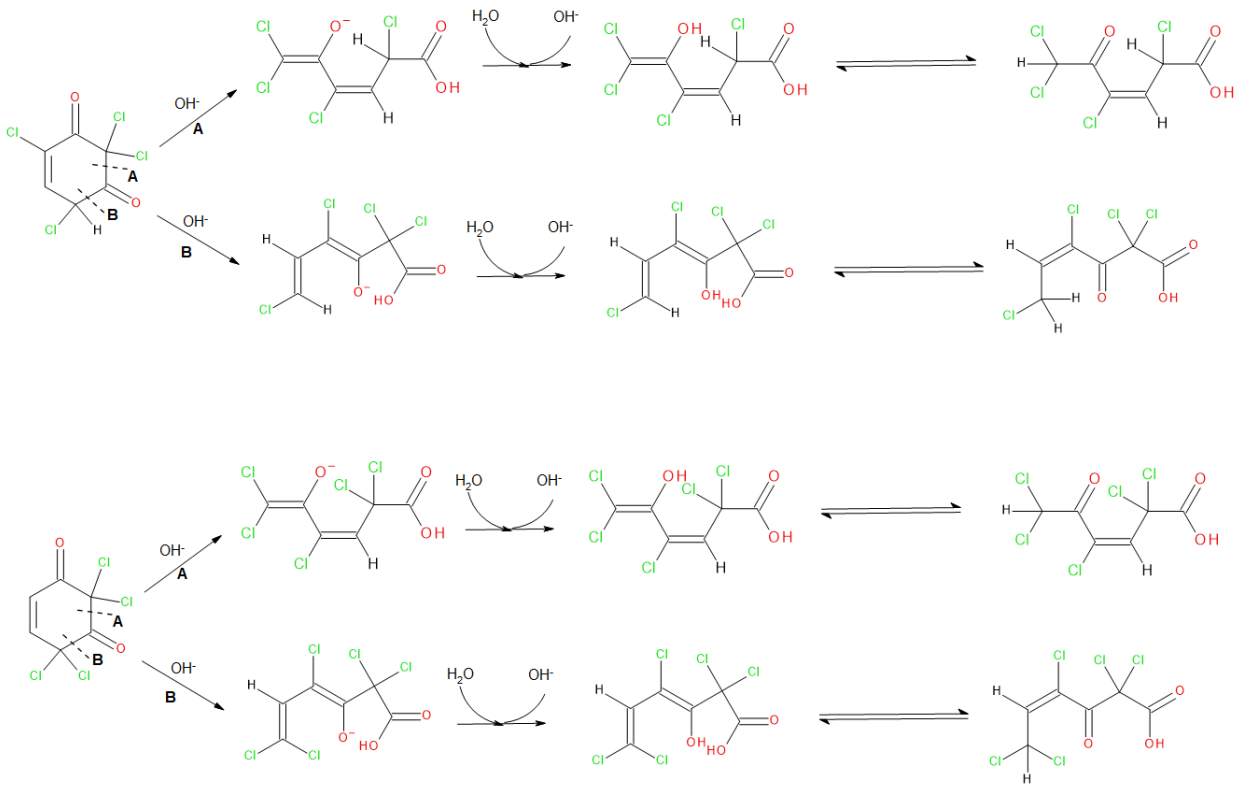

Figure 6-4. Proposed reaction pathways for ring cleavage around the 3- position of the tetra- and penta- chloro hexenediones

Table 6-1 summarizes the energetics for both the tetra- and penta- choloro rings as calculated at the B3LYP/6-31+g(d) level of theory. As can be seen from the results, the first step of ring cleavage to form the enolate intermediate is thermodynamically favorable for ring cleavage at either the A (between the 2- and 3- position) or B (between the 3- and 4- position) locations. For both the tetra- and penta- chloro cases, ring cleavage at the B location is thermodynamically more favorable than the A location. The reason is likely the interaction between the oxyanion of the enolate intermediate with the proton from the nearby hydroxyl group, which stabilizes the intermediate formed from B-cleavage compared to A-cleavage. However, the second step on the reaction pathway that leads to the formation of the enol intermediate from the protonation of the enolate oxyanion is found to be thermodynamically unfavorable for all the studied pathways.

Nevertheless, the overall reaction combining both steps is still thermodynamically favorable for the ring cleavage at the A position but not at the B position. These results suggest that the ring cleavage at the A-position proceeds via a concerted reaction mechanism rather than a step-wise mechanism, and that the formation of the enol from the enolate intermediate is not thermodynamically favorable (Figure 6-5). The third step involving the formation of the keto-carboxylic acids is found to be thermodynamically favorable for all cases.

Table 6-1. Reaction energies and activation free energies (at 298 K and 1 atm) in kcal/mol

	Open ring A	ΔG_r (kcal/mol)	Open ring B	ΔG_r (kcal/mol)
pentachloro	step 1	-33.118011	step 1	-35.40376298
	step 2	32.071734	step 2	37.384030
	step 3	-10.81891404	step 3	-13.74149329
	Open ring A	ΔG_r (kcal/mol)	Open ring B	ΔG_r (kcal/mol)
tetrachloro	step 1	-35.736939	step 1	-42.26720541
	step 2	31.494155	step 2	45.938760
	step 3	-8.650305691	step 3	-15.86549202

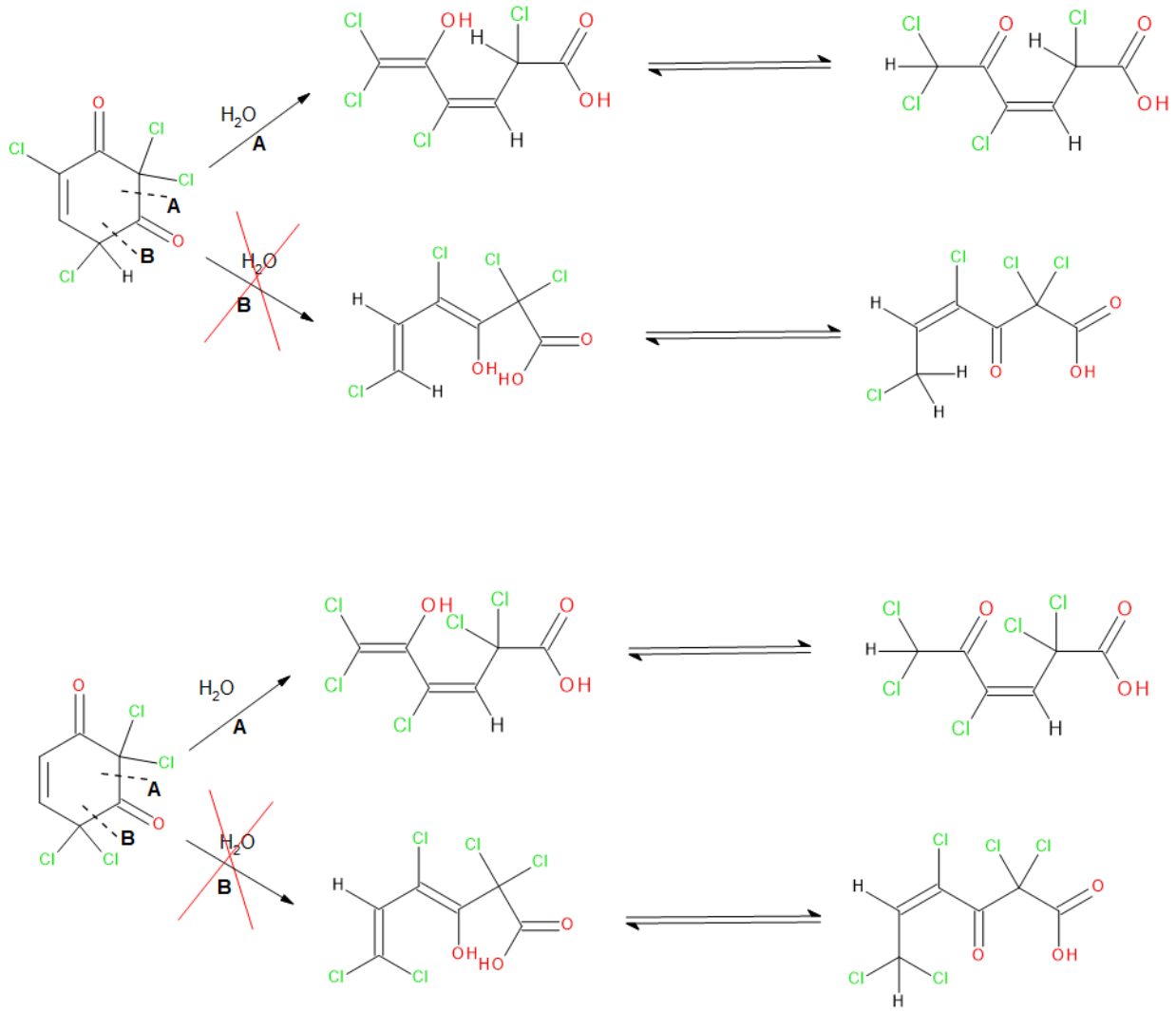

Figure 6-5. Concerted reaction mechanism for ring cleavage

Nevertheless, the activation barriers for this reactions are relatively large ($\Delta G^{\ddagger}$ = 55.184 kcal/mol and 54.885 kcal/mol for the tetrachloro and pentachloro cases respectively). The structures of both transition states are depicted in figure 6-6.

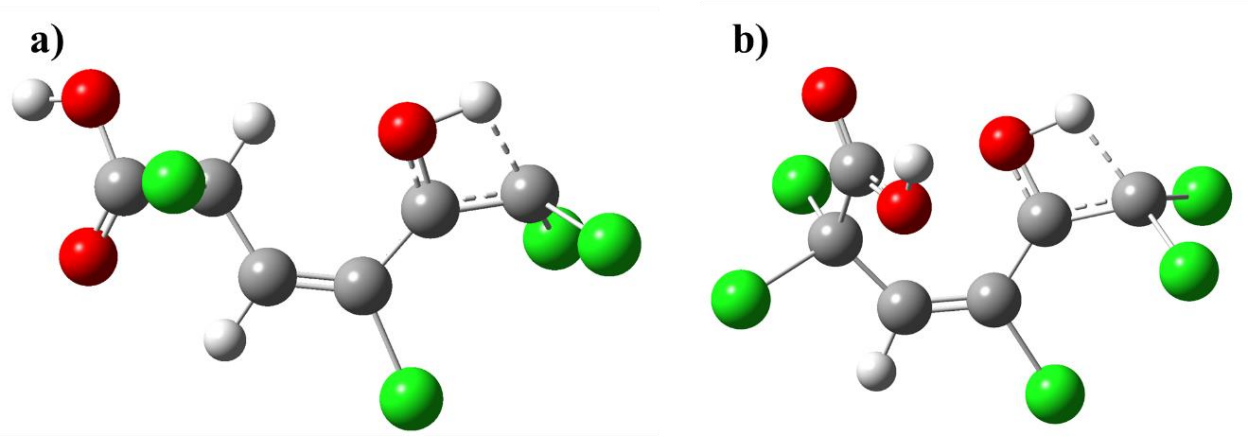

Figure 6-6. Structures of the transition states for proton transfer after ring cleavage for a) tetra- and b) penta- chloro cases

Following ring cleavage, the reaction pathway is proposed to involve multiple steps of decarboxylation and halogenation, which is eventually followed by base catalyzed hydrolysis to form chloroform. The proposed pathway following ring cleavage at the A-location for the pentachloro case is depicted in Figure 6-7. Following the formation of the keto-carboxylic acid intermediate, the reaction may proceed via either decarboxylation mechanism (elementary steps D1, and P1) followed by a halogenation mechanism (elementary steps E2, and C2), or vice versa (C1, E1 followed by D2, and P2).

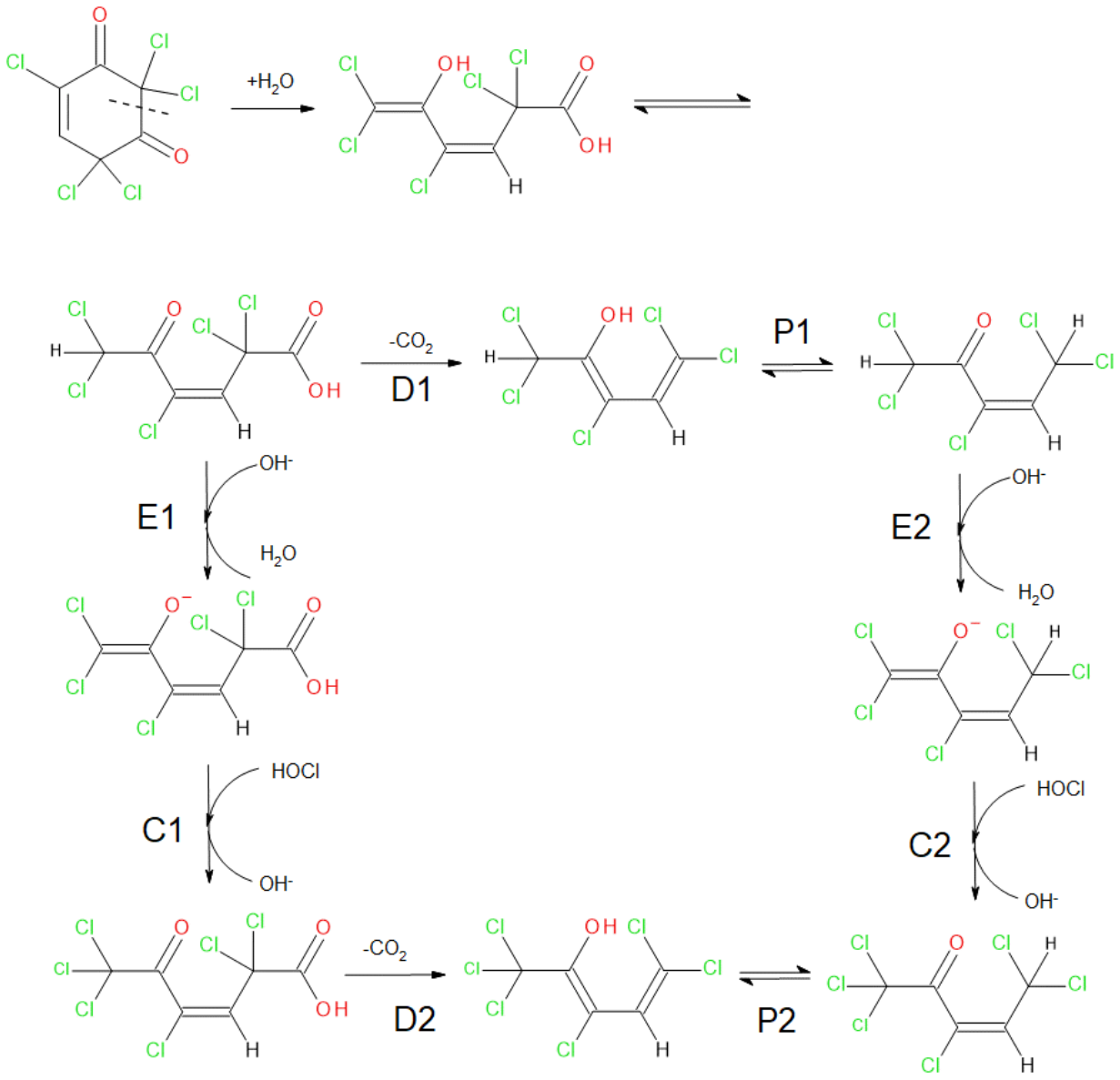

Figure 6-7. Proposed reaction pathway showing decarboxylation and chlorination steps

The decarboxylation reaction involves two elementary steps. The first step features the concerted formation of CO_2 and the protonation of the carbonyl oxygen to form an enol intermediate, while the second step involves proton transfer to regenerate carbonyl. Similarly, halogenation is proposed to proceed via two steps. The first step involves base catalyzed enolization of the keto-

carboxylic acid by removal of the alpha proton to form the corresponding enolate intermediate. Enolate anions are particularly strong nucleophiles and can hence react rapidly with HOCl in the following step. Table 6-2 summarizes the results of the calculations for the depicted elementary steps.

Table 6-2. Reaction energies and activation free energies (at 298 K and 1 atm) in kcal/mol

Reaction Step	ΔG_r (kcal/mol)	$\Delta G^{\ddagger}$ (kcal/mol)
E1	-22.35061556	N/A
E2	-24.27581317	N/A
C1	-13.85253728	9.934094979
C2	-12.93735305	10.42687
D1	-21.34032607	24.57827251
D2	-20.32815405	26.3346702
P1	-12.04189771	24.05869506
P2	-13.88551915	23.60375103

In the proposed mechanism, both decarboxylation reactions (D1, and D2) and the consequent proton transfer reactions (P1, and P2) are thermodynamically favorable (Table 6-2). The activation barrier for the D1 decarboxylation reaction of the pentachloro intermediate $\Delta G^{\ddagger}$ = 24.578 kcal/mol is lower than that for the D2 reaction of the hexachloro intermediate $\Delta G^{\ddagger}$ = 26.334 kcal/mol, and is also more thermodynamically favorable (ΔG_r = -21.340 kcal/mol for D1 and -20.328 kcal/mol for D2, respectively). However, the activation barrier for the subsequent proton transfer is lower for the hexachloro case (P2) $\Delta G^{\ddagger}$ = 23.604 kcal/mol than that for the pentachloro case (P1) $\Delta G^{\ddagger}$ = 24.0587 kcal/mol, and is also more thermodynamically favorable (ΔG_r = -12.042 kcal/mol for P1

and -13.886 kcal/mol for P2, respectively). The structures of the transition states for the four elementary reactions are depicted in Figure 6-8.

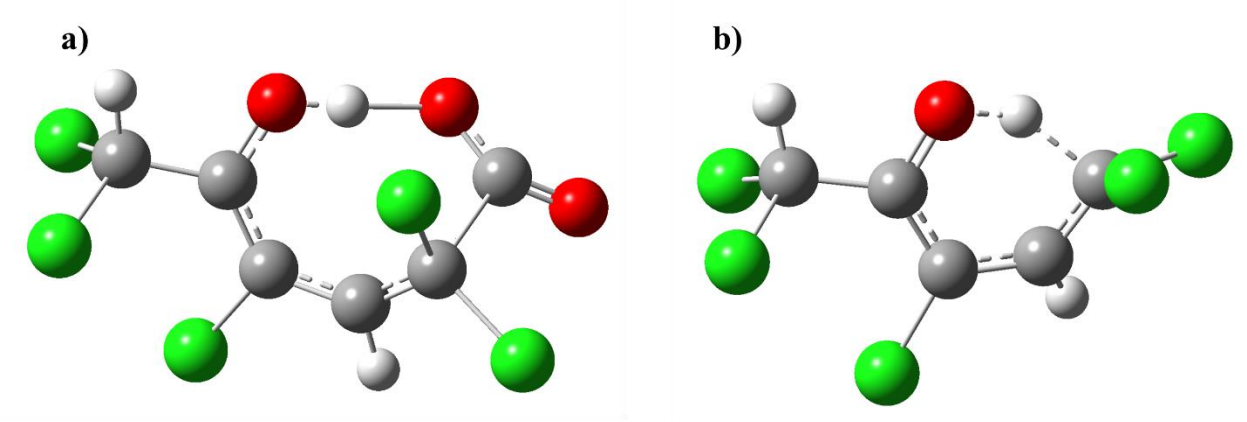

Figure 6-8. Structure of the transition state for the decarboxylation reaction elementary steps a) D1 and b) P1

The transition states for the halogenation reactions C1, and C2 could not be found using the PCM solvation model, and hence for these calculations the SMD solvation model was used to get accurate results for the transition states. Both halogenation steps are found to have activation barriers that are relatively lower than all the other elementary steps throughout the pathway ($\Delta G^{\ddagger}$ = 9.934 kcal/mol for the C1 reaction and $\Delta G^{\ddagger}$ = 10.427 kcal/mol for the C2 reaction). This suggests that the chlorination steps are the most kinetically favorable compared to the other elementary steps. Furthermore, the formation of the enolate anions by base-catalyzed enolization reactions (E1, and E2) was found to be thermodynamically favorable. However, the transition states for both enolization steps (E1 and E2) could not be located using neither the PCM nor the SMD solvation models. Therefore, a more sophisticated approach, such as the cluster-continuum approach, can be used to accurately model solvent effects by accounting for the direct involvement of the solvent.

This approach involves modeling each species as a microsolvated cluster that contains the solute plus several explicitly modeled water molecules, further embedded in an SMD implicit continuum model solvent.

An alternative mechanism for the halogenation reaction under acidic conditions can proceed via the direct attack of the HOCl-H_3O^+ on the C=C bond of the enol intermediate resulting from the ring cleavage at the A-site, which leads to the protonation of the ketone group forming a cation. This is followed by the deprotonation of the carbonyl by water that acts as a weak base, which reforms the carbonyl compound similar to the product of the C1 reaction.

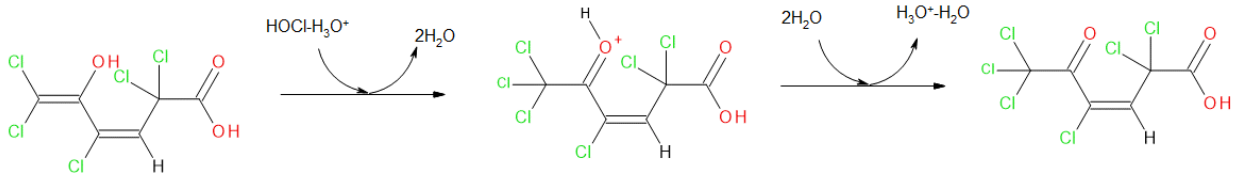

The structure of the transition state for the first halogenation step is depicted in Figure 6-9. The activation barrier of this mechanism $\Delta G^{\ddagger}$ = 11.354 kcal/mol is comparable to the main mechanism of base catalyzed enolization followed by direct halogenation (C1, and C2 reactions). Yet overall reaction rate may be limited by the subsequent steps.

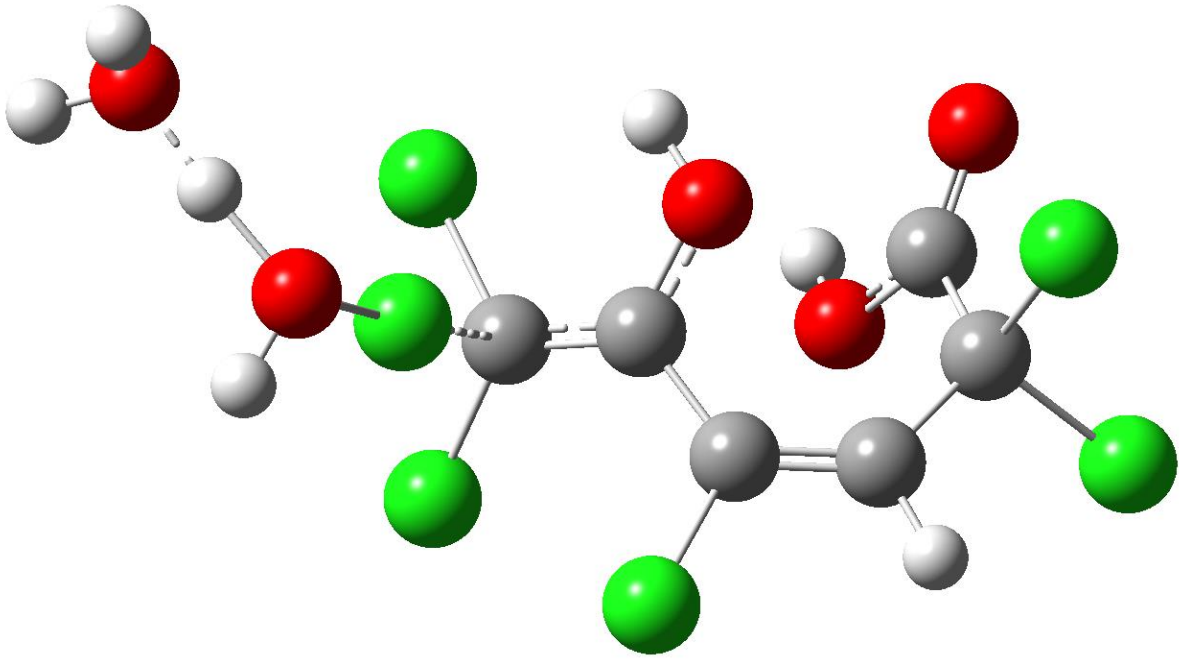

Figure 6-9. Structure of the transition state for the chlorination reaction under acidic conditions

6.5 Conclusions

This study proposes employing first-principles calculations to investigate the molecular mechanisms of trihalomethane formation from the chlorination of model humic precursors. Quantum chemical computations are used to explore the reaction mechanism, and to study the kinetics and thermodynamics of the reaction pathway. The proposed framework is demonstrated by elucidating the chlorination mechanism of resorcinol (1,3-dihydroxybenzene), which has been identified in the literature as an efficient precursor for the formation of chloroform. Computational results bring new insights into the structures of intermediates and transition states, kinetics of the elementary reactions along the mechanism, and identifying the dominant formation pathways.

6.6 References

Arnold, W.A., Bolotin, J., Von Gunten, U., Hofstetter, T.B., 2008. Evaluation of functional groups responsible for chloroform formation during water chlorination using compound specific isotope analysis. Environ. Sci. Technol. 42 (21), 7778–7785.

Bond, T., Goslan, E.H., Parsons, S.A., Jefferson, B., 2012. A critical review of trihalomethane and haloacetic acid formation from natural organic matter surrogates. Environ. Technol. Rev. 1 (1), 93–113.

Bond, T., Graham, N., 2017. Predicting chloroform production from organic precursors. Water Res. 124, 167–176.

Bond, T., Henriet, O., Goslan, E.H., Parsons, S.A., Jefferson, B., 2009. Disinfection byproduct formation and fractionation behavior of natural organic matter surrogates. Environ. Sci. Technol. 43 (15), 5982–5989.

Boyce, S.D., Hornig, J.F., 1983. Reaction pathways of trihalomethane formation from the halogenation of dihydroxyaromatic model compounds for humic acid. Environ. Sci. Technol. 17 (4), 202–211.

Brown, D., Bridgeman, J., West, J.R., 2011. Predicting chlorine decay and THM formation in water supply systems. Rev. Environ. Sci. Biotechnol. 10 (1), 79–99.

Criquet, J., Rodriguez, E.M., Allard, S., Wellauer, S., Salhi, E., Joll, C.A., von Gunten, U., 2015. Reaction of bromine and chlorine with phenolic compounds and natural organic matter extracts - Electrophilic aromatic substitution and oxidation. Water Res. 85, 476–486.

Deborde, M., von Gunten, U., 2008. Reactions of chlorine with inorganic and organic

compounds during water treatment-Kinetics and mechanisms: A critical review. Water Res. 42 (1–2), 13–51.

Gallard, H., Von Gunten, U., 2002. Chlorination of natural organic matter: Kinetics of chlorination and of THM formation. Water Res. 36 (1), 65–74.

Heasley, V.L., Burns, M.D., Kemalyan, N.A., Mckee, T.C., Schroeter, H., Teegarden, B.R., Whitney, S.E., 1989. Aqueous chlorination of Resorcinol. Environmenlul Toxicol. Chem. 8 (4), 523–524.

Heasley, V.L., Fisher, A.M., Herman, E.E., Jacobsen, F.E., Miller, E.W., Ramirez, A.M., Royer, N.R., Whisenand, J.M., Zoetewey, D.L., Shellhamer, D.F., 2004. Investigations of the reactions of monochloramine and dichloramine with selected phenols: Examination of humic acid models and water contaminants. Environ. Sci. Technol. 38 (19), 5022–5029.

Lebedev, A.T., Shaydullina, G.M., Sinikova, N.A., Harchevnikova, N. V., 2004. GC-MS comparison of the behavior of chlorine and sodium hypochlorite towards organic compounds dissolved in water. Water Res. 38 (17), 3713–3718.

Liu, Y.D., Selbes, M., Zeng, C.C.-C., Zhong, R., Karanfil, T., 2014. Formation Mechanism of NDMA from Ranitidine, TMA and Other Tertiary Amines during Chloramination: A Computational Study. Environ. Sci. Technol. 48 (15), 1–19.

Liu, Y.D., Zhong, R., 2017. Comparison of N-nitrosodimethylamine formation mechanisms from dimethylamine during chloramination and ozonation: A computational study. J. Hazard. Mater. 321, 362–370.

Rebenne, L.M., Gonzalez, A.G., Olson, T.M., 1996. Aqueous chlorination kinetics and mechanism of substituted dihydroxybenzenes. Environ. Sci. Technol. 30 (7), 2235–2242.

Trogolo, D., Mishra, B.K., Heeb, M.B., Von Gunten, U., Arey, J.S., 2015. Molecular mechanism of NDMA formation from N, N-dimethylsulfamide during ozonation: Quantum chemical insights into a bromide-catalyzed pathway. Environ. Sci. Technol. 49 (7), 4163–4175.

Yang, M., 2017. New Insights into Trihalomethane and Haloacetic Acid Formation Potentials: Correlation with the Molecular Composition of Natural Organic Matter in Source Water.

Yu, H., Ge, P., Chen, J., Xie, H., Luo, Y., 2017. The degradation mechanism of sulfamethoxazole under ozonation: a DFT study. Environ. Sci. Process. Impacts 19 (3), 379–387.

Zhang, S., Yu, G., Chen, J., Wang, B., Huang, J., Deng, S., 2014. Unveiling formation mechanism of carcinogenic N-nitrosodimethylamine in ozonation of dimethylamine: A density functional theoretical investigation. J. Hazard. Mater. 279, 330–335.

Chapter 7

Computational Materials Design of SnO_2 Nanostructured Sensors for the Online Monitoring of Volatile Disinfection Byproducts

Parts of the results presented in this chapter were published in:

A. A. Abokifa, K. Haddad, J. Fortner, C. S. Lo, and P. Biswas. Sensing Mechanism of Ethanol and Acetone at Room Temperature by SnO_2 Nano-columns Synthesized by Aerosol Routes: Theoretical Calculations Compared to Experimental Results. Journal of Materials Chemistry A 2018, 6, 2053-2066

Other parts are currently under review in:

A. A. Abokifa, K. Haddad, B. Raman, J. Fortner, and P. Biswas. Room Temperature Sensing Mechanism of SnO_2 towards Chloroform: Ab-initio Theoretical Calculations Compared to Sensing Experiments. Sensors and Actuators B: Chemical (Submitted - March 2018)

7.1 Abstract

SnO_2 is a semiconducting metal oxide that is broadly employed as the active sensing material in chemiresitive gas sensors. Recent studies demonstrated the capability of SnO_2 sensors to detect various gases, including volatile organic compounds (VOCs), at room temperature. In this study, room temperature sensing of chloroform ($CHCl_3$), which is one of the most ubiquitous disinfection byproduct in drinking water, using SnO_2 nanostructured thin films synthesized via a single-step aerosol chemical vapor deposition (ACVD) process is demonstrated. The sensing mechanism is investigated by means of dispersion-corrected density functional theory (DFT) calculations and *ab inito* molecular dynamics (AIMD) simulations of chloroform's adsorption on the (110) surface facet of rutile SnO_2. Theoretical calculations demonstrate that the direct adsorption of chloroform on the stoichiometric and the oxygen defective (110) surface is thermodynamically favorable. Upon their adsorption, chloroform molecules donate charge to the surface inducing a drop in the sensor's resistance that promotes the sensing response. Long-range dispersive interactions are found to play a significant role in chloroform binding to SnO_2, and generally account for more than 50% of the calculated adsorption energies. AIMD simulations in the canonical (NVT) ensemble at room temperature show that chloroform molecules minimally interact with the ionosorbed oxygen species (O_2^-) suggesting that the sensing mechanism is mainly attributed to the direct binding of chloroform molecules on the sensor's surface. Taken together, the results of this study suggest that nanostructured metal-oxide materials are promising material candidates for the room temperature sensing of chlorinated volatile organic compounds, with potential for real-time monitoring applications.

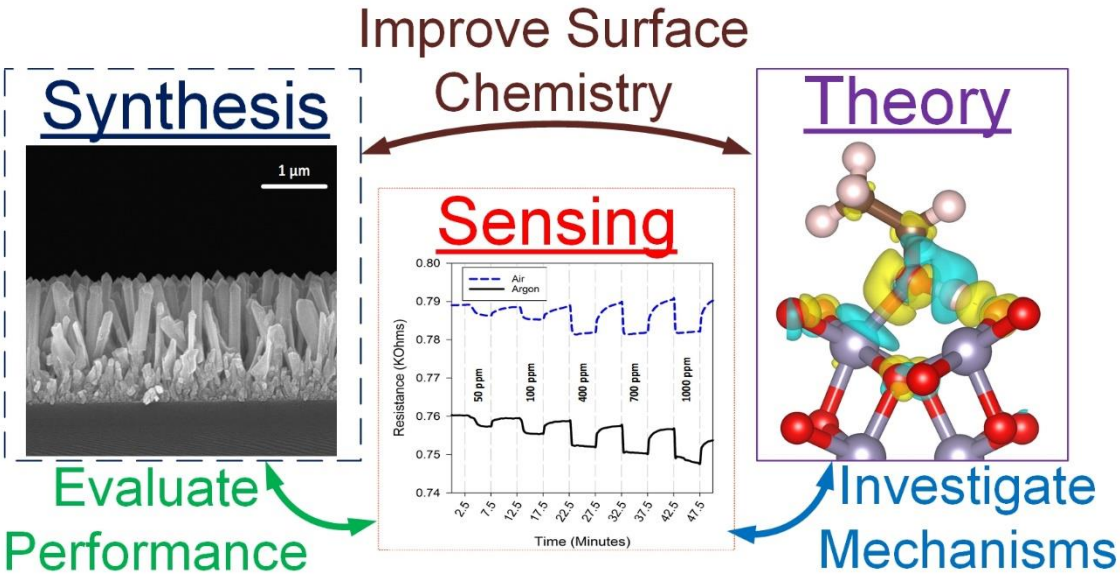

Figure 7-1. Graphical Abstract of the work presented in Chapter 7. A useful feedback loop: insights from theoretical calculations are used for rational design of nanosensors and for elucidating surface interactions

7.2 Introduction

Chloroform ($CHCl_3$ - Trichloromethane) is a chlorinated volatile organic compound (Cl-VOC) with well-documented toxicity and carcinogenic effects [1,2]. It is widely used as a solvent in the chemical and pharmaceutical industries, and as a precursor for the large-scale production of fluoropolymers and refrigerants. Industrial waste and spills are known to be the primary sources of chloroform emission to the environment [3]. Additionally, chloroform is one of the most ubiquitous disinfection byproducts (DBPs) in drinking water systems, which are commonly produced during water treatment as a result of the reactions between chlorine-based disinfectants and residual natural organic matter [4,5]. Water supply utilities routinely sample the finished drinking water in their systems to test for the presence of chloroform and other toxic trihalomethane compounds (THMs) in order to protect public health and to ensure compliance with regulatory limits [6].

Traditional methods used for the analysis of THMs in the aqueous phase include direct aqueous injection, liquid-liquid extraction, and solid-phase extraction. In addition, headspace (HS) sampling techniques, including static HS, dynamic HS (purge and trap) [7], and solid phase microextraction (SPME) [8] methods, have gained notable popularity because they capitalize on the inherent volatility of THMs enabling direct sampling in the vapor phase to reduce interference [9]. However, most of these techniques still rely on traditional methods, such as gas chromatography (GC) coupled with either mass spectrometry (MS) or electron capture detection (ECD) [10], which makes them costly, bulky, and time-consuming. A promising alternative is to implement chemiresistive gas sensor arrays, traditionally known as electronic noses [11], for the real-time detection of THMs through headspace sampling.

Semiconducting metal-oxides are commonly employed as the active sensing material in chemiresistive gas sensors owing to their high sensitivity, unique chemical and physical stability, scalability, and low cost [12–14]. Previous studies demonstrated the successful application of various metal-oxide sensors for the detection of chloroform vapor. For example, Nie et al. prepared a chloroform sensor based on $ZnO/CuO/Al_2O_3$ composites that displayed optimal performance at 200 °C [15]. Şennik et al. fabricated Pd-loaded TiO_2 nanowires that showed high sensitivity towards chloroform at 200 °C [16]. Despite such material advances, the high working temperatures (150-400 °C) typically required to operate such sensors effectively reduce their long-term stability and complicate their miniaturization [17]. As a result, recent research efforts have aimed at fabricating resistive metal-oxide sensors with enhanced room temperature sensing capabilities [17]. Recently, Perillo and Rodrigues demonstrated room temperature chloroform detection with a sensor based on TiO_2 nanotubes [18], while Zhou et al. [19] achieved the same using bilayer composite thin films of ZnO and reduced graphene oxide (RGO).

Tin dioxide (SnO_2) is an n-type semiconducting metal-oxide that displayed a robust room temperature response towards several gases of environmental interest, such as NO_2 [20–24], CO [25,26], H_2 [25–27], and NH_3 [28]. To this point, no previous studies focused on investigating the room temperature sensing of chloroform by SnO_2 despite its well-known sensitivity towards other VOCs such as ethanol [25,29–32] and acetone [33]. A few studies have included chloroform as an interfering gas while examining the specificity of their SnO_2-based sensors, including NiO doped SnO_2 nanospheres [34], SiO_2@SnO_2 core-shell nanofibers [35], SnO_2 quantum dots on RGO [36], and nanostructured WO_3–SnO_2 [37]. Interestingly, all the above-mentioned sensors showed little to no response towards chloroform compared to the other tested analytes. It is noteworthy that for all of these studies, the active materials were all composites, i.e. they featured SnO_2 coupled with

other metal-oxides, or carbon-based materials. Although relying on such composite materials is now common practice for the fabrication of resistive sensors, mainly to enhance their sensitivity at ambient temperature, it also complicates the sensor synthesis/scale-up compared to single-component materials. Alternatively, sensors based on bare-SnO_2 have relatively higher potential for mass production and broad-scale application, especially if adequate sensitivity at room temperature is achieved. Hence, a necessary first step towards the rational design of efficient SnO_2 sensors for broad-scale applications in sensor arrays, and to improve upon their sensitivity and specificity, is to explore the fundamental aspects of their surface chemistry and sensing mechanism towards Cl-VOCs.

The primary sensing mechanism of chemiresistive gas sensors is generally attributed to the surface adsorption of the analyte molecules and the accompanying charge transfer, which induces a change in the electrical conductivity of the oxide. Hence, theoretical *ab initio* quantum chemical calculations have been routinely used in the literature to supplement experimental efforts by delivering an atomistic level understanding of the thermodynamic and electronic properties of the surface-adsorbate systems. A few theoretical investigations examined the adsorption of chloroform on different substrates, including pristine and doped graphene [38,39], graphene oxide [40], single wall carbon nanotubes [41], ZnF_2 [42], and Pd-Au [3]. Yet, to our knowledge, no first-principles studies have been conducted for chloroform's adsorption on the surface of rutile SnO_2.

Recently, our group used a facile aerosol chemical vapor deposition (ACVD) process to prepare nanostructured SnO_2 thin-film sensors that exhibited a strong room temperature sensing response towards VOCs with different degrees of polarity [43,44]. With the help of theoretical calculations, we postulated that the sensing response is triggered by the direct adsorption of the polar VOC molecules on the surface of SnO_2, which is accompanied by the release of charge from

the adsorbate molecules to the surface [45]. Here, we conduct a thorough study of the room temperature sensing of chloroform by bare-SnO_2 sensors. The sensing response of the ACVD fabricated thin film sensors towards chloroform at different vapor concentrations is demonstrated. Further, corresponding *ab initio* density functional theory (DFT) calculations are conducted to deliver a fundamental understanding of the sensing mechanism by providing atomic-level insights into the surface interaction mechanisms, considering the role of surface oxygen defects and long-range dispersive interactions. A detailed investigation of the adsorption energetics and geometries, as well as the deformations in the charge density and the electronic structures, is provided. *Ab initio* molecular dynamics (AIMD) simulations are then used to examine the adsorption mechanisms at room temperature in the presence of oxygen from the ambient atmosphere.

7.3 Experimental Details

The SnO_2 nanostructured thin films are deposited using a single-step gas-phase deposition process (ACVD), which has been previously used to synthesize thin films for energy storage, solar energy [46], and electrochemical sensing [47]. In the ACVD system, described elsewhere [44], the films are deposited at a temperature of 550 °C using a tetramethyl tin (TMT, Sigma-Aldrich) precursor carried by nitrogen gas (11 sccm) and a dilution flow rate of oxygen at 100 sccm. For all samples, the feeder tube to substrate distance is set at one centimeter and the deposition time is set at 17 minutes. The nanostructured thin films are deposited directly onto Au/Cr interdigitated electrodes on a silicon substrate (IDE, 20 fingers, 50 µm wide and 2.4 µm long, spaced 50 µm apart). The gas sensing experiments are performed using a bubbler and mass flow controllers to produce five different concentrations of chloroform— 300, 500, 600, 700, and 1000 ppm—for a five-minute exposure period followed by a five-minute degassing period. A dilution flow of dry, filtered air (hydrocarbon trap, model HT200-4 Agilent) is introduced to ensure a gas flow rate of 750 sccm is

consistently delivered to the sensor manifold. In addition, this carrier stream also helps control the concentration of chloroform vapors delivered to the manifold containing the sensors. The resistance measurements are performed with an NI PXI-4071 Digital Multimeter in the 1 kOhm test range. The results are analyzed with a low pass filter (3rd order, lowpass digital Butterworth filter) in MATLAB.

7.4 Computational Methods

7.4.1 Density Functional Theory (DFT) Calculations

All calculations were performed with the Vienna *ab initio* simulation package (VASP version 5.3.5) [48,49]. The projector augmented wave (PAW) method [50,51], with the frozen-core approximation, is used with a 500 eV energy cutoff. The Sn 4d states are treated as valence states. For the exchange-correlation (XC) functional, we employed the generalized gradient approximation (GGA) with the formulation proposed by Perdew–Burke–Ernzerhof (PBE) [52]. Bader charge analysis was performed to analyze the charge transfer between the surface and the adsorbate molecules. We chose to limit our focus to the (110) surface because it is the most thermodynamically favorable facet of rutile SnO_2 [53]. The perfect (110) surface (110-sto) is modelled here as a *p*(2×2) surface slab cleaved from the fully relaxed bulk rutile structure (a=b= 4.830 Å, c= 3.243 Å, $\alpha = \beta = \gamma = 90^o$) with an imposed additional vacuum layer of 15 Å to avoid interactions with periodic images in the z-direction. The modeled surface slab consists of four (Sn_2O_4) tri-layers (Figure 7-2), with a total of 96 atoms ($Sn_{32}O_{64}$). An oxygen vacancy is introduced by removing one of the bridging oxygen atoms (O_{br}) from the topmost atomic layer to create the partially reduced (oxygen defective) surface (110-red). For all geometry optimization calculations, the top two tri-layers are allowed to relax while the bottom two layers are fixed at bulk positions. For the adsorption calculations, a chloroform molecule is adsorbed on one side of

the slab, and dipole corrections are employed to generate accurate adsorption energies. Since the noncovalent interactions are expected to play an important role in our study, the empirical van der Waals corrections, as prescribed by Grimme [54] (DFT-D3) with Becke-Jonson (BJ) damping are considered in all calculations. For geometry optimization, the conjugate gradient algorithm is used to relax the atomic positions until the Hellmann-Feynman forces on each ion are smaller than 0.02 eV/Å and have an overall energy convergence of 10^{-5} eV. For the Brillouin zone integration, the k-meshes are generated automatically using the Monkhorst–Pack (MP) method with a (4×2×1) k-point mesh. Density of states (DOS) calculations were conducted on the most stable adsorption configurations using a denser k-point mesh of (20×20×1) to obtain accurate electronic structures. The linear tetrahedron method with Blöchl corrections is used to determine how the partial occupancies are set for each orbital.

7.4.2 Ab-initio Molecular Dynamics (AIMD) Simulations

To study the interactions between chloroform and the (110) surface of SnO_2 under ambient conditions, we perform *ab initio* molecular dynamics (AIMD) simulations considering the canonical (NVT) ensemble in VASP. Similar to the DFT calculations, the GGA-PBE functional with the D3(BJ) dispersion corrections are employed. To simulate a large interface for surface interactions between SnO_2 and the adsorbate molecules, a *p*(4×2) simulation box consisting of 192 atoms (4 layers of $Sn_{16}O_{32}$) with surface dimensions of (12.98 Å × 13.66 Å) is used, and a vacuum space of 20 Å is imposed above the surface. An energy cutoff of 300 eV is employed for the AIMD simulations, and the k-space is sampled only at the Γ-point given the large size of the simulation box. A Nosè-Hoover thermostat is applied to conduct constant temperature simulations at T = 298 K. A time step of 0.5 femtoseconds (fs) is used to integrate the equations of motion, and 15 pecoseconds (ps) trajectories (30,000 steps) are generated for all adsorbate–adsorbent systems for

each simulation. Three simulation ensembles were conducted for: (1) the perfect (110) surface; (2) the partially reduced (110) surface; and (3) the partially reduced (110) surface with pre-adsorbed oxygen molecules.

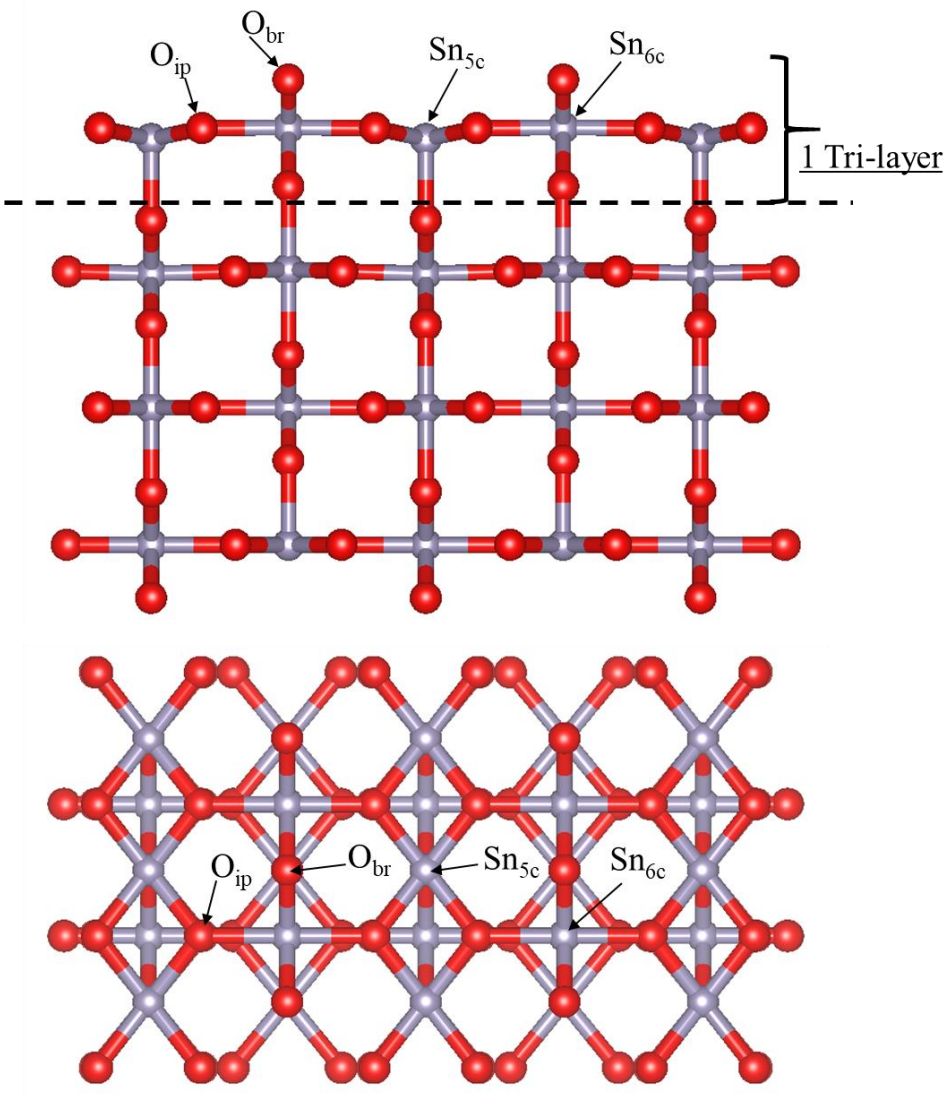

Figure 7-2. A surface slab of four tri-layers representing the stoichiometric (110) surface of rutile SnO_2. The topmost layer features four atom types: O_{br} is the bridging oxygen, O_{ip} is the in-plane oxygen, Sn_{5c} is the five-fold coordinated tin, and Sn_{6c} is the six-fold coordinated tin.

7.5 Results and Discussion

7.5.1 Room temperature sensing response of SnO_2 towards Chloroform

ACVD deposited SnO_2 nanostructured thin films are first experimentally tested for their sensing response to chloroform at room temperature. A representative trace showing the characteristic response of the nanostructured SnO_2 films at room temperature is depicted in Figure 7-3. In addition, the inset shows an SEM image of the nanostructured thin films, which were more thoroughly characterized and shown to have the (110), (101), and (211) facets exposed, as reported in previous work [44]. The introduction of chloroform evokes a step-wise decrease in resistance during the exposure periods, which indicate that charge is transferred from the adsorbed chloroform molecule to the surface.

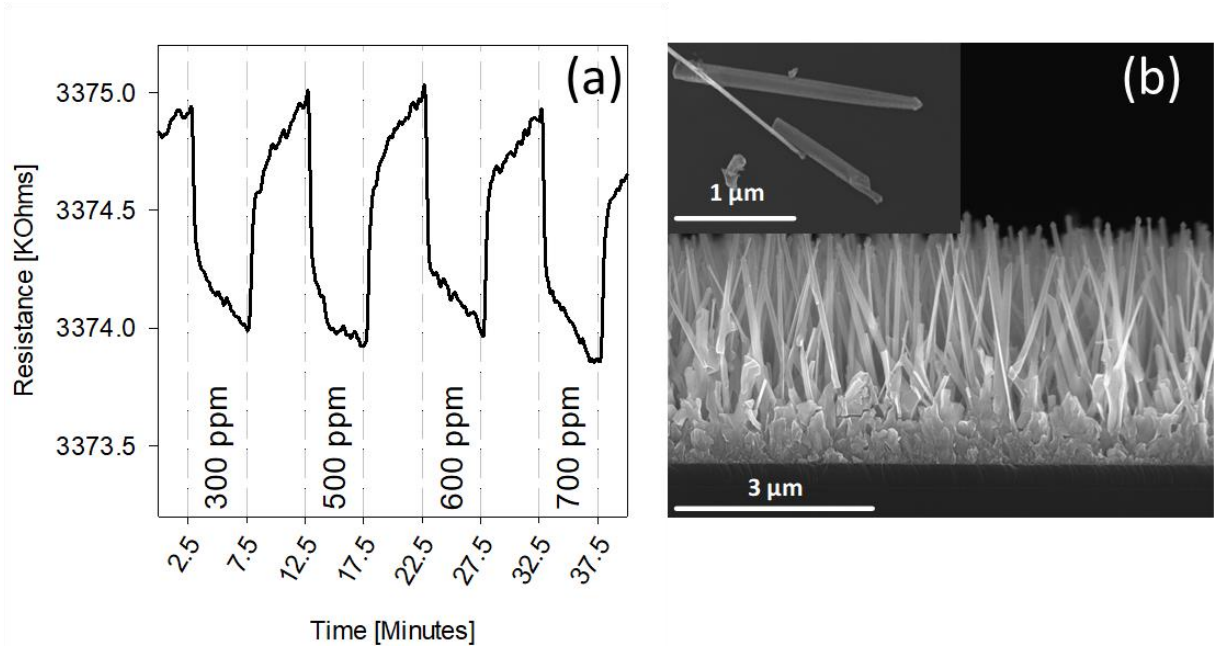

Figure 7-3. (a) Representative trace of the gas sensing response of SnO_2 nanostructured thin films towards chloroform. (b) SEM images of nanostructured thin films and a single column (inset).

The sensing response of resistive metal-oxide sensors at increased temperatures has been classically attributed to the change in the sensor's resistance resulting from the surface interactions between the analyte gas molecules and the ionosorbed oxygen species [55]. Oxygen molecules from the ambient atmosphere first adsorb on the surface of the metal-oxide, and then ionize to form superoxide species (O_2^-) by uptaking free electrons from the conduction band. At higher temperatures (>200 °C), superoxide molecules dissociate after capturing extra electrons from the surface to form oxygen ions (O^- and O^{2-}) according to the following mechanism [56]:

$$O_2(\text{gas}) \rightarrow O_2(\text{ads}) \qquad (7-1)$$

$$O_2(\text{ads}) + e^- \rightarrow O_2^-(\text{ads}) \qquad (7-2)$$

$$O_2^-(\text{ads}) + e^- \rightarrow 2O^-(\text{ads}) \qquad (7-3)$$

$$O^-(\text{ads}) + e^- \rightarrow O^{2-}(\text{ads}) \qquad (7-4)$$

The trapping of the metal-oxide's free electrons by the pre-adsorbed oxygen species reduces its carrier concentration and conductivity before introducing the target vapor. Trapped electrons are then released back to the surface when the target gas molecules interact with the pre-adsorbed oxygen species resulting in a measurable drop in the resistance. For this processes, the ionosorbed (O^-) anions are generally regarded as the most chemically active reaction centers that enable the detection of various gases [57]. For example, Nie et al. suggested that the sensing mechanism of their $ZnO/CuO/Al_2O_3$ composites is attributed to the catalytic oxidation of chloroform molecules at the surface according to the following reaction [15]:

$$CHCl_3(g) + O^-(\text{ads}) \rightarrow COCl_2(g) + HCl(g) + e^- \qquad (7-5)$$

However, since the dissociation of the less chemically active (O_2^-) species (Equation 7-3 in the abovementioned mechanism) only takes place at elevated temperatures, the oxidation of the chloroform molecules is unlikely to occur at room temperature. In a recent study, we found that the room-temperature response of the ACVD-deposited SnO_2 thin film sensors towards ethanol and acetone under argon conditions was identical to that observed under ambient conditions [45]. Furthermore, theoretical results elucidated that ethanol and acetone do not interact with the pre-adsorbed (O_2^-) species on the surface of SnO_2 suggesting that the room temperature sensing mechanism of polar VOC molecules by SnO_2 sensors is primarily driven by their direct adsorption on the surface. Herein, we investigate the direct adsorption of chloroform on the surface of SnO_2 by means of DFT calculations. We then demonstrate the interaction of chloroform molecules with the SnO_2 surface in both the presence and absence of pre-adsorbed oxygen species by means of *ab initio* MD simulations at room temperature.

7.5.2 Adsorption geometries and energetics

Adsorption on the perfect (110) surface

To begin, we conduct a thorough investigation of the possible configurations by which chloroform may adsorb on the stoichiometric surface of SnO_2. The topmost layer of a perfect (110) surface slab comprises four different atom types (Figure 7-2), namely the five-fold coordinated tin (Sn_{5c}), six-fold coordinated tin (Sn_{6c}), bridging oxygen (O_{br}), and in-plane oxygen (O_{ip}). Chloroform, on the other hand, features a distorted tetrahedral geometry with three electronegative chlorine atoms and one hydrogen atom. Six possible adsorption configurations are identified considering the partial charges and electronegativities of the surface atoms and the adsorbate molecule. Figure 7-4 shows the six configurations before and after relaxation. The six configurations can be broadly classified into three categories depending on the orientation of the hydrogen atom that can point

either upwards (H_{up}) or downwards (H_{dn}), or adopt a horizontal orientation (H_{hl}). It is important to note that these configurations are defined for the surface-adsorbate systems before conducting the geometry optimization calculations because, after relaxation, these systems evolve into new configurations that are less readily definable. For the first category (H_{up}), the H atom is pointing upwards away from the surface, while the three electronegative Cl atoms interact with the surface Sn cations; either with one Sn_{6c} and two Sn_{5c} ($H_{up1,sto}$) or with one Sn_{5c} and two Sn_{6c} ($H_{up2,sto}$). For the second category (H_{dn}), the H atom faces downwards perpendicular to the surface and directly interacts with a surface oxygen atom; either the O_{ip} ($H_{dn1,sto}$) or the O_{br} ($H_{dn2,sto}$). The third configuration (H_{hl}) involves two modes of interaction; the first is a close interaction between the horizontally oriented H atom and a surface O_{br} atom, while the second is a rather loose (distant) interaction between either one Cl atom ($H_{hl1,sto}$) or two Cl atoms ($H_{hl2,sto}$) and the underlying surface Sn_{5c} cations.

The energy of adsorption (E_{ads}) is defined as the difference in the total energy when the chloroform molecule is adsorbed on the surface, and when it is isolated in the vapor phase:

$$E_{ads} = \Delta E_{tot} = -[E_{surf+mol} - (E_{surf} + E_{mol})] \qquad (7-6)$$

where, $E_{surf+mol}$ is the total energy of the surface with the adsorbed molecule in the optimized adsorption configuration, and E_{surf} and E_{mol} are the optimized energies of the clean surface slab and the isolated gas molecule, respectively. According to this definition, a positive value for the adsorption energy indicates an exothermic process, i.e. the adsorption is thermodynamically favorable. The calculated adsorption energies are listed in Table 7-1. The adsorption energies for the different configurations on the stoichiometric surface are within the range of 0.69 eV to 1.00 eV, with the exception of the $H_{dn2,sto}$ configuration whereby the adsorption is drastically less stable than all the other configurations (E_{ads}=0.35 eV).

Table 7-1. Adsorption energy (eV), dispersion energy (eV), and charge transfer for the adsorption of chloroform on the stoichiometric and reduced SnO2 (110) surface. The configurations are ranked in a descending order by E_{ads} from the most stable to the least stable. A negative sign for the charge transfer indicates net electron gain by the surface.

Surface	Configuration	E_{ads} (eV)	ΔE_{disp} (eV)	Charge Transfer
(110-sto)	$H_{dn1,sto}$	1.004	0.589	-0.109
	$H_{hl2,sto}$	0.938	0.518	-0.08
	$H_{hl1,sto}$	0.925	0.494	-0.073
	$H_{up1,sto}$	0.734	0.582	-0.106
	$H_{up2,sto}$	0.688	0.523	-0.061
	$H_{dn2,sto}$	0.347	0.257	-0.018
(110-red)	$H_{dn1,red}$	0.754	0.52	-0.065
	$H_{hl2,red}$	0.621	0.471	-0.039
	$H_{hl1,red}$	0.604	0.397	0.249
	$H_{up3,red}$	0.564	0.502	-0.028
	$H_{up1,red}$	0.558	0.496	-0.032
	$H_{up2,red}$	0.555	0.533	-0.05

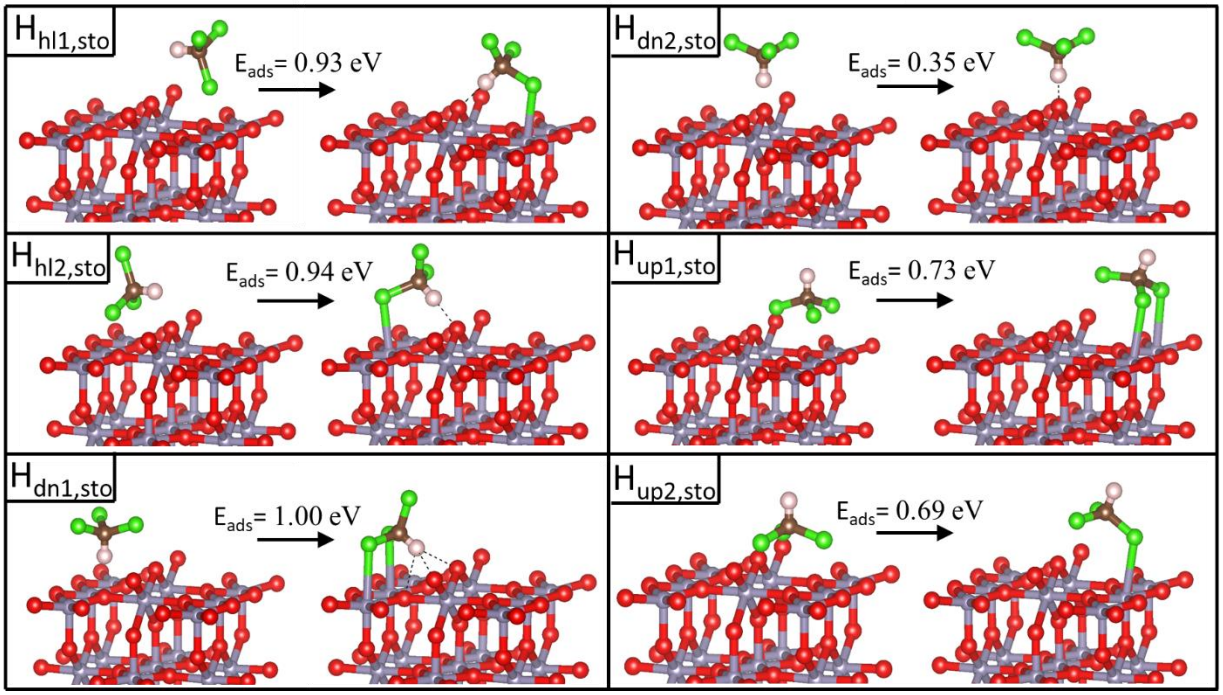

Figure 7-4. Studied configurations of chloroform before and after adsorption on the perfect (110) surface. Red color represents oxygen atoms, gray is tin, green is chlorine, brown is carbon, and white is hydrogen.

For the calculated adsorption energies, the $H_{dn1,sto}$ configuration is found to be the most stable (1.00 eV), followed by the two H_{hl} configurations (~0.93 eV), then the two H_{up} configurations (~0.7 eV). Here, a consistent trend is observed, where the adsorption energy appears to increase as the number of binding modes between the chloroform molecule and the surface increases. For example, the relaxed structure for the most stable configuration ($H_{dn1,sto}$) comprises two distinct modes of binding: (i) through electrostatic interactions between the H atom and nearby surface O_{br} and O_{ip} atoms (bond lengths = 2.44~2.51 Å), and (ii) through covalent interactions between two Cl atoms and surface Sn_{5c} cations (bond length = 2.91 Å). Although the relaxed structures for the H_{hl} configurations also feature two binding modes, their adsorption energies are

relatively less stable than $H_{dn1,sto}$ since only one Cl atom (instead of two) interacts with the surface Sn_{5c}, while the other two point away from the surface. Relaxed H_{up} and $H_{dn2,sto}$ configurations include only one binding mode either between Cl atoms and surface Sn_{5c} centers, or between H and a surface O_{br} atom, which justifies their lower adsorption energy compared to the other configurations.

Taking a closer look at the most stable configuration ($H_{dn1,sto}$), the adsorption energy of (1.00 eV) indicates a weak chemisorption phenomenon, which is also supported by the minor distortions observed in the geometry of the chloroform molecule following its adsorption on the surface. For example, the C-Cl bonds for the two Cl atoms binding to the surface Sn_{5c} cations stretch by 1.58% from 1.771 Å before relaxation to 1.799 Å after relaxation. However, it is noteworthy that the GGA method used herein slightly overestimates the C-Cl bonds in chloroform compared to the experimentally observed length of 1.762 Å, which is consistent with previous GGA-based theoretical studies [42].

Previous calculations for chloroform adsorption on carbon-based materials, such as graphene [39] and graphene oxide [40], were found to yield adsorption energies in the range of 0.2-0.4 eV, which are notably less stable than our calculated energies for rutile SnO_2. For the adsorption on pristine graphene, the H_{up} configurations featuring the Cl_3 tripod interacting with carbon atoms appeared to be the most stable (E_{ads} = ~0.36 eV) [39]. Nevertheless, the adsorption energy on graphene is still considerably lower than the corresponding H_{up} configurations on SnO_2 (E_{ads} = ~0.7 eV), which can be attributed to the higher polarity, and thus the strength, of the covalent Sn-Cl bonds compared to the C-Cl bonds formed between chloroform and graphene. Furthermore, the calculated binding energy for chloroform adsorption on the rutile (110) surface of SnO_2 (1.00 eV) is considerably more stable than the previously calculated value on the rutile

(110) surface of ZnF_2 (0.20 eV) using a similar dispersion corrected D3 method [42]. Yet, the ZnF_2 study only considered the upright adsorption configuration with one chlorine atom interacting with the undercoordinated metallic Zn center similar to the ($H_{hl1,sto}$) configuration in our study.

Role of bridging oxygen vacancies ($O_{br\text{-}vac}$)

Oxygen vacancies are one of the most common defect sites on the surfaces of semiconducting metal-oxides. They are hence expected to play a critical role in the surface interactions between SnO_2 surface and chloroform molecules, and thus affect the sensing mechanism. On the (110) surface of SnO_2, bridge-bonded oxygen vacancies ($O_{br\text{-}vac}$) are the most prevalent [58] since they exhibit the lowest formation energy compared to other O_{vac} types [59]. The removal of a bridging oxygen atom gives rise to a pair of under coordinated five-fold tin cations (Sn_{5c}). Previous experimental studies suggest that the presence of surface oxygen vacancies enhances room temperature sensing response of SnO_2 nanocrystals to NO_2 [23], which is in agreement with theoretical work demonstrating that the presence of $O_{br\text{-}vac}$ leads to stronger adsorption and a larger charge transfer [60]. However, in a recent study, our group found that $O_{br\text{-}vac}$ reduced the stability of the adsorption of ethanol and acetone on the (110) and (101) surfaces of SnO_2 [45], indicating that surface oxygen vacancies exert different effects on the adsorption of different molecules depending on their properties.

Similar to the perfect surface, six possible configurations are identified for chloroform adsorption on the reduced (110) surface with a bridging oxygen vacancy ($O_{br\text{-}vac}$), which can be defined according to the same classification of H_{up}, H_{dn}, and H_{hl}. The six configurations before and after relaxation are displayed in Figure 6-5. A corresponding configuration to the $H_{dn2,sto}$ configuration on the perfect surface does not exist for the reduced case since the bridging oxygen atom is now missing. Instead, a third H_{up} configuration is defined for the reduced surface ($H_{up1,red}$)

in which one Cl atom is placed near the O_{br} vacancy site, and thus interacts with the two under coordinated Sn_{5c} cations that emerge after vacancy formation. Further, both H_{hl} configurations on the reduced surface feature a Cl atom filling the vacancy site, while the H atom interacts with the nearby bridging oxygen O_{br} atom.

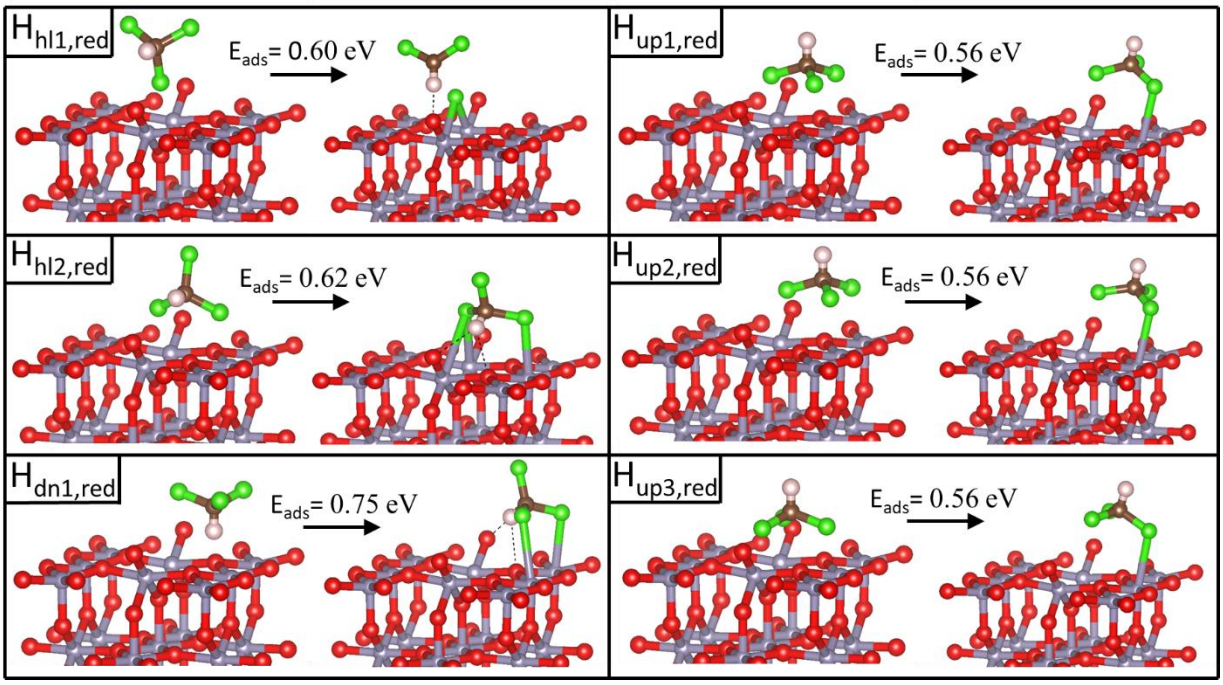

Figure 7-5. Studied configurations of chloroform before and after adsorption on the oxygen-defective (110) surface. Red color represents oxygen atoms, gray is tin, green is chlorine, brown is carbon, and white is hydrogen.

For all configurations, the calculated adsorption energies for chloroform on the defective surface (ΔE_{ads}= 0.56-0.75 eV) are less stable than those calculated for a perfect surface, indicating weaker binding on the reduced surface. Yet, similar to the adsorption on the stoichiometric surface, a clear relationship between binding strength and the number of binding modes between the molecule and the reduced surface in the optimized geometry is observed. Once more, the $H_{dn1,red}$ configuration exhibits the highest adsorption strength (0.75 eV) on the defective surface, followed by the H_{hl} configurations (~0.61 eV), and the H_{up} configurations (~0.56 eV).

Focusing on the most stable configuration ($H_{dn1,red}$), the relaxed structure shows a slight distortion from the corresponding configuration on the stoichiometric surface mainly because the $O_{br\text{-}vac}$ breaks the overall symmetry causing the horizontally oriented H atom to interact with only one, rather than two, surface O_{br} atoms. This considerably stretches one of the Cl-Sn_{5c} bonds to 3.27 Å, while the other Cl-Sn_{5c} bond retains a similar bond length of (2.91 Å) to that observed for the stoichiometric case. Correspondingly, the interaction between the H atom and surface O_{br} atom exhibits a shorter bonding distance of 2.15 Å, compared to the 2.44 Å seen for the perfect surface indicating a stronger electrostatic interaction. A similar stretching in the C-Cl bond to 1.799 Å is observed for the reduced case.

Although the $H_{hl1,red}$ is only the third most stable configuration for chloroform adsorption on the defective surface, its relaxed structure exhibits a unique feature that is not observed for any other configuration on either the reduced or the stoichiometric surfaces. After relaxation, the Cl atom near the defect location dissociates and goes to fill the bridging oxygen vacancy (O_{br}) site, while the conjugate dichloromethyl group ($CHCl_2$) binds to the adjacent O_{br} atom. This observation suggests that the dechlorination of the chloroform molecule over the reduced surface is thermodynamically possible.

Role of dispersive (vdW) interactions

The effective tripod of three electronegative chlorine atoms on one side of the chloroform molecule gives rise to a finite dipole moment that significantly affects its adsorption properties [40]. Thus, long-range vdW interactions are considered in our calculations based on the empirical dispersion corrections proposed by Grimme (D3) in conjunction with the Becke-Johnosn (BJ) damping technique. In this method, the total corrected energy of the system E_{tot} is the summation of the conventional DFT energy E_{DFT}, and an additional energy term that accounts for dispersive interactions E_{disp} [61]. Hence, by using a similar formula to the one employed for calculating the adsorption energy, the contribution of dispersive interactions between the surface and the adsorbate molecule can be evaluated as:

$$E_{ads} = \Delta E_{tot} = \Delta E_{DFT} - \Delta E_{disp} \qquad (7-7)$$

The calculated values of the dispersion energy for the stoichiometric and the oxygen defective surfaces are given in Tables 1. For all the studied systems, the contribution of dispersive interactions to the adsorption energy is significant (>50%). For the most stable configuration on the stoichiometric surface ($H_{dn1,sto}$), dispersive interactions account for 59% of the adsorption energy (1.00 eV) indicating a weak chemisorption process. On the other hand, the contribution of dispersive interactions is higher (69%) for the most stable configuration on the reduced surface, while the adsorption energy is lower (0.75 eV), suggesting a strong physisorption phenomena on the defective surface. In general, the contribution of dispersion to the adsorption energy for the reduced surfaces (66%-96%) is greater than stoichiometric surfaces (53%-79%), despite the fact that the magnitudes of the dispersion energies are almost similar for both cases. This can be simply explained by the higher total adsorption energies on the stoichiometric surfaces due to the strong electrostatic interactions between the H atom and surface oxygen atoms.

7.5.3 Electronic Structure Calculations

Charge transfer mechanisms

To further elucidate the sensing mechanism of SnO_2 towards chloroform, we conducted Bader Charge Analysis [62] for all the adsorption configurations highlighted in the previous sections (Table 1). For both the stoichiometric and oxygen defective surfaces, adsorption of chloroform is accompanied by the release of charge from the molecule to the surface, which is in agreement with the drop in the film's resistance observed in the sensing experiments. The only exception is the $H_{hl1,red}$ case for chloroform dechlorination over the reduced surface, where the molecule uptakes a net charge of 0.25 e after adsorption. The reversal in the charge transfer direction for this particular configuration can be attributed to the high electronegativity of the dissociated Cl atom filling the $O_{br\text{-}vac}$ site, which uptakes charge from the undercoordinated Sn_{5c} cations that possess excess charge due to vacancy formation [45].

Figure 7-6 displays the differential charge density plots for the most stable configurations on the stoichiometric and oxygen defective surfaces. The plotted charge density deformation is described as:

$$\Delta\rho = \rho_{(surf+mol)} - (\rho_{surf} + \rho_{mol}) \qquad (7-8)$$

The blue color represents the regions experiencing charge density depletion, indicating the release of electrons, while the yellow color represents the regions with a gain in the charge density due to the trapping of electrons. As can be observed from the figures, an excess charge density (yellow isosurface) is accumulated around the surface bridging oxygen (O_{br}) and in-plane oxygen (O_{ip}) atoms in the topmost layer from either the stoichiometric or the reduced surface, accompanied by a charge depletion zone (blue isosurface) localized around the H atom from chloroform. This

indicates that surface oxygen atoms act as electrophilic centers that uptake charge from the chloroform molecule upon adsorption, which also explains the net release of charge from chloroform to SnO_2. Bader charge analysis demonstrates that for the stoichiometric case, surface oxygen atoms from the topmost layer gain a total of 0.086 e while the H atom from chloroform loses 0.123 e. For the reduced case, surface oxygen atoms gain 0.075 e while H loses 0.117 e. In both cases, part of the charge lost by the hydrogen atom is also localized over the adjacent carbon atom. In addition to the electrostatic interaction between the surface oxygens and chloroform's hydrogen, another strong covalent interaction is observed between surface Sn_{5c} centers and Cl atoms for both the stoichiometric and reduced surfaces. This can be visualized by inspecting the charge depletion zones (blue) around both atoms, while a charge accumulation zone (yellow) is simultaneously formed along the line connecting their centers, indicating strong electron sharing between the two atoms as a clear sign of covalent bonding. Yet, the formed Sn-Cl bond is polar as indicated by the small charge accumulation (yellow) zone localized around the more electronegative chlorine atoms.

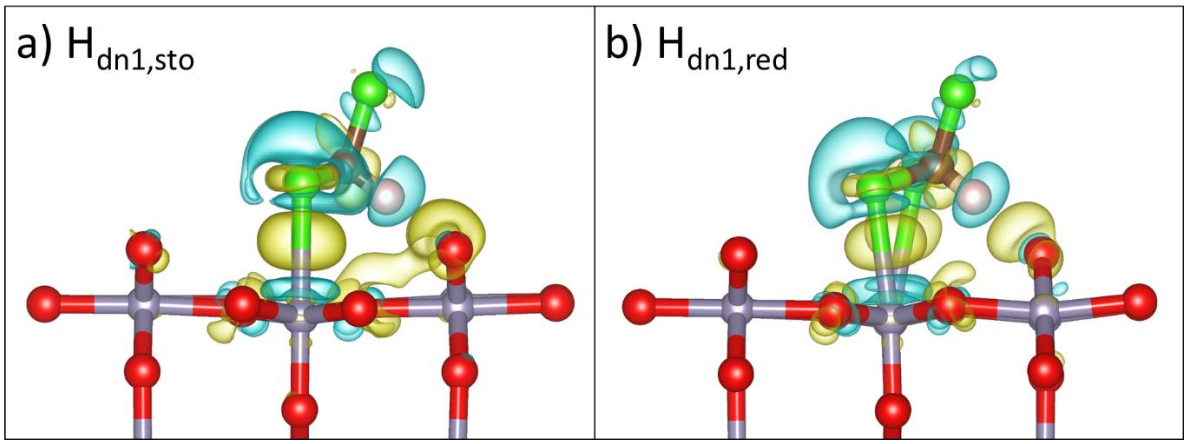

Figure 7-6. Charge density deformation plots for the most stable configurations of chloroform adsorption on the (a) stoichiometric (110) surface, and (b) reduced (110) surface. Blue and yellow colors represent zones experiencing a charge density depletion and accumulation, respectively.

Density of states analysis

Further insight into how chloroform adsorption influences the electronic properties of the SnO_2 sensor can be gained by conducting density of states (DOS) calculations. Figure 7-7 shows the total density of states (TDOS) plots of the chloroform molecule before and after adsorption on the stoichiometric surface for the most stable configuration ($H_{dn1,sto}$). Two major changes can be observed. First, the free state is characterized by isolated peaks corresponding to discrete molecular orbitals, while the adsorbed state features a clear broadening in the peaks near the HOMO level. Regardless, no significant change is observed for deep states ($E \leq -10$ eV), where the peaks remain sharp and isolated. Such broadening in the peaks of the adsorbed molecule indicates a strong hybridization with the orbitals of the surface, which is additional evidence of covalent-like bonding between the molecule and the surface. The second observation is that the TDOS peaks of the adsorbed molecule are shifted towards lower energies. Previous studies attributed the shifting of the orbital energy levels to charge transfer corresponding to ionic bonding, while peak broadening was attributed to covalent bonding [63]. Based on these classifications, the electronic structure of the adsorbed molecule is altered due to strong orbital hybridization with the SnO_2 surface orbitals, which supports the hypothesis that adsorption on the stoichiometric surface is a chemical adsorption phenomena. To understand the nature of this hybridization, the projected density of states (PDOS) for each atom type in the free chloroform molecule (i.e. C, H, and Cl) were inspected. The peaks near the Fermi level are found to mainly consist of the p-states of the Cl atoms. To demonstrate orbital coupling between the molecule and the surface, the PDOS of the Cl atoms in the adsorbed chloroform molecule is plotted in Figure 7-8, together with the PDOS of the surface Sn_{5c} centers at which the molecule binds as previously mentioned. The hybridization seems

to take place mainly within the valence band region of the SnO_2 surface. In this region, PDOS of the two atoms show a strong overlap between the p-states of Cl, and the s- and d-states of Sn_{5c}.

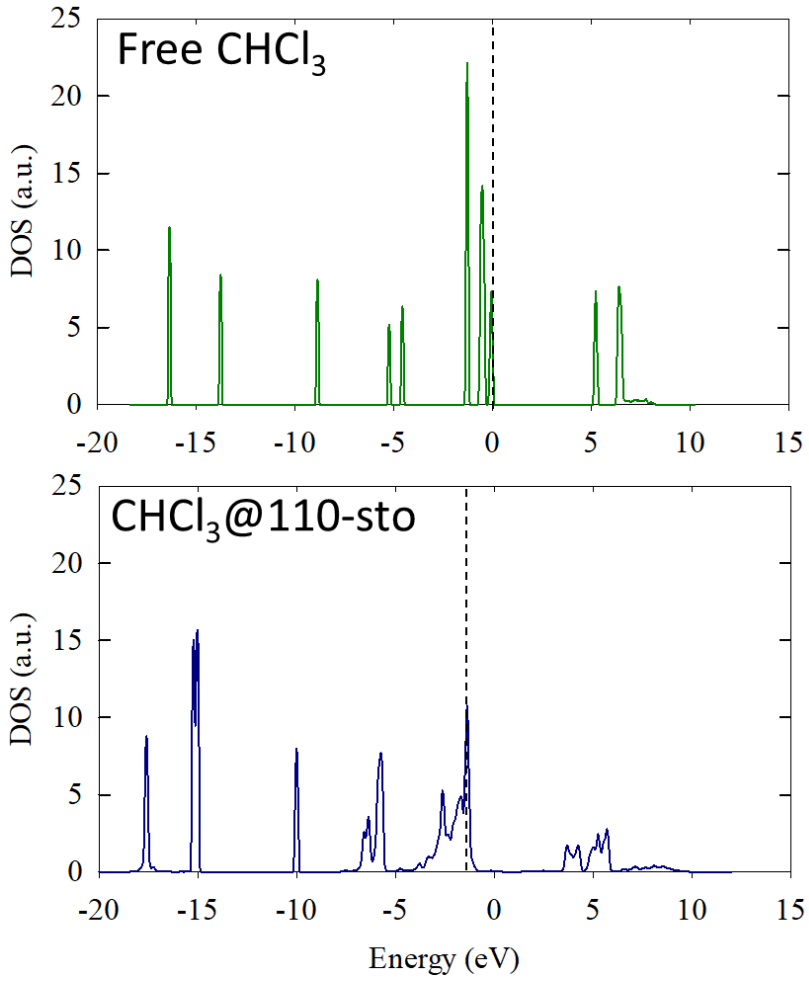

Figure 7-7. The total density of states (TDOS) plot of the chloroform molecule before and after adsorption on the stoichiometric (110) surface. The zero energy is set to the HOMO level of the free chloroform molecule isolated in the vacuum space above the surface.

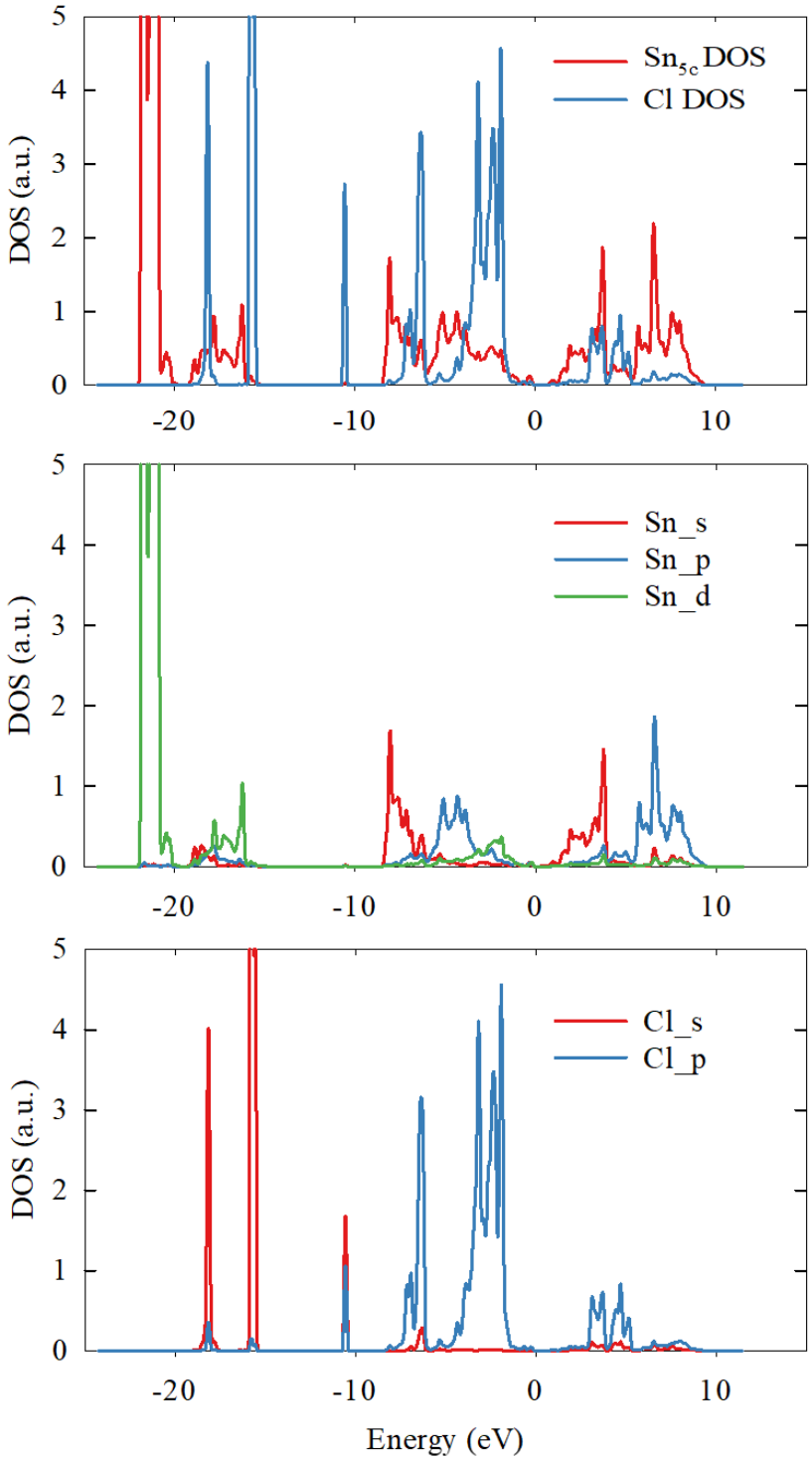

Figure 7-8. The projected density of states (PDOS) plots of the bonded Cl atoms and surface Sn_{5c} centers for the case of chloroform adsorption on the stoichiometric (110) surface. The zero energy is set to the VBM of the stoichiometric surface.

7.5.4 Ab-initio Molecular Dynamics Simulations at Room Temperature

To elucidate the sensing mechanism at room temperature, we perform AIMD simulations on the (110) surface for (1) the stoichiometric case, (2) the oxygen defective case, and (3) the oxygen defective case with pre-adsorbed oxygen species. For scenarios (2) and (3), two bridging oxygen atoms are removed from the topmost atomic layer to create the reduced surface (25% of the exposed O_{br} atoms). For each scenario, three chloroform molecules are randomly placed at a large distance above the surface (~5 Å) at the beginning of the simulation and then allowed to move freely under canonical conditions (NVT) for the entire simulation period (15 ps). For all scenarios, chloroform molecules descend gradually towards the surface as the simulation proceeds and then adsorb initially at random locations after a short period (3~4 ps). Molecules then diffuse laterally across the surface for a longer period (5~6 ps), during which different binding configurations are sampled. Eventually, the simulation equilibrates when all the chloroform molecules find their most stable adsorption sites on the surface, at which they vibrate periodically for the rest of the simulation period (last 5~7 ps). Figure 7-9 shows the change in the free energy of the ionic system during the AIMD simulation for the stoichiometric surface, where it can be observed that the energy of the system initially drops as the molecules approach the surface, then fluctuates while the molecules sample different adsorption configurations until it eventually reaches a minimum energy state once all the chloroform molecules have met their most stable adsorption sites.

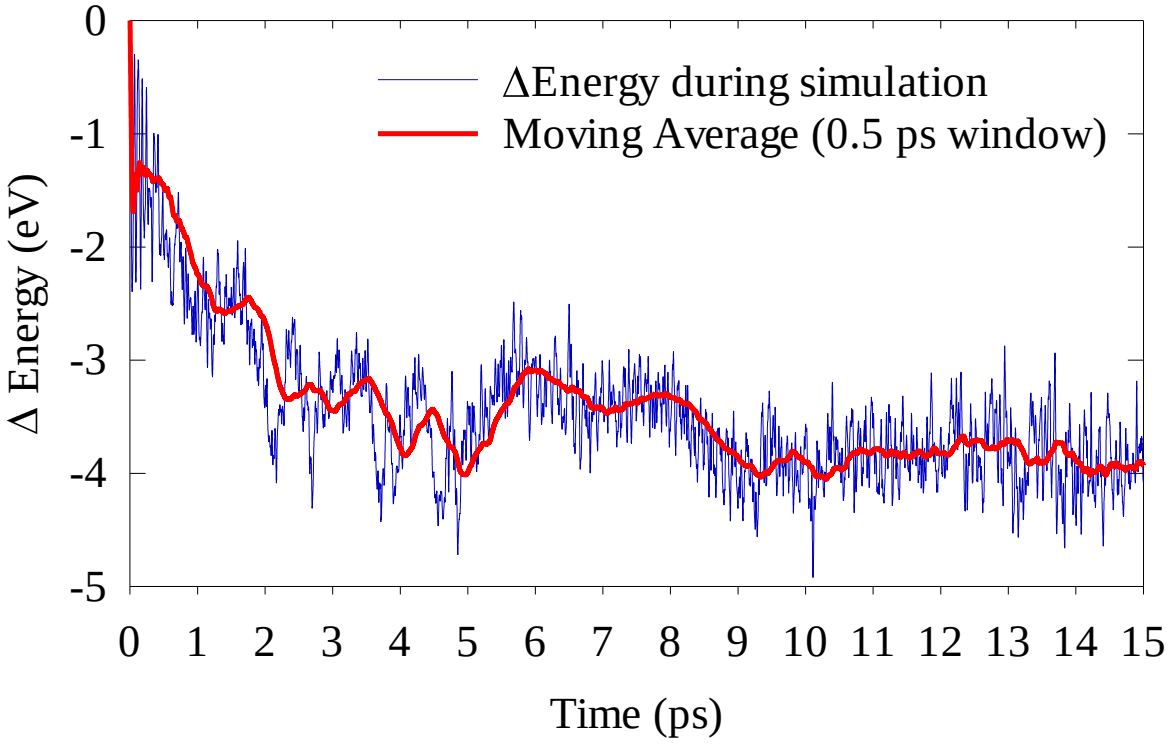

Figure 7-9. Change in the total energy of the system during the AIMD simulation of chloroform adsorption on the stoichiometric (110) surface.

Figure 7-10 depicts a final snapshot of the AIMD simulations after 15 ps for the three simulated scenarios. For the first scenario (stoichiometric surface – Figure 7-10a), the final adsorption configuration of two out of the three chloroform molecules is identical to the most stable ($H_{dn1,sto}$) configuration predicted by the DFT calculations with two Cl atoms bound to Sn_{5c} centers while the H atom interacts with the neighboring two O_{br} atoms and one O_{ip} atom interchangeably. The third configuration, however, resembles the $H_{up1,sto}$ configuration where the H atom is pointing upwards, while two Cl atoms interact with Sn_{5c} centers. For the second scenario (reduced surface – Figure 7-10b), each of the three chloroform molecules takes a different final configuration, where only one molecule adopts the most stable ($H_{dn1,red}$) configuration. One of the other two molecules adopts the ($H_{hl2,red}$) configuration, the second most stable for the reduced surface, in which one Cl

fills the O_{br} vacancy location, the other Cl interacts with the neighboring Sn_{5c} center, and the H atom interacts with a surface O_{br} atom. Interestingly, the third molecule takes a configuration identical to the most stable configuration on the stoichiometric surface ($H_{dn1,sto}$). These results suggest that, at room temperature, chloroform molecules do not necessarily adopt the most stable configuration; instead, they might be 'trapped' in another thermodynamically stable configuration for a certain period.

For the third scenario (reduced surface with pre-adsorbed O_2), two oxygen molecules are first introduced to the system at a similar 5 Å distance from the reduced surface. The NVT simulations were then run for 5 ps before introducing the three chloroform molecules to ensure that oxygen molecules pre-adsorb on the surface. The two oxygen molecules find stable binding sites at the oxygen defect location almost immediately (< 0.5 ps). They take the straddled binding configuration whereby one oxygen atom fills the vacancy site, while the other interacts with the neighboring Sn_{5c} atom. Following their adsorption on the surface, the O=O bonds stretch by up to 0.31 Å (from 1.23 Å before adsorption to 1.54 Å after adsorption). Despite the stretching, O=O bonds do not break completely during the simulation, which confirms that the majority of the pre-adsorbed oxygen species at room temperature are (O_2^-) rather than (O^-) in agreement with our previous DFT results [45].

After introducing the three chloroform molecules, they do not show any particular interaction with the pre-adsorbed oxygen molecules, except during the second phase of sampling different adsorption configuration where the H atom is sometimes seen electrostatically attracted to one of the oxygen atoms in a fashion similar to their attraction to surface O_{br} atoms. The final configuration (Figure 7-10c), however, does not show any interaction between chloroform and pre-adsorbed O_2. Instead, all three molecules take configurations similar to the adsorption on the

stoichiometric surface at the Sn_{5c} centers. It is important to note that the topmost layer has 16 Sn atoms, only half of which are five-fold coordinated Sn_{5c} centers. Thus, following oxygen adsorption, only 6 Sn_{5c} centers are available for chloroform adsorption through Cl-binding, which should be enough to bind all the three chloroform molecules with the most stable $H_{dn1,sto}$ configuration where each molecule binds to two Sn_{5c} centers. However, only one chloroform molecule was able to find this configuration, while the other two took the $H_{hl1,sto}$ configuration with only one Cl atom bound to Sn_{5c} while the other being consistently repelled by the pre-adsorbed oxygen atom. These results suggest that pre-adsorbed oxygen species might force chloroform molecules to adopt less stable configurations if their surface concentration is high enough to pre-occupy all the oxygen vacancies (and thus the neighboring Sn_{5c} centers) on the surface. In general, AIMD results suggest that pre-adsorbed oxygen species play a minimal role in the sensing mechanism at room temperature since the incoming chloroform molecules prefer binding directly to the surface rather than interacting with them.

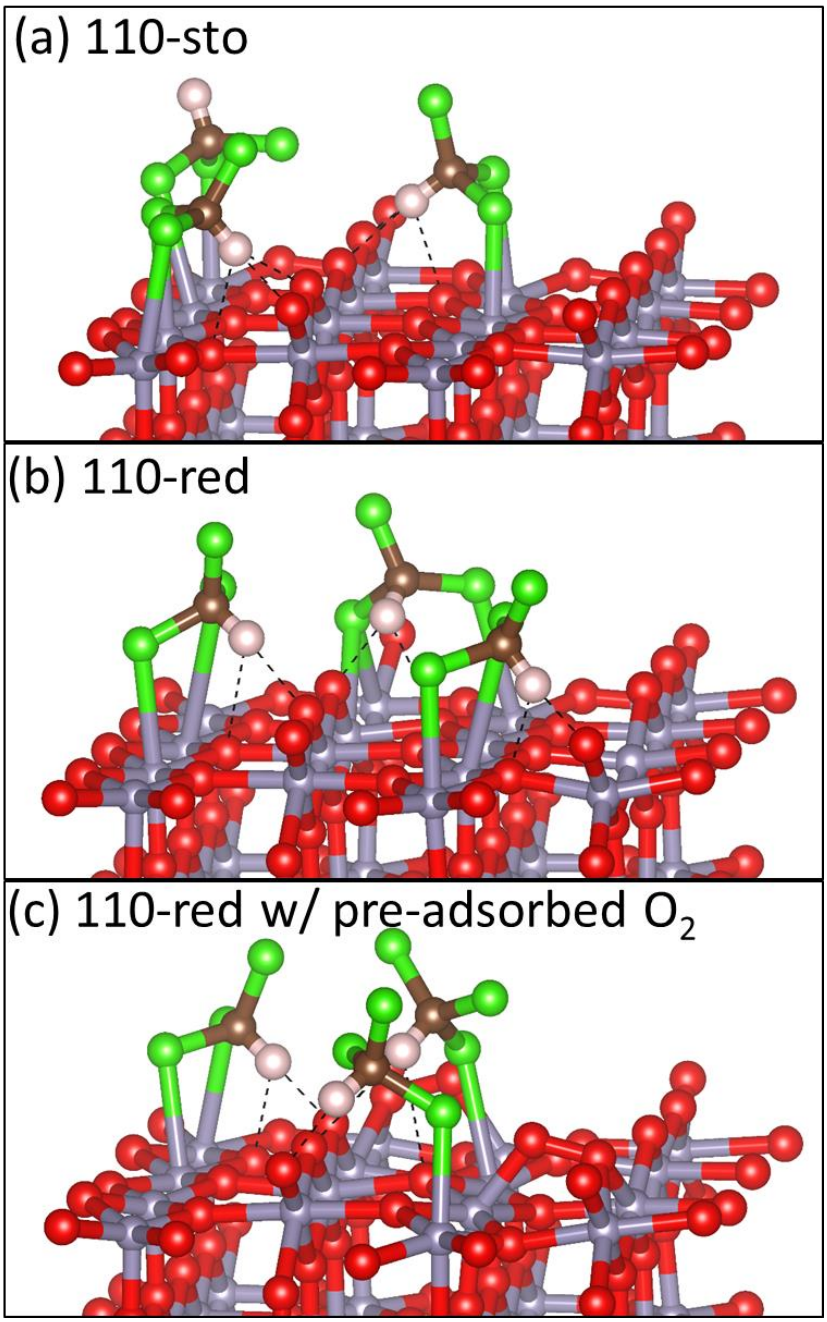

Figure 7-10. A final snapshot of the *ab initio* molecular dynamics (AIMD) simulation at 15 ps for the (a) stoichiometric (110) surface, (b) reduced (110) surface, and (c) reduced (110) surface with pre-adsorbed O_2 species.

7.6 Conclusions

Chloroform is a toxic volatile organic compound that is widely present in a variety of systems. Room temperature sensing of chloroform by nanostructured SnO_2 thin film sensors is demonstrated both theoretically and experimentally. Thin SnO_2 films are prepared using a single-step aerosol chemical vapor deposition (ACVD) process that has a strong potential for scale-up. Dispersion-corrected density functional theory calculations of chloroform's adsorption on the SnO_2 surface were used to elucidate the sensing mechanism. Calculations show that chloroform's adsorption on both the stoichiometric and oxygen defective (110) surface of rutile SnO_2 is thermodynamically favorable, and with binding energies that are much stronger than previously calculated energies for chloroform's adsorption on carbon-based materials. Chloroform molecules are observed to donate charge to the SnO_2 surface following their adsorption, which triggers a sensing response by lowering the resistance of the thin film sensors, and is in agreement with the observed sensing response. The electronic structure of the chloroform molecule is strongly distorted after adsorption and the density of states features a strong orbital hybridization between the surface and the molecule, which suggests a chemical adsorption phenomenon. *Ab initio* molecular dynamics simulations are implemented to examine the adsorption mechanism at room temperature in the presence of oxygen from the ambient atmosphere. Simulations demonstrate that chloroform molecules minimally interact with the pre-adsorbed oxygen species (O_2^-), supporting the hypothesis that the primary sensing mechanism at room temperature is attributed to the direct adsorption of chloroform molecules on the sensor's surface rather than due to interactions with the ionosorbed oxygen. Taken together, the results of this study suggest that chemiresistive metal-oxide gas sensor arrays can provide a cheaper and more portable alternative to traditional gas analysis methods, such as GC-MS or GC-ECD, for the detection of chlorinated volatile organic

compounds in industrial and environmental systems. More specifically, such sensor arrays can be implemented for the real-time monitoring of carcinogenic trihalomethane compounds in drinking water supply systems, which is of significant importance for protecting public health.

7.7 Acknowledgments

Partial support from the Lucy and Stanley Lopata Endowment and McDonnell Academy Global Energy and Environmental Partnership (MAGEEP) at Washington University in St. Louis is gratefully acknowledged.

7.8 References

[1] R.J. Flanagan, D.J. Pounder, A chloroform-related death: Analytical and forensic aspects, Forensic Sci. Int. 197 (2010) 89–96.

[2] Toxicological Profile for Chloroform, Agency Toxic Subst. Dis. Regist. (1997).

[3] L. Xu, X. Yao, A. Khan, M. Mavrikakis, Chloroform Hydrodechlorination over Palladium-Gold Catalysts: A First-Principles DFT Study, ChemCatChem. 8 (2016) 1739–1746.

[4] A.A. Abokifa, Y.J. Yang, C.S. Lo, P. Biswas, Investigating the role of biofilms in trihalomethane formation in water distribution systems with a multicomponent model, Water Res. 104 (2016) 208–219.

[5] A.A. Abokifa, Y.J. Yang, C.S. Lo, P. Biswas, Water quality modeling in the dead end sections of drinking water distribution networks, Water Res. 89 (2016) 107–117.

[6] X. Wang, Y. Mao, S. Tang, H. Yang, Y.F. Xie, Disinfection byproducts in drinking water and regulatory compliance: A critical review, Front. Environ. Sci. Eng. 9 (2015) 3–15.

[7] L. Zoccolillo, L. Amendola, C. Cafaro, S. Insogna, Improved analysis of volatile halogenated hydrocarbons in water by purge-and-trap with gas chromatography and mass spectrometric detection, J. Chromatogr. A. 1077 (2005) 181–187.

[8] D.H. Cho, S.H. Kong, S.G. Oh, Analysis of trihalomethanes in drinking water using headspace-SPME technique with gas chromatography, Water Res. 37 (2003) 402–408.

[9] L. Alexandrou, B. Meehan, P. Morrison, O. Jones, A New Method for the Fast Analysis of Trihalomethanes in Tap and Recycled Waters Using Headspace Gas Chromatography with Micro-Electron Capture Detection, Int. J. Environ. Res. Public Health. 14 (2017) 527.

[10] J.L. Pérez Pavón, S. Herrero Martín, C. García Pinto, B. Moreno Cordero, Determination of trihalomethanes in water samples: A review, Anal. Chim. Acta. 629 (2008) 6–23.

[11] S.W. Chiu, K.T. Tang, Towards a chemiresistive sensor-integrated electronic nose: A review, Sensors. 13 (2013) 14214–14247.

[12] N. Barsan, D. Koziej, U. Weimar, Metal oxide-based gas sensor research: How to?, Sensors Actuators, B Chem. 121 (2007) 18–35.

[13] C. Wang, L. Yin, L. Zhang, D. Xiang, R. Gao, Metal oxide gas sensors: Sensitivity and influencing factors, Sensors. 10 (2010) 2088–2106.

[14] K. Wetchakun, T. Samerjai, N. Tamaekong, C. Liewhiran, C. Siriwong, V. Kruefu, A. Wisitsoraat, A. Tuantranont, S. Phanichphant, Semiconducting metal oxides as sensors for environmentally hazardous gases, Sensors Actuators, B Chem. 160 (2011) 580–591.

[15] M.X. Nie, X.Z. Li, S.R. Liu, Y. Guo, ZnO/CuO/Al2O3 composites for chloroform detection, Sensors Actuators, B Chem. 210 (2015) 211–217.

[16] E. Şennik, U. Soysal, Z.Z. Öztürk, Pd loaded spider-web TiO2 nanowires: Fabrication, characterization and gas sensing properties, Sensors Actuators, B Chem. 199 (2014) 424–432.

[17] J. Zhang, X. Liu, G. Neri, N. Pinna, Nanostructured Materials for Room-Temperature Gas Sensors, Adv. Mater. 28 (2016) 795–831.

[18] P.M. Perillo, D.F. Rodríguez, A room temperature chloroform sensor using TiO_2 nanotubes, Sensors Actuators B Chem. 193 (2014) 263–266.

[19] Y. Zhou, X. Lin, Y. Wang, G. Liu, X. Zhu, Y. Huang, Y. Guo, C. Gao, M. Zhou, Study on gas sensing of reduced graphene oxide/ZnO thin film at room temperature, Sensors Actuators, B Chem. 240 (2017) 870–880.

[20] M. Law, H. Kind, B. Messer, F. Kim, P. Yang, Photochemical sensing of NO_2 with SnO_2 nanoribbon nanosensors at room temperature, Angew. Chemie - Int. Ed. 41 (2002) 2405–2408.

[21] J.D. Prades, R. Jimenez-Diaz, F. Hernandez-Ramirez, S. Barth, A. Cirera, A. Romano-Rodriguez, S. Mathur, J.R. Morante, Equivalence between thermal and room temperature UV light-modulated responses of gas sensors based on individual SnO_2 nanowires, Sensors Actuators, B Chem. 140 (2009) 337–341.

[22] C. Jiang, G. Zhang, Y. Wu, L. Li, K. Shi, Facile synthesis of SnO_2 nanocrystalline tubes by electrospinning and their fast response and high sensitivity to NO_x at room temperature, CrystEngComm. 14 (2012) 2739–2747.

[23] Y. Wei, C. Chen, G. Yuan, S. Gao, SnO_2 nanocrystals with abundant oxygen vacancies:

Preparation and room temperature NO_2 sensing, J. Alloys Compd. 681 (2016) 43–49.

[24] B.-Y. Wei, M.-C. Hsu, P.-G. Su, H.-M. Lin, R.-J. Wu, H.-J. Lai, A novel SnO_2 gas sensor doped with carbon nanotubes operating at room temperature, Sensors Actuators B Chem. 101 (2004) 81–89.

[25] Y. Wang, X. Jiang, Y. Xia, A Solution-Phase, Precursor Route to Polycrystalline SnO_2 Nanowires That Can Be Used for Gas Sensing under Ambient Conditions, J. Am. Chem. Soc. 125 (2003) 16176–16177.

[26] G. Lu, L.E. Ocola, J. Chen, Room-temperature gas sensing based on electron transfer between discrete tin oxide nanocrystals and multiwalled carbon nanotubes, Adv. Mater. 21 (2009) 2487–2491.

[27] L.L. Fields, J.P. Zheng, Y. Cheng, P. Xiong, Room-temperature low-power hydrogen sensor based on a single tin dioxide nanobelt, Appl. Phys. Lett. 88 (2006) 263102.

[28] N. Van Hieu, L.T.B. Thuy, N.D. Chien, Highly sensitive thin film NH3 gas sensor operating at room temperature based on SnO2/MWCNTs composite, Sensors Actuators, B Chem. 129 (2008) 888–895.

[29] Q. Zhao, Y. Gao, X. Bai, C. Wu, Y. Xie, Facile synthesis of SnO2 hollow nanospheres and applications in gas sensors and electrocatalysts, Eur. J. Inorg. Chem. (2006) 1643–1648.

[30] G. Chen, S. Ji, H. Li, X. Kang, S. Chang, Y. Wang, G. Yu, J. Lu, J. Claverie, Y. Sang, H. Liu, High-Energy Faceted SnO2-Coated TiO2 Nanobelt Heterostructure for Near-Ambient Temperature-Responsive Ethanol Sensor, ACS Appl. Mater. Interfaces. 7 (2015) 24950–24956.

[31] J.M. Wu, A room temperature ethanol sensor made from p-type Sb-doped SnO2 nanowires., Nanotechnology. 21 (2010) 235501.

[32] D. Zhang, J. Liu, H. Chang, A. Liu, B. Xia, Characterization of a hybrid composite of SnO_2 nanocrystal-decorated reduced graphene oxide for ppm-level ethanol gas sensing application, RSC Adv. 5 (2015) 18666–18672.

[33] D. Zhang, A. Liu, H. Chang, B. Xia, Room-temperature high-performance acetone gas sensor based on hydrothermal synthesized SnO2-reduced graphene oxide hybrid composite, RSC Adv. 5 (2015) 3016–3022.

[34] G. Zhang, X. Han, W. Bian, J. Zhan, X. Ma, Facile synthesis and high formaldehyde-sensing performance of NiO–SnO_2 hybrid nanospheres, RSC Adv. 6 (2016) 3919–3926.

[35] Y. Liu, P. Yang, J. Li, K. Matras-Postolek, Y. Yue, B. Huang, Formation of SiO_2@SnO_2 core–shell nanofibers and their gas sensing properties, RSC Adv. 6 (2016) 13371–13376.

[36] R.K. Mishra, S.B. Upadhyay, A. Kushwaha, T.-H. Kim, G. Murali, R. Verma, M. Srivastava, J. Singh, P.P. Sahay, S. Hee Lee, SnO_2 quantum dots decorated on RGO: a superior sensitive, selective and reproducible performance for a H_2 and LPG sensor, Nanoscale. 7 (2015) 11971–11979.

[37] A.K. Nayak, R. Ghosh, S. Santra, P.K. Guha, D. Pradhan, Hierarchical nanostructured WO_3–SnO_2 for selective sensing of volatile organic compounds, Nanoscale. 7 (2015) 12460–12473.

[38] Y.L. Tian, J.F. Ren, W.W. Yue, M.N. Chen, G.C. Hu, X.B. Yuan, Adsorption of chloroform on N-doped and Al-doped graphene: A first-principle study, Chem. Phys. Lett. 685 (2017)

344–348.

[39] J. Åkesson, O. Sundborg, O. Wahlström, E. Schröder, A van der Waals density functional study of chloroform and other trihalomethanes on graphene, J. Chem. Phys. 137 (2012) 174702–104709.

[40] E. Kuisma, C.F. Hansson, T.B. Lindberg, C.A. Gillberg, S. Idh, E. Schröder, Graphene oxide and adsorption of chloroform: A density functional study, J. Chem. Phys. 144 (2016) 184704–174702.

[41] E.C. Girão, Y. Liebold-Ribeiro, J.A. Batista, E.B. Barros, S.B. Fagan, J. Mendes Filho, M.S. Dresselhaus, A.G. Souza Filho, Functionalization of single-wall carbon nanotubes through chloroform adsorption: theory and experiment., Phys. Chem. Chem. Phys. 12 (2010) 1518–24.

[42] A.A. Tamijani, E. Ebrahimiaqda, Probing the (110)-Oriented plane of rutile ZnF 2 : A DFT investigation, J. Phys. Chem. Solids. 111 (2017) 63–69.

[43] K. Haddad, Material Synthesis and Device Design for Sensor Arrays and their Application in the Analysis of Volatile Organic Compounds, Ph.D. Thesis, Washington University in St. Louis, 2018.

[44] K. Haddad, A. Abokifa, S. Kavadiya, T.S. Chadha, P. Shetty, Y. Wang, J. Fortner, P. Biswas, Growth of single crystal, oriented SnO2 nanocolumn arrays by aerosol chemical vapour deposition, CrystEngComm. 18 (2016) 7544–7553.

[45] A.A. Abokifa, K. Haddad, J. Fortner, C.S. Lo, P. Biswas, Sensing Mechanism of Ethanol and Acetone at Room Temperature by SnO2 Nano-columns Synthesized by Aerosol Routes:

Theoretical Calculations Compared to Experimental Results, J. Mater. Chem. A. 6 (2018) 2053–2066.

[46] E. Thimsen, N. Rastgar, P. Biswas, Nanostructured TiO2 films with controlled morphology synthesized in a single step process: Performance of dye-sensitized solar cells and photo watersplitting, J. Phys. Chem. C. 112 (2008) 4134–4140.

[47] T. Soundappan, K. Haddad, S. Kavadiya, R. Raliya, P. Biswas, Crumpled graphene oxide decorated SnO2 nanocolumns for the electrochemical detection of free chlorine, Appl. Nanosci. 7 (2017) 645–653.

[48] G. Kresse, J. Furthmüller, Efficient iterative schemes for *ab initio* total-energy calculations using a plane-wave basis set, Phys. Rev. B. 54 (1996) 11169–11186.

[49] G. Kresse, J. Furthmüller, Efficiency of ab-initio total energy calculations for metals and semiconductors using a plane-wave basis set, Comput. Mater. Sci. 6 (1996) 15–50.

[50] G. Kresse, D. Joubert, From ultrasoft pseudopotentials to the projector augmented-wave method, Phys. Rev. B. 59 (1999) 1758–1775.

[51] P.E. Blöchl, Projector augmented-wave method, Phys. Rev. B. 50 (1994) 17953–17979.

[52] J.P. Perdew, K. Burke, M. Ernzerhof, Generalized Gradient Approximation Made Simple, Phys. Rev. Lett. 77 (1996) 3865–3868.

[53] J. Oviedo, M.J. Gillan, Energetics and structure of stoichiometric SnO2 surfaces studied by first-principles calculations, Surf. Sci. 463 (2000) 93–101.

[54] S. Grimme, Semiempirical GGA-type density functional constructed with a long-range dispersion correction, J. Comput. Chem. 27 (2006) 1787–1799.

[55] A. Gurlo, R. Riedel, In situ and operando spectroscopy for assessing mechanisms of gas sensing, Angew. Chemie - Int. Ed. 46 (2007) 3826–3848.

[56] A. Gurlo, Interplay between O2 and SnO2: oxygen ionosorption and spectroscopic evidence for adsorbed oxygen, ChemPhysChem. 7 (2006) 2041–2052.

[57] M. Habgood, N. Harrison, An ab initio study of oxygen adsorption on tin dioxide, Surf. Sci. 602 (2008) 1072–1079.

[58] M. Tang, Z. Zhang, Q. Ge, A DFT-based study of surface chemistries of rutile TiO2 and SnO2(110) toward formaldehyde and formic acid, Catal. Today. 274 (2016) 103–108.

[59] F. Trani, M. Causa', D. Ninno, G. Cantele, V. Barone, Density functional study of oxygen vacancies at the SnO2 surface and subsurface sites, Phys. Rev. B. 77 (2008) 245410.

[60] M. Epifani, J.D. Prades, E. Comini, E. Pellicer, M. Avella, P. Siciliano, G. Faglia, A. Cirera, R. Scotti, F. Morazzoni, J.R. Morante, The role of surface oxygen vacancies in the NO2 sensing properties of SnO2 nanocrystals, J. Phys. Chem. C. 112 (2008) 19540–19546.

[61] J. Klimeš, A. Michaelides, Perspective: Advances and challenges in treating van der Waals dispersion forces in density functional theory, J. Chem. Phys. 137 (2012) 120901.

[62] W. Tang, E. Sanville, G. Henkelman, A grid-based Bader analysis algorithm without lattice bias, J. Phys. Condens. Matter. 21 (2009).

[63] M. Viitala, O. Cramariuc, T.T. Rantala, V. Golovanov, Small hydrocarbon adsorbates on SnO2(110) surfaces: Density functional theory study, Surf. Sci. 602 (2008) 3038–3042.

Chapter 8

Conclusions and Future Directions

8.1 Summary of the Dissertation

To guarantee the efficient and sustainable operation of our aging water supply system, advanced computational tools for the simulation and management of the water quality need to be developed. A water supply system can be visualized as a huge reactor with numerous processes taking place at a wide range of length and time scales. The formation and degradation of the various compounds are dictated by the chemical interactions taking place at the molecular level, while their fate and transport at the continuum scale is controlled by the various mass transfer phenomena. This highlights the need for developing a multi-scale modeling framework that is capable of providing the finest description of each of the phenomena of interest at its appropriate scale of resolution, while simultaneously linking these scales to render a high fidelity representation of the system. The main objective of the presented work is to demonstrate and apply multi-scale modeling techniques to understand the fundamental physical, chemical, and biological processes that dictate the water quality in the supply system. Towards this goal, this dissertation focused on creating computational models at three interdependent scales of resolution:

8.1.1 Continuum Scale Modeling

In the context of water distribution systems, continuum-scale models are the most useful since they enable the prediction of the spatiotemporal concentration profiles of the different water constituents, while incorporating the influence of the dynamic hydraulics in the system on their fate and transport. Hence, the main focus of this dissertation was on developing advanced reactive-transport models for the simulation of the chemical and microbiological deterioration of drinking water quality as it travels through the distribution network and inside premise plumbing by simulating the decay and transport of disinfectants, the formation and transport of disinfection byproducts and biomass, and the release of lead.

In **Chapter 2**, an advanced transport modeling technique capable of accurately simulating the low-flow dead-end zones of the distribution system is developed. The model considers both dispersive solute transport mechanisms and the spatiotemporal distribution of flow demands. Comparison against field measurements of free chlorine and fluoride tracer revealed that the simulation results of the newly developed model are more accurate than previously developed advection-based models, and advection-dispersion models in the literature. The approximation of spatial aggregation of flow demands for simulating water quality was found to cause substantial errors in the simulation of disinfectant transport and decay in the dead-ends.

In **Chapter 3**, a multi-species reactive transport model is developed to simulate the dynamic interplay between the various water constituents, including the transformation of the biodegradable fraction of natural organic matter (NOM) into biomass through biofilm growth, biomass release through biofilm detachment under shear stresses, and DBP formation from the parallel reactions of chlorine with precursors of both microbial and non-microbial origin. This model is used to investigate the role of biofilms in the formation and fate of disinfection byproducts in the pipes of the distribution system. Simulation results revealed that fast bacterial regrowth in the system increases the contribution of biomass-derived precursors to the total THMs budget, especially if high initial chlorine doses were applied to preserve the microbiological quality of the finished water. The results highlighted the importance of integrating bacterial dynamics modeling with predictive DBPs formation models.

In **Chapter 4**, a transport model for the simulation of particulate and dissolved lead release from full and partially replaced LSLs was developed by coupling a mass transfer model with a stochastic residential water demand generator to investigate the effect of normal household usage (NHU) flow patterns on lead exposure. Applying the model within a Monte-Carlo simulation

framework, the partial replacement of the LSL was predicted to result in releasing spikes with significantly high concentrations of particulate lead (1011.9±290.3 µg/L) that were five times higher than those released from the full LSL. Sensitivity analysis revealed that the intensity of flow demands significantly affects particulate lead release, while dissolved lead levels were more dependent on the lengths of stagnation periods. The results highlighted the importance of incorporating realistic demand simulations in conjunction with the transport model for the accurate estimation of total lead exposure.

8.1.2 System Scale Modeling

Chapter 5 considers the design problem of finding the optimal layout and scheduling of booster chlorination systems from a new perspective. While previous studies in the literature focused on applying different optimization routines to enhance the accuracy and computational speed of solving the optimization problem, this study looked further into examining the influence of the underlying water quality model used to conduct the simulations on the outcomes of the optimization. To this end, the advection-dispersion-reaction (ADR) transport model that was developed for the accurate simulation of dead-end pipes is linked to a genetic algorithm based optimization routine. The objective function is formulated and solved to find the optimal locations and chlorine-dosing schedules of the booster stations that minimize the total cost of booster construction and operation, while maintaining a sufficient residual throughout the distribution network. The results of this study suggest that optimization outcomes generated by EPANET simulations may produce a booster chlorination system that fails to maintain an adequate residual concentration in the periphery pipes of a real-life water distribution system. The results highlight the importance of considering dispersive solute transport, as well as the excessive residence times encountered in the dead-end sections, in the water quality simulations conducted for network

optimization problems. While this study addressed the optimization of booster chlorination systems, its implications extend to a wide array of network optimization applications, including pump scheduling for water quality optimization, optimal sensor placement for reactive contaminant detection, and design of real-time boost-response systems.

8.1.3 Molecular Scale Modeling

Chemical interactions and material properties result from quantum mechanical interactions between atoms or molecules, hence, quantum chemical calculations were employed in this study to investigate the molecular mechanisms leading to the formation of disinfection byproducts, and to study the surface chemistry of novel nanomaterials applied for their sensing.

Chapter 6 proposes employing first-principles calculations to investigate the molecular mechanisms of trihalomethane formation from the chlorination of model humic precursors. Quantum chemical computations are used to explore the reaction mechanism, and to study the kinetics and thermodynamics of the reaction pathway. The proposed framework is demonstrated by elucidating the chlorination mechanism of resorcinol (1,3-dihydroxybenzene), which has been identified in the literature as an efficient precursor for the formation of chloroform. Computational results bring new insights into the structures of intermediates and transition states, kinetics of the elementary reactions along the mechanism, and identifying the dominant formation pathways.

Chapter 7 demonstrated the room temperature sensing of chloroform by nanostructured SnO_2 thin film sensors both theoretically and experimentally. Thin SnO_2 films are prepared using a single-step aerosol chemical vapor deposition (ACVD) process that has a strong potential for scale-up. Dispersion-corrected density functional theory calculations of chloroform's adsorption on the SnO_2 surface were used to elucidate the sensing mechanism. Calculations show that chloroform's adsorption on the surface of rutile SnO_2 is thermodynamically favorable. Chloroform molecules

are observed to donate charge to the SnO_2 surface following their adsorption, which triggers a sensing response by lowering the resistance of the thin film sensors, and is in agreement with the observed sensing response. Taken together, the results of this study suggest that chemiresistive metal-oxide gas sensor arrays can provide a cheaper and more portable alternative to traditional gas analysis methods, such as GC-MS or GC-ECD, for the detection of chlorinated volatile organic compounds in industrial and environmental systems. More specifically, such sensor arrays can be implemented for the real-time monitoring of carcinogenic trihalomethane compounds in drinking water supply systems, which is of significant importance for protecting public health.

8.2 Future Directions

8.2.1 Impacts of water conservation practices on water quality

As the overall domestic per-capita water consumption continues to decline under the enhanced efficiency of water use fixtures and widespread embracement of water conservation practices, concerns have arisen over the implications of the decreased flow velocities on the water quality, especially in these problematic zones. It is hence important to study the effects of the increased residence time on the water quality in the low-flow sectors of the distribution network under various potential water conservation scenarios. A combined framework that joins the advanced transport models described in Chapter 2 with the detailed reactions developed in Chapter 3 is required to assess the impacts of water conservation practices. Furthermore, as more water utilities shift from using chlorine to chloramine as their disinfectant of choice, the formation of the currently unregulated nitrogenous disinfection byproducts (N-DBPs) is expected to increase, which poses a public health concern given their toxicity. Thus, future work should aim at expanding the proposed framework to incorporate the formation of emerging byproducts, especially N-DBPs, such as nitrosamines and haloacetonitriles.

It is noteworthy that the multi-species model proposed in chapter 3 offers a great deal of flexibility in the simulation of different constituents thanks to the underlying numerical scheme used to solve the governing transport equations. The split operator method (SOM) offers an efficient way to decouple the transport and the reaction compartments of the model by splitting the governing mass balance partial differential equations (PDEs) into a set of independent PDEs for the transport (advection and dispersion/diffusion) of each constituent, and a separate system of coupled ordinary differential equations (ODEs) for the reactions of all constituents. Hence, other solutes can be readily included in the model by simply adjusting the set of ODEs provided that the correct reaction expressions and parameters are included. This applies to, for example, replacing the reaction terms of the disinfectant from those corresponding to free chlorine to reflect the reactions of chloramine with NOM and biomass. Assuming that a similar two-constituent second-order kinetic model is used; the kinetic parameters in equations S-3.1 to S-3.10 can be changed based on data from bench-scale experiments and then calibrated and validated against pilot scale or field measurements following the same procedure described in Chapter 3. For instance, the yield coefficient for DBP formation in equation S-3.5 and the biomass inactivation coefficient in equation S-3.4 will likely be lower for the case of chloramine compared to free chlorine, which is a stronger oxidant. In addition, the formation of other N-DBPs can be included if kinetic data for their formation is available from bench scale experiments.

Furthermore, a modeling framework that incorporates the multi-species reactive transport model proposed in chapter 3 can be developed to study the intrusion of microbial contaminants through the cracks of the pipes and junctions. The intrusion of microbiological pathogens usually takes place when low or negative pressure episodes occur at or near such cracks, and in the presence of an external contamination source (such as leakage from sewer mains). The intrusion

is controlled by numerous factors, all of which have been extensively studied in the previous literature, including the magnitude and duration of the low/negative pressure event, the pathway for pathogen entry, pathogen occurrence in the external source of contamination, and volume of water that may enter through the different pathways. Yet, the fate and transport of such pathogenic species after they enter the pipes of the distribution system has not been well studied although it significantly dictates the public exposure. Using this framework, the mechanisms by which such microorganisms can be harbored within the existing biofilms, their decay via interactions with the disinfectant, and the role of the hydraulics can be examined.

8.2.2 Water quality deterioration in premise plumbing systems due to lead corrosion

The recent crisis in Flint, MI drew attention to the significant public health hazards of lead poisoning through the exposure to Pb-contaminated drinking water. Pb contamination results from the internal corrosion of Pb-containing materials in contact with water. While the major source of lead in drinking water is typically the lead service line (LSL), which generally accounts for 50-75% of Pb concentrations measured at the tap, other plumbing components such as Pb-containing fixtures, fittings, and solder can also contribute to the total lead at the tap. Chapter 4 focused on developing a transport model for the simulation of particulate and dissolved lead release from full and partially replaced LSLs. This can be incorporated into a comprehensive computational tool for the simulation of lead release from the various premise-plumbing components. Such tool can be useful for the estimation of total lead concentrations at the tap, and the comprehensive framework can be used for predicting areas in the supply system with an elevated risk of high Pb levels by linking lead release models with the reactive transport models that simulate the water chemistry in the distribution system.

In addition, a computational modelling system that incorporates the lead release model developed in Chapter 4 into a Monte Carlo probabilistic framework for simulating lead emissions within a water supply area can be developed to mimic the real-world variation in the factors controlling lead release from LSLs. Such modeling framework can help water utilities assess the impacts of proposed changes to water treatment on lead release, design sampling procedures to evaluate lead exposure, or optimize corrective measures to lower lead levels in their systems. The utility needs to first calibrate the presented model using data from pilot scale studies that examine lead release in their systems. In these pilot studies, it is preferred to use harvested pipe sections cut from aged LSLs to match the prevalent lead scales in their systems. After calibration, the model can be used in conjunction with the stochastic flow generator to assess lead levels in a simulated water supply zone under a range of different scenarios. The input parameters characterizing each scenario can be classified into three different categories: (i) Parameters related to the water chemistry and types of lead scales (plumbosolvency), (ii) Water use patterns (demand parameters), and (iii) LSL geometric characteristics (length, diameter). Statistical Distribution based on data collected from the field (ii, and iii) + pilot scale experiments with harvested LSL sections (i) can be used to generate the inputs for the Monte-Carlo simulations. This modeling framework can then be used to evaluate various sampling strategies and to identify optimal intervention measures to control Pb levels, or be incorporated into a risk assessment tool for lead exposure that considers the variability in Pb concentration across the system.

Another important point for future research is related to the description of particulate lead transport. As discussed in section 4.3.1, particulate transport in fluid flow is governed by multiple phenomena that include convection, diffusion, coagulation, and deposition. These phenomena are dependent on the particle size; hence, particulate transport can be best described by tracking the

evolution of particle size distribution, which can be achieved using a governing transport equation similar to equation 4-2. Yet, since accurate measurements of the size distributions of lead particulates released from lead service lines had not been done in the previous literature, at least up until this work was published, the use of this extensive formulation was not possible at this stage. A modeling approach that considers the size distribution of lead particles and their coagulation under different water chemistry scenarios will be very helpful.

Furthermore, particulate lead generation from partially replaced lead service lines needs to be investigated by future studies. It is well known that the significant disturbances caused by cutting and connecting the copper pipe to the partially replaced lead service line destabilizes the existing scales in the remaining section of the lead pipe, which leads to the release of Pb particles on the short term as observed in numerous pilot-scale experiments and field sampling data. Yet, long-term release of particulate lead from partially replaced service lines was also observed, which suggests that galvanic corrosion plays a key role in the generation of Pb particles. This process is likely caused by the structural destabilization of the lead-oxide layer that is caused by the galvanic corrosion of the underlying lead pipe in which elemental lead is oxidized to Pb^{2+}. This is indeed supported by previous pilot scale studies that showed that the galvanic currents display minimal reduction even after several months following the partial replacement of the LSL. One possible way to account for this important mechanism in the model is by changing the generation term in equation 4-8, from being empirically calibrated to experimental data, to a one that incorporates the galvanic current. Alternatively, the mechanism for particle generation can be based on aqueous nucleation, which could be either homogenous or heterogenous (i.e. catalyzed by the presence of other solids). In this case, both the dissolved and particulate lead models should be linked to account for the transformation between the two phases.

8.2.3 Real-time Optimization and Management of the Water Quality

Optimization of the water quality in the supply system can be achieved by linking water treatment processes to the real-time (RT) hydraulic and water quality conditions in the distribution system. Nevertheless, simulating the water quality in the entire system is computationally expensive, which inhibits running the optimization algorithms in RT. Future studies should aim to develop advanced real-time modeling and optimization techniques capable of handling large on-line monitoring and control data to enable better water quality management. To achieve this goal, modern optimization techniques, such as Bayesian optimization, can be adopted to enable RT optimization of the expensive objective functions by minimizing the number of required simulations to find the optimal solution. In addition, machine learning can be used to build cheaper surrogate models to imitate the complexity of the physics-based water quality models. Building on the transport models developed under theme one, ideas in the real-time optimization of disinfectant dosing and corrosion control treatment to maximize disinfectant residuals and minimize lead levels in the system can be explored. Furthermore, a framework for finding optimal network sectorization scenarios through stochastic modeling approaches to maximize the water quality while minimizing treatment/operation costs can be very useful.

In addition, a framework similar to the one presented in chapter 5 for the optimization of booster chlorination systems can be developed for optimizing the locations of water quality monitors for contaminant intrusion detection. The decision variables, in this case, are the locations of a given number of monitoring stations, and the objective function will target minimizing the expected time of contaminant detection and minimizing public exposure to the contaminant under a range of different possible contamination scenarios. The influence of using an advanced water quality model for simulating both a conservative and reactive contaminants on the outcomes of the

optimization can be examined. This problem can also be expanded to a multi-objective optimization framework by optimizing the location of the monitoring stations for regulatory monitoring (e.g. placing the monitors in locations with the highest potential for DBP formation or lowest chlorine residuals), in addition to the rapid detection of deliberate or accidental contaminant intrusion.

8.2.4 Leveraging Advances in Materials Science Research for on-line Sensing

Current advances in applied nanoscience have offered promising solutions to many of the challenges associated with improving and managing water quality. The past decade has witnessed a revolution in developing functional nano-based materials for the efficient and cost-effective sensing of water quality parameters, including metal/metal-oxide nanoparticles and carbon-based materials. Advancing the design of nanoscale sensors with high sensitivity and specificity towards water contaminants is of significant interest for the purposes of water quality monitoring and management. A key factor that controls the performance of such nano-based sensors is their surface chemistry because it dictates the adsorption and transformation mechanisms of different compounds. First principles simulation techniques based on quantum chemistry can hence provide valuable guidance, as they are capable of simulating surface interactions with an atomistic-scale resolution. A useful feedback loop can be established in which insights from theoretical calculations are used for the rational design of these nanomaterials and applied to elucidate their surface catalysis mechanisms.

Analysis of regulated disinfection byproducts typically involves rigorous sampling techniques that are commonly off-line, costly, and time-intensive. A promising alternative is to capitalize on the inherent volatility of many of the drinking water DBPs, such as trihalomethanes, to enable headspace sampling with chemiresistive vapor sensors, commonly known as e-noses.

Semiconducting metal oxides are commonly employed as the active sensing material in such resistive gas sensors because of their high sensitivity, unique chemical and physical stability, scalability, and low cost. Nevertheless, the high working temperature (150-400 °C) typically required to operate these sensors reduces their long-term stability and complicates their miniaturization. Computational chemistry methods can be used to investigate and tune the surface chemistry of metal-oxide sensors to enable their operation at ambient temperatures with high sensitivity and selectivity towards regulated DBPs. Chapter 7 focused on understanding the adsorption and surface interaction mechanisms of ethanol and acetone as model polar VOCs, as well as chloroform as a model trihalomethane, on tin dioxide (SnO_2) nanosensors. To enhance the sensitivity, this framework can be extended to other metal-oxide candidates such as ZnO, CuO, and Al_2O_3, and their composites with carbon-based materials, such as reduced graphene oxide (RGO) and doped graphene. In addition, computational screening of metal dopants, such as Pt, Pd, Au, and Ni, and the tuning of functional groups on carbon-based materials, can be pursued to enhance the selectivity of the sensors towards specific DBPs of interest.

Appendix I

Real-Time Identification of Cyber-Physical Attacks on Water Distribution Systems via Machine Learning Based Anomaly Detection Techniques

Results presented in this chapter are currently under review in:

A. A. Abokifa, K. Haddad, C. Lo, and P. Biswas. Real-Time Identification of Cyber-Physical Attacks on Water Distribution Systems via Machine Learning Based Anomaly Detection Techniques. Journal of Water Resources Planning and Management (Revision submitted – April 2018)

I.1 Abstract

Smart water infrastructures are prone to cyber-physical attacks that can disrupt their operations or damage their assets. An algorithm is developed to identify suspicious behaviors in the different cyber-physical components of a smart water distribution system. The algorithm incorporates multiple modules of anomaly-detection techniques to recognize different types of anomalies in the real-time monitoring and control data. Trained artificial neural networks are used to detect unusual patterns that do not conform to normal operational behavior. Principal component analysis is conducted to decompose the high-dimensional space occupied by the sensory data to uncover global anomalies. The algorithm is trained using a historical dataset of trusted observations and tested against a validation and a test dataset, both featuring a group of simulated attack scenarios. The proposed approach successfully identifies all the attacks featured in the BATtle of the Attack Detection ALgorithms (BATADAL) datasets with high sensitivity and specificity. Nevertheless, the performance is sensitive to high background noise in the sensory data.

I.2 Introduction

Numerous water utilities have recently started adopting smart technologies in their drinking water distribution systems (DWDSs) to improve their overall performance, efficiency, and reliability. Smart water distribution networks belong to the group of modern cyber-physical systems (CPSs), in which on-line monitoring, data collection and transmission, real-time computation, and automated operation of the functional processes are tightly integrated (Lee 2008). Hence, smart water grids commonly rely on a coordinated network of distributed sensors and remote actuators, which are typically linked to programmable logic controllers (PLCs). A PLC is an embedded device that handles the data of its linked infrastructure component and simultaneously controls its operation. Process monitoring and control data is usually collected by a supervisory control and data acquisition (SCADA) system, which is a centralized computer that analyzes the data, performs simulations and/or optimization computations, and coordinates the operation of the cyber-physical system in real-time (Shamir and Salomons 2008). The increased interest in embracing smart network technologies over the past decade has been complemented with a consistent growth in the development of related industrial tools and solutions, such as advanced metering technologies (Cominola et al. 2015), sensor networks, data analytics tools, and automation systems. Nevertheless, the enhanced connectivity instigated by such advanced control technology has concurrently opened the door to a novel class of security vulnerabilities that were not inherent to the physical infrastructure system (Laszka et al. 2017; Rasekh et al. 2016).

Despite the numerous merits of implementing modern networking technologies in the sector of critical infrastructure systems, linking the physical components of the infrastructure with cyber-space can expose these systems to the vast realm of cyber-based threats. From a national security standpoint, water infrastructure systems, including drinking water treatment facilities and

distribution networks, possess a sensitive disposition given the critical role they play in the sustainable development of modern communities. This role makes WDSs a highly attractive target for cyber-attacks that can be potentially perpetrated by terrorists, subversives, and adversary states. These attacks can target the SCADA module, the sensors that monitor the system's processes, the PLCs that locally operate the physical components of the infrastructure or the wireless communication routes between the different elements of the CPS. Such cyber-based attacks are capable of remotely perturbing the performance of the system, providing unauthorized parties with access to critical and confidential information, and -if sophisticated enough- can result in physical damage to the assets of the infrastructure. Additionally, such attacks can compromise the water quality by altering automated treatment schemes or by targeting water quality sensors to suppress contamination warnings, which can pose a significant threat to public safety (Laszka et al. 2017).

The last decade has witnessed a spike in the number of cyber-security incidents involving water infrastructure systems. In 2015, the US Department of Homeland Security (DHS) reported that the Industrial Control Systems-Cyber Emergency Response Team (ICS-CERT) received and responded to 25 cyber-related incidents that targeted water and wastewater systems, making it the third highest targeted sector by cyber incidents after critical manufacturing and energy (DHS ICS-CERT 2015). Two well-cited examples for the type of threats that modern water systems face are the cyber-attacks that targeted the SCADA systems of the Maroochy Water Services in Queensland, Australia (Slay and Miller 2008), and the water utility of Boca Raton, Florida (Horta 2007). To mitigate similar threats in the future, previous studies discussed the importance of establishing a mature cyber-security culture within the water industry in order to reduce the susceptibility of smart WDSs to cyber-attacks (Panguluri et al. 2017). Moreover, imposing additional security measures on the different components of the CPS, including the remote

sensors/actuators, the communications network, and the SCADA module (Mathur 2017) can potentially enhance their resilience in the face of cyber-attacks. However, the relatively extended periods of the WDS operation implies that the probability that one of its components is attacked at least once during its lifetime is non-negligible (Taormina et al. 2016). Thus, developing strategies that can effectively detect any abnormal behavior in the different domains of the cyber-physical system in real-time is of prime importance in order to prevent service interruptions and protect both the system's assets and public health. The general problem of the detection and identification of attacks on cyber-physical systems, as well as intrusion detection for the underlying SCADA systems, has been addressed by several studies (Gao et al. 2010; Maglaras and Jiang 2014; Pasqualetti et al. 2013). Nevertheless, most of the previous efforts were devoted to detecting attacks on smart power grids and communication networks (Kosut et al. 2010; Sridhar and Govindarasu 2014), with disproportionately less emphasis on water infrastructure systems.

For drinking water distribution networks, the broad topic of detecting physical-based threats has been previously investigated by several studies that mainly focused on the classical problems of fault detection (Eliades and Polycarpou 2012; Izquierdo et al. 2007; Srirangarajan et al. 2013) and contamination event detection (Arad et al. 2013; Housh and Ohar 2017a; b; Ohar et al. 2015; Perelman et al. 2012). While the problems of detecting cyber-based and physical-based threats both belong to the general class of event identification, three important differences exist between these two problems, namely the spatial and temporal resolutions, and attack concealment (Housh and Ohar 2018). The most fundamental difference is that cyber-based attacks can be potentially concealed by the attacker in order to cover any traces in the sensory data. Attack concealment can be done by means of a deception attack, in which the attacker alters the observations received by the SCADA system by sending false plausible values instead of the real

suspicious ones (Taormina et al. 2017). One possible way to do this is by conducting a “replay attack” in which observations during normal operations are recorded by the attacker, and then replayed to the SCADA system during the attack, which makes the detection of such stealthy attacks a very challenging task.

A few attempts have been made to tackle the problem of cyber-physical attacks detection on water infrastructure systems. Amin et al. (2013a; b) investigated the detection and isolation of cyber-attacks on the SCADA system of an irrigation canal network using an approximate hydrodynamic model. Yet, their work was not extended to pressurized looped WDSs. Almalawi et al. (2016) proposed an intrusion detection method to detect SCADA tailored attacks based on a data-driven clustering technique with a demonstration on a simple WDS model example. Recently, Taormina et al. (2017) developed a modeling framework to assess the hydraulic response of water distribution networks to cyber-physical attacks. The framework consists of two components, namely an attack model that can define the elements of the CPS that can be attacked as well as the types of attacks that can target each element, and a modelling toolbox (implemented in EPANET software) that further simulates the effects of different classes of cyber-attacks on the operation of water distribution systems. Nevertheless, their work focused on simulating and characterizing cyber-attacks rather than their detection and identification.

This study aims to develop an approach for the identification of cyber-physical attacks on WDSs in real-time by detecting suspicious anomalies in the SCADA observations using machine-learning techniques, namely principal component analysis (PCA) and artificial neural networks (ANNs). The design goals of the detection algorithm are: i) to determine the existence of an ongoing attack with maximum speed and reliability; ii) to avoid issuing false alarms and to recognize when the system is no longer under attack, iii) to identify which components of the

cyber-physical infrastructure have been compromised during the attack, and iv) to reliably distinguish between anomalies caused by cyber-attacks and measurement noise. The algorithm is first trained using a trusted set of SCADA observations, then validated, and tested against two different datasets comprising a group of simulated malicious attack scenarios.

I.3 Case Study and Datasets

A medium-sized water distribution network, C-Town network, is used as a benchmark for algorithm development and application. C-Town network consists of 388 nodes connected by 429 links. Water storage and distribution across the network are supplied by seven tanks (T1-T7) whose water levels control the operation of eleven pumps (PU1-PU11) grouped into five pumping stations (PS1-PS5), and one control valve (V2). This network was recently used for the BATtle of the Attack Detection ALgorithms (BATADAL) (Abokifa et al. 2017; Taormina et al. 2018) (https://batadal.net/). The system implements a smart water grid technology featuring a set of remote sensors and actuators in order to monitor and control the operation of all tanks, functioning valves, and pumping stations. These sensors/actuators are connected to nine PLCs that transmit the data to a centralized SCADA system, which coordinates the network operation in real-time.

As described in the BATADAL, the system is subject to a group of simulated cyber-physical attacks that perturb the functionality of the actuators, alter the readings of the deployed sensors, and interfere with the connections between the networked components in the cyber-layer. These attacks are generated with the *MATLAB* modeling toolbox *epanetCPA*, which allows the simulation of the hydraulic response of water distribution systems to cyber-physical attacks using EPANET (Taormina et al. 2017). Three independent datasets are used to *train*, *validate*, and *test* the algorithm, respectively. The first (training) dataset comprises historical SCADA observations generated for a period of one year (on an hourly basis) prior to the deployment of the smart

technology. This dataset is guaranteed to contain no attacks, and hence, it is used to train the algorithm to recognize the normal behavior of the system. The second (validation) dataset was generated for a six-month period following the deployment of the smart technology and contains seven different simulated attack scenarios (Table I-1). This dataset is used to validate the performance of the proposed technique in detecting cyber-physical attacks. In addition, a sensitivity analysis is performed at this step to adjust the different parameters of the algorithm to yield best detection performance. Similarly, the third (test) dataset was generated for a three-month period and contains seven simulated attacks (Table I-2). The test dataset is used herein to verify the efficiency of the tuned algorithm in identifying multiple attacks in a real-time stream of observations that the algorithm has never seen before (i.e. was not part of the training/validation process).

Table I-1. Specifications of the simulated attacks featured in the validation dataset

Att#	Start time End time [dd/mm/yyyy hh]	Attack Details
1	13/09/2016 23 16/09/2016 00	Low level in T7 due to SCADA sending wrong control settings to PLC9. Alteration of T7 water levels reaching SCADA with a replay attack.
2	26/09/2016 11 27/09/2016 10	Similar to Attack #1, but with SCADA concealment extended to pumps PU10/PU11 FLOW and STATUS readings.
3	09/10/2016 09 11/10/2016 20	False low levels readings sent from T1 by PLC2. This triggers PLC1 to keep pumps PU1/PU2 ON, driving T1 to overflow. Concealment of T1 water level increase via progressive offsetting.
4	29/10/2016 19 02/11/2016 16	Similar to Attack #3, but with SCADA concealment performed using replay attack for T1 water levels, PU1/PU2 FLOW and SETTING readings, and PRESSURE at pumps outlet.
5	26/11/2016 17 29/11/2016 04	Working speed of PU7 reduced to 0.9 of nominal speed causing lower water levels in T4.
6	06/12/2016 07 10/12/2016 04	Similar to Attack #5, but speed reduced to 0.7 and water level drop in T4 concealed from SCADA with a replay attack.
7	14/12/2016 15 19/12/2016 04	Similar to Attack #6, but concealment extended to pumps PU6/PU7 FLOW and STATUS readings.

Table I-2. Specifications of the simulated attacks featured in the test dataset

Att#	Start time End time [dd/mm/yyyy hh]	Attack Details
1	16/01/2017 09 19/01/2017 06	Change the Levels of T3 at which PU4 and PU5 operate. Lower levels of T3, which are altered with replay attack for concealment. Replay attacks for concealing pump flows and settings. Inlet and outlet pressure readings are not altered.
2	30/01/2017 08 02/02/2017 00	Attack on sensor readings from T2 to PLC3. T2 reads always LOW and PLC3 keeps the valve V2 OPEN. Concealment done with a polyline on T2.
3	09/02/2017 03 10/02/2017 09	Deliberately Switching PU3 ON
4	12/02/2017 01 13/02/2017 07	Deliberately Switching PU3 ON
5	24/02/2017 05 28/02/2017 08	Similar to Attack 2 but with replay attacks to alter also V2 FLOW/SETTINGS, and suction/discharge pressure readings (P_J14, P_J422)
6	10/03/2017 14 13/03/2017 21	Change the levels at which PU10 and PU11 operate based on T7. PU10 and PU11 will switch continuously. Water levels in T7 are altered using replay attack, so are PU flows/settings and outlet/inlet pressure. Inlet pressure concealments terminate before the end of the other attacks.
7	25/03/2017 20 27/03/2017 01	T4 signal arriving PLC6 is altered

I.4 Anomaly Characterization

In an ideal scenario, the utility should possess an accurate hydraulic model of its WDS that is routinely calibrated by the collected monitoring data. The presence of such a model would be of value in detecting abnormal system behaviors and can provide useful insights if used in conjunction with an algorithm that analyzes the data from the SCADA system. In such a framework, detection of cyber-physical attacks (CPAs) is driven by precise simulations of the system dynamics (Housh and Ohar 2018). Nevertheless, a clear limitation arises for such *"model-based"* approaches in cases where accurate water demand patterns in the system are not readily available or if the network model is computationally expensive prohibiting real-time evaluations (Abokifa et al. 2016). Thus, to reduce the dependence of the designed algorithm on the availability of a calibrated network model, the attack detection problem considered herein is exclusively dependent on the given SCADA observations. Hence, identification of attacks is only achieved through employing anomaly detection techniques that target discovering irregularities in the data induced by cyber-physical attacks. In other words, the main aim of the proposed "*data-based*" approach is to search for *extended inconsistencies* in the observations that can be interpreted as indicators or "fingerprints" inflicted by an ongoing attack. An anomaly can be generally defined as a data point (or a series of points) that does not conform to a well-defined notion of normal behavior (Chandola et al. 2009; Hawkins 1980). Hence, a first step to detect anomalies in a given set of observations is to define a domain (subset) of observations that are trusted to represent the normal behavior of the system. In our case, this domain is defined by the first (training) dataset of historical SCADA observations.

Taormina et al. (2017) provides a thorough discussion on how the operation of WDSs is altered in response to CPAs. Here, we discuss the different classes of anomalies that can be induced by CPAs in the sensory data of WDSs, and propose a different approach to detect each class.

Simple Outliers vs Contextual anomalies

In the context of detecting cyber-physical attacks on WDSs, the definition of an anomaly should not be limited to the identification of "simple outliers", i.e. data points that lie beyond certain historical fences defined based on a reference dataset representing normal (expected) behavior. An example of this is an attack that persistently shuts down a pumping station resulting in excessively low levels in one or more tanks. However, a cyber-physical attack can interfere with the performance of one of the infrastructure components in a way that alters its operational patterns -compared to the normal conditions-, while maintaining its performance characteristics (e.g. tank level or pumping flow rate) within the normal historic min/max bounds. In this case, the anomalous pattern is described as a "contextual anomaly" rather than a simple outlier, which means that the suspicious observation is anomalous within a specific temporal context based on the previous observations, regardless of its magnitude.

To illustrate the difference between these two types of anomalies, Figure 1-a shows a series of anomalous data points observed in the flow data of Pump 1 in the second (validation) dataset. These anomalies correspond to the third attack event (Table I-1). As can be seen, the suspicious data points are noticeably lower in magnitude compared to the minimum historic bound recorded in the first (training) dataset. On the other hand, Figure 1-b shows an anomalous pattern in the flow data of Pump 7, which corresponds to the fifth attack in the validation dataset. In this case, the magnitudes of the anomalous points are well within the previously defined historic bounds.

Nevertheless, pump performance has been clearly interrupted as shown by the evident change in the flow patterns.

In this study, “simple outliers” are detected by comparing the observations to certain statistical fences determined by a given number of standard deviations below and above the mean, and interquartile ranges above and below the upper and lower quartiles. On the other hand, identifying “contextual anomalies” that do not conform to the regular operational patterns requires training the algorithm to “learn” these patterns in the first place. This can be accomplished using a supervised machine-learning algorithm that is trained to forecast a future data point from a series of previous observations. In this study, we used Artificial Neural Networks (ANNs) for this task due to their known capability of modeling complex nonlinear relationships. ANNs were previously used to forecast dynamic time series patterns of water resources variables (Maier and Dandy 2000), and applied to forecast the dynamic hydraulic and water quality states for water distribution networks by creating surrogate models (meta-models) (Broad et al. 2010, 2015; May et al. 2008; Razavi et al. 2012; Romano and Kapelan 2014). In this study, we use ANNs to model the patterns of each individual sensor/actuator, and anomalies are detected by comparing the observed data points against the values predicted by the ANNs model.

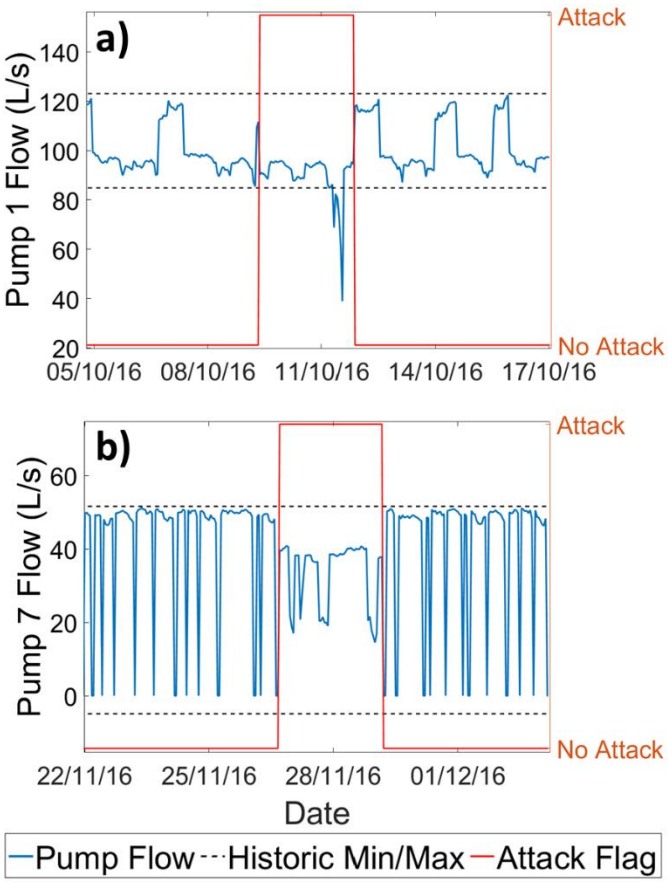

Figure I-1. Validation dataset observations for: (a) Pump 1 flow during attack 3 (simple outlier), and (b) Pump 7 flow during attack 5 (contextual anomaly). Attack Flag indicates when the system is subject to one of the simulated attacks.

Stealthy attacks and global anomalies

As previously discussed, one of the most challenging aspects regarding the detection of cyber-based threats on water distribution systems, and a one that sets it apart from the traditional problem of physical fault detection, is the potential for attack concealment. This may involve replaying part of the historical observations to make the data appear normal. Such *stealthy* attacks may interfere with the performance of multiple components of the WDS without significantly altering the individual characteristics of any of them. For instance, in the seventh attack scenario featured in the validation dataset (Table I-1), the attacker conceals the SCADA readings of the water level in T4, and the flow and status of pumps PU6/PU7 with a replay attack. Hence, detection methods that separately analyze the data from each of these individual sensors, such as statistical fences and ANN models discussed in the previous section, may miss such attacks since the induced anomalies in each of the data arrays will likely be below their detection limits. This highlights the need for incorporating an additional detection method that aims to discover such "global anomalies" by analyzing the combined data obtained from all sensors in the multi-dimensional space.

In this study, we use principal component analysis (PCA), a linear dimensionality reduction technique (Cunningham and Ghahramani 2014; Jolliffe and Cadima 2016), to project the observed multi-dimensional data from all sensors onto a set of principal components. By doing this, anomalies in the data arrays corresponding to all the monitors are synergized, which gives a magnified response enabling the capture of global anomalies corresponding to stealthy attacks (Lakhina et al. 2004). The fundamental concept here is that, for water distribution systems, a certain degree of correlation exists between the global observations made by all the monitors (sensors/actuators) at any given time step. When the attacker conceals the readings of a subset of

these sensors during a certain time step, the concealed readings will not follow this correlation even if they still follow the normal pattern for the concealed component.

To illustrate this concept, Figure 2 depicts a simple case of two sensors with a set of observations comprising an anomaly. The time sequence of the observations is not relevant here, since we are only interested in the correlation between the readings of the two sensors regardless of when these observations are made. The anomalous reading corresponds to a one that the attacker concealed in the data of one of the sensors (sensor 1 in this case). By looking at the projections on the axes representing the two sensors, the anomalous reading appears to fall within the max/min bounds of all observations. Yet, by projecting the data on the principal components, it becomes clear how the concealed point appears as an anomaly on the second principal component.

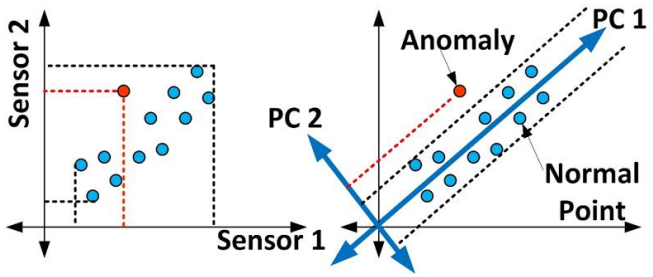

Figure I-2. Schematic of anomaly detection by PCA projection

I.5 Algorithm Development and Anomaly Detection

The detection algorithm is designed as an "ensemble model" featuring four different modules. Each module targets the detection of a specific class of outliers/anomalies separately (Figure 3). The first module checks whether the given SCADA observations follow the actuator rules defined for the system, while the second module focuses on finding simple statistical outliers with excessively high or low magnitudes. The third module aims at revealing contextual anomalies using trained ANN models, and the fourth module targets discovering global anomalies in the multi-dimensional space using PCA. Anomalies from the four modules are then integrated by means of an alarm watch *window* method as discussed in the following subsections.

Module 1: verification of actuator rules

The first module checks that the operational statuses of the pumps and valves follow the appropriate control rules based on the observed water levels in their controlling tanks at all times. For example, in the given C-Town system, Pump 1 operation is controlled by the water level in Tank 1. Actuator control rules dictate that a drop in the tank level below 4 m triggers the operation of Pump 1 by switching it on, which should change its status to (S_PU1 = 1). Pump operation should carry on until the tank level goes above 6.3 meters, at which the pump should be switched off changing the status to (S_PU1 = 0). Thus, these rules might be violated if the system is subject to a "deception" attack that manipulates the communications between the PLC connected to the tank level sensor and that connected to pump actuator. The module returns a flag for each data point that violates any of the rules depicted in the input file.

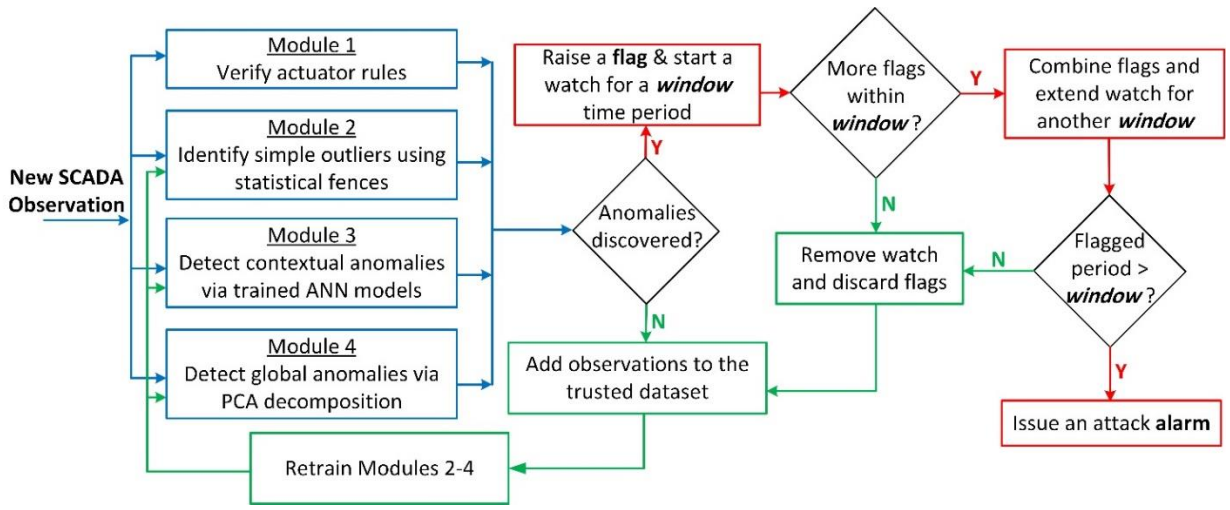

Figure I-3. Schematic diagram of the attack detection algorithm

Module 2: detection of simple outliers via statistical fences

The second module focuses on detecting outliers with suspiciously high/low magnitudes compared to statistical bounds based on historical observations. Let A be the training dataset, which is an $(N \times M)$ matrix comprising N observations (time-steps) from M monitors (sensors/actuators). Hence, $A = [\xi_1, \xi_1, \dots, \xi_M]$, where $\xi_i = [x_{1,i}, x_{2,i}, \dots, x_{j,i}, \dots, x_{N.i}]^T$ is the vector of N observations made by monitor *i*, and $x_{j,i}$ is the observation made by monitor i during time step j. A simple statistical approach to detect outliers in a new observation made by one of the monitors can be done by specifying certain boundaries for each monitor i defined by multiples of the standard deviation above and below the mean, or based on the interquartile range (IQR) as follows:

$$\text{Upper fence: } u_i = \max(\mu_i + n_i^u \sigma_i \ , \ \ Q3_i + m_i^u [Q3_i\text{-}Q1_i]) \tag{1}$$

$$\text{Lower fence: } l_i = \min(\mu_i\text{-}n_i^l \sigma_i \ , \ \ Q1_i\text{-}m_i^l [Q3_i\text{-}Q1_i]) \tag{2}$$

where, u_i and l_i are the designated upper and lower boundaries for monitor i; μ_i and σ_i are the mean and standard deviation of data vector ξ_i, respectively; $Q1_i$ and $Q3_i$ are the lower and upper quartiles of the data array ξ_i, respectively; n_i^u and n_i^l are the standard deviation multipliers

representing the upper and lower fences; and m_i^u and m_i^l are the interquartile range multipliers for the upper and lower fences, respectively. The upper and lower multipliers of the standard deviation and the IQR (i.e. $n_i^{u,l}$ and $m_i^{u,l}$) are defined based on the maximum and minimum values recorded in the training dataset for each monitor. The first module compares new observations by any of the monitors, e.g. in the validation or test datasets, to the upper and lower fences, and returns a flag for any observation lying beyond these fences, with an arbitrary tolerance margin (5%).

Module 3: detection of contextual anomalies via ANN models

Herein, ANN models are used to construct the forecasted patterns for each of the monitored hydraulic parameters based on the learned system performance from the training dataset to uncover anomalous patterns. To this end, ANN models are designed to predict a single future reading from a series of previous observations for each of the monitors. A multi-layer perceptron (MLP) neural network model is used, which is a computational model consisting of multiple layers of inter-connected artificial neurons. Each neuron performs a nonlinear computation, and the weighted sum of the outputs from all the neurons in one layer is fed to the neurons of the following layer (feed-forward NN).

ANN models architecture

A separate ANN model is constructed for each individual monitor. The output layer consists of one neuron, while the input layer consists of a set of I input neurons, which comprises the array of previous observations used to predict the next observation. A single layer of hidden neurons is employed, with a number of hidden neurons that is equal to the number of neurons in the input layer. Therefore, each monitor's training data array ξ_i containing N observations is split into a group of (N-I) training sets, with each set consisting of I inputs and one desired output. For

example, the first set for any monitor *i* will comprise observations $[x_{1,i}, x_{2,i}, \ldots, x_{I,i}]$ as inputs and $[x_{I+1,i}]$ as the desired output. The output of each neuron k can be written as:

$$y_k = g\left(\sum_{r=1}^{I} x_{r,k} w_{r,k} + w_{0.k}\right) \tag{3}$$

where, y_k is the output of neuron k, $x_{r,k}$ and $w_{r,k}$ are the input and the weight coefficient of neuron k in the current layer from neuron r in the preceding layer, $w_{0.k}$ is the bias coefficient of neuron k, and g is the hyperbolic-tangent sigmoid transfer function defined as:

$$g(z) = \frac{2}{1 + e^{-2z}} - 1 \tag{4}$$

By tuning the weights assigned to each neuron, the desired relationship between the inputs and the outputs of the ANN can be established. This process is known as training or learning, and in this study, it is done using a backpropagation algorithm that adjusts the weight coefficients of the ANN through minimizing the error between model predictions and the observations for each one of the (N-I) training sets using the Levenberg-Marquardt optimization algorithm incorporated in the MATLAB R2016a Neural Network Toolbox™.

The performance of the ANN forecasting model mainly depends on its architecture. Typically, increasing the number of neurons enhances the accuracy, yet it also increases the complexity and computational burden of training the model. The maximum training error generated from the constructed ANN models for the water level in Tank 1 with different architectures was studied. Each architecture is characterized by a different size (i.e. number of neurons) for the hidden layer, which is also equivalent to number of input observations I. Error bars represent the standard deviation of five different ANN models constructed for each architecture. As expected, the accuracy of the trained ANNs increases consistently with increasing the size of the input/hidden layer since the number of previous observations propagated into the

model to forecast a future data point increases. Nevertheless, no significant enhancement is observed for architectures with $I > 40$ neurons. Similar behavior is also observed in the models for Pump 1 flow. Thus, an input/hidden layer size of $I = 40$ is selected for all ANN models to achieve an acceptable performance with minimal complexity.

Data Pre-processing

Prior to constructing the ANN models, we observed that the raw hydraulic data for tank levels, pumping flow rates, and pressures, comprises sharp fluctuations on short time intervals (Figure 1), which makes training the ANNs a complex and computationally demanding process. Therefore, instead of using raw observations, preprocessing is first conducted by projecting the data into a spectral frequency domain representation of the time series signal in order to generate a smoothed form of the data that preserves the same structure but with less frequent fluctuations. To do that, the Fast Fourier Transform (FFT) of the signal is obtained to decompose the time series data into its underlying frequencies for each of the given data arrays ($\boldsymbol{\xi}_i$). Then, the raw data is smoothed using a third degree low pass Butterworth filter, with a cutoff frequency that corresponds to 50% of the cumulative amplitude of the signal. Figure 4 shows the flow data for pumps 1 and 7 before and after smoothing for the same attack events displayed in Figure 1. It demonstrates that the filtered data clearly features the same anomalies existing in the raw data for both types of anomalies, but the high frequency fluctuations are significantly smoothed. In addition to facilitating the ANN training process, smoothing the data decreases the training error, which results in a higher forecasting accuracy for the trained models and enhances anomaly detection.

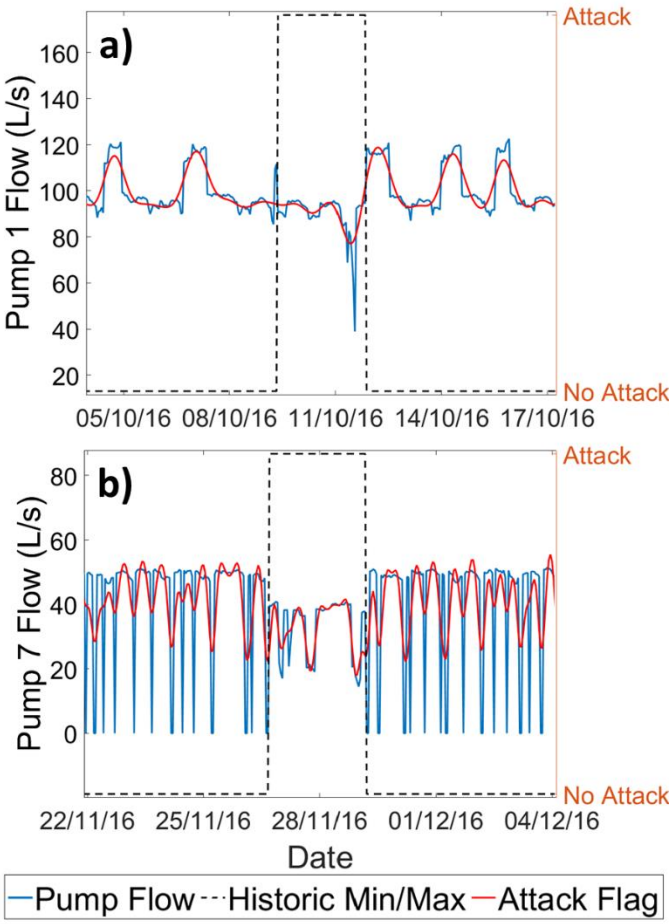

Figure I-4. Raw vs. smoothed data for: (a) Pump 1 flow (simple outlier), and (b) Pump 7 flow (contextual anomaly).

Anomaly detection via ANN

To define anomalies using the trained ANNs, a different technique should be used in place of the previously described statistical fences (Equations 1, & 2). Herein, anomalous observations are defined based on their deviation from the values predicted by the ANN model, and thus, the accuracy of the model in forecasting normal observations should be considered in such evaluation. Therefore, outliers should be defined based on how large their prediction errors are in comparison with the maximum error encountered in forecasting observations of the training dataset. For each monitor i, the maximum training error can be written as:

$$\epsilon_i^{train} = \max_s\left(\left|o_{i,s}^{train}\text{-}p_{i,s}^{train}\right|\right) \tag{5}$$

where, $o_{i,s}$ and $p_{i,s}$ are the desired (observed) and predicted outputs of training set s for monitor i. In this study, observations in both the validation and test datasets that have a prediction error greater than the maximum training error multiplied by a specific factor α are considered anomalous:

$$\left|o_i^{valid/test}\text{-}p_i^{valid/test}\right| \geq \alpha\ \epsilon_i^{train} \tag{6}$$

To demonstrate this, Figure 5-a shows the smoothed flow observations for pump 10 for the validation dataset as well as the predicted values by the ANN model. The depicted threshold is equal to ($\pm\epsilon^{train}$). The deviation (error) between the predicted and observed points during the attack event is clearly larger than that when the system is not under attack (Figure 5-b).

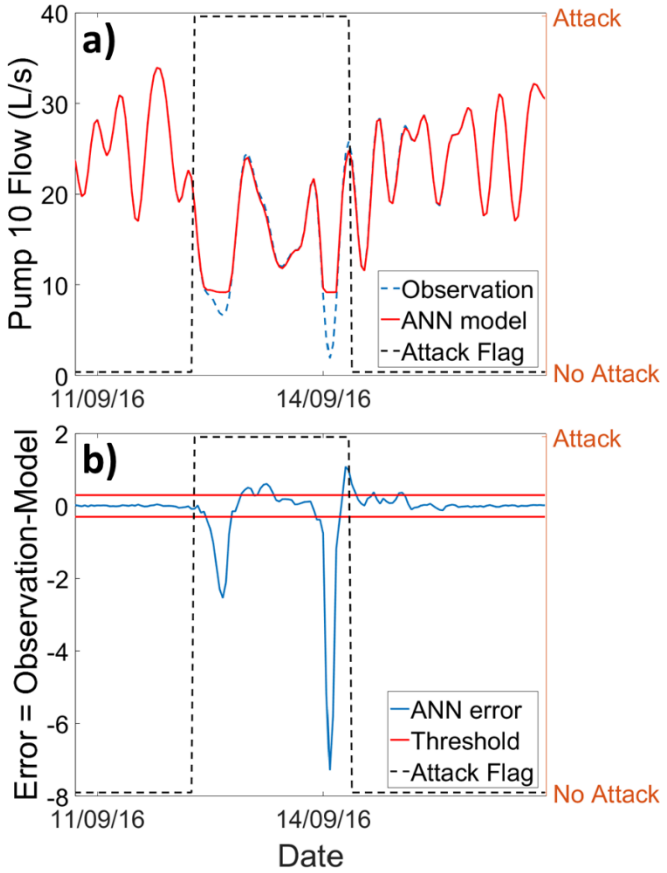

Figure I-5. (a) Smoothed data for pump 10 flow, and (b) error between observed and modeled flow by the trained ANNs.

Module 4: detection of global anomalies via PCA decomposition

PCA is a coordinate transformation method that has been previously used to detect traffic anomalies in networked systems (Huang et al. 2007; Lakhina et al. 2004; Lee et al. 2013). It can be used to re-map a given set of multi-dimensional data points onto new axes known as the principal components (PCs). Each PC points in the direction representing the maximum variance remaining in the data after accounting for the variance in the preceding components. Hence, the first PC captures the maximum variance in the data that can be projected on a single axis, while

the following orthogonal PCs capture the remaining variance, with each component capturing the largest variance for the next orthogonal direction. The set of M principal components $\{p_l\}_{l=1}^{M}$ is defined as (Lakhina et al. 2004):

$$p_l = \arg\max_{\|v\|=1} \left\| \left(Z - \sum_{j=1}^{l-1} Z p_j p_j^T \right) v \right\| \tag{7}$$

which can be solved by evaluating the M eigenvectors of the covariance data matrix: $\Sigma_Z = \frac{1}{N} Z^T Z$, where Z is the standardized (z-score) version of the training observations matrix A. Evaluation of the principal components and projections of the sensory data are conducted using the Statistics and Machine Learning Toolbox™ incorporated in MATLAB R2016a.

Projections on the Normal and Anomalous Subspaces

In the context of anomaly detection, PCs can be split into two sets corresponding to the normal and anomalous subspaces (Lakhina et al. 2004; Ringberg et al. 2007). The first set representing the "normal subspace" consists of the PCs that contain most of the natural variation in the data (e.g. PC1 in Figure 2). On the other hand, the rest of the PCs that only capture minimal variability are representative of the "anomalous subspace" in which the projections of anomalous observations appear more distinctive (e.g. PC2 in Figure 2). Herein, the first 14 principal components $\{p_l\}_{l=1}^{14}$ are found to capture 99% of the variance in the training data matrix, which unveils the low intrinsic dimensionality of the observations matrix. Therefore, they are considered representative of the normal subspace, while the rest of the principal components $\{p_l\}_{l=15}^{31}$ represent the anomalous subspace. To demonstrate the difference between the two subspaces, Figure 6 shows the projections of the validation dataset observations on PC1 and PC18 representing the normal and anomalous subspaces, respectively. For the projections on PC18, anomalous observations induced by the first four attacks clearly appear to have either excessively high or low

values compared to other observations reported when the system is not under attack, which facilitates their detection. On the other hand, projections on PC1 comprise no clear outliers, even during an ongoing attack, since they mostly correspond to the normal periodic patterns of the data. In this study, anomalous observations are defined as the ones yielding projections that are further than γ standard deviations above or below the mean projection ($\mu_l \pm \gamma\sigma_l$) for any of the anomalous subspace principal components.

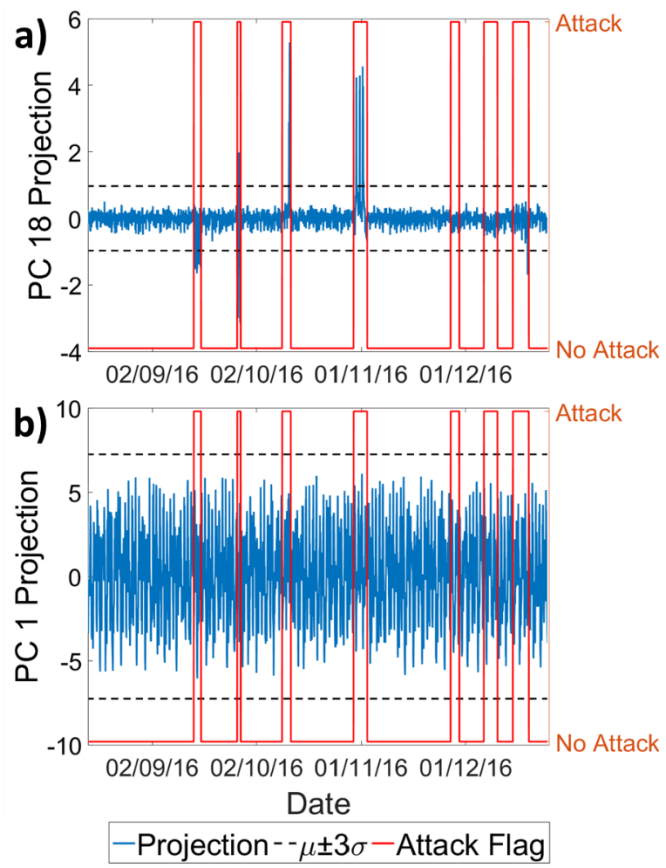

Figure I-6. Projections of the validation dataset on: (a) PC18 (anomalous subspace), and (b) PC1 (normal subspace).

Leave One Out (LOO) Approach

In addition to directly using the projections of the data points on the PCs to find anomalies, we also implement the leave one out (LOO) methodology demonstrated by Lee et al. 2013, which examines the effect of adding the observations of interest on changing the direction of the principal components. We first start by evaluating the initial PCs of the training observations matrix A. Then we proceed by adding each of the observations from the validation or test datasets to the training dataset, and then re-evaluating the principal components each time. With adding a new observation, the directions of the resulting PC vectors are expected to deviate from the original directions, and the angle of the deviation will be dependent on the outlier-ness of the added observation. Therefore, an anomalous data instance will yield a larger deviation than the one generated by adding a normal data instance as shown in Figure 7-a. The deviation can be quantified by calculating the cosine similarity between the directions of the PCs before and after adding the observation as:

$$\mathrm{Sim}_l = 1\text{-}\cos(\theta) = 1\text{-}\left|\frac{\langle p_l, \hat{p}_l\rangle}{\|p_l\|\|\hat{p}_l\|}\right| \tag{8}$$

where p_l and $\hat{p}_l$ are the principal component vectors before and after adding the data instance. According to this definition, the similarity can take any value between 0 and 1, with ($\mathrm{Sim} = 1$) corresponding to the largest deviation (i.e. p_i and $\hat{p}_i$ are orthogonal), and ($\mathrm{Sim} = 0$) representing the smallest deviation (i.e. p_i and $\hat{p}_i$ have similar orientation). Figure 7-b shows the similarity plot inflicted by the projections of the validation dataset on PC15 of the anomalous subspace. Anomalous points corresponding to attack events have clearly larger deviations relative to normal observations collected when the system is not under attack. Thus, observations having a cosine similarity more than γ standard deviations above the mean ($\mu + \gamma\sigma$) are considered anomalous.

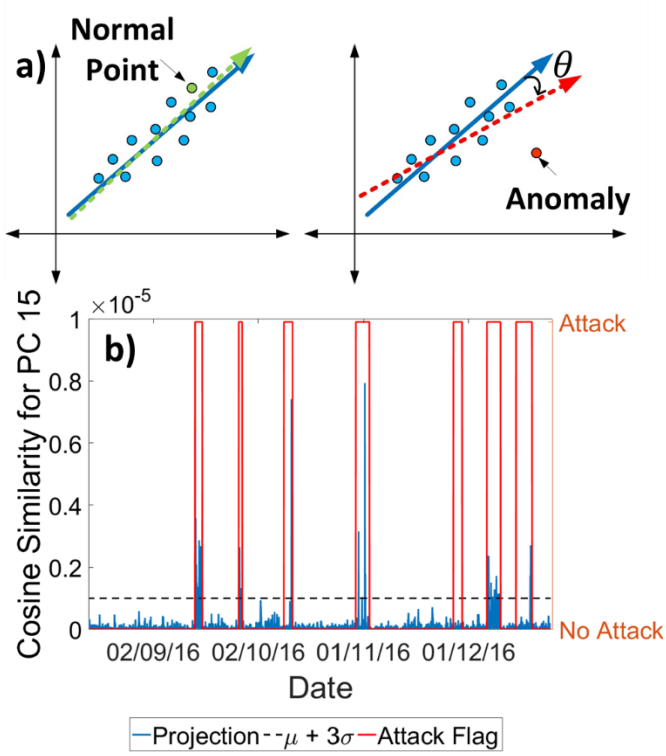

Figure I-7. (a) Schematic of the Leave One Out (LOO) method for a normal vs anomalous observation, and (b) Cosine similarity for projections on PC 15.

Integration of the four modules and real-time operation

Alarm watch *window*

The detection algorithm operates in a real-time fashion, where the time-series observations are analyzed one-by-one by each of the four modules (Figure 3). If any of the four modules discovers an anomaly in the incoming data stream, the algorithm raises a flag to mark the anomalous point. Since the anomaly can be induced either by a benign data point or by an actual attack, the algorithm puts the system under watch for a user-specific *window* time-period. If a second anomaly is detected during the watch *window*, the entire period between the first and second anomalies is flagged, and the watch is extended for another *window* starting from the second discovered anomaly. This process is repeated until no more anomalies are discovered within a *window* period

starting from the last discovered anomaly. The algorithm issues an attack alarm only if the total flagged period between the first and last discovered anomalies is longer than a user-specific threshold period, which in this study is taken equal to the *window* period for simplicity. Conversely, if no alarm is issued, the algorithm stops the watch and discards the discovered flags. Benign observations are then added to the pool of trusted data that is used to re-train modules 2, 3 and 4.

While the employed approach performs well in detecting the attacks featured in the BATADAL dataset, enhancements can still be made to the way the algorithm implements the *window* period method. For example, the frequency and magnitude of anomalies discovered during the watch *window* can be factored in. This means that anomalies simultaneously detected by more than one module, or whose deviations from the detection thresholds are very large, should have more weight in determining the existence of an attack. Another modification can be by changing the detection thresholds to become more stringent during the watch *window*. The algorithm can also use a probability-based method similar to those employed by previous studies (Arad et al. 2013; Perelman et al. 2012), which can be done by recursively updating the probability of an event with the detection of every new anomaly, using Bayes' rule for example, to decide whether an anomalous sequence of observations corresponds to an event.

Module retraining and thresholds update

To elucidate the re-training processes of the three modules, assume we start with the previously mentioned training observations matrix $A(N \times M)$. The incoming vector of observations from all monitors at the following time-step $N + 1$ can be written as $[x_{N+1,1}, \dots, x_{N+1,i}, \dots, x_{N+1,M}]$. For instance, this can correspond to the observations made by all M monitors during the first time-step in the validation or test datasets. If no anomalies are discovered, this vector is added to the training

data matrix A, thus increasing its size by one row, i.e. $([N+1] \times M)$. The user can specify the maximum permissible size for the training data matrix, beyond which, the oldest observations will be discarded to accommodate newer ones. Module 2 is re-trained by re-calculating all the previously defined statistical properties (μ_i, σ_i, $Q1_i$, and $Q3_i$) and thresholds ($n_i^{u,l}$, and $m_i^{u,l}$). For module 3, ANN models for all monitors are re-trained, and the maximum training error (ϵ_i^{train}) is re-evaluated for each monitor to update its detection threshold. Module 4 is re-trained by re-evaluating the set of M principal components $\{p_i\}_{l=1}^{M}$, and re-calculating the mean and standard deviation of the projections (μ_l, and σ_l) on the anomalous subspace PCs to update their detection thresholds. It should be noted that, while the threshold coefficients for modules 3 and 4, i.e. α and γ, are fixed throughout the process, the detection thresholds are updated during retraining since they depend on ϵ_i^{train}, μ_l, and σ_l. These dynamic thresholds are particularly useful for systems with large seasonal variations in water demands, which was not the case in the BATADAL datasets.

The frequency at which each of the three modules is re-trained using the updated data matrix is user-specific, but is also subject to some restrictions. While modules 2 and 4 can be retrained with every new row of observations added to the data matrix, re-training the ANN models is restricted by having a sequence of $I+1$ benign observations with no interrupting attacks. In addition, retraining the ANN models is the most computationally demanding among the three modules, which may limit how frequently they can be re-trained without needing additional computational resources. Algorithm users can set the initial weight coefficients for the re-training process to those of the previously trained ANN models instead of random values to reduce the computational burden. Besides, while not examined herein, users may want to periodically discard, or at least double-check, some of the anomalous observations that do not end up being labeled as attacks instead of using them for retraining. Accordingly, anomalous instances that are extremely

far from the alarm thresholds, or that raise flags by more than one module are good candidates for exclusion.

I.6 Results and Discussion

Algorithm validation and performance tuning

To assess the efficiency of the proposed technique in identifying CPAs, the trained algorithm is applied to the second (validation) dataset with seven simulated attacks (Table I-1). A combined performance metric score is implemented to quantify the efficiency of the algorithm in detecting attacks both quickly and reliably and to tune its performance by finding the best *window*.

Performance Metrics

Using a similar approach to the one adopted in the BATADAL (Taormina et al. 2018), algorithm performance is evaluated using a combined score metric (*S*) that consists of two components, namely Time-To-Detection (S_{TTD}) which reflects the time required for detecting a threat, and Confusion-Matrix (S_{CM}) which quantitatively determines the quality of recognizing true threats:

$$S = (S_{TTD} + S_{CM})/2 \tag{9}$$

The first component S_{TTD} represents the performance metric for the time to detection as a ratio of the total attack duration ΔT for all the existing attacks in the dataset:

$$S_{TTD} = 1\text{-}\frac{1}{N_A}\sum_{i=1}^{N_A}\frac{TTD_i}{\Delta T_i} \tag{10}$$

where N_A is the number of attacks. According to this definition, S_{TTD} can take any value between zero and 1, with $S_{TTD} = 0$ representing the worst case scenario where none of the attacks is detected while they are taking place (i.e. $TTD_i = \Delta T_i$), while $S_{TTD} = 1$ represents the ideal case scenario where all attacks are detected immediately (i.e. $TTD_i = 0$). The second component S_{CM}

represents the Area Under the Curve (AUC) which is a metric used to maximize true alarms while minimizing false alarms (Powers 2011):

$$S_{CM} = \frac{TPR + TNR}{2} \tag{11}$$

TPR is the Ture-Positive-Rate, which is the ratio of true positive (TP) alarms to the sum of true-positives (TP) and false-negatives (FN), and thus it represents the sensitivity of the algorithm to detect true threats. TNR is the True-Negative-Rate, which is the ratio of true negative (TN) alarms to the sum of true-negatives and false-positives (FP), and hence TNR quantifies the specificity of the algorithm in recognizing when the system is not under attack. Therefore, S_{CM} can take any value between 0 and 1, with $S_{CM} = 1$ representing and ideal case where no false positives and no false negatives are labeled by the algorithm, while $S_{CM} = 0$, represents the worst case where the algorithm can't label any true positives or negatives. Nevertheless, S_{CM} should practically be greater than 0.5, which is the score achieved by a naïve algorithm that predicts that the system is under attack at all times. Hence, the overall performance score should take a value in the range [0.75-1] for the detection technique to be deemed successful.

Attack detection performance

Figure 8-a shows a plot of the attacks detected by the algorithm compared to the actual attacks in the validation dataset. As can be seen from the figure, the algorithm is able to detect all the seven simulated attacks, together with one false attack of a relatively shorter duration (between the fourth and fifth attacks). For all the detected attacks, the algorithm labels the start of the threat almost at, or even slightly before, the official attack start-time. This means that the time to detection (the time needed by the algorithm to recognize an attack) is near zero for all the labeled attacks ($\forall\ i, TTD_i \cong 0$), which is translated to a high *TTD* score of ($S_{TTD} = 0.984$). This can be attributed to the fact that an alarm watch is immediately triggered at the detection of the first anomaly, which

may happen to be induced by a benign observation right before the beginning of the attack. This is followed by the discovery of other anomalies during the *window* period, which are combined by the algorithm and are eventually translated into a labeled attack. Additionally, Figure 8-a shows that the algorithm is able to maintain the true alarm status for as long as the actual attack is still active. This is mainly because the algorithm extends the watch period until no extra flags are discovered within a similar *window* starting from the last discovered flag. However, this also leads to the algorithm falsely extending the alarm periods for a few time steps after the formal end of the actual attack for most attacks (attacks 1, 3, 5 and 6).

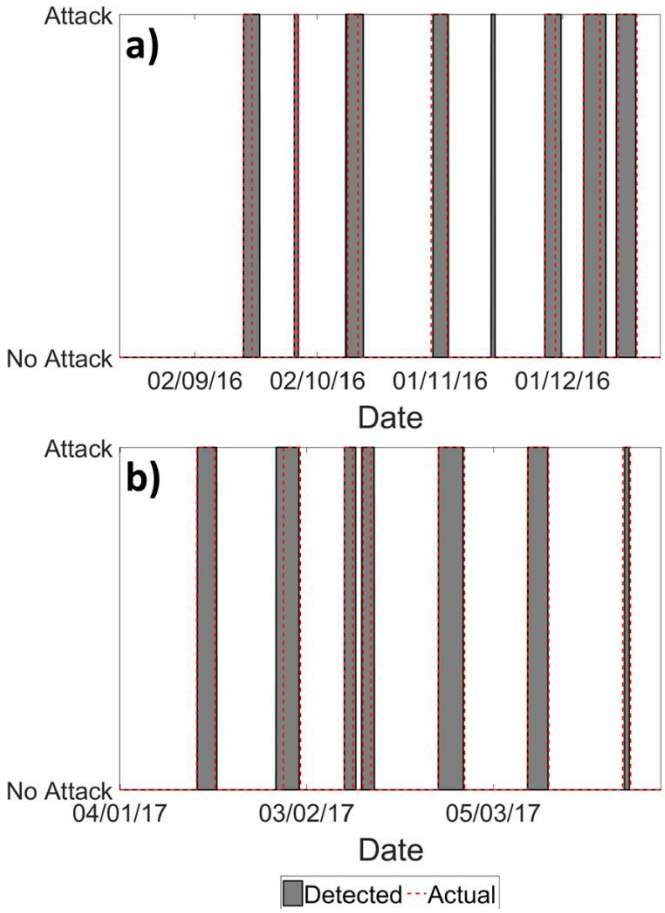

Figure I-8. Detected vs. labeled attack for: (a) validation dataset, and (b) test dataset.

It is noteworthy that the time-to-detection (TTD) as defined in the BATADAL does not reflect the practical time taken by the proposed algorithm when operated in a real-time fashion. This is because the attack alarm is issued after a *window* period has elapsed starting from when the first anomaly is discovered. Nevertheless, since the algorithm was able to label all the simulated attacks at or before their actual start, the practical TTD for real-time operation is expected to be less than the *window* period.

For the validation dataset, the confusion matrix score of the algorithm is slightly less than the time to detection score ($S_{CM} = 0.953$), which is attributed to its low true negative rate ($TNR = 0.946$). This is due to the relatively large number of false positives ($FP = 4.764\%$) that mainly correspond to the extended alarm periods after the end of the true attacks as well as the one false attack detected. Nevertheless, the algorithm has a significantly lower number of false negatives ($FN = 0.479\%$), which is more essential since undetected attacks can yield serious consequences if they resulted in physical damage to the infrastructure or if the water quality is compromised. The overall performance score of the algorithm for the validation dataset is sufficiently close to unity ($S = 0.968$), indicating a satisfactory performance.

Role of each module

Figure 9 shows the attacks detected by each of the four modules for the validation dataset. It can be seen that, for most of the detected attacks, each module was able to pick up some of the anomalies. Nevertheless, none of the modules was able to detect all of the seven simulated attacks independently. Thus, compiling the flags detected by all four modules is necessary to detect all attacks with high speed and reliability. The third and fourth modules (ANNs, and PCA) appear to be the most efficient in terms of accurately detecting most of the attacks at the right start times, while each of the first and second modules fully detected only two of the seven attacks. Moreover,

the drop in the calculated performance score when only the third and fourth modules are used to detect attacks is negligible ($S = 0.966$), reflecting the dominance of the ANN and PCA methods.

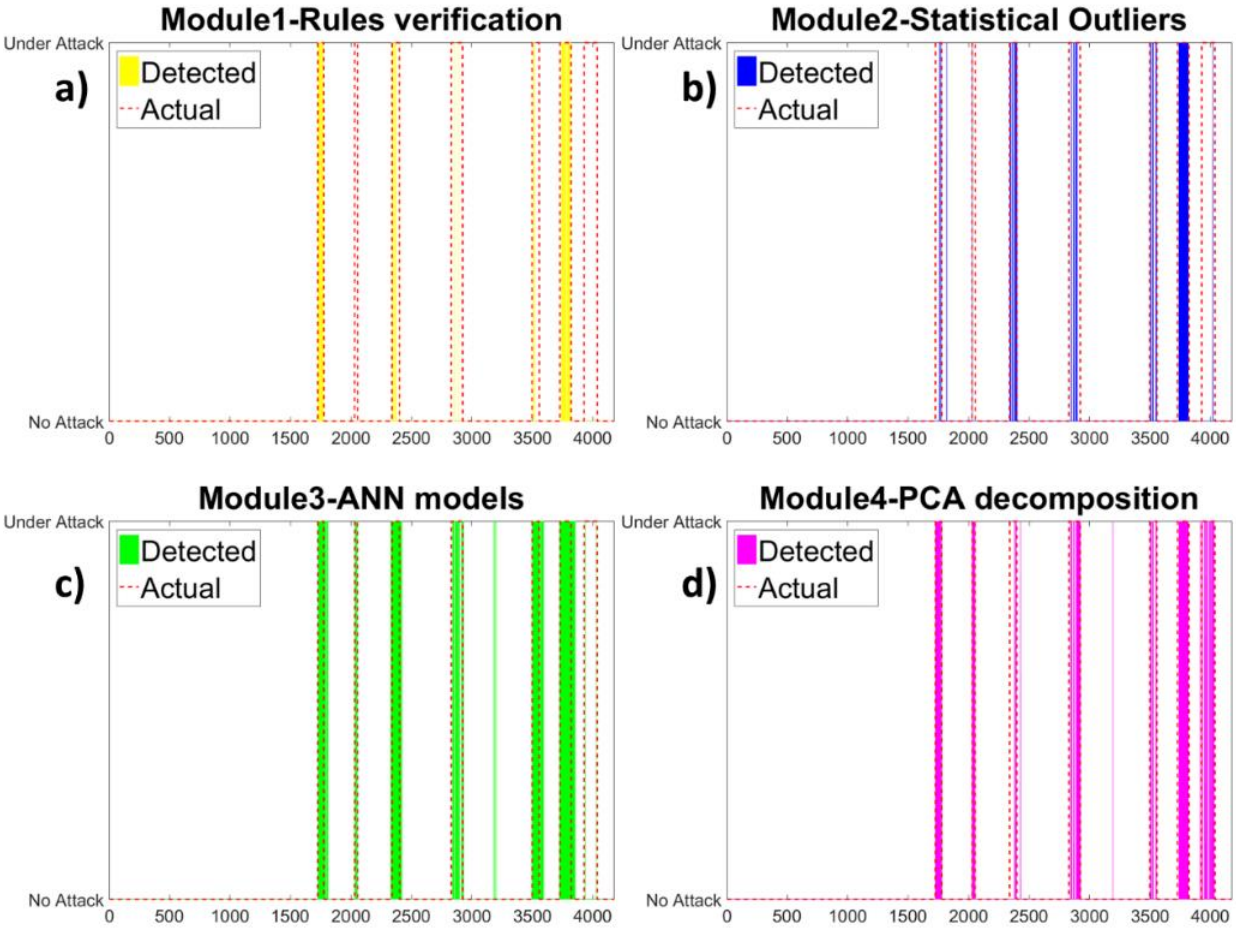

Figure I-9. Role of each module in attacks detection for the validation dataset

It is worth mentioning that the fourth module (PCA) is the only one that appropriately detected the seventh attack event, while the three other modules failed to detect it even partially. During this attack, the individual behavior of each of the attacked network elements does not

display any exceptionally suspicious inconsistencies due to attack concealment. Nevertheless, projecting their combined data on the principal components of the anomalous subspace shows a clear anomalous sequence during the seventh attack event (Figure 10). PCA was able to detect this attack since it takes into consideration the naturally existing correlation between the collected readings from different sensors in order to identify anomalous behaviors that can go undetected when data from each sensor is only analyzed independently. While this demonstrates the critical role of the fourth module in detecting such global anomalies, it is important to note that the PCA module also yields a group of sporadic falsely labeled flags induced by benign observations. However, most of these flags are eventually discarded by the algorithm because they are not typically followed by any more flags within the *window* period.

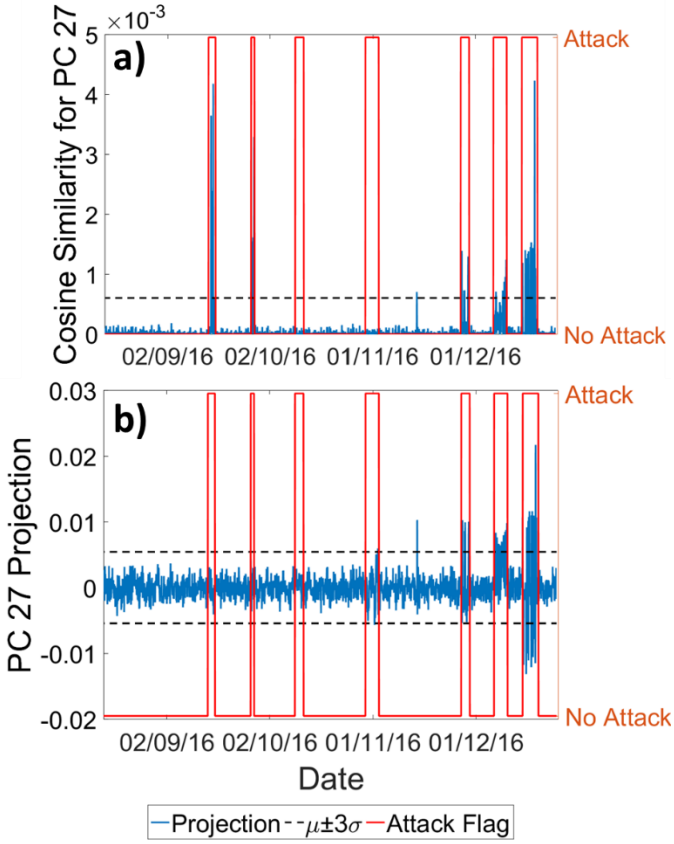

Figure I-10. PCA for the detection of seventh attack in the validation dataset in which the affected system components were concealed by the attacker

Optimal alarm *window*

The fact that the algorithm flags some of the benign observations sheds light on two important aspects of the proposed approach: (i) the sensitivity of the detected outliers to the threshold limits, and (ii) the effect of the *window* size on the algorithm performance. It is imperative that using a more stringent threshold criteria for defining an anomalous observation would typically improve the detection of attacks by minimizing the number of false negative alarms, yet, this would also lead to a higher number of false-positive alarms because noisy observations that do not necessarily correspond to an attack can still be flagged. Therefore, before applying the algorithm to new datasets, calibration should be conducted to draw the appropriate line between normal and anomalous data instances based on the characteristics of the system. While the second module requires no calibration since the detection thresholds ($n_i^{u,l}$, and $m_i^{u,l}$) are defined based on the maximum and minimum values in the training dataset, the threshold coefficients for the third and fourth modules, i.e. α and γ, require calibration. In this study, these parameters were selected by enumeration to yield the best performance for each module separately ($\alpha = 5$, and $\gamma = 3$). Another alternative to this approach is to use a different threshold coefficient for the ANN model of each monitor $\{\alpha_i\}_{i=1}^{M}$, as well as each principal component $\{\gamma_i\}_{i=1}^{M}$ instead of the global settings used herein. While this will increase the number of calibration parameters from two to $2M$, it is expected to enhance the performance of the algorithm. An optimization routing, e.g. genetic algorithm, can be used to perform the calibration instead.

A similar effect can also be inflicted by the chosen *window*, since a larger *window* means that the system is put under an alarm watch for extended periods of time even when no flags are being detected. On the other hand, a shorter *window* can result in missing most of the attacks since the majority of the flags will be discarded within a short period if no more flags are discovered.

Figure 11-a shows the effect of the size of the alarm-watch *window* period on each of the three performance metrics. It demonstrates that an optimal *window* period can be selected to achieve the best performance, while smaller and larger windows would generally yield less accurate results. It is noteworthy here that finer sampling frequencies can enable the users to choose a shorter *window* without compromising on the accuracy. This will shorten the delay period before an attack alarm is issued after a series of anomalous observations is detected.

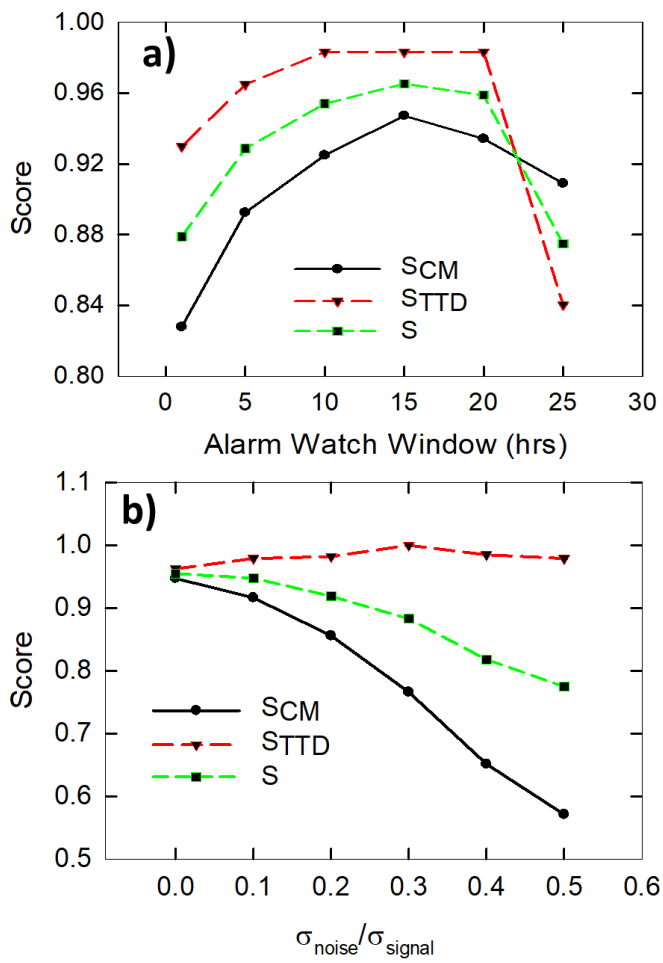

Figure I-11. (a) Sensitivity analysis for the *window* period selection for the validation dataset, and (b) Effect of measurement noise on detection performance for the test dataset.

Attack localization

Only the first three modules of the detection algorithm are capable of attack localization, which is identifying the actual components of the cyber-physical system that were directly targeted or affected by the attack. This is because they rely on analyzing the data from each sensor/actuator individually, while the fourth module (PCA) only recognizes global anomalies without specifying which component is the actual source of the anomaly. For all the detected attacks, the algorithm picks anomalies in the observations obtained from multiple sensors/actuators at the same time; however, most of these anomalies are typically concentrated in the data from only two or three elements. Table I-3 lists the localized attacks as identified by the algorithm from the anomalies in the validation dataset, while Table I-1 shows the actual attacked components during each attack scenario. For instance, during the first attack, the water level information of Tank 7 is manipulated, which jeopardizes the operations of Pumps 10 and 11. While the algorithm does not specify Tank 7 as an attacked component, it still discovers the inflicted anomalous observations in the flow of the corresponding pumps. Thus, for this attack, the algorithm can only give multiple probable scenarios without necessarily specifying which one is true. For example, the detected anomalies can correspond to a direct attack on the actuators connected to the pumps, the manipulation of the connection between Tank 7 sensor (PLC9) and pumps actuators (PLC5), or a direct attack on the tank sensor (PLC9). Similarly, for most of the attacks, the algorithm is able to identify either the actual targeted components or the sensors/actuators that immediately control or are controlled by its operation. However, this is not the case for the fourth attack, where the readings of Tank 1 level sent to PLC2 are manipulated and the operation of pumps 1 and 2 is compromised, yet the corresponding anomalies are picked up from multiple elements. The majority of these anomalies are concentrated in the suction pressure observations of Valve 2 and pumping stations 4 and 5,

which are distributed across more than one PLC, and do not have any common connectivity with the truly targeted components (Table I-1). Thus, for this attack, the algorithm is neither able to localize the actual attacked components, nor the immediately affected ones. Still, such confusion is expected based on the study of Taormina et al. (2017), where they showed that the same hydraulic response for the WDS can be reached due to drastically different attack scenarios.

Table I-3. Attack localization results for the validation and test datasets

Dataset	Att#	Detected Attack Components
Validation	1	PU11 Flow / PU10 Flow / PS5 DP
	2	PS5 DP
	3	T1 Level / PU1 Flow / PS1 DP / V2 SP
	4	V2 SP / PS5 SP / PS4 SP
	5	PU6 Flow / T4 Level
	6	PU6 Flow / PU7 Flow
	7	PS3 DP
Test	1	PS2 DP
	2	V2 DP / PS2 SP / PS3 SP / PU7 Flow / T2 Level
	3	PU3 Flow / PU2 Flow
	4	PU3 Flow / PU1 Flow / T1 Level / PU2 Flow
	5	PS2 SP / PS3 SP / PU7 Flow
	6	PS4 SP / T6 Level / V2 SP
	7	PS3 DP

Algorithm testing and effect of measurement noise

Detecting Attacks in the test dataset

The tuned algorithm is finally tested against the third test dataset containing approximately 3 months of observations and featuring seven different attack scenarios (Table I-2). This fresh dataset has not been involved in either the training or the validation of the algorithm and thus can reflect the actual performance in detecting CPAs in new observations. Figure 8-b displays the actual attacks featured in the dataset plotted against the attacks detected by the algorithm. Similar to the validation dataset, the algorithm detects all the seven attacks in the test dataset demonstrating high detection efficiency. In addition, the algorithm identifies the existence of the threat at or before the formal start time of the actual attack for most of the attacks. Nevertheless, the time-to-detection score for the test dataset ($S_{TTD} = 0.963$) is clearly less than the validation dataset. This can be attributed to the delay encountered in detecting the seventh attack, which also happened to be the shortest attack in the test dataset resulting in a high ($TTD_i/\Delta T_i$) ratio. Although the percentage of false positives in the test dataset ($FP = 3.159\%$) is less than that encountered in the validation dataset, the confusion matrix score for the test dataset ($S_{CM} = 0.947$) is still lower than the validation dataset. This is mainly because the test dataset yields a higher percentage of true negatives ($FN = 1.292\%$) than the validation dataset due to the delayed identification of the seventh attack scenario. Thus, the overall performance score of the test dataset (S=0.955) is lower than that of the validation dataset, which is expected since the selection of the *window* period was conducted for the latter.

By inspecting the labeled attacks by each of the four modules for the test dataset, it was clear that the fourth module (PCA decomposition) is the most efficient in appropriately detecting all the seven attacks. Similar to the validation dataset, PCA was the only module capable of

detecting the sixth attack that induces only minor anomalies in the observations of each individual sensor/actuator due to concealment, and thus can only be discovered by a coordinate transformation method. It is worth noting that the first module does not detect any attacks in the test dataset since during the attacks all the actuator rules were precisely followed. This scenario can take place if the attacker had intimate knowledge of the system, which could be gained through eavesdropping on network communications. This allows the attacker to conceal the apparent sensor/actuator readings to obey the rules at all times, corresponding to a highly sophisticated attack. Table I-3 lists the localized attacks as identified by the algorithm from the anomalous observations in the test dataset. Similar to the validation dataset, the algorithm identifies the actual compromised or the immediately affected network components for the majority of the attacks.

Effect of noise

Since the algorithm adopts a "data-based" approach for the detection of cyber-physical attacks by isolating anomalous observations, it is important to test its robustness against outliers caused by measurement noise that does not necessarily correspond to an attack. So far, the datasets that were used in the training, validation, and testing of the algorithm are considered to correspond to a group of perfect monitors. However, a real-life sensor signal will typically constitute some degree of undesired noise that either takes the form of a continuous or a semi-continuous uniform background noise, or can be a group of outliers with different magnitudes that are randomly encountered across the time series signal. The algorithm can readily isolate and discard the flags inflicted by the latter form of noise thanks to the *window* period rule as previously demonstrated. Nevertheless, the former type of uniform noise can be confusing to the detection algorithm because of its continuous nature, which might cause a series of anomalous observations that can be interpreted by the algorithm as an attack.

To test the robustness of the detection technique to sensor noise, the algorithm is applied to the test dataset after adding Gaussian background noise to the observations in the test dataset. For each observation, a noise component is randomly generated from a normal distribution with a zero mean and a standard deviation equivalent to a chosen fraction of the standard deviation of the clear signal ($\sigma_{\text{noise}}/\sigma_{\text{signal}}$) and then added to the clear signal. A range of different standard deviations is tested, starting from zero up to 0.5, which correspond to a perfectly clear signal and a highly noisy signal, respectively. Figure 11-b shows the three performance scores for each tested scenario with different ($\sigma_{\text{noise}}/\sigma_{\text{signal}}$) ratios. As expected, the detection performance of the algorithm drops as the signal noise increases. The overall performance score (S) drops consistently due to the decrease of the confusion matrix score (S_{CM}), while the time to detection score does not change much. It should be noted that for these tests, the second module (simple outlier detection) is turned off. The extended periods of anomalous observations caused by the signal noise lead the algorithm to label them as attacks, which resulted in a near trivial solution (S=0.761) for the case of $\sigma_{\text{noise}}/\sigma_{\text{signal}} = 0.5$, where the algorithm labels almost the entire simulation period as a continuous attack event. Thus, noise reduction might be crucial for successfully applying this approach if the data has a high degree of noise.

I.7 Conclusions

Implementing smart networking technologies in the sector of water infrastructure systems has expanded the domain of potential threats from the traditional risks associated with direct physical attacks that commonly aim at sabotaging the infrastructure equipment or compromising the water quality, to the risks of malicious attacks originating in the cyber-space. In this study, an algorithm is developed for the detection of cyber-physical attacks on smart water distribution systems. The algorithm employs multiple anomaly detection techniques to spot different types of

anomalous observations in the sensory data. Artificial neural network models are first trained to predict the regular patterns of the system's operation and then used to identify suspicious observations that are inconsistent with the normal behavior of the system. Principal component analysis is conducted to decompose the multi-dimensional sensory data matrix into two sub-spaces representing the normal and the anomalous projections, which efficiently discovers global anomalies that are caused by highly concealed attacks.

The algorithm performs well in detecting all the simulated attacks in the validation and test datasets with short or no delays. Nevertheless, it tends to put the system under a false attack status for a few time-steps after the real threat no longer exists. Integrating the flags detected by all modules is shown to be necessary to detect and localize all attack scenarios with high efficiency. Yet, the principal component analysis appears to be the most reliable component of the algorithm, especially in discovering stealthy attacks that induce minor inconsistencies in the sensory data because of attack concealment. For most of the identified attacks, the algorithm was generally able to localize the system elements that are impacted by the threat. Nevertheless, for one of the attacks, the algorithm could identify neither the actual targeted elements, nor those that are immediately affected by their operation, because the discovered anomalies were dispersed in the observations from multiple unrelated sensors/actuators.

The algorithm shows a robust performance in the face of mild measurement noise. However, high noise adversely affects the detection ability as the algorithm confuses the extended anomalies caused by random noise with those inflicted by an actual attack. In addition, several anomalous events can still take place during usual operation of systems, such as pipe bursts or pump shut-offs, which might be interpreted by the algorithm as a deliberate attack on the system.

I.8 Acknowledgments

Partial support from the Lucy and Stanley Lopata Endowment at Washington University in St. Louis is gratefully acknowledged.

I.9 References

Abokifa, A. A., Haddad, K., Lo, C. S., and Biswas, P. (2017). "Detection of Cyber Physical Attacks on Water Distribution Systems via Principal Component Analysis and Artificial Neural Networks." *Proceedings of World Environmental and Water Resources Congress 2017*, 676–691.

Abokifa, A. A., Yang, Y. J., Lo, C. S., and Biswas, P. (2016). "Water quality modeling in the dead end sections of drinking water distribution networks." *Water Research*, 89, 107–117.

Almalawi, A., Fahad, A., Tari, Z., Alamri, A., Alghamdi, R., and Zomaya, A. Y. (2016). "An Efficient Data-Driven Clustering Technique to Detect Attacks in SCADA Systems." *IEEE Transactions on Information Forensics and Security*, 11(5), 893–906.

Amin, S., Litrico, X., Sastry, S., and Bayen, A. M. (2013a). "Cyber security of water SCADA systems - Part I: Analysis and experimentation of stealthy deception attacks." *IEEE Transactions on Control Systems Technology*, 21(5), 1963–1970.

Amin, S. M., Litrico, X., Sastry, S. S., and Bayen, A. M. (2013b). "Cyber Security of Water SCADA Systems - Part II: Attack Detection Using Enhanced Hydrodynamic Models." *IEEE Transactions on Control Systems Technology*, 21(5), 1679–1693.

Arad, J., Housh, M., Perelman, L., and Ostfeld, A. (2013). "A dynamic thresholds scheme for contaminant event detection in water distribution systems." *Water Research*, 47(5), 1899–1908.

Broad, D. R., Dandy, G. C., and Maier, H. R. (2015). “A systematic approach to determining metamodel scope for risk- based optimization and its application to water distribution system design.” *Environmental Modeling & Software*, 69, 382–395.

Broad, D. R., Maier, H. R., and Dandy, G. C. (2010). “Optimal Operation of Complex Water Distribution Systems Using Metamodels.” *Journal of Water Resources Planning and Management*, 136(4), 433–443.

Chandola, V., Banerjee, A., and Kumar, V. (2009). “Anomaly Detection: A Survey.” *ACM computing surveys (CSUR)*, 41(3), 15–58.

Cominola, A., Giuliani, M., Piga, D., Castelletti, A., and Rizzoli, A. E. (2015). “Benefits and challenges of using smart meters for advancing residential water demand modeling and management: A review.” *Environmental Modelling & Software*, 72, 198–214.

Cunningham, J. P., and Ghahramani, Z. (2014). “Linear Dimensionality Reduction: Survey, Insights, and Generalizations.” *Journal of Machine Learning Research*, 16, 2859–2900.

DHS ICS-CERT. (2015). “U.S. Department of Homeland Security – Industrial Control Systems-Cyber Emergency Response Team, Year in Review.” *https://ics-cert.us-cert.gov/*.

Eliades, D. G., and Polycarpou, M. M. (2012). “Leakage fault detection in district metered areas of water distribution systems.” *Journal of Hydroinformatics*, 14(4), 992–1005.

Gao, W., Morris, T., Reaves, B., and Richey, D. (2010). “On SCADA control system command and response injection and intrusion detection.” *eCrime Researchers Summit, IEEE 2010*.

Hawkins, D. M. (1980). *Identification of outliers*. Springer.

Horta, R. (2007). “The city of Boca Raton: A case study in water utility cybersecurity.” *Journal - American Water Works Association*, 99(3), 48–55.

Housh, M., and Ohar, Z. (2017a). “Integrating physically based simulators with Event Detection

Systems: Multi-site detection approach." *Water Research*, 110, 180–191.

Housh, M., and Ohar, Z. (2017b). "Multiobjective Calibration of Event-Detection Systems." *Journal of Water Resources Planning and Management*, 143(8), 6017004.

Housh, M., and Ohar, Z. (2018). "Model-based Approach for Cyber-Physical Attack Detection in Water Distribution Systems." *Water Research*, 139, 132–143.

Huang, L., Nguyen, X., Garofalakis, M., Jordan, M. I., Joseph, A., and Taft, N. (2007). "In-Network PCA and Anomaly Detection." *Advances in Neural Information Processing Systems*, 19, 617–624.

Izquierdo, J., López, P. A., Martínez, F. J., and Pérez, R. (2007). "Fault detection in water supply systems using hybrid (theory and data-driven) modelling." *Mathematical and Computer Modelling*, 46(3–4), 341–350.

Jolliffe, I. T., and Cadima, J. (2016). "Principal component analysis : a review and recent developments." *Philosophical Transactions of the Royal Society A*, 374(2065), 20150202.

Kosut, O., Jia, L. J. L., Thomas, R. J., and Tong, L. T. L. (2010). "Malicious Data Attacks on Smart Grid State Estimation: Attack Strategies and Countermeasures." *Smart Grid Communications, IEEE 2010*, 220–225.

Lakhina, A., Crovella, M., and Diot, C. (2004). "Diagnosing network-wide traffic anomalies." *ACM SIGCOMM Computer Communication Review*, 34(4), 219–230.

Laszka, A., Abbas, W., Vorobeychik, Y., and Koutsoukos, X. (2017). "Synergic Security for Smart Water Networks: Redundancy, Diversity, and Hardening." *Proceedings of the 3rd International Workshop on Cyber-Physical Systems for Smart Water Networks*, 21–24.

Lee, E. A. (2008). "Cyber Physical Systems: Design Challenges." *11th IEEE International Symposium on Object Oriented Real-Time Distributed Computing*, 363–369.

Lee, Y. J., Yeh, Y. R., and Wang, Y. C. F. (2013). “Anomaly detection via online oversampling principal component analysis.” *IEEE Transactions on Knowledge and Data Engineering*, 25(7), 1460–1470.

Maglaras, L. A., and Jiang, J. (2014). “Intrusion detection in SCADA systems using machine learning techniques.” *Science and Information Conference, IEEE 2014*, 626–631.

Maier, H. R., and Dandy, G. C. (2000). “Neural networks for the prediction and forecasting of water resources variables: A review of modelling issues and applications.” *Environmental Modelling & Software*, 15(1), 101–124.

Mathur, A. (2017). “SecWater: A Multi-Layer Security Framework forWater Treatment Plants.” *Proceedings of the 3rd International Workshop on Cyber-Physical Systems for Smart Water Networks*, 29–32.

May, R. J., Dandy, G. C., Maier, H. R., and Nixon, J. B. (2008). “Application of partial mutual information variable selection to ANN forecasting of water quality in water distribution systems.” *Environmental Modelling & Software*, 23(10–11), 1289–1299.

Ohar, Z., Lahav, O., and Ostfeld, A. (2015). “Optimal sensor placement for detecting organophosphate intrusions into water distribution systems.” *Water Research*, 73, 193–203.

Panguluri, S., Nelson, T. D., and Wyman, R. P. (2017). “Creating a Cyber Security Culture for Your Water/Waste Water Utility.” *Cyber-Physical Security*, Springer International Publishing, 133–159.

Pasqualetti, F., Dorfler, F., and Bullo, F. (2013). “Attack detection and identification in cyber-physical systems.” *IEEE Transactions on Automatic Control*, 58(11), 2715–2729.

Perelman, L., Arad, J., Housh, M., and Ostfeld, A. (2012). “Event detection in water distribution systems from multivariate water quality time series.” *Environmental science & technology*,

46(15), 8212–8219.

Powers, D. (2011). “Evaluation: from precision, recall and F-measure to ROC, informedness, markedness and correlation.” *Journal of Machine Learning Technologies*, 2(1), 37–63.

Rasekh, A., Hassanzadeh, A., Mulchandani, S., Modi, S., and Banks, M. K. (2016). “Smart Water Networks and Cyber Security.” *Journal of Water Resources Planning and Management*, 142(7), 1816004.

Razavi, S., Tolson, B. A., and Burn, D. H. (2012). “Numerical assessment of metamodelling strategies in computationally intensive optimization.” *Environmental Modelling & Software*, 34, 67–86.

Ringberg, H., Soule, A., Rexford, J., and Diot, C. (2007). “Sensitivity of PCA for traffic anomaly detection.” *ACM SIGMETRICS Performance Evaluation Review*, 35(1), 109–120.

Romano, M., and Kapelan, Z. (2014). “Adaptive water demand forecasting for near real-time management of smart water distribution systems.” *Environmental Modelling & Software*, Elsevier, 60, 265–276.

Shamir, U., and Salomons, E. (2008). “Optimal Real-Time Operation of Urban Water Distribution Systems Using Reduced Models.” *Journal of Water Resources Planning and Management*, 134(2), 181–185.

Slay, J., and Miller, M. (2008). “Lessons learned from the Marchoory Water Breach.” *Critical Infrastructure Protection*, Boston: Springer, 73–82.

Sridhar, S., and Govindarasu, M. (2014). “Model-based attack detection and mitigation for automatic generation control.” *IEEE Transactions on Smart Grid*, 5(2), 580–591.

Srirangarajan, S., Allen, M., Preis, A., Iqbal, M., Lim, H. B., and Whittle, A. J. (2013). “Wavelet-based burst event detection and localization in water distribution systems.” *Journal of Signal*

Processing Systems, 72(1), 1–16.

Taormina, R., Galelli, S., Tippenhauer, N. O., Salomons, E., and Ostfeld, A. (2016). "Simulation of cyber-physical attacks on water distribution systems with EPANET." *Proceedings of the Singapore Cyber-Security Conference (SG-CRC) 2016*, 14, 123–130.

Taormina, R., Galelli, S., Tippenhauer, N. O., Salomons, E., and Ostfeld, A. (2017). "Characterizing cyber-physical attacks on water distribution systems." *Journal of Water Resources Planning and Management*, 143(5), 4017009.

Taormina, R., Galelli, S., Tippenhauer, N. O., Salomons, E., Ostfeld, A., Eliades, D. G., Aghashahi, M., Sundararajan, R., Pourahmadi, M., Banks, M. K., Brentan, B. M., Campbell, E., Lima, G., Manzi, D., Ayala-Cabrera, D., Herrera, M., Montalvo, I., Izquierdo, J., Luvizotto, E., Chandy, S. E., Rasekh, A., Barker, Z. A., Campbell, B., Shafiee, M. E., Giacomoni, M., Gatsis, N., Taha, A., Abokifa, A. A., Haddad, K., Lo, C. S., Biswas, P., Pasha, M. F. K., Kc, B., Somasundaram, S. L., Housh, M., and Ohar, Z. (2018). "The Battle of the Attack Detection Algorithms: Disclosing Cyber Attacks on Water Distribution Networks." *Journal of Water Resources Planning and Management*, Accepted(DOI: 10.1061/(ASCE)WR.1943-5452.0000969).

Appendix II

List of Codes

A number of computer codes and simulation programs have been developed throughout the work presented in this dissertation. A subset of these codes and programs are available for download from the author's profile on GitHub: **https://github.com/aabokifa**

A list of the developed codes and programs, along with a brief description of each, is provided below.

1- WU-DESIM: (Washington University - Dead End SIMulator)

A C++ code linked to EPANET programmers' toolkit. The program simulates the water quality in the dead-end pipes of any given distribution system while accounting for solute dispersion and the realistic spatial distribution of the flow demands along the dead-end pipe.

2- WU-MSRT (Washington University - Multiple Species Reactive Transport)

A MATLAB code for simulating the reactive transport of multiple species in the pipes of water distribution systems. The code numerically solves the coupled advection-dispersion-reaction equations for all the different constituents in two compartments: bulk flow and biofilm.

3- WU-LRSIM (Washington University-Lead Release SIMulator)

A MATLAB/C++ code for simulating the release and transport of dissolved and particulate lead from lead service lines. The code numerically solves the 2-D convection diffusion equation for both dissolved and particulate lead suspended in the bulk flow, and the mass balance for the releasable lead particulates attached to the LSL wall.

4- WU-ADAL (Washington University- Attack Detection ALgorithm)

A MATLAB code for the real-time identification of cyber-physical attacks on smart water distribution systems. The code integrates trained Artificial Neural Network (ANN) models and

Principal Component Analysis (PCA) to detect suspicious behaviors in the different components of the distribution system resulting from cyber-based attacks on the SCADA system.

Curriculum Vitae

Ahmed A. Abokifa

Ph.D. Candidate
Department of Energy, Environmental & Chemical Engineering
Washington University in St. Louis
Campus Box 1180, One Brookings Drive, St. Louis, MO 63130
E-mail: ahmed.abokifa@wustl.edu; Phone: +1 (314) 585-9634

Education

Ph.D. **Washington University in St. Louis** *Anticipated:* ***2013-2018***
Energy, Environmental & Chemical Engineering (EECE)

M.Sc. **Cairo University** ***2011-2013***
Irrigation and Hydraulics Engineering, Civil Engineering Department

B.Sc. **Cairo University** ***2007-2011***
Civil Engineering

Research Experience

Doctoral Research

Thesis: "*Developing Multi-Scale Models for Water Quality Management in Drinking Water Distribution Systems*"
Advisor: Prof. Pratim Biswas

- Developed a mathematical model for simulating the transport and interactions of multiple biochemical species in drinking water distribution systems to investigate disinfection byproducts formation from the reaction of chlorine with biofilm-derived precursors.
- Created a mathematical model for simulating dissolved and particulate lead release and transport into drinking water from lead service lines considering realistic water use patterns.
- Created an advanced water quality modeling approach for the low-flow sections of drinking water distribution systems considering accurate spatiotemporal distribution of flow demands.
- Studied the optimal design and operation of booster chlorination systems in water distribution networks using an advanced advection-dispersion multi-species water quality model.
- Developed an algorithm for the real-time identification of cyber-physical threats on water distribution systems using multiple layers of machine-learning anomaly detection techniques.
- Investigated the surface chemistry of nanostructured SnO_2 sensors to elucidate their room temperature sensing mechanisms towards disinfection byproducts using molecular simulations.

Masters Research

Thesis: "*Modeling Soil Aquifer Treatment Processes during Managed Aquifer Recharge considering Soil Heterogeneity and Parametric Uncertainty*"
Advisor: Prof. Ahmed E. Hassan

- Developed a model for simulating the subsurface transport and attenuation of organic micropollutants, such as pharmaceuticals and endocrine disruptors, during soil aquifer treatment processes associated with managed aquifer recharge of treated wastewater effluents.
- Implemented a Monte-Carlo framework to study the uncertainty in the removal efficiency considering a range of operational scenarios, various contaminant compounds, and heterogeneity in the unsaturated zone soil conditions.

Teaching Experience

Washington University in St. Louis - *Co-instructor*

Thermodynamics II - EECE 204	(SP 2017)

Washington University in St. Louis - *Teaching Assistant*

Modeling and Computing in Chemical Engineering – ChE 275	(SP2015)
Transport Phenomena – ChE 367	(FL2014)

American University in Cairo - *Teaching Assistant*

Design of Water Resources Systems – CENG 472	(SP2013)

Cairo University - *Teaching Assistant*

Engineering Hydraulics	(FL2012)
Coastal and Harbor Engineering	(SP2012)
Design of Irrigation Structures	(SP2012)
Engineering Hydraulics	(FL2011)
Water Resources Engineering	(FL2011)

Teaching Programs and Certificates

Preparation in Pedagogy	Washington University in St. Louis	2016-2018
WU-CIRTL Associates	Washington University in St. Louis	2016-2018

Honors and Awards

2018 Graduate Student Teaching Award of EECE Dept., Washington University in St. Louis

2018 Innovyze Excellence in Computational Hydraulics/Hydrology Award from AAEES/AEESP

2017 Best Presentation Award, Mid-American Environmental Engineering Conference (MAEEC)

2017 Graduate Student Research Award of EECE Dept., Washington University in St. Louis

2017 Second Place Award, Battle of the Attack Detection Algorithms (EWRI Congress 2017)

2017 Invited Judge for the St. Louis Area Undergraduate Research Symposium (STLAURS)

2013 Henry G. Schwartz Jr. Graduate Fellowship, EECE Dept., Washington Univ. in St. Louis

2012 Irrigation and Hydraulic Engineering Department Graduate Scholarship, Cairo University

2011 Best Graduation Project Award (Design of Irrigation Systems & Hydraulic Structures)

2011 Graduation with Honor – 5th Rank Award (Top 1%), Civil Engineering, Cairo University

Journal Publications

[1] A. A. Abokifa, Y. J. Yang, C. S. Lo, P. Biswas. Water Quality Modeling in the Dead End Sections of Drinking Water Distribution Networks. ***Water Research*** 2016, 89, 107-117.

[2] K. Haddad, **A. Abokifa**, S. Kavadiya, T. S. Chadha, P. Shetty, Y. Wang, J. Fortner, P. Biswas. Growth of Single Crystal Oriented SnO_2 Nanocolumn Arrays by Aerosol Chemical Vapour Deposition. ***CrystEngComm*** 2016, 18 (39), 7544-7553.

[3] A. A. Abokifa, Y. J. Yang, C. S. Lo, P. Biswas. Investigating the Role of Biofilms in Trihalomethane Formation in Water Distribution Systems with a Multicomponent Model. ***Water Research*** 2016, 104, 208-219.

[4] A. A. Abokifa and P. Biswas. Modeling Soluble and Particulate Lead Release into Drinking Water from Full and Partially Replaced Lead Service Lines**.** ***Environmental Science & Technology*** 2017, 51 (6), 3318-3326.*

*featured in several news outlets (https://acs.altmetric.com/details/17123687)

[5] J. Li, H. Li, Y. Ma, Y. Wang, **A. Abokifa**, C. Lu, and P. Biswas. Spatiotemporal Distribution of Indoor Particulate Matter Concentration with a Low-cost Sensor Network. ***Building and Environment*** 2017, 127, 138-147.

[6] A. A. Abokifa, K. Haddad, J. Fortner, C. S. Lo, and P. Biswas. Sensing Mechanism of Ethanol and Acetone at Room Temperature by SnO_2 Nano-columns Synthesized by Aerosol Routes: Theoretical Calculations Compared to Experimental Results**.** ***Journal of Materials Chemistry A*** 2018, 6, 2053-2066.

[7] R. Taormina, S. Galelli, ... , **A. A. Abokifa**, P. Biswas, et al. The Battle of the Attack Detection Algorithms. ***Journal of Water Resources Planning and Management*** (Accepted, DOI: 10.1061/(ASCE)WR.1943-5452.0000969)

[8] A. Maheshwari, **A. A. Abokifa**, R. D. Gudi, P. Biswas. Co-ordinated, Decentralization based Optimization of Disinfectant Dosing in Large-Scale Water Distribution Networks. ***Journal of Water Resources Planning and Management*** (Accepted – April 2018)

In peer-review

[9] A. A. Abokifa, K. Haddad, B. Raman, J. Fortner, and P. Biswas. Room Temperature Sensing Mechanism of SnO_2 towards Chloroform: *Ab-initio* Theoretical Calculations Compared to Sensing Experiments. ***Sensors and Actuators B: Chemical*** (Submitted - March 2018)

[10] A. A. Abokifa, K. Haddad, C. Lo, and P. Biswas. Real-Time Identification of Cyber-Physical Attacks on Water Distribution Systems via Machine Learning Based Anomaly Detection Techniques. ***Journal of Water Resources Planning and Management*** (Revision submitted – April 2018)

[11] K. Haddad, **A. Abokifa**, S. Kavadiya, B. Lee, S. Banerjee, B. Raman, P. Banerjee, C. S. Lo, J. Fortner, P. Biswas. SnO_2 Nanostructured Thin Films for Room Temperature Gas Sensing of Volatile Organic Compounds. ***ACS Applied Materials & Interfaces*** (Submitted – April 2018)

[12] A. A. Abokifa, A. Maheshwari, R. D. Gudi, and P. Biswas. Optimizing Booster Chlorination in Water Distribution Systems: Impact of the Dead-End Sections. ***Water Research*** (Submitted – May 2018)

Manuscripts in preparation

[13] A. Maheshwari, **A. A. Abokifa**, R. D. Gudi, P. Biswas. *Effects of water chemistry changes in the drinking water distribution system on lead concentrations at the tap – A Modeling Approach*.

[14] A. A. Abokifa and P. Biswas. *A Computational Modeling Tool for the Comprehensive Assessment of Lead Levels in Drinking Water Supply Systems.*

[15] K. Haddad, **A. A. Abokifa**, S. An, B. Raman, P. Banerjee, J. Fortner, P. Biswas. *Exploring the role of morphology and functionalization on the room-temperature gas sensing performance of graphene oxide*.

Conference Proceedings

[1] A. A. Abokifa, K. Haddad, C. S. Lo, P. Biswas. Detection of Cyber-Physical Attacks on Water Distribution Systems via Principal Component Analysis and Artificial Neural Networks. ***World Environmental and Water Resources Congress* 2017**, 676-691

[2] A. Maheshwari, **A. A. Abokifa**, R. D. Gudi, P. Biswas. Two-Point Constraint Control of Water Quality in Distribution Networks. ***15th International Computing & Control for the Water Industry Conference 2017*** (CCWI2017: F98)

[3] A. A. Abokifa and P. Biswas. Optimal Placement and Operation of Booster Chlorination Stations using an Advection-Dispersion Transport Model for Chlorine Decay in the Dead-End pipes. ***World Environmental and Water Resources Congress* 2018** (Submitted)

[4] A.A. Abokifa and P. Biswas. Planning the Post-Disaster Response and Restoration of Water Distribution Systems using Multi-Objective Evolutionary Algorithms. ***1st international Water Distribution Systems Analysis / Computing & Control for the Water Industry joint conference*** **2018** (In preparation)

Conference Presentations (First author and presenter)

[1] A. Abokifa and P. Biswas (2017) Modeling Soluble and Particulate Lead Release into Drinking Water from Full and Partially Replaced Lead Service Lines. ***Mid-American Environmental Engineering Conference****, October 2017 – St. Louis, MO.**

**Won the best presentation award*.

[2] A. Abokifa and P. Biswas (2017) A Computational Modeling Tool for the Assessment of Lead Levels in a Drinking Water Supply System. ***American Chemical Society National Meeting and Exposition****, August 2017 – Washington, D.C.*

[3] A. Abokifa et al. (2017) Detection of Cyber-Physical Attacks on Water Distribution Systems via Principal Component Analysis and Artificial Neural Networks. ***World Environmental and Water Resources Congress****, May 2017 - Sacramento, CA.**

*Won the second place award (https://batadal.net/results.html).

[4] A. Abokifa et al. (2017) WUDESIM: A Software for Water Quality Simulation in the Dead Ends of Water Distribution Systems. ***World Environmental and Water Resources Congress****, May 2017 - Sacramento, CA*

[5] A. Abokifa et al. (2016) Investigating the Role of Biofilms in the Formation of Disinfection Byproducts (DBPs) with a Multi-Component Reactive Transport Model. ***World Environmental and Water Resources Congress****, May 2016 - West Palm Beach, FL.*

[6] A. Abokifa et al. (2014) Water Quality Modeling in the Dead End Sections of Drinking Water Distribution Networks. ***Mid-American Environmental Engineering Conference****, October 2014 - Rolla, MO.*

Upcoming Presentations

[7] A. Abokifa and P. Biswas (2018). Multiscale Modeling of Dead-Ends of Drinking Water Distribution Systems: Disinfectant Transport to DBP Formation to Lead Release. ***American Chemical Society National Meeting and Exposition****, March 2018 – New Orleans, LA*

[8] A. Abokifa and P. Biswas (2018). Optimal Placement and Operation of Booster Chlorination Stations using an Advection-Dispersion Multi-Species Reactive Transport Model. ***World Environmental and Water Resources Congress****, May 2018 – Minneapolis, MN*

[9] A. Abokifa and P. Biswas (2018). Planning the Post-Disaster Response and Restoration of Water Distribution Systems using Multi-Objective Evolutionary Algorithms. ***1st international WDSA/CCWI joint conference****, July 2018 – Kingston, Canada*

[10] A. Abokifa et al. (2018). Exploring the room temperature sensing mechanism of SnO_2 nano-columns synthesized by aerosol routes towards volatile organic compounds: theoretical calculations compared to experimental results. ***AAAR 10th International Aerosol Conference (IAC),*** *September 2018 – St. Louis, MO*

Grants and Proposals

Assisted in writing

NSF	Innovations at the Nexus of Food, Energy, and Water Systems (INFEWS).	**2016**
EPA	National Priorities: Impacts of Water Conservation on Water Quality in Premise Plumbing and Water Distribution Systems.	**2016**
EPA	National Priorities: Transdisciplinary Research into Detecting and Controlling Lead in Drinking Water.	**2017**

Computational resources

Stampede, XSEDE: 500,000 core/hours to perform *ab-initio* calculations **2016**

Professional Service

2017-2018 Chair of the graduate students search committee for new faculty recruitment, Energy, Environmental, and Chemical Engineering Dept., Washington Univ. in St. Louis

2016-2017 Energy, Environmental, and Chemical Engineering Dept. graduate student representative at the Graduate Council of Washington Univ. in St. Louis

2014-2015 Graduate student search committee for new faculty recruitment, Energy, Environmental, and Chemical Engineering Dept., Washington Univ. in St. Louis

2014-Present **Journal referee** for Environmental Science and Technology; Journal of Water Resources Planning and Management; Journal of Aerosol Science; The Journal of Physical Chemistry C; Physical Chemistry Chemical Physics.